CHARACTERIZATION OF MATERIAL PROPERTIES, MICROARCHITECTURE, AND MECHANICS OF BONE FROM SUBJECTS WITH TYPE 2 DIABETES MELLITUS

A Dissertation

Presented to the Faculty of the Graduate School

of Cornell University

In Partial Fulfillment of the Requirements for the Degree of

Doctor of Philosophy

by

Heather Brittany Hunt

December 2018

CHARACTERIZATION OF MATERIAL PROPERTIES, MICROARCHITECTURE, AND MECHANICS OF BONE FROM SUBJECTS WITH TYPE 2 DIABETES MELLITUS

Heather Brittany Hunt, Ph. D.

Cornell University 2018

People with type 2 diabetes mellitus (T2DM) have normal to high bone mineral densities, but counterintuitively have greater fracture risks than people without T2DM, even after accounting for potential confounders like BMI and falls. Therefore, T2DM may alter aspects of the quality of bone, independently of bone mass, through metabolic or biochemical mechanisms as a result of a T2DM disease state. The main objective of this research was to elucidate the material factors that increase fragility in T2DM by characterizing the material properties, microarchitecture, and mechanics of bone from subjects with and without T2DM. The tissue material properties of bone from two clinical populations and from a rodent model of T2DM were evaluated, and the microarchitecture and and mechanics were evaluated for one of the clinical populations. In the rodent model of T2DM, mice with T2DM had more mineralized tissue, more mature collagen, and less heterogenous mineral properties compared to non-DM littermate controls, all of which are consistent with an older tissue that has undergone less remodeling. Tissue properties of the iliac crest from post-menopausal women varied with different stages of glycemic control, from normal glucose tolerance, impaired glucose tolerance, and overt T2DM. Glycemic derangement was associated with increased mineralization, decreased collagen maturity, and atypical

mineral maturation, all of which can alter the mechanics of bone. Finally, femoral neck cancellous bone from men with T2DM had increased mineralization, a less mature mineral, more numerous trabeculae, and greater accumulation of non-enzymatically-formed collagen crosslinks compared to men without T2DM. The mechanical properties of the T2DM specimens reflected these alterations: stiffness and strength were greater in the T2DM specimens because of the greater mineral content and improved microarchitecture. Regression modeling of post-yield toughness demonstrated a significant deleterious impact of mineral maturity and non-enzymatic crosslinks once the improvement in microarchitecture was mathematically accounted for. Together, these results indicate a beneficial effect of T2DM on cancellous microarchitecture, but a deleterious effect of T2DM on the collagen matrix and mineral maturation. In conclusion, this work aids in the understanding of how bone becomes more fragile with T2DM, and this work is clinically relevant because it demonstrates that different populations of T2DM patients may have distinctly different bone fragilities as a result of varying tissue composition and microarchitecture.

BIOGRAPHICAL SKETCH

Heather Brittany Hunt was born and raised in Colorado where she grew up skiing in Breckenridge, exploring the United States Air Force Academy gyms and chemistry labs, and playing sports along the Front Range. She is the second youngest of seven children and an extrovert who loves to be around family and friends.

Heather graduated with her B.S. in Engineering Physics at the Colorado School of Mines in 2012. For three years, she worked in the joint labs of Dr. Thomas Furtak and Dr. Reuben Collins where she learned semiconductor fabrication and characterization for photovoltaic applications. During her time at the Colorado School of Mines, Heather was an avid proponent of physics outreach for K-12 students and an honored member of the McBride Honors Society, through which she earned a minor in Public Affairs.

From the summer of 2012 to the summer of 2013, Heather worked at HRL Laboratories in Malibu, California where she fabricated semiconductor devices. Heather's mentors at HRL encouraged Heather to continue her education (hoping she would stay close and attend UCLA), and Heather ultimately decided to pursue a doctorate in Materials Science and Engineering at Cornell University.

At Cornell, Heather moved away from semiconductors and began work with Dr. Eve Donnelly studying the effects of type 2 diabetes mellitus on bone. Transitioning from fabricating electronic materials to characterizing a biological material was a giant leap; however, her tremendous mentorship and lifelong friends at Cornell and in Ithaca helped ensure her success.

Upon graduating, Heather will, again, dive into a wildly different field as she beings work as an Analyst in the Baseball Operations department with the Minnesota Twins.

For P.H.H. and F.H.M.

ACKNOWLEDGMENTS

I am full of gratitude for my mentors, colleagues, friends, and family. During the last five years, my incredible supporters were there to guide me through unsure times, to offer me a helping hand or shoulder to lean on when I needed encouragement, and to cheer me over the many hurdles of earning a doctoral degree. I am indebted to each and every one of them beyond what words can express.

First and foremost, I thank my committee members, Dr. Eve Donnelly, Dr. Lara Estroff, and Dr. Christopher Hernandez. From the start, Eve believed in my potential to learn the biology, chemistry, and mechanics of bone, despite me having an almost exclusive background in semiconductors. Eve's mentorship style towards me grew and changed as I grew and changed as a researcher, and she is undoubtedly one of my greatest advocates and allies. Lara and Chris provided unrivaled expertise in regards to biochemistry, biomineralization, biomechanics, and statistics, all of which strengthened the impact of my research and broadened our understanding of how diseases, like type 2 diabetes mellitus, can affect bone tissue. In addition to contributing to my professional development, Eve, Lara, and Chris are all staunch supporters of women and under-represented communities in STEM fields, and I have greatly benefited from their dedication and commitment to ensuring equal representation and opportunity for all. I consider my time with Eve, Lara, and Chris to be an enormous privilege, and I know their lessons, in and outside of the lab, will forever stay with me.

This research would not have been possible without the dedication of our collaborators at the Hospital for Special Surgery, Johns Hopkins Medicine, and the University of Colorado Anschutz Medical Campus. I had the incredible opportunity to work alongside Joe Lane, M.D., Adele Boskey, Ph.D., Kendal Moseley, M.D., and Karen King, Ph.D, all of whom are distinguished and consummate role models in their own right.

I cannot thank Pablo Palomino and Erik Taylor enough for making each and every day in the lab better. The three of us bickered like siblings, but we have always had each other's best interests at heart. Who knew that friendship and trust were built on donuts, Rockstars, and Gatorades?

Also, where would the Donnelly lab be without our posse of undergraduate researchers? I am proud to have mentored such promising students. Michelle Chin, Vinny Wang, Carolina Salazar, David Diaz, Jared Pearl, Sarah Burke, Nick Miller, Kim Hemmerling, Maho Koga, and Kelsie Lopez all deserve special shout-outs for their seemingly endless collecting of FTIRI data, without which this dissertation would not have been possible (at least not in under 10 years).

To my amazing friends: I could not have done this without you. Your constant presence, whether inside the lab or not, helped keep me grounded and not take myself or graduate school too seriously. I never dreamed that I would have so many fun, thoughtful, sincere, and truly brilliant people in my life, and I couldn't be more proud that most of them are women. So here's a big, gushy thank you to the following people who went above and beyond as a friend to me in the last five years: Oliver, Steph, Cristina, Abby G., Angela, Jennie, Kara, Sanlin, Kevin, Rachel, Hilary,

Duncan, Ben T., Coit, Aubryn, Abbey, Erik, Annika, Ashley, Somer, Jodi, Kim, Katie, Abby B., and Laura.

And last, but never least, I save the biggest thank you to my family and soon-to-be husband, Ben Mac Murray. I learned assertiveness, determination, and courage from my sisters, Theresa, Ashley, Leah, Nano, and Tin Cho and loyalty, honesty, and perseverance from my brothers, Tommy, Jimmy, and David. These qualities are ingrained in me, and I wouldn't be half the woman I am today without their ardent support. I am also blessed with many wonderful moms: My "real mom" encourages me to explore the edges of my abilities and shoot for the stars, my "pre-mom" is a safe haven of warmth and love, and my "bonus mom" is a constant reminder that success comes in all forms. My dad has been and always will be my number one fan and vice versa. He picks me up during the downs, raises me higher during the ups, and is anything and everything I could ask for in a father and best friend. And finally, one big last thank you to my fiancé, Ben, for being the best man in my life. Ben and I have been at each other's sides since the moment we met, and I owe him infinite gratitude for everything he does to make me a better version of myself.

TABLE OF CONTENTS

CHAPTER 1

INTRODUCTION

1.1 *T2DM and Fracture Risk*

Diabetes mellitus is an increasingly prevalent disease, and each year the economic and healthcare burden of diabetes grows. According to the Center of Disease Control's 2017 statistics, 12% of Americans have diabetes and the prevalence increases to 25% for Americans over the age of 65. Of people with diabetes, 90-95% have type 2 diabetes mellitus (T2DM), which is also known as adult-onset diabetes or non-insulin dependent diabetes.[1] People with T2DM, on average, have twice the medical expenditures per year as those without T2DM[1] and a 10 year shorter expected lifespan.[2] Cardiovascular disease is responsible for ~70% of T2DM-related mortality, and other serious health complications that are common include stroke, retinopathy, nephropathy, renal disease, cardiovascular disease, extremity numbness, and loss of limb.[1,3]

In addition to these complications, people with T2DM also have an increased risk of bone fracture compared to people without T2DM,[4–7] which can have devasting consequences for life expectancy and risk of future fractures.[8,9] A recent retrospective study showed that one-year survival probability was just 68% for people with T2DM versus 87% for people without T2DM.[9] The higher fracture incidence for people with T2DM is well-established;[4–7] however, the underlying causes for T2DM-related fragility fractures are not fully understood.

One of the main confounding factors is that people with T2DM have normal to high bone mineral density (BMD) measured by bone densitometry (DEXA),[10–12] which is typically associated with reduced fragility fracture risk. For a given BMD, however, people with T2DM have a greater fracture risk than those without T2DM.[7] The 10-year hip fracture risk for both men and women is greater for those with T2DM compared to those without T2DM, regardless of BMD, and the risk increases further for those with T2DM on insulin (Figure 1.1-1).

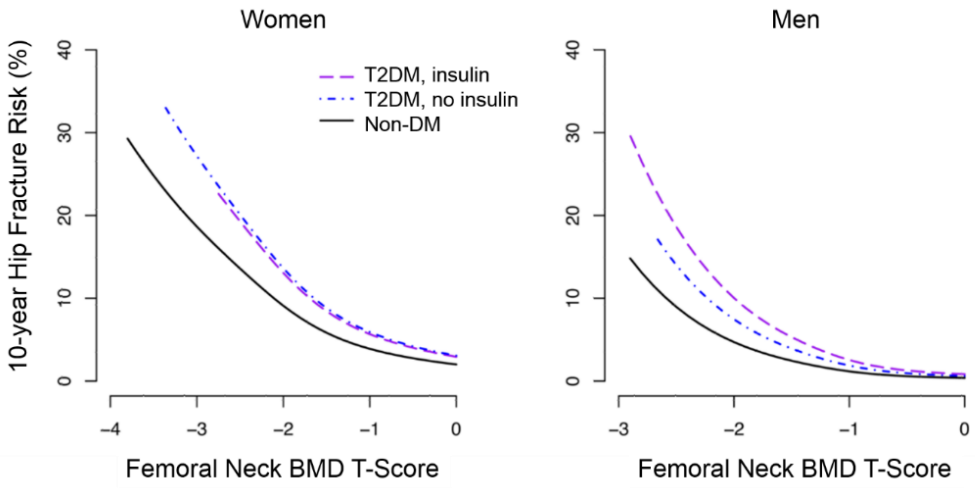

Figure 1.1-1: 10-Year hip fracture risk versus femoral neck BMD T-score for women (left) and men (right) without T2DM, with T2DM and non on insulin treatment, and with T2DM and on insulin treatment. Figure credit: adapted from Schwartz, A. V. et al. *JAMA*. (2011).

The greater fracture risk for people with T2DM that is not fully accounted by the quantity of bone (i.e., BMD) indicates that other factors influence bone fragility. These other factors are collectively referred to as bone quality and include tissue material properties, microarchitecture, and accumulation of microdamage (Figure 1.1-2).

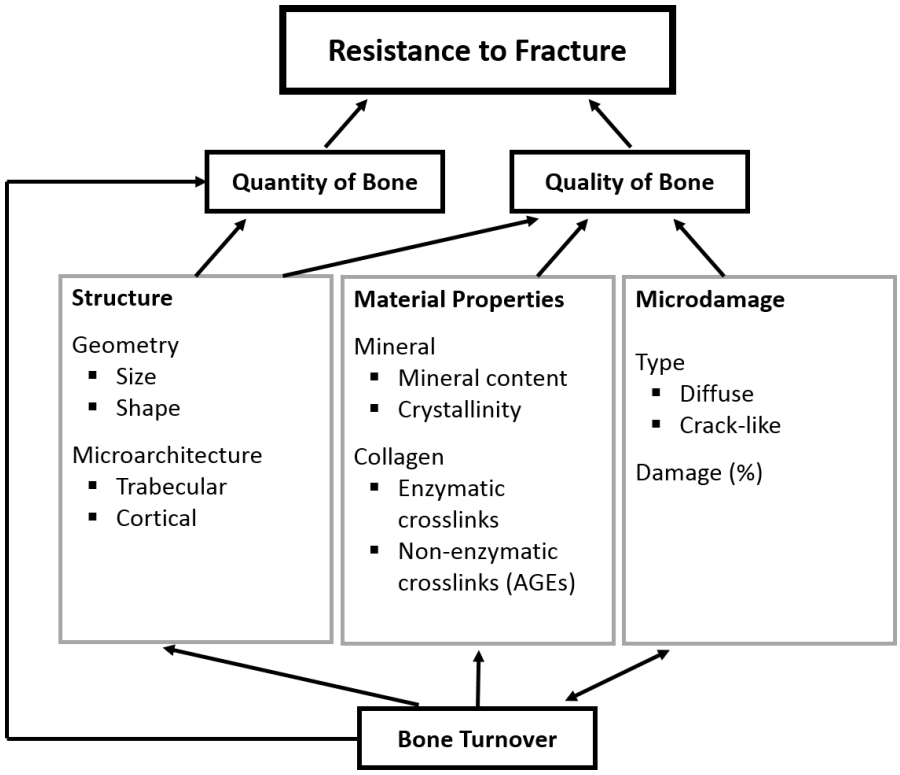

Figure 1.1-2: Bone quality is the summation of other factors that influence bone's ability to resist fracture that are not bone mass.

T2DM can alter tissue material properties and architecture by several mechanisms, including 1) hyperglycemia, 2) hyperinsulinemia, and 3) oxidative stress. Hyperglycemia, the condition of having elevated blood sugar, is hypothesized to affect bone in two main ways. The first is through disruption and suppression of bone remodeling processes, and the second is through the formation and accumulation of advanced glycation endproducts (AGEs). In contrast to hyperglycemia, insulin is an anabolic agent, and hyperinsulinemia is hypothesized to be, in part, responsible for the greater BMD observed in people with T2DM.[13] Oxidative stress, which is the imbalance of reactive oxygen species and antioxidants,[14] is hypothesized to be the pathogenic factor that leads to T2DM, first by causing insulin resistance and β-cell disfunction, then by impairing glucose tolerance.[15] Similar to hyperglycemia, oxidative stress can lead to the accumulation of AGEs, and it has also been implicated in vascular tissue damage associated with T2DM.[15] The extent to which the deleterious effects on bone of hyperglycemia and oxidative stress are balanced by the beneficial effects on bone of hyperinsulinemia is unknown, and it is possible that the effects vary with T2DM severity.

Changes in bone quality with T2DM as a result of hyperglycemia, hyperinsulinemia, or oxidative stress are believed to manifest first at the molecular level in bone.[16–18] The hierarchical structure of bone enables these molecular changes to subsequently affect macroscopic mechanical properties.

1.2 *Bone Quality and the Hierarchical Composite Structure of Bone*

Bone is a hierarchical composite structure comprised of imperfect hydroxyapatite

(HA), type 1 collagen, water, and non-collagenous proteins that aggregate into a vascularized network.[19] The organic matrix is laid down first, then it undergoes mineralization. Because bone is a hierarchical structure, small changes at the molecular-level can have drastic effects at larger length scales. Moreover, because bone is a composite structure, macroscale changes may be a result of bone quality alterations in the organic matrix or in the inorganic mineral. Figure 1.2-1 shows the hierarchical organization of bone and its constituent organic and inorganic materials.

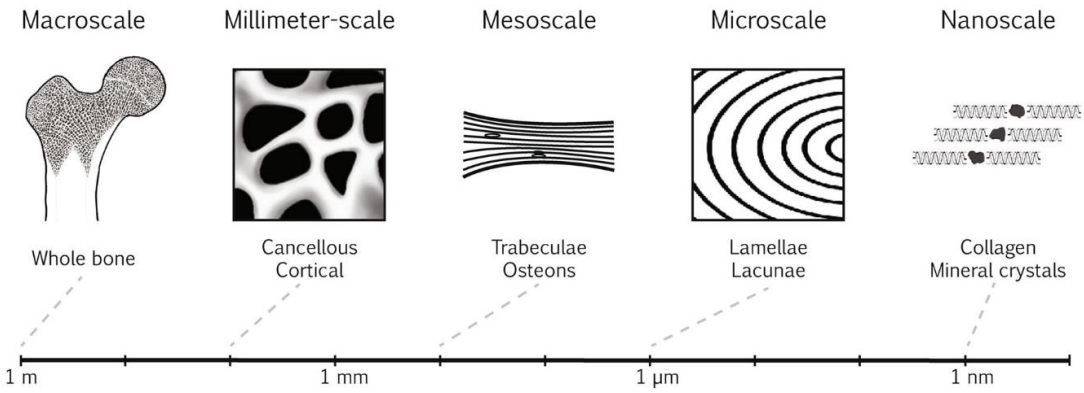

Figure 1.2-1: The hierarchical structure of bone from its constituent materials at the nanoscale (right) to the whole bone at the macroscale (left). Figure credit: adapted from Hunt, H. B. et al. *Clin. Rev. Bone. Miner. Metab.* (2016).

Bone is ~30 wt% organic matrix, 90% of which is type 1 collagen.[20] The organic matrix has highly ordered secondary and tertiary structures that are governed by the alignment of collagen molecules. Osteoblasts secrete tropocollagen, a right-handed triple helical molecule around 300 nm in length and 1.6 nm in diameter (Figure 1.2-2**Error! Reference source not found.**).[21,22] Approximately one-third of

the amino acids in type 1 collagen are glycine, which allows the individual collagen chains to compactly align and hydrogen bond within the helix; one-sixth of the amino acids are either proline or hydroxyproline; and the remaining residues are naturally occurring amino acids such as lysine and arginine, which are particularly important in post-translational processes that assemble higher level structures.[20,23,24]

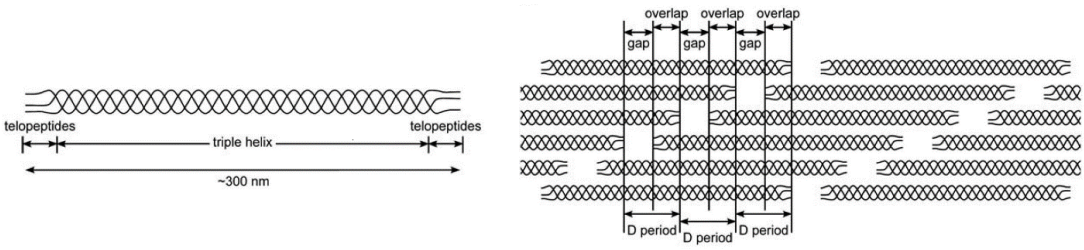

Figure 1.2-2: Triple helix structure of collagen molecule (left), staggered array of collagen molecules (right). Figure credit: adapted from Streeter, I. et al. Soft Matter. (2011).

Post-translational modifications to the osteoblast-secreted collagen molecules stabilize bone's organic matrix by chemically crosslinking adjacent molecules. Crosslink formation is initialized at the non-helical termini via enzymatic reactions of lysyl oxidase with telopeptide lysine and hydroxylysine residues (Lys and Hyl). First, lysyl oxidase deaminates the residues of Lys or Hyl producing allysine or hydroxyallysine, then two nearby allysine or hydroxyallysine residues undergo a condensation reaction that connects the two collagen molecules together with a divalent crosslink.[20] Over time, the divalent crosslink that connects the telopeptide ends of two collagen molecules matures into a trivalent crosslink by reacting with the helical portion of a third collagen molecule. The locations of the residues in immature

divalent and mature trivalent crosslinks are highly controlled and occur at specific amino acid sequences.[20]

The enzymatically controlled crosslinking described above allows for higher-ordered assembly of the organic matrix. Specifically, five collagen molecules arrange into fibrils that consist of a quarter-staggered array with a D-period of 67 nm (Figure 1.2-2), and these fibrils further assemble into larger fibers. The 67 nm D-period is maintained, such that gap channels occur throughout a fiber.[20,21,25]

In addition to enzymatic crosslinks that further stabilize the collagen matrix, non-enzymatic crosslinking can also occur. Non-enzymatic glycation (NEG), also known as the Maillard reaction, is the reaction of an amino group with a sugar (e.g., glucose, ribose).[26] The reaction between an amino group (typically on Lys or Arg) and a sugar and an creates a Schiff base, which then undergoes spontaneous Amadori rearrangement to a more stable ketosamine. Finally, a dehydration of the ketosamine into reductones or to other short-chain hydrolytic fission products produces AGEs (Figure 1.2-3).[16,27]

AGEs manifest as additional crosslinks in the collagen matrix; however, unlike the formation of enzymatic crosslinks, the location and number of AGEs are not controlled. It is therefore possible for AGEs to form between two adjacent collagen molecules or within a single collagen molecule;[28] however, it is currently unknown if AGEs can take the place of enzymatic crosslinks. In addition, there are hundreds of different AGEs, which complicates understanding of how they function and form.[26]

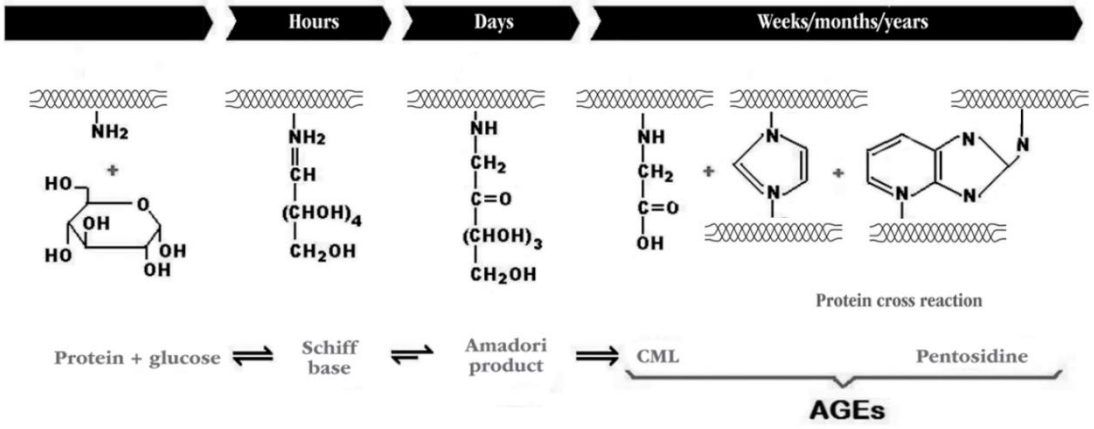

Figure 1.2-3: States of the non-enzymatic glycation reaction, or Maillard reaction. Note: The triple helix collagen molecules are not drawn to scale. CML = carboxymethllysine. Figure credit: adapted from Oliveira, E. J. Bras. Patol. e Med. Lab. (2013).

Mineralization of the organic matrix begins in the gap regions of fibrils approximately 5-10 days after the secretion of the matrix by osteoblasts.[29] The mineral in bone is nominally HA, which has the chemical formula $Ca_{10}(PO_4)_6(OH)_2$; however, biologic HA is non-stoichiometric and poorly crystalline. As a result of its large surface area, biological HA easily incorporates other ions like Mg^{2+}, Na^{+}, F^{-}, and CO_3^{2-} that are present in the surrounding extracellular fluid.[30]

HA is nucleated in an apatitic core located in the gap regions of the quarter-staggered collagen and along the fibrils. A hydration layer surrounds the apatitic core and allows for the necessary ion exchange for crystals to grow and mature.[30] Once the crystal reaches its final size, typically 95% of the theoretical maximum for the space in the collagen matrix, the hydration layer diminishes leaving just the HA. The resulting HA crystals are platelet-shaped (1-7 nm thick, 10-80 nm wide, and 15-200

nm long) and arrange themselves parallel to one other with their crystallographic c-axis aligned with the collagen's longitudinal direction.[30]

As bundles of fibrils join to create fibers, the structural organization of the tissue at this level is either lamellar or woven bone. Lamellar bone is the predominant structure in mature bone, and it is characterized by highly ordered layers, or lamellae, of bone approximately 3 μm thick.[31] The fibers within a lamellae have a primary orientation, but the orientation from one layer to the next.[31–33] Unlike lamellar bone, woven bone is poorly oriented and can be loosely packed.[32] Woven bone can be laid down very quickly and, consequently, is found in fracture callouses and embryonic bone.[31]

Lamellar bone comprises the cortical and cancellous structures from the micro-scale up to the millimeter-scale. In cortical bone, the lamellae have a cylindrical motif that surrounds osteons. In cancellous bone, the lamellae are organized in "packets" that layer into a porous network.[32] Cortical bone is more dense and is found along the outer surfaces of bones, while cancellous bone is has large, marrow-filled cavities and is found at the ends of long bones and in the center of vertebrae.[32]

1.3 *Microarchitecture, Remodeling, and Microdamage*

The microarchitectures of cortical and cancellous differ in terms of organization and porosity. Cortical bone is characterized by average cortical thickness, cortical porosity, cross-sectional area, and cortical area fraction.[34] Cancellous bone, on the other hand, is characterized by bone volume fraction, trabecular thickness, trabecular separation,

trabecular number, degree of anisotropy, connective density, and plate-like or rod-like.[34]

The microarchitecture of bone is highly influenced by the extent of remodeling, the process of old bone being replaced with new bone.[35] During remodeling, old, damaged tissue is removed by osteoclasts, and then bone-forming cells called osteoblasts are recruited to lay down the organic matrix (Figure 1.3-1).[36]

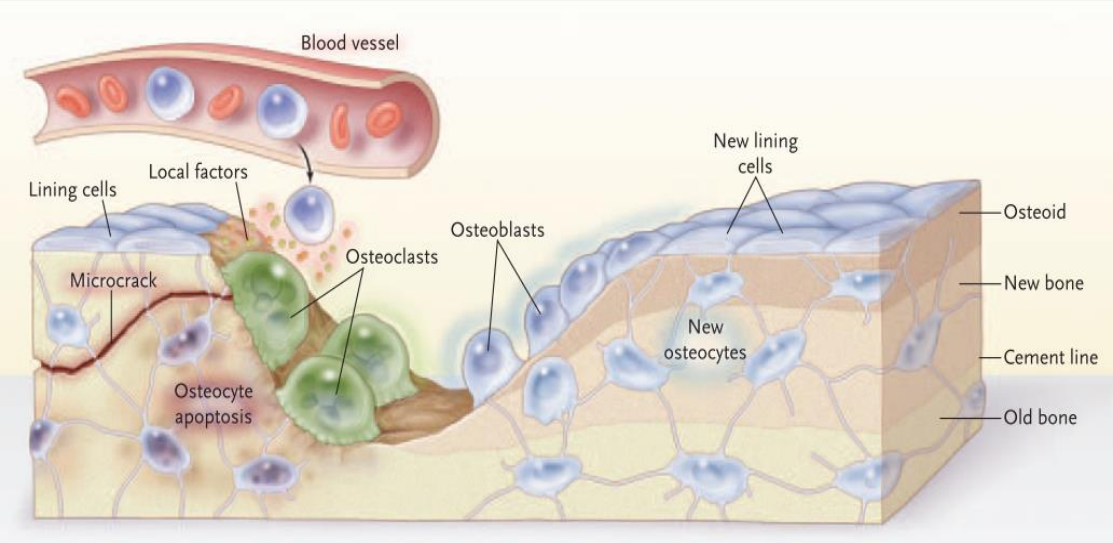

Figure 1.3-1: The cells and features of the bone remodeling process. Figure credit: Seeman et al. *N. Engl. J. Med.* (2006).

Bone is constantly remodeling, and the adult skeleton turnover rate can reach 10% each year.[37] A mismatch in bone resorption and bone formation rates within the remodeling process can lead to bone loss. For example, incomplete refilling of cavities that have been resorbed by osteoclasts leads to net bone loss over time.[35] Moreover, bone loss over time can change the structure of cancellous bone from plate-like to rod-

like, which will affect the mechanical behavior of the tissue.[38,39]

Formation of microdamage catalyzes the remodeling process. Specifically, when the osteocyte network within bone tissue is damaged and osteocyte apoptosis occurs, osteoclast resorption is signaled and quickly begins at the damage location.[40]

Microdamage accumulates in both the cortical and cancellous compartments with age.[41] Two main types of damage have been identified: crack-like and diffuse.[42] Crack-like damage indicates less energy needed to propagate a crack and is consistent with a more brittle material. Diffuse-like damage, on the other hand, is consistent with a more ductile material.[42]

1.4 *Bone Quality and its Relation to Mechanical Performance*

Bone fracture is inherently a biomechanical event;[43] therefore, the importance of bone quality measures (i.e., tissue material properties, microarchitecture, microdamage) lies in the ability of these measures to explain the mechanical performance of bone.

Bone derives its strength and stiffness from the inorganic mineral and its toughness and plasticity from the surrounding organic matrix.[44–46] Thus, alterations in the organic matrix can manifest differently than alterations in the mineral. Inhibiting the formation of mature enzymatic crosslinks from immature crosslink in rats resulted in a decrease in energy to failure, but did not change the stiffness.[47] Conversely, vitamin D deficient rats had reduced tissue mineral content, which corresponded to a reduction in stiffness and strength, yet there were minimal changes to the collagen.[48]

In addition to the degree of mineralization of bone, the extent of ion substitution, size variation, and heterogeneity of the mineral have specific implications for the functionality of the bone. In osteoporosis and aging, both of which are associated with a high fracture risk, crystal size is greater and the distribution width of crystal sizes is more narrow.[49] Larger than optimal crystals are hypothesized to affect bone's ability to respond to a load; however, these parameters have not yet been directly correlated. Moreover, the less heterogeneous crystallinity is hypothesized to decrease the fracture resistance of bone.[49]

The accumulation of AGEs is implicated for the decreased fracture resistance in aged bone as well as with T2DM.[50–52] Greater accumulation of tissue AGEs in bone from subjects with T2DM compared to controls has been reported,[53,54] and in general, more AGE crosslinks within the collagen matrix leads to a stronger, stiffer bone.[55] Just as with increased mineral content, the increase in stiffness and strength due to AGE accumulation can come at the cost bone's overall toughness.[44–46]

1.5 *Current Status of Research/Literature Review*

The effects of T2DM on bone have been studied in animal models,[53,56,57] *in vitro*,[58–61] in cross-sectional studies,[62–68] *in vivo*,[67] and recently *ex vivo* in a clinical population of patients with osteoarthritis undergoing total hip arthroplasty.[69] While all contribute to the understanding of the effects of T2DM on bone as a whole, dissimilar methods make the results of each study difficult to compare. Moreover, no direct link between alterations in bone quality and decreased mechanical performance has been formed.

Animal models of T2DM point to an accumulation of AGEs, altered collagen crosslink profiles, and reduced energy absorption capabilities compared to controls.[53,56,70] In a rodent model for T2DM, the T2DM rats became diabetic around 12 months of age which coincided with a decrease in energy absorption and maximum load and an increase in the AGE pentosidine in the T2DM rats versus age-matched controls (Figure 1.5-1: **Fasting blood glucose (upper left), pentosidine (lower left),**

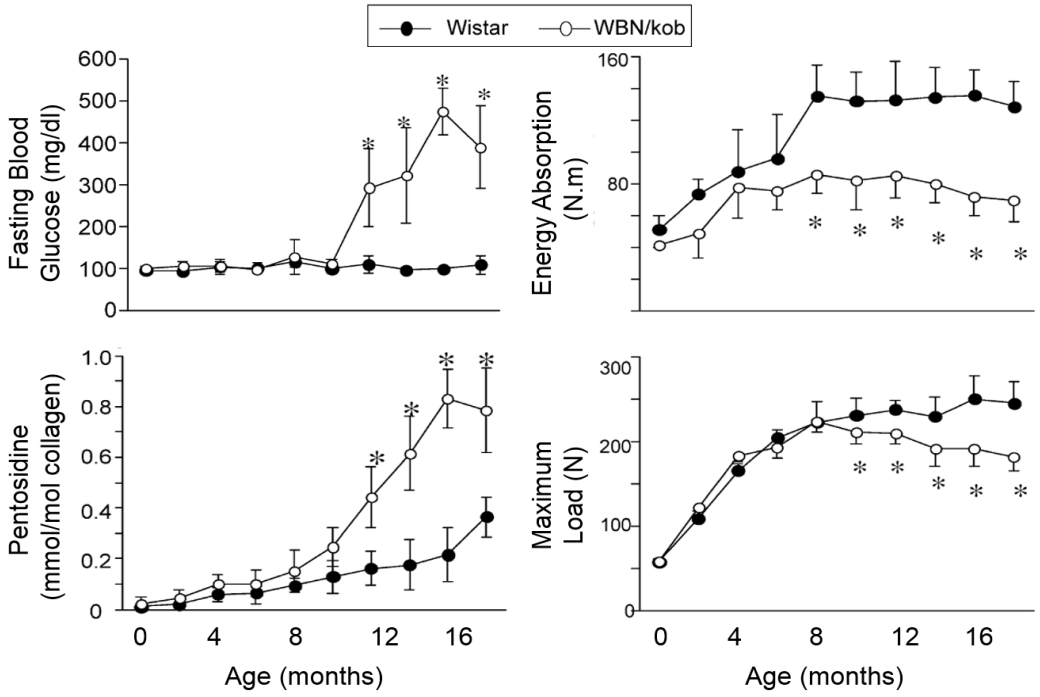

Figure 1.5-1: Fasting blood glucose (upper left), pentosidine (lower left), energy absorption (upper right), and maximum load (lower right) for T2DM WBN/kob rats versus Wistar controls. * indicates $p < 0.05$. Figure credit: adapted from Saito et al. *Osteoporo. Int*. (2006).

energy absorption (upper right), and maximum load (lower right) for T2DM WBN/kob rats versus Wistar controls. * indicates $p < 0.05$. Figure credit: adapted from Saito et al. *Osteoporo. Int.* (2006).Figure 1.5-1).

In vitro studies provide the bulk of evidence of AGE accumulation and altered remodeling processes in hyperglycemic conditions. Incubating human and bovine tissue in highly concentrated ribose and glucose solutions (at least 100x greater than physiologic conditions) have been used to study aging and T2DM, albeit much accelerated system. These studies demonstrated that AGE accumulation in cancellous and cortical bone and that tissue with higher AGE content was associated with decreased energy absorption capabilities.[58–61] Additionally, *in vitro* studies in AGE-modified collagen compared to non-AGE modified collagen report decreased osteoblast proliferation and differentiation[71–73] and decreased osteoclast differentiation,[74] which all point to a decrease in bone turnover.

In cross-sectional studies of people with and without T2DM, people with T2DM had lower bone formation markers[62–67] and bone resorption markers than those without T2DM, [65–67] and these findings were corroborated by histomorphometric analyses.[68]

To date, only one *in vivo* study has been conducted in people with and without T2DM. Using a handheld microindentation instrument known as an OsteoProbe Reference Point Indenter (RPI), the researchers indented tibial bone with a known force and correlated the displacement of the probe tip with a calibration block of plastic to calculate a bone material strength index (BMSi). Men and women with

T2DM had greater BMSi compared to those without T2DM, and the BMSi was inversely correlated with 10-year HbA1c.[67] The indentation distance of the OsteoProbe has not been validated with standard mechanical testing outcomes, thus how these results relate to stiffness, strength, and toughness is unknown.[75] Despite this limitation, this study demonstrates that worsening glycemic control is associated with mechanical performance at the tissue-level.

A recent *ex vivo* study that used explants of femoral head tissue from people with and without T2DM undergoing total hip arthroplasty analyzed serum AGEs, fluorescent tissue AGEs, microarchitecture, and mechanical performance.[69] The microarchitecture of the cortical and cancellous tissue used in this study did not differ between groups, nor did tissue fluorescent AGEs. Creep indentation distance measured with cyclic RPI in cortical tissue was greater in the T2DM group compared to the non-DM group, but no differences in stiffness, strength, or post-yield properties were observed in cancellous bone.[69] The lack of difference in mechanical properties between groups was likely due to the similarities of microarchitecture between the groups, especially in the cancellous tissue where mechanical performance is dominated by BV/TV. Moreover, the characterization of tissue material properties was limited in this study to fluorescent AGEs, so insight into how T2DM affects the organic and inorganic constituents of bone is incomplete. Nevertheless, this study adds to the understanding of bone composition, microarchitecture, and mechanics in people with T2DM.

1.6 *Research Objectives*

The objective of this work was to characterize the tissue material properties, microarchitecture, and mechanical performance of tissue from subjects with and without T2DM. The main hypothesis is that the presence of excess glucose in the blood due to hyperglycemia will alter bone's structure and composition which will in turn deleteriously affect mechanical performance.

The contributions of this work to the broader understanding of T2DM and bone fragility are: 1) this work elucidates the material factors that increase fragility in T2DM through the characterization of material properties, microarchitecture, and mechanics of type 2 diabetic bone compared to non-diabetic bone, and 2) this work relates the observed material changes to the pathophysiology of T2DM.

1.7 *Dissertation Overview and Organization*

Chapter 1, the Introduction, details the greater fracture risk in people with T2DM compared to those without T2DM, which motivates the bulk of this dissertation. The proposed mechanisms for how T2DM can change bone quality are briefly described. The constituent materials that make bone a composite material and the complex hierarchical structure of bone that spans several length scales are discussed in detail, and how these features can affect bone mechanical performance is also considered. A brief summary of the current state of relevant literature is given, followed by a statement of research objectives for this work.

Chapter 2 covers techniques available to study bone quality from geometric,

compositional, and mechanical frameworks. Many of the techniques described are utilized in subsequent chapters. This chapter was published as the following paper:[76]

> Hunt, H. B. & Donnelly, E. Bone Quality Assessment Techniques: Geometric, Compositional, and Mechanical Characterization from Macroscale to Nanoscale. *Clin. Rev. Bone Miner. Metab.* 14, 133–149 (2016).

Chapter 3 investigates the tissue material properties and AGE content in the KK-Ay mouse model of T2DM compared to littermate controls. Fourier transform infrared imaging, high-performance liquid chromatography, and fluorescence spectrophotometry were used to characterize the tissue material properties. This chapter was published as the following paper:[70]

> Hunt, H. B., Pearl, J. C., Diaz, D. R., King, K. B. & Donnelly, E. Bone Tissue Collagen Maturity and Mineral Content Increase With Sustained Hyperglycemia in the KK-Ay Murine Model of Type 2 Diabetes. J. *Bone Miner. Res*. 33, 921–929 (2017).

Chapter 4 is a clinical study characterizing the tissue material properties in cortical and cancellous tissue from women with varying levels of glucose derangement. Post-menopausal women were recruited and assigned to the following groups: normal glucose tolerance, impaired glucose tolerance, and T2DM. This study is the first to capture the intermediate impaired glucose tolerance group. This chapter is the basis for the following paper in preparation:

> Hunt, H. B., Miller, N. A., Hemmerling, K.J., Koga, M., Lopez, K. A.,

Moseley, K. F. & Donnelly, E. Bone tissue composition in post-menopausal women varies with glycemic control from normal glucose tolerance to type 2 diabetes mellitus. *J. Bone Miner. Res.* (2019).

Chapter 5 is a clinical study characterizing the tissue material properties, microarchitecture, and mechanical performance of cancellous bone from men with and without T2DM. This study was the first to characterize the mineral and collagen components of tissue from humans with T2DM and the first to report significant differences in tissue AGE accumulation in human tissue between humans with and without T2DM. This chapter is the basis for the following paper that has been submitted and is in review:[77]

Hunt, H. B. et al. Altered tissue composition, microarchitecture, and mechanical performance in cancellous bone from men with type 2 diabetes mellitus. *J. Bone Miner. Res.* (2018).

Chapter 6 summarizes and discusses the key results of Chapters 2-5 and proposes directions for future research.

1.8 *References*

1. Centers for Disease Control Prevention. *Diabetes 2014 Report Card*. *Cdc* **TTY,** (2014).
2. Leal, J., Gray, A. M. & Clarke, P. M. Development of life-expectancy tables for people with type 2 diabetes. *Eur. Heart J.* **30,** 834–839 (2009).
3. Moseley, K. F. Type 2 diabetes and bone fractures. *Curr. Opin. Endocrinol. Diabetes. Obes.* **19,** 128–35 (2012).
4. Nicodemus, K. K. & Folsom, A. R. Type 1 and type 2 diabetes and incident hip fractures in postmenopausal women. *Diabetes Care* **24,** 1192–1197 (2001).
5. Bonds, D. E., Larson, J. C., Schwartz, A. V., *et al.* Risk of Fracture in Women with Type 2 Diabetes: the Women's Health Initiative Observational Study. *J Clin Endocrinol Metab* **91,** 3404–3410 (2006).
6. Schwartz, A. V, Sellmeyer, D. E., Ensrud, K. E., *et al.* Older women with diabetes have an increased risk of fracture: a prospective study. *J.Clin.Endocrinol.Metab.* **86,** 38 (2001).
7. Schwartz, A. V., Vittinghoff, E., Bauer, D. C., *et al.* Association of BMD and FRAX Score With Risk of Fracture in Older Adults With Type 2 Diabetes. *JAMA* **305,** 2184 (2011).
8. Looker, A. C., Eberhardt, M. S. & Saydah, S. H. Diabetes and fracture risk in older U.S. adults. *Bone* **82,** (2016).
9. Gulcelik, N. E., Bayraktar, M., Caglar, O., Alpaslan, M. & Karakaya, J. Mortality after Hip Fracture in Diabetic Patients. *Exp. Clin. Endocrinol. Diabetes* **119,** 414–418 (2011).

10. De Liefde, I. I., Van Der Klift, M., De Laet, C. E. D. H., *et al.* Bone mineral density and fracture risk in type-2 diabetes mellitus: The Rotterdam Study. *Osteoporos. Int.* **16,** 1713–1720 (2005).

11. Kanis, J. A., Johnell, O., Oden, A., *et al.* Ten year probabilities of osteoporotic fractures according to BMD and diagnostic thresholds. *Osteoporos. Int.* **12,** 989–995 (2001).

12. Walsh, J. S. & Vilaca, T. Obesity, Type 2 Diabetes and Bone in Adults. *Calcified Tissue International* **100,** (2017).

13. Thrailkill, K. M., Lumpkin, C. K., Bunn, R. C., Kemp, S. F. & Fowlkes, J. L. Is insulin an anabolic agent in bone? Dissecting the diabetic bone for clues. *Am. J. Physiol. Endocrinol. Metab.* **289,** E735-45 (2005).

14. Betteridge, D. J. What is oxidative stress? *Metabolism.* **49,** 3–8 (2000).

15. Wright, E., Scism-Bacon, J. L., Glass, L. C. & Glass, L. Oxidative stress in type 2 diabetes: the role of fasting and postprandial glycaemia. *Int. J. Clin. Pract.* **60,** 308–14 (2006).

16. Monnier, V. M., Mustata, G. T., Biemel, K. L., *et al.* Cross-linking of the extracellular matrix by the Maillard reaction in aging and diabetes: An update on ‘a puzzle nearing resolution’. *Ann. N. Y. Acad. Sci.* **1043,** 533–544 (2005).

17. Monnier, V. M., Sell, D. R., Dai, Z., *et al.* The role of the Amadori product in the complications of diabetes. *Ann. N. Y. Acad. Sci.* **1126,** 81–88 (2008).

18. Snedeker, J. G. & Gautieri, A. The role of collagen crosslinks in ageing and diabetes - the good, the bad, and the ugly. *Muscles. Ligaments Tendons J.* **4,** 303–8 (2014).

19. Garnero, P. The contribution of collagen crosslinks to bone strength. *Bonekey Rep.* **1,** 182 (2012).

20. Knott, L. & Bailey, A. J. Collagen cross-links in mineralizing tissues: A review of their chemistry, function, and clinical relevance. *Bone* **22,** 181–187 (1998).

21. Sherman, V. R., Yang, W. & Meyers, M. A. The materials science of collagen. *J. Mech. Behav. Biomed. Mater.* **52,** 22–50 (2015).

22. Streeter, I. & Leeuw, N. H. A molecular dynamics study of the interprotein interactions in collagen fibril. *Soft Matter* 3373–3382 (2011). doi:10.1039/C0SM01192D

23. Szpak, P. Fish Bone Chemistry and Ultrastructure: Implications for Taphonomy and Stable Isotope Analysis. *J. Archaeol. Sci.* **38,** 3358–3372 (2011).

24. Kar, K., Amin, P., Bryan, M. A., *et al.* Self-association of collagen triple helic peptides into higher order structures. *J. Biol. Chem.* **281,** 33283–90 (2006).

25. Stock, S. R. The Mineral–Collagen Interface in Bone. *Calcif. Tissue Int.* **97,** 262–280 (2015).

26. Sroga, G. E. & Vashishth, D. UPLC methodology for identification and quantitation of naturally fluorescent crosslinks in proteins: A study of bone collagen. *J. Chromatogr. B Anal. Technol. Biomed. Life Sci.* **879,** 379–385 (2011).

27. Oliveira, M. I. A., Souza, E. M. de, Pedrosa, F. de O., *et al.* RAGE receptor and its soluble isoforms in diabetes mellitus complications. *J. Bras. Patol. e*

Med. Lab. **49,** 97–108 (2013).

28. Gautieri, A., Redaelli, A., Buehler, M. J. & Vesentini, S. Age- and diabetes-related nonenzymatic crosslinks in collagen fibrils: Candidate amino acids involved in Advanced Glycation End-products. *Matrix Biol.* **34,** 89–95 (2014).
29. Bala, Y., Farlay, D., Delmas, P. D., Meunier, P. J. & Boivin, G. Time sequence of secondary mineralization and microhardness in cortical and cancellous bone from ewes. *Bone* **46,** 1204–1212 (2010).
30. Bala, Y., Farlay, D. & Boivin, G. Bone mineralization: From tissue to crystal in normal and pathological contexts. *Osteoporos. Int.* **24,** 2153–2166 (2013).
31. Currey, J. D. The structure and mechanics of bone. *J. Mater. Sci.* **47,** 41–54 (2012).
32. Weiner, S. & Wagner, H. D. The Material Bone: Structure-Mechanical Function Relations. *Annu. Rev. Mater. Sci.* **28,** 271–298 (1998).
33. Reznikov, N., Chase, H., Brumfeld, V., Shahar, R. & Weiner, S. The 3D structure of the collagen fibril network in human trabecular bone: Relation to trabecular organization. *Bone* **71,** (2015).
34. Bouxsein, M. L., Boyd, S. K., Christiansen, B. A., *et al.* Guidelines for assessment of bone microstructure in rodents using micro-computed tomography. *J. Bone Miner. Res.* **25,** 1468–1486 (2010).
35. Parfitt, A. M. Age-related structural changes in trabecular and cortical bone: Cellular mechanisms and biomechanical consequences. *Calcif. Tissue Int.* **36,** (1984).
36. Seeman, E. Bone quality: The material and structural basis of bone strength. *J.*

Bone Miner. Metab. **26,** 1–8 (2008).

37. Kini, U. & Nandeesh, B. N. Physiology of Bone Formation, Remodeling, and Metabolism. in *Radionuclide and Hybrid Bone Imaging* 29–57 (Springer-Verlag Berlin Heidelberg, 2012). doi:10.1007/978-3-642-02400-9

38. Liu, X. S., Sajda, P., Saha, P. K., *et al.* Complete Volumetric Decomposition of Individual Trabecular Plates and Rods and Its Morphological Correlations With Anisotropic Elastic Moduli in Human Trabecular Bone. *J. Bone Miner. Res.* **23,** 223–235 (2007).

39. Wang, J., Zhou, B., Liu, X. S., *et al.* Trabecular plates and rods determine elastic modulus and yield strength of human trabecular bone. *Bone* **72,** 71–80 (2015).

40. Cheung, M. B. S. W., Majeska, R., Kennedy, O., *et al.* Osteocytes : Master Orchestrators of Bone. *Calcif. Tissue Int.* **94,** 5–24 (2014).

41. Burr, D. B. Bone material properties and mineral matrix contributions to fracture risk or age in women and men. *J. Musculoskelet. Neuronal Interact.* **2,** 201–204 (2002).

42. Schaffler, M. B., Pitchford, W. C., Choi, K. & Riddle, J. M. Examination of compact bone microdamage using back-scattered electron microscopy. *Bone* **15,** 483–488 (1994).

43. Hernandez, C. J. & Keaveny, T. M. A biomechanical perspective on bone quality. *Bone* **39,** 1173–1181 (2006).

44. Launey, M. E., Buehler, M. J. & Ritchie, R. O. On the Mechanistic Origins of Toughness in Bone. *Annual Review of Materials Research* **40,** 25–53 (2010).

45. Hernandez, C. J. & van der Meulen, M. C. Understanding Bone Strength Is Not Enough. *J. Bone Miner. Res.* **32,** 1157–1162 (2017).

46. Currey, J. D. The design of mineralised hard tissues for their mechanical functions. *J. Exp. Biol.* **202,** 3285–3294 (1999).

47. Paschalis, E. P., Tatakis, D. N., Robins, S., *et al.* Lathyrism-induced alterations in collagen cross-links influence the mechanical properties of bone material without affecting the mineral. *Bone* **49,** 1232–1241 (2011).

48. Donnelly, E., Chen, D. X., Boskey, A. L., Baker, S. P. & Van Der Meulen, M. C. H. Contribution of mineral to bone structural behavior and tissue mechanical properties. *Calcif. Tissue Int.* **87,** 450–460 (2010).

49. Boskey, A. & Mendelsohn, R. Infrared analysis of bone in health and disease. *J. Biomed. Opt.* **10,** 31102 (2005).

50. Ulrich, P. & Cerami, A. Protein Glycation, Diabetes, and Aging. *Recent Prog. Horm. Res.* **56,** 1–21 (2001).

51. Odetti, P., Rossi, S., Monacelli, F., *et al.* Advanced glycation end products and bone loss during aging. *Ann. N. Y. Acad. Sci.* **1043,** 710–717 (2005).

52. Poundarik, A. A., Wu, P. C., Evis, Z., *et al.* A direct role of collagen glycation in bone fracture. *J. Mech. Behav. Biomed. Mater.* **52,** (2015).

53. Saito, M., Fujii, K., Mori, Y. & Marumo, K. Role of collagen enzymatic and glycation induced cross-links as a determinant of bone quality in spontaneously diabetic WBN/Kob rats. *Osteoporos. Int.* **17,** 1514–1523 (2006).

54. Oren, T. W., Botolin, S., Williams, A., Bucknell, A. & King, K. B.

Arthroplasty in veterans: analysis of cartilage, bone, serum, and synovial fluid reveals differences and similarities in osteoarthritis with and without comorbid diabetes. *J. Rehabil. Res. Dev.* **48,** 1195–210 (2011).

55. Nyman, J. S. Effect of diabetes on the fracture resistance of bone. *Clin. Rev. Bone Miner. Metab.* **11,** 38–48 (2013).

56. Creecy, A., Uppuganti, S., Merkel, A. R., *et al.* Changes in the Fracture Resistance of Bone with the Progression of Type 2 Diabetes in the ZDSD Rat. *Calcif. Tissue Int.* **99,** 289–301 (2016).

57. Fajardo, R. J., Karim, L., Calley, V. I. & Bouxsein, M. L. A review of rodent models of type 2 diabetic skeletal fragility. *J. Bone Miner. Res.* **29,** 1025–1040 (2014).

58. Vashishth, D., Gibson, G. J., Khoury, J. I., *et al.* Influence of nonenzymatic glycation on biomechanical properties of cortical bone. *Bone* **28,** 195–201 (2001).

59. Tang, S. Y., Zeenath, U. & Vashishth, D. Effects of non-enzymatic glycation on cancellous bone fragility. *Bone* **40,** 1144–1151 (2007).

60. Sroga, G. E. G. E. G. E., Siddula, A., Vashishth, D., Gundberg, C. & Vashishth, D. Glycation of human cortical and cancellous bone captures differences in the formation of maillard reaction products between glucose and ribose. *PLoS One* **10,** 1–19 (2015).

61. Karim, L., Tang, S. Y., Sroga, G. E. & Vashishth, D. Differences in non-enzymatic glycation and collagen cross-links between human cortical and cancellous bone. *Osteoporos. Int.* **24,** 2441–2447 (2013).

62. Pedrazzoni, M., Ciotti, G., Pioli, G., *et al.* Osteocalcin levels in diabetic subjects. *Calcif. Tissue Int.* **45,** 331–336 (1989).

63. Dobnig, H., Piswanger-Sölkner, J. C., Roth, M., *et al.* Type 2 Diabetes Mellitus in Nursing Home Patients: Effects on Bone Turnover, Bone Mass, and Fracture Risk. *J. Clin. Endocrinol. Metab.* **91,** 3355–3363 (2006).

64. Shu, A., Yin, M. T., Stein, E., *et al.* Bone structure and turnover in type 2 diabetes mellitus. *Osteoporos. Int.* **23,** 635–641 (2012).

65. Akin, O., Göl, K., Aktürk, M. & Erkaya, S. Evaluation of bone turnover in postmenopausal patients with type 2 diabetes mellitus using biochemical markers and bone mineral density measurements. *Gynecol. Endocrinol.* **17,** 19–29 (2003).

66. Gerdhem, P., Isaksson, A., Åkesson, K. & Obrant, K. J. Increased bone density and decreased bone turnover, but no evident alteration of fracture susceptibility in elderly women with diabetes mellitus. *Osteoporos. Int.* **16,** 1506–1512 (2005).

67. Farr, J. N., Drake, M. T., Amin, S., *et al.* In vivo assessment of bone quality in postmenopausal women with type 2 diabetes. *J. Bone Miner. Res.* **29,** 787–795 (2014).

68. Krakauer, J. C., McKenna, M. J., Buderer, N. F., *et al.* Bone loss and bone turnover in diabetes. *Diabetes* **44,** 775–782 (1995).

69. Karim, L., Moulton, J., Van Vliet, M., *et al.* Bone microarchitecture, biomechanical properties, and advanced glycation end-products in the proximal femur of adults with type 2 diabetes. *Bone* **114,** 32–39 (2018).

70. Hunt, H. B., Pearl, J. C., Diaz, D. R., King, K. B. & Donnelly, E. Bone Tissue Collagen Maturity and Mineral Content Increase With Sustained Hyperglycemia in the KK-Ay Murine Model of Type 2 Diabetes. *J. Bone Miner. Res.* **33,** 921–929 (2017).

71. McCarthy, A. D., Etcheverry, S. B., Bruzzone, L., *et al.* Non-enzymatic glycosylation of a type I collagen matrix: effects on osteoblastic development and oxidative stress. *BMC Cell Biol.* **2,** 16 (2001).

72. Katayama, Y., Akatsu, T., Yamamoto, M., Kugai, N. & Nagata, N. Role of nonenzymatic glycosylation of type I collagen in diabetic osteopenia. *J. Bone Miner. Res.* **11,** 931–937 (2009).

73. Terada, M., Inaba, M., Yano, Y., *et al.* Growth-inhibitory effect of a high glucose concentration on osteoblast-like cells. *Bone* **22,** 17–23 (1998).

74. Valcourt, U., Merle, B., Gineyts, E., *et al.* Non-enzymatic glycation of bone collagen modifies osteoclastic activity and differentiation. *J. Biol. Chem.* **282,** 5691–5703 (2007).

75. Allen, M. R., McNerny, E. M. B., Organ, J. M. & Wallace, J. M. True gold or pyrite: A review of reference point indentation for assessing bone mechanical properties in vivo. *J. Bone Miner. Res.* **30,** 1539–1550 (2015).

76. Hunt, H. B. & Donnelly, E. Bone Quality Assessment Techniques: Geometric, Compositional, and Mechanical Characterization from Macroscale to Nanoscale. *Clin. Rev. Bone Miner. Metab.* **14,** 133–149 (2016).

77. Hunt, H. B. Altered tissue composition, microarchitecture, and mechanical performance in cancellous bone from men with type 2 diabetes mellitus. *J.*

Bone Miner. Res. (2018).

CHAPTER 2

BONE QUALITY ASSESSMENT TECHNIQUES: GEOMETRIC, COMPOSITIONAL, AND MECHANICAL CHARACTERIZATION FROM MACROSCALE TO NANOSCALE

2.1 *Introduction*

Measurements of areal bone mineral density (aBMD) assessed by dual-energy x-ray absorptiometry (DEXA) have historically been the standard for fracture risk prediction. However, the quantity of bone measured by aBMD incompletely describes fracture risk.[1] The ability of bone to resist fracture is influenced by the mass of the bone; its spatial distribution, including geometry and microarchitecture; and its material properties. Geometric characteristics include macroscopic features such as the cross-sectional properties of the whole bone, as well as smaller scale features such as the trabecular architecture. Tissue material properties include elastic modulus, strength, and fracture toughness, which are influenced by the composition and organization of the mineral and matrix components, as well as the presence of microdamage. These geometric, compositional, and material factors contribute to the "quality" of bone, and by extension to fracture resistance, independently of bone quantity. Therefore, for the purpose of this review, we define bone quality as the geometric and material factors that contribute to fracture resistance independently of aBMD.

Measurement techniques that evaluate bone quality to supplement DEXA-

assessed aBMD are sought to improve prediction, and thereby eventual prevention, of fragility fractures across diseased and aging populations.[2] However, the ability to improve assessment of bone's resistance to fracture from DEXA-assessed aBMD alone is complicated by the fact that the most direct assessment of fracture resistance, *ex vivo* destructive mechanical testing, cannot be performed *in vivo*.

This review covers commonly used bone quality measurement techniques, with an emphasis on the newest or most recently improved techniques, as well as those that are used *in vivo*. In particular, we compare the methods available for assessment of the geometric, compositional, and mechanical properties that contribute to bone quality; we detail their outcome measures; and we offer examples of how each technique is used currently or can be used in the future. Furthermore, each section is organized in descending order of the length scale of each assessment. Figure 2.1-1 positions each characterization method in terms of bone's hierarchical structure, and Table 2.1-1 summarizes important features of each characterization technique.

Figure 2.1-1: The five levels associated with bone quality measurements are depicted on a logarithmic scale of the hierarchical structure of bone. Along the top from left to right, representative images of bone using the imaging techniques of HRpQCT (adapted with permission from [134]), qBEI (adapted with permission from [135]), FTIRI of crystallinity (adapted with permission from [136]), and AFM (adapted with permission from [137]) are shown. The field of view of the representative images corresponds with the scale bar. Along the bottom, each characterization technique is categorized as geometric, compositional, or mechanical and is depicted by a bar showing the approximate range of resolutions currently achievable. Abbreviations: AFM = atomic force microscopy; FTIR = Fourier transform infrared; HPLC = high-performance liquid chromatography; HRMRI = high-resolution magnetic resonance imaging; HRpQCT = high-resolution peripheral quantitative computed tomography; Micro-CT = micro-computed tomography; NMR = nuclear magnetic resonance imaging; qBEI = quantitative backscattered electron imaging; QCT = quantitative computed tomography; RPI = reference point indentation; SAXS = small-angle x-ray scattering; SEM = scanning electron microscopy; TGA = thermogravimetric analysis; XRD = x-ray diffraction.

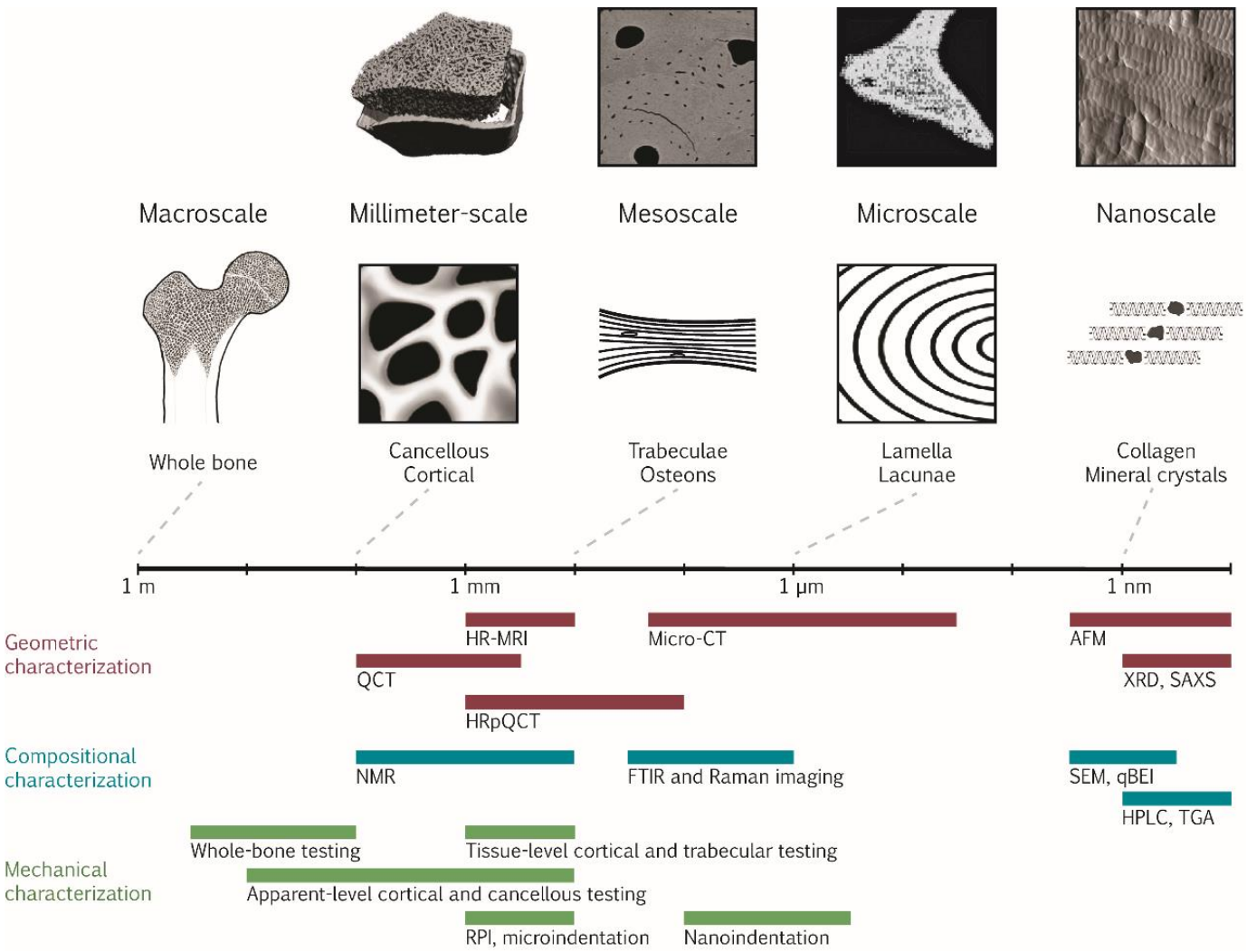
Macroscale
Millimeter-scale
Mesoscale
Microscale
Nanoscale
Whole bone
Cancellous
Cortical
Trabeculae
Osteons
Lamella
Lacunae
Collagen
Mineral crystals
1 m
1 mm
1 µm
1 nm
Geometric characterization
HR-MRI
Micro-CT
AFM
QCT
XRD, SAXS
HRpQCT
Compositional characterization
NMR
FTIR and Raman imaging
SEM, qBEI
HPLC, TGA
Mechanical characterization
Whole-bone testing
Tissue-level cortical and trabecular testing
Apparent-level cortical and cancellous testing
RPI, microindentation
Nanoindentation

Table 2.1-1: Summary of important features of each characterization method, categorized by geometric, compositional, or mechanical. Geometric and compositional abbreviations: BMD = bone mineral density; BMDD = bone mineral density distribution; BV/TV = bone volume fraction; Ct.D = cortical density; Ct.Po = cortical porosity; Ct.Th = cortical thickness; Tb.A = trabecular anisotropy; Tb.Conn = trabecular connectivity; Tb.D = trabecular density; Tb.N = trabecular number; Tb.Th = trabecular thickness; Tb.Sp = trabecular separation. Mechanical abbreviations: BMSi = bone material strength index; CID = creep indentation distance; ID = indentation distance.

	Length scale of analysis	**Destructive?**	**Testing environment**	**Research phase**	**Compositional component(s) evaluated**	**Spatially resolved?**	**Outcome variables**
Geometric Characterization							
Magnetic resonance imaging	100's μm to m	No	*in vivo, ex vivo*	Broad clinical use	water	Yes	BV/TV; Tb.D; Tb.Th; Tb.Sp; Tb.N; Tb.Conn; Tb.A; Ct.D; Ct.Th; Ct.Po
Quantitative computed tomography	100's μm	No	*in vivo, ex vivo*	Broad clinical use	mineral	Yes	BMD; bone geometry; Ct.Th
High-resolution peripheral quantitative computed tomography	10's μm to mm	No	*in vivo*	Clinical research	mineral	Yes	BV/TV; Ct.D; Tb.D; Tb.Th; Tb.Sp; Tb.N
Micro-computed tomography	50 nm to mm	No	*in vivo* on small animals, *ex*	Translational research	mineral	Yes	BV/TV; Tb.D; Tb.Th; Tb.Sp; Tb.N;

			vivo				Tb.Conn; Tb.A; Ct.D; Ct.Th; Ct.Po, quantification of microdamage, osteocyte lacunae
Atomic force microscopy	Å to μm	No; polished surface required	*ex vivo*	Basic research	mineral, matrix	Yes	surface topology; stiffness mapping
X-ray diffraction	Å to nm	Yes; powdering of non-crystalline samples	*ex vivo*	Basic research	mineral	No	degree of mineralization; crystal size and perfection; atomic spacing
Small-angle x-ray scattering	Å to nm	No	*ex vivo*	Basic research	mineral, matrix	Yes	crystal shape, thickness, orientation
Compositional Characterization							
Nuclear magnetic resonance	100's μm	No	*in vivo, ex vivo*	Basic research	mineral, matrix, water	No	BMD; water content
Fourier transform infrared spectroscopy	μm to mm	Yes; sample homogenization or embedding	*ex vivo*	Translational research	mineral, matrix	Yes	mineral:matrix; carbonate:phosphate;

		required					collagen maturity; crystallinity; tissue maturity
Raman spectroscopy	μm to mm	No; polished surface required	*in vivo, ex vivo*	Translational research	mineral, matrix	Yes	mineral:matrix; carbonate:phosphate; collagen maturity; crystallinity
Scanning electron microscopy: secondary electrons	nm to mm	Yes; conductive coating required	*ex vivo*	Basic research	mineral, matrix	Yes	surface topology
Scanning electron microscopy: quantitative backscattered electron imaging	nm to mm	No; polished surface required	*ex vivo*	Basic research	mineral	Yes	BMDD
High-performance liquid chromatography	Å to nm	Yes	*ex vivo*	Basic research	matrix	No	collagen crosslinks; bone turnover markers; amino acid composition
Thermal gravimetric	Å to nm	Yes	*ex vivo*	Basic research	mineral, matrix, water	No	ash fraction

analysis							
Mechanical Characterization							
Whole-bone testing	mm to m	Yes	*ex vivo*	Basic research	mineral, matrix, water	No	structural stiffness, strength, toughness
Apparent-level cortical and cancellous testing	µm to cm	Yes	*ex vivo*	Basic research	mineral, matrix, water	No	apparent-level stiffness, strength, toughness
Tissue-level cortical and trabecular testing	100's µm to mm	Yes	*ex vivo*	Basic research	mineral, matrix, water	No	tissue-level stiffness, strength, toughness
Microindentation	100's µm	No; polished surface required	*ex vivo*	Basic research	mineral, matrix, water	Yes	hardness
Reference point indentation	100's µm	No	*in vivo, ex vivo*	Translational research	mineral, matrix, water	Yes	BMSi; ID; maximum force; energy dissipation; CID; loading slope; unloading slope
Nanoindentation	µm	No; polished surface required	*ex vivo*	Basic research	mineral, matrix, water	Yes	hardness; unloading modulus

2.2 *Geometric Characterization*

The organization and distribution of cortical and cancellous bone vary throughout the skeleton and with each bone's function. By evaluating the geometric properties of cortical and cancellous bone at a variety of length scales (Figure 2.1-1), their influence on bone quality at larger length scales can be assessed. Because cancellous bone is generally more sensitive to pathologic changes than cortical bone due to its relatively greater metabolic activity, cancellous sites are highly clinically significant for diseased or aging populations. The length scale required to characterize cancellous bone geometry is typically smaller than that for cortical bone; thus, while many of the techniques described here focus on cancellous bone structure, they can also be used to characterize similarly sized, or larger, features in cortical bone. In addition, the research question drives the selection of the technique used to characterize geometric features: for example, if the research question addresses cortical thickness, then techniques that characterize millimeter-scale features in bone are adequate, and techniques capable of characterizing trabecular architecture (micron-scale features) may be unnecessary.

Therefore, identification of the key length scale or feature size of interest is critical to selection of the appropriate technique for characterization of geometric features of bone. At the micron- to nanometer-scale, bone is composed of a complex hierarchical structure of lamellae and mineralized collagen fibers that can be probed with advanced materials characterization techniques, including atomic force microscopy, x-ray diffraction, and x-ray scattering. The micron to millimeter scale

tissue structures can be characterized with micro-computed tomographic techniques. Finally, the macroscopic structures can be characterized with clinical imaging modalities such as computed tomography and MRI. Key advantages of many of the techniques discussed in the following sections include the ability to 1) generate true volumetric bone densities (reported in g/cm3), as opposed to aBMD calculated via DEXA, and 2) make multiple measurements within the same individual over time, allowing for longitudinal assessment of bone geometry and microarchitecture with aging or treatment.

2.2.1 High-Resolution Magnetic Resonance Imaging (MRI)

Magnetic resonance imaging (MRI) is a widely available, nonionizing clinical modality used to image the water in skeletal tissues *in vivo*. MRI utilizes a large magnet to align the magnetic poles of the protons in the tissue being imaged, and then a radio frequency signal specific to hydrogen is added. Upon removing the radio wave, the magnetic vector associated with each proton relaxes and causes another radio wave to be emitted. The emitted radio wave can subsequently be analyzed for the time required for the proton to relax after the initial radio wave signal, as well as for the time required for the axial spin to return to its resting state. Because these two characteristic times vary for different types of tissue (e.g., bone, fat, marrow), a tissue-specific image can be created.[3]

While standard clinical MRI techniques do not resolve trabecular bone, high-resolution MRI (HR-MRI) techniques can provide 3-D information on trabecular bone at peripheral sites (e.g., the radius, tibia, and calcaneus) with a resolution on the order

of trabecular dimensions (in-plane resolution: ~110 μm, slice thickness: ~300 μm).[4–7] MR imaging measures the water in marrow cavities; thus, trabecular architecture is derived from the negative MR image. Recent advancements allow for imaging of the proximal femur, a major site of clinical interest, though the signal-to-noise ratio (SNR) and the resolution (in plane resolution: ~250 μm, slice thickness: ~500 μm) are lower than those at peripheral sites.[5] The outcomes from MRI are bone volume fraction (BV/TV), trabecular thickness (Tb.Th), trabecular separation (Tb.Sp), trabecular number (Tb.N), trabecular anisotropy and connectivity, cortical thickness (Ct.Th), and cortical porosity (Ct.Po).[5,8]

MRI studies show promise for monitoring osteoporosis treatment[9] and predicting fracture risk clinically.[10] MRI scans can also be used to generate 3-D bone geometry for finite element analysis (FEA) models, a numerical method that can be used to computationally predict a bone's mechanical response to loading (see review by Hernandez, this issue). An FEA study using 3-D reconstructions of bone from MRI and micro-computed tomography images found stiffness to strongly correlate between the two imaging modalities, suggesting MRI-based models are suitable predictors of mechanical performance.[11] Some of the main drawbacks of MRI include limited ability to resolve trabeculae, low SNR, and high cost; however, the former two issues are being addressed with improved data collection and processing methods.[12]

2.2.2 Quantitative Computed Tomographic Imaging

Quantitative computed tomography (QCT) assesses 3-D bone geometry and volumetric bone mineral density (vBMD) *in vivo*. vBMD measurements differ from

aBMD measurements in that vBMD measures a true volumetric density (g/cm^3), while aBMD is the mass of bone mineral within the 2-D scan area (g/cm^2).

In QCT, x-ray radiation is directed at an object of interest, and the attenuation of the x-rays as they interact with the object is recorded by a detector opposite the radiation source. The x-ray source and detector rotate around the object, and tomographic algorithms create a 3-D image reconstruction. Inclusion of a mineral standard or phantom in the scans allows for calculation of vBMD.

Cortical and cancellous bone compartments can be distinguished using QCT (Figure 2.1-1). The resolution of standard clinical QCT (in-plane resolution: ~500 μm) is sufficient to measure cortical thickness and volume; however, it is insufficient to characterize trabecular microarchitecture, as the thickness of individual trabeculae range from 50 to 300 μm.[13] QCT is particularly useful for imaging clinically relevant sites such as the spine and hip, though cortical volume measurements of the spine may include some subcortical bone.[13–15]

Peripheral QCT (pQCT) imaging is a subset of QCT that allows QCT measurements to be taken at appendicular sites.[13] pQCT offers finer resolution (in plane resolution: ~200 to 500 μm) than QCT, but delivers higher effective radiation doses to patients and thus is limited to use on the peripheral sites,[16] where the effective radiation dose is relatively low. For example, a QCT scan on an axial site delivers an effective radiation dose on the order of 5 mSv, while a pQCT scan of a peripheral site delivers an effective radiation dose less than 0.01 mSv.[17]

2.2.3 High-Resolution QCT (HRpQCT)

High-resolution peripheral quantitative computed tomography (HRpQCT) allows for *in vivo* measurement of vBMD and resolution of cortical and trabecular features. The principle of image generation is similar to that of QCT systems, and the use of a calibration phantom allows conversion of x-ray attenuation to bone density. Similar to pQCT, HRpQCT can distinguish between cortical and cancellous bone regions; however, the resolution of HRpQCT is higher and can more accurately measure cancellous bone morphology. Sites available for HRpQCT assessment include the distal radius, distal tibia, hand, and fingers. Direct outcome measurements from HRpQCT include cortical bone density, trabecular bone density, total bone density, and mean cortical thickness. Using post-scanning algorithms, calculations of Tb.Th, Tb.Sp, and Tb.N are possible.[18]

The newest commercial HRpQCT system (XtremeCT II, Scanco Medical, Brüttisellen, Switzerland) features a nominal isotropic pixel size as small as 17 μm; however, most of the published literature reports the use of a nominal isotropic pixel size between 82 μm and 270 μm.[19] At a resolution of 82 μm, cortical and trabecular bone are distinguishable, allowing for separate vBMD measurements of cortical and trabecular regions; however, trabecular thickness-independent algorithms are necessary to compute trabecular microarchitectural parameters,[19] and cortical pore size may be below scan resolution.[20] Moreover, partial volume effects may arise in trabecular microarchitecture measurements because trabecular parameters (e.g., thickness and separation) are on the order of the scan's spatial resolution.

The clinical applicability of HRpQCT is exemplified in studies showing microarchitectural differences between postmenopausal and premenopausal women as well as osteoporotic and osteopenic women,[19] between type 2 diabetic and non-diabetic patients,[21] and between risedronate- and placebo-treated menopausal women.[22] Another major benefit of HRpQCT is the ability to generate patient-specific FEA models of bone to assess its mechanical performance in different loading conditions. For example, stiffness and failure load derived from HRpQCT-based micro-FEA data from the radius and tibia were correlated with vertebral and non-vertebral fractures.[23]

The effective radiation dose per HRpQCT scan is around 3 μSv, orders of magnitude lower than that delivered by QCT and pQCT scans.[24] Recent reviews highlight the promise for clinical use of HRpQCT.[24,25] Disadvantages of this technique include 1) the availability of HRpQCT systems is currently limited to academic medical centers, and 2) the relatively few anatomic sites that can be imaged.

2.2.4 Micro-Computed Tomography (Micro-CT)

Micro-computed tomography (micro-CT) is used to characterize 3-D bone geometry and trabecular microarchitecture of biopsies or other excised tissues *ex vivo* or key skeletal regions of interest of small animals *in vivo*. Nominal resolution of micro-CT ranges from 1 to 100 μm, but recent advances have increased the nominal isotropic resolution for *ex vivo* analyses to 50 nm (Zeiss Xradia 800 Ultra, Zeiss, Oberkochen, Germany). Similar to QCT and HRpQCT, tomographic algorithms generate micro-CT 3-D images, but the attenuation data is collected in a slightly different manner:

desktop micro-CT scanners designed for *ex vivo* specimens often have a rotational specimen stage and a stationary x-ray source and detector, while scanners designed for *in vivo* small animal scans have a stationary stage and a rotational source-detector gantry.

From 3-D micro-CT data reconstructions, trabecular microarchitecture is characterized through outcomes such as BV/TV, Tb.Th, Tb.Sp, Tb.N, trabecular connectivity and anisotropy measurements, and tissue mineral density (TMD) (g/cm^3). TMD has the same units as vBMD, but, unlike vBMD, the volume of interest for TMD excludes voids and soft tissue; TMD therefore represents the density of the bone material itself, whereas vBMD may include porosity. In addition, measures of cortical porosity and thickness can also be calculated; however, adequate scan resolution should be carefully considered to achieve accurate cortical porosity measurements.[26]

In small animals, micro-CT can be used to monitor skeletal morphology over time,[27] and in human biopsies, it can determine the effects of a drug therapy[28] or a disease condition on bone morphology.[29] Quantification of microdamage[30,31] and osteocyte lacunae in human biopsies or animal models is also possible, though isotropic resolutions less than 1 μm may be required, necessitating the use of a high-resolution desktop scanner or synchrotron source.[32]

The primary advantages of this technique include the ability to characterize the details of trabecular architecture, microdamage, and even the osteocyte network; however, finer resolutions come at a cost of longer scan durations and greater radiation exposure. In addition, the specimen sizes that can be scanned *ex vivo* at the

highest resolutions are limited (~100 mm diameter, 140 mm length).

2.2.5 Atomic Force Microscopy (AFM)

Atomic force microscopy (AFM) measures the force deflections that arise when a cantilever beam with an atomically sharp tip is scanned over a sample's surface. Collection of topographic images with a sub-nanometer spatial resolution are possible.[33] In addition to imaging topography, AFMs can be used to manipulate sample surfaces (e.g., functionalization) and measure forces (e.g., stiffness mapping).

AFM has been used to document collagen fibril alignment and structure, including the 67 nm quarter-stagger fibril alignment,[34] as well as bone's sub-fibrillar structure.[35] It is also possible to image mineral platelets and the topology of fractured specimens.[36] Technological improvements now allow for high-speed AFM (HS-AFM) which maintains the nanometer resolution, but scans complete within seconds rather than minutes.[37] HS-AFM can therefore be used to measure dynamic processes including surface functionalization and diffusion.

One major advantage of AFM over other imaging techniques is the ability to image and probe samples in saline or other liquids, thereby maintaining the sample near biological conditions. Furthermore, AFM maintains a sub-nanometer resolution without the preparative steps like fixation, staining, metal coating, and critical point drying that are required for other imaging techniques like transmission electron microscopy (TEM). Disadvantages of AFM include a small scan area (scan area: hundreds of μm by hundreds of μm, height amplitude limit: 10 to 20 μm) and image

distortion of some topological features such as overhangs and steep edges.

2.2.6 X-ray Diffraction and Scattering

X-ray Diffraction (XRD)

For *ex vivo* studies, x-ray diffraction (XRD) is the gold standard for characterizing the structure of bone mineral. In XRD, an incident beam of x-rays on a sample results in a diffracted ray with variations in intensity due to constructive and destructive interference from planes of atoms within the sample. The x-ray source and the detector are rotated through a range of angles, and the resulting data is processed to determine atomic spacing and structure. The primary outcomes of this technique are the spacings between various atomic planes; crystallite size can also be estimated from the plane spacing data.

The first XRD analysis of bone nearly a century ago established the mineral as hydroxyapatite.[38] Since then, XRD studies have increased in versatility, leading to important insights including the degree of mineralization and crystallinity as functions of tissue and animal age,[39] the effect of crystallinity changes on mineral strain,[40] and the effects of impurity substitution (e.g., fluoride, strontium, magnesium) into the hydroxyapatite lattice.[41]

The key advantage of XRD is that it provides detailed information on the structure of bone mineral crystals. Because sample homogenization is necessary and powdering non-crystalline samples is standard, XRD is typically destructive, despite the diffraction process itself being nondestructive.[42]

Small-angle X-ray Scattering (SAXS)

Small-angle x-ray scattering (SAXS) is a complementary technique to standard XRD that does not require homogenization of samples. In SAXS, the scattered rays from an incident x-ray beam are measured instead of the diffracted rays as in XRD. Outcome measurements from SAXS include crystal shape, average crystal thickness, and crystal orientation.[43]

The advent of synchrotrons, which produce high energy, monochromatic x-rays, allowed SAXS characterization of bone tissue. The use of *in situ* synchrotron imaging has enabled a 3-D reconstruction of a trabecula with complete ultrastructural details,[44] analysis of the internal stresses of cortical bone during a compressive load,[45] studying the load transfer between the mineral and organic matrix of bone at the nanoscale,[46] and evaluating strained microdamage at a resolution of 30 nm.[47] These studies show promise for translating structural measurements directly into mechanical property characterizations.

Key advantages of SAXS include the ability to image non-crystalline samples with minimal sample preparation, which allows for detailed insights into bone's nanoscale structure, variations in tissue mineral density, and damage accumulation. However, SAXS suffers from a lower SNR than XRD; thus, a synchrotron source is required for these measurements.

2.3 ***Compositional Characterization***

The nanoscale building blocks of bone are an organic matrix, composed mainly of

type 1 collagen, a hydroxyapatite-like mineral, and water. In general, the collagen matrix provides bone's ductility, the mineral provides bone's stiffness and strength,[48] and the water provides bone's viscoelastic, or time-dependent, behavior.[49] Because toughness, which characterizes a bone's ability to absorb energy before failure (see review by Burr, this issue), arises from the combination of ductility and strength, the collagen, mineral, and water components of bone are critical to fracture resistance. Therefore, characterization of the mineral, matrix, and water components of bone lends insight into bone quality and their contribution to structural integrity of whole bones.[50,51]

2.3.1 Nuclear Magnetic Resonance (NMR)

Nuclear magnetic resonance (NMR), also called magnetic resonance spectroscopy or nuclear paramagnetic resonance, operates using the same principles as MRI. Whereas MRI is typically used to image the water in a tissue, NMR can be used to measure other isotopes. NMR uses the responses of isotopes to an external magnetic field to generate compositional information about the sample being scanned. The response of a particular isotope to an external magnetic field is unique and depends on the isotope's molecular environment, and the parameter used to describe an isotope's response is called chemical shift. The two isotopes used to study bone with NMR are ^{1}H and ^{31}P. Although the feasibility of measuring cortical and cancellous tibial bone BMD has been demonstrated *in vivo* using ^{31}P,[52] a low SNR remains a key challenge for this isotope.[53] Therefore, here we focus primarily on ^{1}H, or proton, NMR.

Proton NMR is used to characterize the water content in bone. Water in bone

plays roles in transporting ions during mineralization, damping during mechanical loading, and regulating bone formation via fluid flow-mediated mechanotransduction. The water in bone falls into two main categories: bound and unbound. Bound water exists in Ca^{2+} coordination sites on the mineral and is associated with collagen fibrils. Unbound water, or bulk water, exists in the pores of the Haversian system and is used as an inverse measure of bone density.(54)

Both varieties of water in bone are distinguishable through proton NMR.(55) In a study investigating water content, aging, and mechanical properties *ex vivo*, bound water increased with age while unbound water correlated to porosity. Additionally, both bound and unbound water influenced mechanical properties.(56) The important roles of water in bone and the push towards its use in clinical measurements is described in a recent review.(55) Advances in NMR technology in the past several decades have also enabled ultrafast Magic Angle Spinning (MAS) NMR on solid bone samples.(57,58) Ultrafast MAS NMR has the potential help further elucidate the complex structure and order of bone's hierarchical system beyond standard NMR measurements of water content and location.

Two main advantages of NMR are 1) the ability to scan *in vivo* without subjecting the patient to ionizing radiation, and 2) the technique is nondestructive, allowing repeated measurements on the same patient or sample. The principal disadvantage is the low SNR of isotopes other than ^{1}H, which limits NMR's versatility for specimens, like biological tissues, that have high water content.

2.3.2 Vibrational Spectroscopy and Imaging

Infrared (IR) spectroscopy and Raman spectroscopy can be used to determine the chemical signature of a sample. Both techniques rely on the characteristic fingerprints of molecular bond vibrations from a material's constituents. When coupled to a microscope and an array detector, both of these techniques can be used in an imaging mode to assess material composition in a spatially resolved fashion.[59]

In general, strong molecular bond vibrations in the IR spectrum correspond to weak bond vibrations in the Raman spectrum, and vice-versa. The differences in the strength of vibrational modes between IR and Raman arises from complex molecular symmetry, but typically a change in dipole moment indicates an IR active-mode, and a change in polarizability indicates a Raman active-mode. In bone, both IR and Raman spectroscopy can differentiate the molecular signals of the organic matrix components (collagen, proteoglycans, lipids, etc.) from the signals arising from the constituents of the hydroxyapatite (phosphate, carbonate).

FTIR Spectroscopy and Imaging

Fourier transform infrared spectroscopy (FTIR) is used primarily in transmission or absorption mode and requires a thin sample (thickness: ~2 μm). When characteristic frequencies of an incident infrared beam are absorbed by molecular bonds in the sample, the resulting interferogram is Fast Fourier Transformed into a spectrum in the frequency domain. The peaks in the resulting FTIR spectrum are analyzed to identify molecular species, qualitatively determine the amount of specific components, and

provide information on the stoichiometry of a particular molecular species.

The outcome measurements from a typical FTIR spectrum of bone include the mineral to matrix ratio, indicating the extent of mineralization of the organic matrix; the carbonate to phosphate ratio, indicating the extent to which carbonate has been substituted into hydroxyapatite; the collagen maturity, indicating the relative crosslink proportion of mature trivalent crosslinks to immature divalent crosslinks; the crystallinity, a measure of crystal size and perfection; and acid phosphate content, a measure of tissue maturity.[60,61] Furthermore, spatial mapping and information about tissue heterogeneity is possible through FTIR imaging (FTIRI) which allows for characterization of the above parameters across a region of interest with a spatial resolution around 6 μm^2.

FTIR and FTIRI were used to detect differences in the quantity and quality of mineral in diseased Schmid metaphyseal chondrodysplasia bone compared to non-diseased bone,[62] in collagen maturity between bone from rats treated with a lathyrogen and from untreated controls,[63] and in heterogeneity of bisphosphonate treated postmenopausal women with fractures compared to non-fracture controls.[64] Together, these studies exemplify the power of FTIR and FTIRI in evaluating the mineral, organic matrix, and the relationship between the two.

Advantages of FTIR include spatial mapping with FTIRI, concurrent mineral and matrix evaluation, high sensitivity, and a high SNR relative to Raman allowing for faster data collection. A disadvantage of FTIR spectroscopy or imaging is that sample dehydration is required because water dominates the absorption spectrum in the

infrared; thus, analysis of biological tissues in their native hydrated states is precluded. In addition, PMMA embedding and microtoming of thin sections (thickness: ~2 μm) is required for FTIRI. Finally, a disadvantage of FTIRI includes a coarser resolution than related techniques (FTIRI: ~6 μm, Raman imaging: ~1 μm).

Raman Spectroscopy and Imaging

Raman spectroscopy uses the inelastic scattering of incident light on a sample to detect changes in polarizability of molecules. The outcome variables for Raman spectroscopy are similar to those of FTIR, with the exceptions of crystallinity and acid phosphate.[65] Crystallinity in Raman spectroscopy is measured as the inverse of the full-width at half-maximum (FWHM) of the 959 cm^{-1} phosphate peak which is related to the length of the mineral crystallite c-axis.[66]

Within the past decade, *in vivo* Raman capabilities have been realized.[67] Using spatially offset Raman spectroscopy (SORS), millimeter depths human tibial and finger tissue have been scanned.[68] A comprehensive analysis of the feasibility and promise of Raman in a clinical setting is described by Hanlon et al.[69]

Raman imaging offers several advantages relative to FTIRI, including a finer spatial resolution (~1 μm); the ability to scan thick, hydrated specimens, which allows for more versatile use in biological samples; and *in vivo* capabilities. The key drawback of Raman is its relatively low SNR, which substantially increases scan times relative to FTIR.

2.3.3 Scanning Electron Microscopy (EM)

SEM: Secondary Electrons

In scanning electron microscopy (SEM) an electron beam is rastered across a sample surface to determine topographical and compositional information with a resolution of tens of nanometers.[70] As the electrons from the beam contact the sample surface, energy from the incident electron is transferred to an atom in the sample. When this extra energy in the atom is released, a secondary electron is emitted and subsequently detected. Because the primary outcome of this technique is a detailed 2-D image of the specimen surface, secondary outcomes can include parameters quantifying formation and resorption areas in bone undergoing remodeling.[71,72]

SEM imaging has been used to demonstrate collagen fiber orientation and fiber deformation from an excised cortical bone specimen undergoing bending.[73] Furthermore, SEM and energy dispersive x-ray analysis, which allows for analysis of the elemental composition of a specimen, were used in concert to monitor the effect of bisphosphonate treatment on mineral content and quality of fracture healing in rats,[74] These studies demonstrate the capability of SEM to characterize both the organic and mineral components of bone. SEM images also can show the formation and resorption regions associated with bone remodeling.[75]

An advantage of SEM is that it allows higher resolution than standard histology by optical microscopy, and thin sections need not be microtomed. With the exception of environmental SEM, SEM requires a conductive sample to avoid

charging effects at the surface, so samples are typically coated with a thin conductive layer prior to imaging.

SEM: Quantitative Backscattered Electron Imaging (qBEI)

In addition to the signal measured from secondary electrons, SEM imaging also produces a backscattered electron signal which is used to generate a quantitative backscattered electron image (qBEI). As an electron beam is rastered across a sample, some of the incident electrons collide with atoms in the sample causing the electrons to be scattered backwards. The amount of backscattering an electron exhibits is proportional to the atomic number Z of the atom with which it collides; therefore, higher atomic numbered atoms will generate a higher backscattering signal. This is also called Z contrast.

Of the constituents in bone (organic matrix: C, O, H, N, P; mineral: Ca, O, H, P, Mg), calcium has the highest Z number (Z = 20). Calcium dominates qBEI image contrast, and it indicates different stages of mineralization in a tissue. The main outcome measurement for qBEI is bone mineral density distribution (BMDD) which details the degree of mineralization spatially across a region of interest.[76] Unlike standard *in vivo* BMD measurements, BMDD measurements using qBEI require bone tissue to be embedded in a plastic resin and imaged using an SEM. Surface topography greatly affects backscattering; thus, highly polished samples are required.

BMDD measurements using qBEI can be calibrated against a calcium standard to determine calcium weight in clinical biopsies.[76] qBEI is a particularly useful

technique when the mineral component of bone is expected to deleteriously affect bone quality, for example in patients with osteogenesis imperfecta[76] or in fragility fracture patients with acute or chronic illnesses.[77] Additionally, qBEI can characterize BMDD of multiple trabecular or cortical regions quickly at a resolution around 1 μm.[78] A key limitation of qBEI for clinical use is the need for a plastic embedded and polished biopsy.

2.3.4 High-Performance Liquid Chromatography (HPLC)

High-performance liquid chromatography (HPLC) is an analytical chemistry technique used to identify and quantify compounds in a liquid sample. HPLC works by pumping a sample through a column containing porous solid beads of known size and composition. Based on the physical and chemical interactions of the sample components with the column beads, each component elutes from the column at a signature rate, and the concentration of each component is measured precisely with a detector at the eluting end. Typical HPLC outcomes for bone quality are collagen crosslinks, bone turnover markers, and the amino acid composition.

The collagen crosslinks formed through enzymatic and non-enzymatic pathways have different effects on bone quality. Enzymatic crosslinks form through the action of lysyl oxidase and undergo a maturation process from an immature divalent crosslink to a mature trivalent crosslink. Enzymatic collagen crosslinks that have been measured using HPLC include the immature crosslinks of dehydrodihydroxynorleucine (DHLNL) and dehydrohydroxylysinonorleucine (HLNL), and the mature crosslinks of hydroxylysyl pyridinoline (HP) and lysyl

pyridinoline (LP).[79] Enzymatic crosslinks in humans stabilize around 10-15 years of age,[79] and in general are associated with advantageous mechanical stabilization of the collagen matrix and as precursors to mineralization.[80] The specific crosslinks HP and LP are also used as markers for bone turnover.[81] HPLC measurements of non-enzymatic crosslinks include glycation endproducts like pentosidine which has been implicated in reduced bone quality in patients with osteoporosis or type 2 diabetes,[82] and in normal aging.[83]

Important benefits of HPLC are the precise measurement of concentrations of molecular components as low as [picomol] and the ability to measure many components in one test. HPLC is destructive and requires sample homogenization, specialized equipment, and technical expertise. Future improvements will aim for higher selectivity of components, decreased throughput time, and lowered cost.

2.3.5 Thermal Gravimetric Analysis (TGA)

Thermal gravimetric analysis (TGA) characterizes the mass of organic and inorganic constituents in a sample by monitoring the sample's weight change with increasing temperature. For bone, samples are first dried at 110 °C to remove water. Continued heating between 200 and 600 °C causes the organic components to decompose until they are eliminated completely by combustion.[84] The remaining material after heating to 600 °C is called the ash weight, which consists only of the inorganic hydroxyapatite-like mineral in bone. The primary outcome is the ash fraction, which is obtained by dividing the ash weight by the initial dried sample weight.

TGA is the gold standard for determination of the mineral fraction in bone tissue; however, the primary drawback is that it is a destructive technique, leaving behind only the mineral component after combustion.

2.4 *Mechanical Characterization*

A fragility fracture is a mechanical event in a biological system.[85] Bone's resistance to fracture depends on many properties and their interactions including: 1) stiffness, the ability to resist elastic/reversible deformation; 2) strength, the ability to resist plastic/permanent deformation; 3) toughness, the ability to absorb energy during deformation; and 4) fracture toughness, the ability to prevent cracks from initiating and progressing. These properties also change with repetitive loading over time, a process known as fatigue, which is a complex process beyond the scope of this review.[86,87] Although a discussion of fracture toughness testing is beyond the scope of this review, several reviews are available regarding fracture toughness of bone at multiple length scales.[88–90]

Mechanical properties can be assessed at different levels of the bone structural hierarchy (Figure 2.1-1). In specifying a length scale at which to perform a mechanical test, influences from larger length scales can be removed, so that the test includes mechanical influences from the properties at and below the testing scale. For example, if a cancellous core from the proximal femur (mm length scale) is mechanically tested, the whole bone size and shape do not influence the test outcomes, and instead, the smaller scale properties (e.g., microarchitecture, composition, bone volume fraction) affecting the test outcome variables are included. Furthermore, the influence of

heterogeneity and flaws on the outcomes of a mechanical test are highly dependent on the size of the tested sample. More specifically, a small structural or compositional flaw will have a larger effect on a tissue-level mechanical test than the same flaw would have on a whole-bone mechanical test.

The following section details common types of mechanical testing, their outcome variables, and the length scale assessed by each test. Though not discussed in detail here, bone tissue handling and storage conditions (e.g., number of freeze-thaw cycles, tissue fixation, hydration) prior to mechanical testing may strongly influence the test's outcome variables and should be carefully controlled.[91,92]

2.4.1 Whole-bone Testing

Macroscale mechanical testing of whole bones is destructive and therefore only possible in studies using animal models or cadaveric tissue. In general, whole-bone testing involves stabilizing the bone of interest, applying a load (or displacement), and measuring the resulting deformation. The standard bones used for whole-bone testing are long bones and vertebrae, and typical loading modes include compression, tension, and bending.[93] For small animal studies, femoral bending tests are often performed because the diaphyseal cross-section is approximately elliptical, which simplifies subsequent mechanical analyses,[88,91] although other long bones and vertebrae can be tested depending on the research question. Outcome variables for a quasi-static load on a whole bone include a force-displacement curve, structural stiffness, structural strength, and toughness.[94]

Mechanical testing of vertebrae from ovariectomized macaques treated with ibandronate showed significant increases in strength and stiffness with drug treatment,[95] and testing of femora from rats with type 2 diabetes showed decreased strength, stiffness, and energy absorption arising from alterations of the collagen matrix.[96] These studies exemplify the utility of using whole-bone testing to study the effects of drug therapy and disease on the structural properties of bone. Drawbacks of whole-bone testing are that it is inherently destructive, and that this level of analysis is unable to decouple the structural and compositional factors that influence structural properties.

2.4.2 Apparent-level Bulk Cortical and Cancellous Bone Testing

Using regularly-shaped specimens of bulk cortical and cancellous tissue (width: mm to cm, length: mm to cm), mechanical tests allow determination of material properties of each tissue type including apparent-level stiffness, strength, and toughness. At this level of structural hierarchy, the effects of porosity are included in these measurements; thus, the outcomes are apparent-level properties. Testing at a smaller length scales is necessary to isolate tissue-level properties (see Tissue-level Cortical and Trabecular Testing).

Bulk tissue testing shows the mechanical properties of cancellous bone to be highly dependent on bone volume fraction, and, similarly, it shows the mechanical properties of cortical bone to be highly dependent on cortical porosity[97,98] Mechanical properties of both types of bone vary with anatomic site and loading direction,[99,100] which demonstrates the utility of separating mechanical tests by bulk tissue type and

site. Similar to whole bone testing, bulk cortical and cancellous bone testing has proven useful in elucidating the effects of drug therapy, disease, and aging in animal and human studies.[101–104] A disadvantage of using this level of mechanical testing is the necessity for uniformly machined specimens.

2.4.3 Tissue-level Cortical and Trabecular Testing

Performing mechanical testing on the scale of cortical microbeams or individual trabeculae further removes the effect of geometry and structure from mechanical property measurements. Typical dimensions of tissue-level mechanical testing are hundreds of microns in width and height, and hundreds to thousands of microns in length. Due to the technical challenges of testing small specimens, micro-tensile or microbeam bending are favored over micro-compression tests.

Micro-tensile testing of single trabeculae in human vertebral bone revealed large differences in ultimate strain between trabeculae, even within a single donor, thus highlighting the variations in tissue at small scales.[105] Disadvantages of tissue-level testing are the complexity of sample preparation and test design. Also, machining regular prismatic specimens can introduce damage or other testing artifacts, and these limitations should be considered when interpreting tissue-level outcomes.

In addition to tissue-level mechanical testing, tissue-level material properties can also be estimated from whole-bone or apparent-level tests by normalizing the property by the sample's geometry, as determined by micro-CT or other means. Estimation of tissue material properties from whole-bone structural properties relies

on many underlying assumptions, including assuming material homogeneity and a prismatic cross-section, which are not appropriate for whole bones.[91,94] Material properties estimated from whole-bone testing are poorly correlated with material properties assessed directly;[106] thus, material properties should be assessed directly with one of the techniques described below.

2.4.4 Indentation Testing

In an indentation, or hardness, test, the sample is subjected to a single, static force by a small tip, and the resulting indentation depth and size are recorded. In bone, indentation testing can be performed at several length scales, and it gives information regarding the resistance of bone tissue to plastic/permanent deformation.

For all length scales of indentation testing, tissue hydration, tip morphology, surface roughness, loading rate, and sample orientation must be carefully controlled.[107] Embedding samples in resin and polishing the surface can attenuate variability in outcome measures, though dehydration is known to increase hardness.[108]

Microindentation

In a microindentation test, the sample is subjected to a static load, and the resulting geometry of the indentation impression after load removal is used to calculate hardness. Hardness is defined as the force applied divided by the area of the residual indentation, which characterizes the material's resistance to plastic deformation.[109] Microindentation allows for hardness testing at the length scales of individual

trabeculae and osteons of bone.

In one of the foundational studies involving microindentation of bone, microhardness correlated with degree of mineralization.[109] More recently, hardness differences along the three orthogonal directions of parallel-fibered bone were observed, indicating the sensitivity of microindentation to local microstructure.[110] Furthermore, microindentation hardness values can distinguish between severely damaged bone and intact bone,[111] and it has also been used to characterize aged and osteoporotic bone.[107]

Key advantages of microindentation are the simplicity of the technique and the ability to quickly map microhardness across a sample. The main disadvantage is that microindentation has a single outcome measurement, hardness.

Reference Point Indentation

Within the past decade, a new type of indentation testing known as reference point indentation (RPI) was developed. RPI measures bone material properties on a scale similar to that of microindentation *ex vivo*. There are two main RPI devices, the OsteoProbe (Active Life Scientific, Santa Barbara, CA) and the BioDent (Active Life Scientific, Santa Barbara, CA), which operate under different mechanical loading conditions resulting in dissimilar outcome measurements.

The *in vivo* OsteoProbe utilizes a single indent with three phases: 1) a linear preload which passes through soft tissue; 2) a quick impact; and 3) unloading as the probe is removed manually. The outcome variable from the OsteoProbe is called bone

material strength index (BMSi) which is calculated as 100 times the indentation distance increase (IDI) of a calibration block of poly (methyl-methacrylate) divided by the IDI from the preload to the final load. Typical testing includes five or more indents spaced 2 mm apart. This testing practice accounts for bone's heterogeneity and avoids measurement interference from previous indentations.[112] In contrast to the single impact-based OsteoProbe, the BioDent features a cyclic indentation technique with customizable parameters in preconditioning, maximum indentation force, and cycle number. The output measurement is a force-indentation distance curve with each cycle presented on the same plot in real-time, and the outcome parameters achievable for each cycle include: 1) maximum indentation distance; 2) maximum force reached; 3) energy dissipation (energy under the force-displacement curve); 4) creep indentation distance; 5) loading slope; and 6) unloading slope. Furthermore, the variance between cycles of each of these parameters can also be calculated.[113,114]

The physical meaning of the outcome variables of the OsteoProbe and the BioDent are still under debate.[114,115] The impact loading conditions from the OsteoProbe are dissimilar to the relatively slow loading rates of a traditional microhardness test. In addition, the deformation geometry is not measured; thus, a hardness value cannot be determined from OsteoProbe tests. Furthermore, the name BMSi is itself potentially a source of confusion, as it is not a rigorous measurement of strength and has not been correlated with strength from other standard testing modalities.[114] It has been proposed that the OsteoProbe measures cracking of lamellar bone at the periosteal surface of the tibia, and as such, the closest analog of BMSi would be tissue toughness; however, the correlation between BMSi and tissue-level

toughness has also not yet been demonstrated.[116] Similar to the OsteoProbe, efforts to correlate BioDent outcomes to standard mechanical properties have been inconclusive.[114] The BioDent is most similar to a creep or low-cycle fatigue test,[116] but differences in the RPI technology versus standard mechanical testing procedures complicate direct comparisons of outcomes. Furthermore, the outcome measurements from each device were found to be weakly related to each other, if at all, in human cadaveric tibiae.[117]

Empirical evidence for the clinical utility of these techniques is bolstered by several studies using both the OsteoProbe and the BioDent. Studies using the OsteoProbe showed differences in BMSi between patient populations, including a decrease in BMSi in type 2 diabetic patients compared to non-diabetic patients,[118] as well as an increase in BMSi of glucocorticoid treated- compared to non-treated patients.[119] Using the BioDent, the maximum indentation distance and indentation distance increase between the first and last cycle were higher in femoral fracture patients than in non-fracture controls, suggesting the BioDent can distinguish a clinical fracture population.[120]

Key advantages of these techniques include the ability, for the first time, to directly measure mechanical properties of bone tissue *in vivo.* However, the outcome variables await rigorous validation, and standardization of RPI techniques between studies is lacking, complicating comparisons of RPI data across studies.

Nanoindentation

As in a microhardness test, in a nanoindentation test, a tip is loaded into and unloaded from the material of interest to probe the material properties of the sample. However, nanoindentation tests provide more information about the material behavior through the use of depth-sensing transducers. In nanoindentation, when force is applied to the nanoindenter tip, the tip displacement is continuously measured to produce a force-displacement curve. Hardness, representing the average pressure under load, is calculated as the maximum load divided by the indentation contact area; and the reduced modulus, which includes contributions from both the sample and the indenter, is calculated from the slope of the unloading portion of the force-displacement curve.[121] The elastic modulus of the sample, representing its resistance to elastic/reversible deformation, can be calculated from the reduced modulus, the Poisson's ratio of the sample, and the material properties of the indenter.

In bone, nanoindentation has a spatial contact resolution around 1 μm which allows for characterization of the lower levels of bone's hierarchical structure including lamellar and interlamellar regions.[122] Also, new instruments combine the imaging capability of an AFM with the mechanical testing capability of an indenter, thereby allowing for precise control over indentation location (within tenths of nm) and surface morphology.[123] Nanoindentation can be performed in a grid pattern resulting in a stiffness map,[124,125] and it can also be coupled to a Raman spectrometer such that mechanical and compositional information are collected simultaneously (TI 950 TriboIndenter, Hysitron, Minneapolis, MN).

When nanoindentation was used in conjunction with second harmonic

generation imaging on trabecular bone tissue, lamellar bone was harder and had more aligned collagen as compared to interlamellar bone.[126] Several validation studies of anisotropic elastic moduli with acoustic microscopy or tensile testing provide support for the translation of nanoindentation measurements to the macroscale.[127,128] These studies taken together demonstrate the feasibility of incorporating nanoindentation measurements of different sites into larger-scale models.

The capability for dynamic load- and displacement-control during nanoindentation allow acquisition of full force-displacement curves at μm-scale and even sub-μm-scale resolution. Nanoindentation also offers modulus mapping capabilities, and it can be coupled with simultaneous compositional testing like Raman spectroscopy, giving this technique versatility.[129] A drawback of nanoindentation is that its spatial resolution is effectively limited by specimen surface roughness; thus, careful sample preparation (e.g., surface polishing) is required for surface irregularities to be small in comparison to the indentation size.[130]

2.5 *Summary and Discussion*

Direct assessment of bone's resistance to fracture involves destructive mechanical testing, which is infeasible for clinical fracture risk evaluation. Although surrogate measures of fracture risk such as DEXA-assessed aBMD are clinically useful, they have important limitations as predictors of fracture risk,[131] and bone quality measurements can provide complementary information. Here we have reviewed techniques available to assess the geometric and material factors that contribute to bone quality across multiple length scales (Figure 2.1-1) along with some of their key

outcomes and characteristics (Table 2.1-1).

The techniques we review for geometric characterization include imaging technologies spanning length scales from nanometer to meter. These techniques share some common trade-offs, including 1) the size of the sample to be scanned versus the time required to complete a scan, which applies to MRI, all CT-based imaging modalities, and AFM imaging; 2) the scan resolution versus the radiation dose, which applies to *in vivo* characterization techniques that use x-ray sources, including QCT and HRpQCT; and 3) the clinical relevance of a site versus the amount of soft tissue that can interfere with scanning, which applies to MRI, QCT, and HRpQCT. These three trade-offs have attenuated over the past several decades and are expected to improve with future technological advances.

The techniques we review for compositional characterization characterize the collagen, mineral, and water components of bone spanning length scales from nanometer to meter. Of the methods reviewed, NMR and Raman offer *in vivo* capabilities. The remaining techniques require a biopsy, of which FTIR, Raman, SEM, and qBEI require special sample preparation and/or mounting; and HPLC and TGA are destructive. Despite many compositional characterization methods not being particularly well suited for clinical use, they offer powerful insights into the effects of diseases, aging, and drug therapies on bone composition that are typically not obtainable through noninvasive means. In clinical studies, these techniques can be performed on biopsies from a small subset of patients to provide detailed information on bone quality that cannot currently be assessed noninvasively.

Finally, we review the types of mechanical testing available for characterization of the mechanical properties of bone at different levels of structural hierarchy. The contributions of cancellous and cortical bone to whole-bone structural performance, as well as the variations in tissue-level properties, further demonstrate the importance of geometry and composition to bone's mechanical properties. Mechanical testing remains the gold standard for assessment of bone stiffness, strength, toughness, and fracture resistance in cadaveric or animal models. In human clinical studies, bone geometry derived from a noninvasive imaging modality can be used in conjunction with finite element analysis (FEA) validated from cadaveric studies to simulate mechanical testing and predict mechanical properties of clinical populations.[132]

Thus, although no single technique can completely characterize bone quality, many of the techniques discussed here can be synergistically combined to generate a more comprehensive understanding of bone geometry, composition, and mechanical properties. Useful combinations of characterization methods include HR-MRI or HRpQCT used with FEA modeling, which allows for non-invasive prediction of the effects of drug treatment on structural properties in human clinical studies, as well as nanoindentation and Raman spectroscopy, which allows simultaneous examination of the relationship between of compositional and mechanical properties in studies in which biopsies are available.[21,133] Finally, advancements in techniques like Raman imaging and RPI, which were previously feasible only in a laboratory setting, are now enabling their transition into *in vivo* use. These types of *in vivo* characterization are expected to make previously unobtainable patient-specific information on bone quality

available in the clinic.

2.6 *References*

1. Kanis, J. A., Johnell, O., Oden, A., *et al.* Ten year probabilities of osteoporotic fractures according to BMD and diagnostic thresholds. *Osteoporos. Int.* **12,** 989–995 (2001).
2. Donnelly, E., Lane, J. M. & Boskey, A. L. Research perspectives: The 2013 AAOS/ORS research symposium on Bone Quality and Fracture Prevention. *J. Orthop. Res.* **32,** 855–864 (2014).
3. Siegel, M. J. Magnetic resonance imaging of the adolescent female pelvis. *Magn. Reson. Imaging Clin. N. Am.* **10,** 303–324 (2002).
4. Choel, L., Last, D., Duboeuf, F., *et al.* Trabecular alveolar bone microarchitecture in the human mandible using high resolution magnetic resonance imaging. *Dentomaxillofacial Radiol.* **33,** 177 (2004).
5. Krug, R., Burghardt, A. J., Majumdar, S. & Link, T. M. High-Resolution Imaging Techniques for the Assessment of Osteoporosis. *Radiol. Clin. North Am.* **48,** 601–621 (2010).
6. Chang, G., Deniz, C. M., Honig, S., *et al.* MRI of the hip at 7T: Feasibility of bone microarchitecture, high-resolution cartilage, and clinical imaging. *J. Magn. Reson. Imaging* **39,** 1384–1393 (2014).
7. Magland, J. F., Rajapakse, C. S., Wright, A. C., Acciavatti, R. & Wehrli, F. W. 3D fast spin echo with out-of-slab cancellation: A technique for high-resolution structural imaging of trabecular bone at 7 tesla. *Magn. Reson. Med.* **63,** 719–727 (2010).
8. Majumdar, S. Magnetic resonance imaging of trabecular bone structure. *Top.*

Magn. Reson. Imaging **13,** 323–34 (2002).

9. Wehrli, F. W., Ladinsky, G. A., Jones, C., *et al.* In vivo magnetic resonance detects rapid remodeling changes in the topology of the trabecular bone network after menopause and the protective effect of estradiol. *J. Bone Miner. Res.* **23,** 730–40 (2008).

10. Majumdar, S., Genant, H. K., Grampp, S., *et al.* Correlation of trabecular bone structure with age, bone mineral density, and osteoporotic status: in vivo studies in the distal radius using high resolution magnetic resonance imaging. *J. Bone Miner. Res.* **12,** 111–118 (1997).

11. Rajapakse, C. S., Magland, J., Zhang, H., *et al.* Implications of noise and resolution on mechanical properties of trabecular bone estimated by image-based finite-element analysis. *J. Orthop. Res.* **27,** 1263–1271 (2009).

12. Wehrli, F. W., Song, H. K., Saha, P. K. & Wright, A. C. Quantitative MRI for the assessment of bone structure and function. *NMR Biomed.* **19,** 731–764 (2006).

13. Engelke, K., Adams, J. E., Armbrecht, G., *et al.* Clinical Use of Quantitative Computed Tomography and Peripheral Quantitative Computed Tomography in the Management of Osteoporosis in Adults: The 2007 ISCD Official Positions. *J. Clin. Densitom.* **11,** 123–162 (2008).

14. Genant, H. K., Engelke, K. & Prevrhal, S. Advanced CT bone imaging in osteoporosis. *Rheumatology* **47,** (2008).

15. Bousson, V., Le Bras, A., Roqueplan, F., *et al.* Volumetric quantitative computed tomography of the proximal femur: Relationships linking geometric

and densitometric variables to bone strength. Role for compact bone. *Osteoporos. Int.* **17,** 855–864 (2006).

16. Lala, D., Cheung, A. M., Lynch, C. L., *et al.* Measuring apparent trabecular structure with pQCT: A comparison With HR-pQCT. *J. Clin. Densitom.* **17,** 47–53 (2014).

17. Damilakis, J., Adams, J. E., Guglielmi, G. & Link, T. M. Radiation exposure in X-ray-based imaging techniques used in osteoporosis. *Eur. Radiol.* **20,** 2707–2714 (2010).

18. Geusens, P., Chapurlat, R., Schett, G., *et al.* High-resolution in vivo imaging of bone and joints: a window to microarchitecture. *Nat. Rev. Rheumatol.* **10,** 304–13 (2014).

19. Boutroy, S., Bouxsein, M. L., Munoz, F. & Delmas, P. D. In vivo assessment of trabecular bone microarchitecture by high-resolution peripheral quantitative computed tomography. *J. Clin. Endocrinol. Metab.* **90,** 6508–6515 (2005).

20. Burghardt, A. J., Buie, H. R., Laib, A., Majumdar, S. & Boyd, S. K. Reproducibility of direct quantitative measures of cortical bone microarchitecture of the distal radius and tibia by HR-pQCT. *Bone* **47,** 519–528 (2010).

21. Burghardt, A. J., Issever, A. S., Schwartz, A. V, *et al.* High-resolution peripheral quantitative computed tomographic imaging of cortical and trabecular bone microarchitecture in patients with type 2 diabetes mellitus. *J. Clin. Endocrinol. Metab.* **95,** 5045–55 (2010).

22. Bala, Y., Chapurlat, R., Cheung, A. M., *et al.* Risedronate slows or partly

reverses cortical and trabecular microarchitectural deterioration in postmenopausal women. *J. Bone Miner. Res.* **29,** 380–388 (2014).

23. Vilayphiou, N., Boutroy, S., Szulc, P., *et al.* Finite element analysis performed on radius and tibia HR-pQCT images and fragility fractures at all sites in men. *J. Bone Miner. Res.* **26,** 965–973 (2011).

24. Nishiyama, K. K. & Shane, E. Clinical imaging of bone microarchitecture with HR-pQCT. *Curr. Osteoporos. Rep.* **11,** 147–155 (2013).

25. Cheung, A. M., Adachi, J. D., Hanley, D. A., *et al.* High-resolution peripheral quantitative computed tomography for the assessment of bone strength and structure: A review by the canadian bone strength working group. *Curr. Osteoporos. Rep.* **11,** 136–146 (2013).

26. Cooper, D., Turinsky, A., Sensen, C. & Hallgrimsson, B. Effect of voxel size on 3D micro-CT analysis of cortical bone porosity. *Calcif. Tissue Int.* **80,** 211–219 (2007).

27. Boyd, S. K., Davison, P., Müller, R. & Gasser, J. A. Monitoring individual morphological changes over time in ovariectomized rats by in vivo micro-computed tomography. *Bone* **39,** 854–862 (2006).

28. Dempster, D. W., Cosman, F., Kurland, E. S., *et al.* Effects of daily treatment with parathyroid hormone on bone microarchitecture and turnover in patients with osteoporosis: a paired biopsy study. *J. Bone Miner. Res.* **16,** 1846–53 (2001).

29. Armas, L. A. G., Akhter, M. P., Drincic, A. & Recker, R. R. Trabecular bone histomorphometry in humans with Type 1 Diabetes Mellitus. *Bone* **50,** 91–96

(2012).

30. Wang, X., Masse, D. B., Leng, H., *et al.* Detection of trabecular bone microdamage by micro-computed tomography. *J. Biomech.* **40,** 3397–3403 (2007).

31. Tang, S. Y. & Vashishth, D. A non-invasive in vitro technique for the three-dimensional quantification of microdamage in trabecular bone. *Bone* **40,** 1259–1264 (2007).

32. Dong, P., Haupert, S., Hesse, B., *et al.* 3D osteocyte lacunar morphometric properties and distributions in human femoral cortical bone using synchrotron radiation micro-CT images. *Bone* **60,** 172–185 (2014).

33. Giessibl, F. J. AFM's path to atomic resolution. *Mater. Today* **8,** 32–41 (2005).

34. Revenko, I., Sommer, F., Minh, D. T., Garrone, R. & Franc, J. M. Atomic force microscopy study of the collagen fibre structure. *Biol. Cell* **80,** 67–69 (1994).

35. Baselt, D. R., Revel, J. P. & Baldeschwieler, J. D. Subfibrillar structure of type I collagen observed by atomic force microscopy. *Biophys. J.* **65,** 2644–2655 (1993).

36. Thurner, P. J., Oroudjev, E., Jungmann, R., *et al.* Imaging of Bone Ultrastructure using Atomic Force Microscopy. *Mod. Res. Educ. Top. Microsc.* 37–48 (2007).

37. Casuso, I., Kodera, N., Le Grimellec, C., Ando, T. & Scheuring, S. Contact-mode high-resolution high-speed atomic force microscopy movies of the purple membrane. *Biophys. J.* **97,** 1354–1361 (2009).

38. de Jong, W. F. La Substance Minerale Dans les Os. *Recl. des Trav. Chim. des Pays Bas* **45,** 445–448 (1926).

39. Bonar, L. C., Roufosse, A. H., Sabine, W. K., Grynpas, M. D. & Glimcher, M. J. X-ray diffraction studies of the crystallinity of bone mineral in newly synthesized and density fractionated bone. *Calcif. Tissue Int.* **35,** 202–209 (1983).

40. Handschin, R. G. & Stern, W. B. X-ray diffraction studies on the lattice perfection of human bone apatite (Crista Iliaca). *Bone* **16,** (1995).

41. Eanes, E. D. & Hailer, A. W. The effect of fluoride on the size and morphology of apatite crystals grown from physiologic solutions. *Calcif. Tissue Int.* **63,** 250–257 (1998).

42. Tadano, S. & Giri, B. X-ray diffraction as a promising tool to characterize bone nanocomposites. *Sci. Technol. Adv. Mater.* **12,** 64708–11 (2011).

43. Fratzl, P., Groschner, M., Vogl, G., *et al.* Mineral crystals in calcified tissues: A comparative study by SAXS. *J. Bone Miner. Res.* **7,** 329–334 (1992).

44. Georgiadis, M., Guizar-Sicairos, M., Zwahlen, A., *et al.* 3D scanning SAXS: A novel method for the assessment of bone ultrastructure orientation. *Bone* **71,** 42–52 (2015).

45. Almer, J. D. & Stock, S. R. Internal strains and stresses measured in cortical bone via high-energy X-ray diffraction. *J. Struct. Biol.* **152,** 14–27 (2005).

46. Gupta, H. S., Seto, J., Wagermaier, W., *et al.* Cooperative deformation of mineral and collagen in bone at the nanoscale. *Proc. Natl. Acad. Sci.* **103,** 17741–17746 (2006).

47. Brock, G. R., Kim, G., Ingraffea, A. R., *et al.* Nanoscale Examination of Microdamage in Sheep Cortical Bone Using Synchrotron Radiation Transmission X-Ray Microscopy. *PLoS One* **8,** e57942 (2013).

48. Currey, J. D. D. Effects of differences in mineralization on the mechanical properties of bone. *Philos. Trans. R. Soc. Lond. B. Biol. Sci.* **304,** 509–18 (1984).

49. Bembey, A. K., Oyen, M. L. M., Bushby, A. J. & Boyde, A. Viscoelastic properties of bone as a function of hydration state determined by nanoindentation. *Philos. Mag.* **28,** 5691–5703 (2006).

50. Bailey, A. J., Sims, T. J., Ebbesen, E. N., *et al.* Age-related changes in the biochemical properties of human cancellous bone collagen: Relationship to bone strength. *Calcif. Tissue Int.* **65,** 203–210 (1999).

51. Burstein, a H., Zika, J. M., Heiple, K. G. & Klein, L. Contribution of collagen and mineral to the elastic-plastic properties of bone. *J. Bone Joint Surg. Am.* **57,** 956–961 (1975).

52. Robson, M. D., Gatehouse, P. D., Bydder, G. M. & Neubauer, S. Human Imaging of Phosphorus in Cortical and Trabecular Bone In Vivo. *Magn. Reson. Med.* **51,** 888–892 (2004).

53. Kuhn, L. T., Grynpas, M. D., Rey, C. C., *et al.* A comparison of the physical and chemical differences between cancellous and cortical bovine bone mineral at two ages. *Calcif. Tissue Int.* **83,** 146–154 (2008).

54. Wehrli, F. W. & Fernández-Seara, M. A. Nuclear magnetic resonance studies of bone water. *Ann. Biomed. Eng.* **33,** 79–86 (2005).

55. Granke, M., Does, M. D. & Nyman, J. S. The Role of Water Compartments in the Material Properties of Cortical Bone. *Calcif. Tissue Int.* **97,** 292–307 (2015).

56. Nyman, J. S., Ni, Q., Nicolella, D. P. & Wang, X. Measurements of mobile and bound water by nuclear magnetic resonance correlate with mechanical properties of bone. *Bone* **42,** 193–199 (2008).

57. Singh, C., Rai, R. K., Kayastha, A. M. & Sinha, N. Ultra fast magic angle spinning solid - State NMR spectroscopy of intact bone. *Magn. Reson. Chem.* **54,** 132–135 (2016).

58. Mroue, K. H., Nishiyama, Y., Kumar Pandey, M., *et al.* Proton-Detected Solid-State NMR Spectroscopy of Bone with Ultrafast Magic Angle Spinning. *Sci. Rep.* **5,** 11991 (2015).

59. Boskey, A. L. & Mendelsohn, R. Infrared spectroscopic characterization of mineralized tissues. *Vib. Spectrosc.* **38,** 107–114 (2005).

60. Boskey, A. & Mendelsohn, R. Infrared analysis of bone in health and disease. *J. Biomed. Opt.* **10,** 31102 (2005).

61. Spevak, L., Flach, C. R., Hunter, T., Mendelsohn, R. & Boskey, A. Fourier transform infrared spectroscopic imaging parameters describing acid phosphate substitution in biologic hydroxyapatite. *Calcif. Tissue Int.* **92,** 418–428 (2013).

62. Paschalis, E. P., Jacenko, O., Olsen, B., deCrombrugghe, B. & Boskey, A. L. The role of type X collagen in endochondral ossification as deduced by Fourier transform infrared microscopy analysis. *Connect. Tissue Res.* **35,** 371–7 (1996).

63. Paschalis, E. P., Tatakis, D. N., Robins, S., *et al.* Lathyrism-induced alterations in collagen cross-links influence the mechanical properties of bone material without affecting the mineral. *Bone* **49,** 1232–1241 (2011).

64. Donnelly, E., Meredith, D. S., Nguyen, J. T., *et al.* Reduced cortical bone compositional heterogeneity with bisphosphonate treatment in postmenopausal women with intertrochanteric and subtrochanteric fractures. *J. Bone Miner. Res.* **27,** 672–678 (2012).

65. Carden, A. & Morris, M. D. Application of vibrational spectroscopy to the study of mineralized tissues (review). *J. Biomed. Opt.* **5,** 259–268 (2000).

66. Mandair, G. S. & Morris, M. D. Contributions of Raman spectroscopy to the understanding of bone strength. *Bonekey Rep.* **4,** 620 (2015).

67. Matousek, P. & Stone, N. Recent advances in the development of Raman spectroscopy for deep non-invasive medical diagnosis. *J. Biophotonics* **6,** 7–19 (2013).

68. Buckley, K., Kerns, J. G., Parker, A. W., Goodship, A. E. & Matousek, P. Decomposition of in vivo spatially offset Raman spectroscopy data using multivariate analysis techniques. *J. Raman Spectrosc.* **45,** 188–192 (2014).

69. Hanlon, E., Manoharan, R., Koo, T., *et al.* Prospects for in vivo Raman spectroscopy. *Phys. Med. Biol.* **45,** R1-59 (2000).

70. Geith, T., Amarie, S., Milz, S., Bamberg, F. & Keilmann, F. Visualisation of methacrylate-embedded human bone sections by infrared nanoscopy. *J. Biophotonics* **7,** 418–424 (2014).

71. Boyde, A. Improved digital SEM of cancellous bone: Scanning direction of

detection, through focus for in-focus and sample orientation. *J. Anat.* **202,** 183–194 (2003).

72. Boyde, A. & Jones, S. J. Scanning electron microscopy of bone: Instrument, specimen, and issues. *Microsc. Res. Tech.* **33,** 92–120 (1996).

73. Braidotti, P., Branca, F. P. & Stagni, L. Scanning electron microscopy of human cortical bone failure surfaces. *J. Biomech.* **30,** 155–162 (1997).

74. Perdikouri, C., Tägil, M. & Isaksson, H. Characterizing the composition of bone formed during fracture healing using scanning electron microscopy techniques. *Calcif. Tissue Int.* **96,** 11–17 (2015).

75. Boyde, A., Maconnachie, E., Reid, S. A., Delling, G. & Mundy, G. R. Scanning electron microscopy in bone pathology: review of methods, potential and applications. *Scan. Electron Microsc.* 1537–54 (1986).

76. Roschger, P., Fratzl, P., Eschberger, J. & Klaushofer, K. Validation of quantitative backscattered electron imaging for the measurement of mineral density distribution in human bone biopsies. *Bone* **23,** 319–326 (1998).

77. Sutton-Smith, P., Beard, H. & Fazzalari, N. Quantitative backscattered electron imaging of bone in proximal femur fragility fracture and medical illness. *J. Microsc.* **229,** 60–66 (2008).

78. Blouin, S., Puchegger, S., Roschger, A., *et al.* Mapping Dynamical Mechanical Properties of Osteonal Bone by Scanning Acoustic Microscopy in Time-of-Flight Mode. *Microsc. Microanal.* **20,** 924–936 (2014).

79. Eyre, D. R., Dickson, I. R. & Van Ness, K. Collagen cross-linking in human bone and articular cartilage. Age-related changes in the content of mature

hydroxypyridinium residues. *Biochem. J.* **252,** 495–500 (1988).

80. Knott, L. & Bailey, A. J. Collagen cross-links in mineralizing tissues: A review of their chemistry, function, and clinical relevance. *Bone* **22,** 181–187 (1998).

81. Uebelhart, D., Gineyts, E., Chapuy, M. C. & Delmas, P. D. Urinary excretion of pyridinium crosslinks: a new marker of bone resorption in metabolic bone disease. *Bone Miner.* **8,** 87–96 (1990).

82. Saito, M. & Marumo, K. Collagen cross-links as a determinant of bone quality: A possible explanation for bone fragility in aging, osteoporosis, and diabetes mellitus. *Osteoporos. Int.* **21,** 195–214 (2010).

83. Odetti, P., Rossi, S., Monacelli, F., *et al.* Advanced glycation end products and bone loss during aging. *Ann. N. Y. Acad. Sci.* **1043,** 710–717 (2005).

84. Iafisco, M., Foltran, I., Sabbatini, S., Tosi, G. & Roveri, N. Electrospun nanostructured fibers of collagen-biomimetic apatite on titanium alloy. *Bioinorg. Chem. Appl.* **2012,** 123953 (2012).

85. Hernandez, C. J. & Keaveny, T. M. A biomechanical perspective on bone quality. *Bone* **39,** 1173–1181 (2006).

86. Carter, D. R., Hayes, W. C. & Schurman, D. J. Fatigue life of compact bone-II. Effects of microstructure and density. *J. Biomech.* **9,** 211–218 (1976).

87. Carter, D. R. & Hayes, W. C. Compact bone fatigue damage-I. Residual strength and stiffness. *J. Biomech.* **10,** 325–337 (1977).

88. Ritchie, R. O., Koester, K. J., Ionova, S., *et al.* Measurement of the toughness of bone: A tutorial with special reference to small animal studies. *Bone* **43,**

798–812 (2008).

89. Bonfield, W. Advances in the fracture mechanics of cortical bone. *J. Biomech.* **20,** 1071–1081 (1987).

90. Ural, A. & Vashishth, D. Hierarchical perspective of bone toughness – from molecules to fracture. *Int. Mater. Rev.* **59,** 245–263 (2014).

91. Turner, C. H. & Burr, D. B. Basic biomechanical measurements of bone: A tutorial. *Bone* **14,** 595–608 (1993).

92. Nyman, J. S., Roy, A., Shen, X., *et al.* The influence of water removal on the strength and toughness of cortical bone. *J. Biomech.* **39,** 931–938 (2006).

93. Currey, J. D. The structure and mechanics of bone. *J. Mater. Sci.* **47,** 41–54 (2012).

94. Van Der Meulen, M. C. H., Jepsen, K. J. & Miki, B. Understanding bone strength: Size isn't everything. *Bone* **29,** 101–104 (2001).

95. Müller, R., Hannan, M., Smith, S. Y. & Bauss, F. Intermittent ibandronate preserves bone quality and bone strength in the lumbar spine after 16 months of treatment in the ovariectomized cynomolgus monkey. *J. Bone Miner. Res.* **19,** 1787–96 (2004).

96. Saito, M., Fujii, K., Mori, Y. & Marumo, K. Role of collagen enzymatic and glycation induced cross-links as a determinant of bone quality in spontaneously diabetic WBN/Kob rats. *Osteoporos. Int.* **17,** 1514–1523 (2006).

97. Currey, J. D. D. The effect of porosity and mineral content on the Young's modulus of elasticity of compact bone. *J. Biomech.* **21,** 131–139 (1988).

98. Seeman, E. Bone quality: The material and structural basis of bone strength. *J. Bone Miner. Metab.* **26,** 1–8 (2008).

99. Goldstein, S. A. The mechanical properties of trabecular bone: Dependence on anatomic location and function. *J. Biomech.* **20,** 1055–1061 (1987).

100. Reilly, D. T. & Burstein, A. H. The elastic and ultimate properties of compact bone tissue. *J. Biomech.* **8,** (1975).

101. Tang, S. Y., Allen, M. R., Phipps, R., Burr, D. B. & Vashishth, D. Changes in non-enzymatic glycation and its association with altered mechanical properties following 1-year treatment with risedronate or alendronate. *Osteoporos. Int.* **20,** 887–894 (2009).

102. Zimmermann, E. A., Schaible, E., Bale, H., *et al.* Age-related changes in the plasticity and toughness of human cortical bone at multiple length scales. *Proc. Natl. Acad. Sci. U. S. A.* **108,** 14416–21 (2011).

103. Zioupos, P. & Currey, J. D. Changes in the stiffness, strength, and toughness of human cortical bone with age. *Bone* **22,** 57–66 (1998).

104. Fazzalari, N. L. L., Forwood, M. R. R., Smith, K., Manthey, B. A. A. & Herreen, P. Assessment of cancellous bone quality in severe osteoarthrosis: Bone mineral density, mechanics, and microdamage. *Bone* **22,** 381–388 (1998).

105. Hughes, I., Blasiole, B., Huss, D., *et al.* Otopetrin 1 is required for otolith formation in the zebrafish Danio rerio. *Dev. Biol.* **276,** 391–402 (2004).

106. Silva, M. J., Brodt, M. D., Fan, Z. & Rho, J. Y. Nanoindentation and whole-bone bending estimates of material properties in bones from the senescence

accelerated mouse SAMP6. *J. Biomech.* **37,** 1639–1646 (2004).

107. Zysset, P. K. Indentation of bone tissue: A short review. *Osteoporos. Int.* **20,** 1049–1055 (2009).

108. Hoffler, C. E. An Application of Nanoindentation Technique to Measure Bone Tissue Lamellae Properties. *J. Biomech. Eng.* **127,** 1046 (2005).

109. Weaver, J. K. The microscopic hardness of bone. *J. Bone Joint Surg. Am.* **48,** 273–88 (1966).

110. Ziv, V., Wagner, H. D. & Weiner, S. Microstructure-microhardness relations in parallel-fibered and lamellar bone. *Bone* **18,** 417–428 (1996).

111. Dall'Ara, E., Schmidt, R. & Zysset, P. Microindentation can discriminate between damaged and intact human bone tissue. *Bone* **50,** 925–929 (2012).

112. Bridges, D., Randall, C. & Hansma, P. K. A new device for performing reference point indentation without a reference probe. *Rev. Sci. Instrum.* **83,** 044301 (2012).

113. Hansma, P., Turner, P., Drake, B., *et al.* The bone diagnostic instrument II: Indentation distance increase. *Rev. Sci. Instrum.* **79,** 064303 (2008).

114. Allen, M. R., McNerny, E. M. B., Organ, J. M. & Wallace, J. M. True gold or pyrite: A review of reference point indentation for assessing bone mechanical properties in vivo. *J. Bone Miner. Res.* **30,** 1539–1550 (2015).

115. Farr, J. N., Amin, S. & Khosla, S. Regarding "True Gold or Pyrite: A Review of Reference Point Indentation for Assessing Bone Mechanical Properties In Vivo". *J. Bone Miner. Res.* **30,** 2325–2326 (2015).

116. Jepsen, K. J. & Schlecht, S. H. Biomechanical mechanisms: Resolving the

apparent conundrum of why individuals with type II diabetes show increased fracture incidence despite having normal BMD. *J. Bone Miner. Res.* **29,** 784–786 (2014).

117. Karim, L., Van Vliet, M. & Bouxsein, M. L. Comparison of cyclic and impact-based reference point indentation measurements in human cadaveric tibia. *Bone* (2015). doi:10.1016/j.bone.2015.03.021

118. Farr, J. N., Drake, M. T., Amin, S., *et al.* In vivo assessment of bone quality in postmenopausal women with type 2 diabetes. *J. Bone Miner. Res.* **29,** 787–795 (2014).

119. Mellibovsky, L., Prieto-Alhambra, D., Mellibovsky, F., *et al.* Bone tissue properties measurement by reference point indentation in glucocorticoid-induced osteoporosis. *J. Bone Miner. Res.* **30,** 1651–1656 (2015).

120. Guerri-Fernandez, R. C., Nogues, X., Quesada Gomez, J. M., *et al.* Microindentation for in vivo measurement of bone tissue material properties in atypical femoral fracture patients and controls. *J. Bone Miner. Res.* **28,** 162–168 (2013).

121. Oliver, C. & Pharr, M. An improved technique for determining hardness and elastic modulus using load and displacement sensing indentation experiments. *J. Mater. Res.* **7,** 1564–1583 (1992).

122. Zysset, P. K., Edward Guo, X., Edward Hoffler, C., Moore, K. E. & Goldstein, S. A. Elastic modulus and hardness of cortical and trabecular bone lamellae measured by nanoindentation in the human femur. *J. Biomech.* **32,** 1005–1012 (1999).

123. Hengsberger, S., Kulk, A. & Zysset, P. A Combined Atomic Force Microscopy and Nonoindentation Technique to Investigate the Elastic Properties of Bine Structural Units. *Eur. Cells Mater.* **1,** 12–17 (2001).

124. Constantinides, G., Ravi Chandran, K. S., Ulm, F. J. & Van Vliet, K. J. Grid indentation analysis of composite microstructure and mechanics: Principles and validation. *Mater. Sci. Eng. A* **430,** 189–202 (2006).

125. Uskokovic, P. S., Tang, C. Y., Tsui, C. P., Ignjatovic, N. & Uskokovic, D. P. Micromechanical properties of a hydroxyapatite/poly-l-lactide biocomposite using nanoindentation and modulus mapping. *J. Eur. Ceram. Soc.* **27,** 1559–1564 (2007).

126. Donnelly, E., Williams, R. M., Downs, S. a., *et al.* Quasistatic and dynamic nanomechanical properties of cancellous bone tissue relate to collagen content and organization. *J. Mater. Res.* **21,** 2106–2117 (2006).

127. Turner, C. H., Rho, J., Takano, Y., Tsui, T. Y. & Pharr, G. M. The elastic properties of trabecular and cortical bone tissues are similar: Results from two microscopic measurement techniques. *J. Biomech.* **32,** 437–441 (1999).

128. Hengsberger, S., Enstroem, J., Peyrin, F. & Zysset, P. How is the indentation modulus of bone tissue related to its macroscopic elastic response? A validation study. *J. Biomech.* **36,** 1503–1509 (2003).

129. Tai, K., Dao, M., Suresh, S., Palazoglu, A. & Ortiz, C. Nanoscale heterogeneity promotes energy dissipation in bone. *Nat. Mater.* **6,** 454–62 (2007).

130. Donnelly, E., Baker, S. P., Boskey, A. L. & Van Der Meulen, M. C. H. Effects

of surface roughness and maximum load on the mechanical properties of cancellous bone measured by nanoindentation. *J. Biomed. Mater. Res. - Part A* **77,** 426–435 (2006).

131. Marshall, D. & Wedel, H. Meta-analysis of how well measures of bone mineral density predict occurrence of osteoporotic fractures. *Bmj* **312,** 1254–59 (1996).

132. Crawford, R. P., Cann, C. E. & Keaveny, T. M. Finite element models predict in vitro vertebral body compressive strength better than quantitative computed tomography. *Bone* **33,** 744–750 (2003).

133. Baminger, H. Femoral bone strength and its relation to cortical and trabecular changes after treatment with PTH, alendronate, and their combination as assessed by finite element analysis of quantitative CT-scans. *J. fur Miner.* **16,** 208 (2009).

134. Liu, X. S., Stein, E. M., Zhou, B., *et al.* Individual trabecula segmentation (ITS)-based morphological analyses and microfinite element analysis of HR-pQCT images discriminate postmenopausal fragility fractures independent of DXA measurements. *J. Bone Miner. Res.* **27,** 263–272 (2012).

135. Milovanovic, P., Zimmermann, E. A., Riedel, C., *et al.* Multi-level characterization of human femoral cortices and their underlying osteocyte network reveal trends in quality of young, aged, osteoporotic and antiresorptive-treated bone. *Biomaterials* **45,** 46–55 (2015).

136. Boskey, A. L. Bone composition: relationship to bone fragility and antiosteoporotic drug effects. *Bonekey Rep.* **2,** 447 (2013).

137. Wallace, J. M., Chen, Q., Fang, M., *et al.* Type i collagen exists as a distribution of nanoscale morphologies in teeth, bones, and tendons. *Langmuir* **26,** 7349–7354 (2010).

CHAPTER 3

BONE TISSUE COLLAGEN MATURITY AND MINERAL CONTENT INCREASE WITH SUSTAINED HYPERGLYCEMIA IN THE KK-AY MURINE MODEL OF TYPE 2 DIABETES

3.1 *Introduction*

Type 2 diabetes mellitus (T2DM) increases fracture risk for a given bone mineral density (BMD),[1,2] and the greater fracture risk for patients with T2DM persists after adjustment for age, body mass index (BMI), and physical activity.[3] Additionally, T2DM-related fractures are underpredicted by current clinical fracture risk assessment tools that rely heavily on BMD, such as FRAX.[2] Taken together, these findings suggest T2DM degrades bone quality independently of BMD, which motivates further assessment of bone tissue properties from patients with T2DM.

The precise mechanisms responsible for the putative alterations in bone quality that increase T2DM-related fractures are unknown; however, changes in the post-translational modifications of collagen due to hyperglycemia have been suggested as a contributing factor. Post-translational modifications of collagen include 1) crosslinking through enzymatically-mediated processes and 2) the formation of a heterogenous group of reaction products collectively known as advanced glycation endproducts (AGEs) through non-enzymatically-induced processes. Enzymatic crosslinking is controlled by the action of lysyl oxidase and results in the formation of trivalent crosslinks such as hydroxylysylpyridinoline (HP, also referred to as

pyridinoline) and lysylpyridinoline (LP, also referred to as deoxypyridinoline).[4] Non-enzymatically-induced AGEs, on the other hand, form through the reaction of extracellular reducing sugars (e.g., glucose, ribose, fructose) with free amino groups in proteins and can result in non-enzymatic crosslinks, as well as other non-crosslinking AGEs (e.g., carboxymethyl-lysine).[5]

Whereas enzymatic crosslinks strengthen and stabilize the collagen matrix,[6] AGEs decrease energy absorption and embrittle bone tissue in animal models,[7] and in glycated/ribosylated human[8] and bovine tissue *in vitro*.[9] Rodent models supply direct evidence that T2DM impairs whole-bone fracture resistance, and the skeletal phenotypes of rodents with T2DM are typically characterized by substantial reductions in maximum load and inconsistently by reductions in energy to failure and BMD (summarized in [10]). For example, spontaneously diabetic WBN/Kob rats exhibited reduced maximum load and work-to-fracture with no change in BMD compared to controls, and these weakening and embrittlement processes were accompanied by concomitant decreases in enzymatic collagen crosslinks and increases in non-enzymatic collagen crosslinks.[11]

Additionally, AGEs impair bone remodeling processes. In AGE-modified collagen, osteoblastic growth and differentiation were disrupted,[12,13] and apoptosis increased.[14] Observations of reduced bone formation in T2DM patients compared to non-DM controls are also supported by analysis of histomorphometric data[15] and biochemical markers of bone formation.[16–18]

A promising model to study T2DM is the KK-Ay mouse, and to date,

compositional skeletal characteristics of the KK-Ay mice have not been evaluated.[19] Mice from the KK strain exhibit insulin insensitivity and glucose intolerance,[20,21] yet they are neither glucosuric nor hyperglycemic.[20,22,23] The addition of the A^y mutation to the KK mouse induces obesity and a distinguishing yellow coat, and KK-Ay mice exhibit overt glucosuria and hyperglycemia around eight weeks of age.[22,23] When tested in three-point bending, the tibiae of KK-Ay mice had a lower ultimate load compared to controls,[24] which may parallel the impaired structural integrity observed in humans.

Prior studies of the skeletal properties of KK-Ay mice compared to controls consistently report reduced trabecular BMD,[24–26] whereas the findings for cortical vBMD, total aBMD, and bone formation/resorption markers are less consistent. In two studies comparing KK-Ay mice to C57BL/6 controls, one study reported a decrease in cortical area, thickness, and vBMD with a concomitant decrease in osteoblastogenesis and osteoclastogenesis,[24] and in contrast, the other study reported an increase in cortical thickness and vBMD with an upregulation of osteoblast- and osteoclast-related gene expression.[25] While skeletal morphology[24–27] and collagen crosslinks[11,27–29] have been characterized in T2DM bone, compositional data beyond ash weight[30–32] and mineral:matrix ratio (using Raman spectroscopy)[27,32] are limited. These results underscore the need for compartment-specific (i.e., trabecular, cortical) and whole-bone compositional assays of T2DM bone tissue.

Therefore, the objective of this work was to compare the spatially-resolved compositional properties and collagen crosslinks of bone tissue from KK-Ay mice

with overt T2DM (A^y/a) to their non-overt T2DM siblings (a/a). We hypothesized that hyperglycemia would increase tissue-level non-enzymatic crosslinking (due to AGE accumulation) and would increase tissue mineral content and collagen maturity (due to reduced bone turnover) in the A^y/a mice compared to the a/a controls.

3.2 *Materials and Methods*

3.2.1 Obese Mouse Model of T2DM

Male KK.Cg-A^y/J mice were purchased from The Jackson Laboratory at eight weeks of age (002468, Bar Harbor, ME), raised in ventilated cages at 20-22 °C with a 14-hour light-dark cycle, and given free access to standard irradiated chow (2920x, Harlan Laboratories, Inc., Indianapolis, IN). The yellow heterozygous A^y/a mice were used to model T2DM and their black homozygous a/a littermates were used as controls.

The femora used here were the non-operative controls from a study of the effects of T2DM on osteoarthritis progression.[33] At 12 weeks of age, mice within each group (A^y/a: n = 14, a/a: n = 8) were anesthetized and chosen at random to undergo either a destabilization medial meniscus (DMM) or sham procedure on the left distal femora.[34] The right femora used in the current study were not operated or otherwise treated. Body masses at the time of surgery were recorded. A minimum of three blood glucose measurements were performed via tail nick test (Precision Xtra Blood Glucose Test Strips, Abbott Diabetes Care Inc., Alameda, CA), with three of the measurement time points at 8 weeks of age (at purchase from Jackson), 12 weeks

of age (at DMM surgery), and 20 weeks of age (at euthanasia). A lifetime-average blood glucose level (average of all blood glucose measurements for each mouse) greater than 300 mg/dl confirmed hyperglycemic status of the A^y/a mice and euglycemic status of the *a/a* mice.[19] For a subset of the mice (A^y/a: n = 4, *a/a*: n = 4), fasting blood glucose measurements were taken. Because fasting blood glucose in mice may not be representative of steady-state conditions,[35] the blood glucose measurements of these mice were excluded from mean blood glucose calculations for each group. No other treatments were applied to these mice throughout the study. Mice were euthanized with carbon dioxide at 20 weeks of age, and the femora were dissected. The stifle joints (including the distal half of each femur) were allocated to osteoarthritis analyses,[33] and the proximal halves of the femora were allocated to bone tissue compositional analyses for the current study. The proximal femora were wrapped in saline-soaked gauze and frozen at -20 °C. All animal care and procedures were performed at the University of Colorado School of Medicine with the approval of the Institutional Animal Care and Use Committee.

3.2.2 Fourier Transform Infrared Imaging

Fourier transform infrared (FTIR) imaging was used to evaluate bone tissue compositional properties in a spatially resolved fashion. The proximal femora were thawed, dehydrated in graded organic solvents, and embedded in poly(methyl methacrylate) (PMMA). For each of the femora, three non-consecutive, 1-µm-thick longitudinal sections spaced a minimum of 10 µm apart were cut near the midplane of the femur with a microtome (SM2500, Leica Biosystems, Nussloch, Germany) and

placed on BaF_2 windows (Spectral Systems, Hopewell Junction, NY).

FTIR images were collected at two levels of structural hierarchy: 1) a whole-proximal-femur image was generated at 25 µm spatial resolution, and 2) tissue-specific cortical and trabecular regions of interest (ROIs) (size: 400 µm x 500 µm) were generated at 6.25 µm spatial resolution. For each section, a single whole-proximal-femur image, in addition to three cortical and three trabecular ROIs (Figure S1), were collected over the spectral range 800-2000 cm^{-1} at a spectral resolution of 4 cm^{-1} using an infrared imaging system (Spotlight 400, Perkin-Elmer Instruments, Waltham, MA). Subsequently, chemical imaging software (ISys, Malvern Instruments, Worcestershire, UK) was used to remove the background, baseline, and subtract the PMMA spectral contribution from the bone spectra.[36] For five proximal femora, soft tissue on the femoral head was present at the time of PMMA embedding. This soft tissue was excluded from FTIR image analysis with a spectral mask.

For each image, the infrared spectrum at each pixel was analyzed to determine the following parameters: mineral:matrix ratio, carbonate:phosphate ratio, collagen maturity, and mineral crystallinity.[37] The mineral:matrix ratio (area ratio of the phosphate ν_1-ν_3 and amide I peaks) characterizes tissue mineral content;[38,39] the carbonate:phosphate ratio (area ratio of the carbonate ν_2 and phosphate ν_1-ν_3 peaks) characterizes the extent to which carbonate substitutes into the mineral lattice;[40] collagen maturity (the intensity ratio of 1660 cm^{-1} and 1690 cm^{-1}) is related to the ratio of mature, non-reducible collagen crosslinks to immature, reducible collagen crosslinks;[41] and the mineral crystallinity (intensity ratio of 1030 cm^{-1} and 1020 cm^{-1})

is related to crystal size and perfection assessed by x-ray diffraction.[42] Two outcome measurements were obtained for each FTIR parameter from each image: the mean value of all pixels and the distribution width (calculated as the full-width at half-maximum (FWHM) of the Gaussian curve fit to the distribution of pixels, Fig. 2) to assess compositional heterogeneity. Thus, eight outcomes were assessed separately for cortical, trabecular, and whole-proximal-femur ROIs: 1) mean mineral:matrix ratio, 2) mean carbonate:phosphate ratio, 3) mean collagen maturity, 4) mean crystallinity, 5) mineral:matrix ratio FWHM, 6) carbonate:phosphate ratio FWHM, 7) collagen maturity FWHM, and 8) crystallinity FWHM.

3.2.3 High-performance Liquid Chromatography

High-performance liquid chromatography (HPLC) was used to quantify the AGE pentosidine in the whole proximal femur. The enzymatic crosslinks HP and LP were quantified as secondary outcomes.

Following completion of FTIR imaging, the proximal femora were de-embedded from PMMA through agitation in methyl acetate for three days, with a solution change every 24 hours. After de-embedding, the femora were agitated in 100% acetone (24 h), 100% ethanol (24 h), and isopropyl ether (3x, 15 min). After rinsing with DI water, the femora were lyophilized then hydrolyzed in 6 N HCl at 110 °C for 18 h. The hydrolysates were dried in a vacuum centrifuge (Speed Vac SC110A, Savant, Farmingdale, NY) then re-suspended in an internal standard solution containing 10 nM pyridoxine and 2.4 μM homoarginine; 30 μl of internal standard solution was added for every mg of dried bone. The re-suspended samples were

filtered, then diluted 1:5 with 10% acetonitrile (v/v) and 0.5% heptafluorobutyric acid (v/v).

Samples were injected into the column and separated using two isocratic steps.[29,43] A calibrator containing all three crosslinks (pentosidine, HP, LP) was serially diluted 1:2 five times to create a linear calibration curve. The pentosidine standard was purchased from Case Western Reserve University (Cleveland, OH), and the HP and LP standards were purchased from Quidel (8004, Quidel, Athens, OH). Separations were performed with a Gemini-NX C-18 column (Phenomenex, Torrance, CA) connected to a programmable HPLC system (Model 126, Beckman Coulter, Inc., Fullerton, CA). 32 Karat Workstation software (v. 5.0, Beckman Coulter, Inc., Brea, CA) was used to control the autosampler, pump, and fluorimeter (Model FP1520, Jasco, Easton, MD). Data analysis was performed using 32 Karat Workstation software and MATLAB (2012a, The MathWorks, Inc., Natick, MA).

Pentosidine, HP, and LP concentrations were normalized by collagen concentration as determined by hydroxyproline concentration. For the hydroxyproline measurements, an aliquot of the diluted sample from the crosslink analysis was further diluted 1:50 with 6 μM homoarginine in 0.1 M borate buffer (pH 11.4), derivatized using 6 mM 9-fluorenylmethyl chloroformate for 40 minutes, and extracted using pentane. Pentane extraction removes excess FMOC-Cl reagent, FMOC-OH reaction product, and acetone. Three extractions were performed, then 25% (v/v) acetonitrile in 0.25 M boric acid (pH 5.5) was added. The separation of amino acids was run using the same column and system as the crosslink separations using the injection sequence

described by Bank *et al.*[44] Five serial 1:2 dilutions of purified hydroxyproline (Sigma-Aldrich, St. Louis, MO) and 6 μM homoarginine in 0.1 M borate buffer (pH 11.4) were used to make a linear calibration curve for hydroxyproline. Collagen concentration was determined from the constant ratio of hydroxyproline in fibrillar collagen (300 mol hydroxyproline per mol collagen).

The final outcomes for HPLC included concentrations for pentosidine, HP, and LP. The ratio of HP to LP (HP:LP), the total concentration of mature enzymatic crosslinks (HP+LP), and the ratio of pentosidine to mature enzymatic crosslinks (Pentosidine:HP+LP) were also examined.

3.2.4 Statistical Analysis

Mouse characteristics (body mass, lifetime-average non-fasting blood glucose) and collagen crosslinks (pentosidine, HP, LP) were assessed for normality and homogeneity of variances, and a two-tailed Student's t-test was performed to assess differences between groups. A significance level of 0.05 was used for all analyses.

For the eight FTIR outcome variables, cortical, trabecular, and whole-proximal-femur regions were analyzed separately. For each region, a linear mixed model was used to assess the relationship between genotype (A^y/a, a/a) while accounting for the multiple sections analyzed per mouse (3 sections/femur) and for repeated measurements made within each section (3 trabecular ROIs and 3 cortical ROIs). To test if the increased mass of the A^y/a mice vs. controls had an effect on the FTIR outcome variables, subsequent linear mixed models that included the fixed

effect of body mass were analyzed. Pairwise differences between groups were assessed with Tukey post-hoc tests. The reported percent differences for FTIR parameters were calculated from the raw data, while the *p*-values were determined by the linear mixed models.

The relationships of lifetime-average blood glucose with all FTIR imaging and HPLC outcomes were analyzed to elucidate the effects of hyperglycemia on tissue material properties. Cortical, trabecular, and whole-proximal-femur FTIR ROIs were regressed separately with lifetime-average blood glucose to highlight potential region-specific effects of hyperglycemia. Because AGE accumulation may also affect bone turnover, the relationships of pentosidine and the proximal femur FTIR outcomes were also investigated. The HPLC measurements of collagen crosslinks were performed on the homogenized whole proximal femur, so region-specific (i.e., cortical, trabecular) correlations were not assessed between pentosidine and the FTIR imaging outcomes. For all regressions, A^y/a and *a/a* data were pooled because the relationships did not differ between groups ($p > 0.05$).

3.3 ***Results***

3.3.1 Mouse Characteristics

The A^y/a mice experienced hyperglycemia for a minimum duration of 12 weeks and were heavier than their *a/a* littermate controls. In A^y/a mice relative to controls, the lifetime-average non-fasting blood glucose was 83% higher (mean ± SD, A^y/a: 426.5 ± 49.2 mg/dL vs. *a/a*: 234.5 ± 5.1 mg/dL, $p << 0.001$), and body mass at time of DMM

surgery was 16% higher (A^y/a: 36.7 ± 3.8 g vs. *a/a*: 31.5 ± 2.6 g, $p = 0.0024$). Furthermore, hyperglycemia in the A^y/a mice was confirmed over the 12-week study period. The non-fasting blood glucose of the A^y/a mice was 67% greater than the *a/a* mice at 8 weeks of age (A^y/a: 346.2 ± 130.6 mg/dL vs. *a/a*: 207.6 ± 18.5 mg/dL, $p < 0.001$), 114% greater at 12 weeks of age (at DMM surgery): (A^y/a: 413.3 ± 93.2 mg/dL vs. *a/a*: 193.0 ± 11.8 mg/dL, $p < 0.001$), and 76% greater at 20 weeks of age (at euthanasia): (A^y/a: 456.8 ± 76.3 mg/dL vs. *a/a*: 258.5 ± 41.7 mg/dL, $p < 0.001$).

3.3.2 FTIR Imaging: Parameter Distribution Means and Widths

Bone tissue from the A^y/a mice exhibited greater mean collagen maturity and mineral content, and narrower distribution widths of carbonate:phosphate ratio and crystallinity compared to the *a/a* mice.

Compared to *a/a* controls, mean collagen maturity was greater in the A^y/a mice in cortical bone (+12%, $p = 0.0285$; Figure 3.3-1A, Figure 3.3-2A), trabecular bone (+8%, $p = 0.0399$; Figure 3.3-1A, Figure 3.3-2C), and in the whole proximal femur (+7%, $p = 0.0499$; Figure 3.3-1A, Figure 3.3-2B). In the whole proximal femur, the mean mineral:matrix ratio was greater in A^y/a mice compared to controls (+12%, $p = 0.0233$; Figure 3.3-1A, Figure 3.3-2B) and trended towards being greater in cortical bone (+8%, $p = 0.0790$; Figure 3.3-1A). Body mass had a significant positive effect on the mean mineral:matrix ratio in cortical bone ($p < 0.001$); however, no observed effect of body mass on mean mineral:matrix ratio was observed in the trabecular or whole proximal femur regions or in the mean collagen maturity of cortical, trabecular, and whole proximal femur regions. The mean carbonate:phosphate ratio and mean

crystallinity were similar between A^y/a and *a/a* mice across all regions. Distributions were narrower in the A^y/a mice compared to controls for carbonate:phosphate ratio (-19%, $p = 0.0078$; Figure 3.3-1B, Figure 3.3-3A) and crystallinity (-24%, $p = 0.0099$; Figure 3.3-1B, Figure 3.3-3B) in the whole proximal femora. The distribution widths were similar for all other parameters.

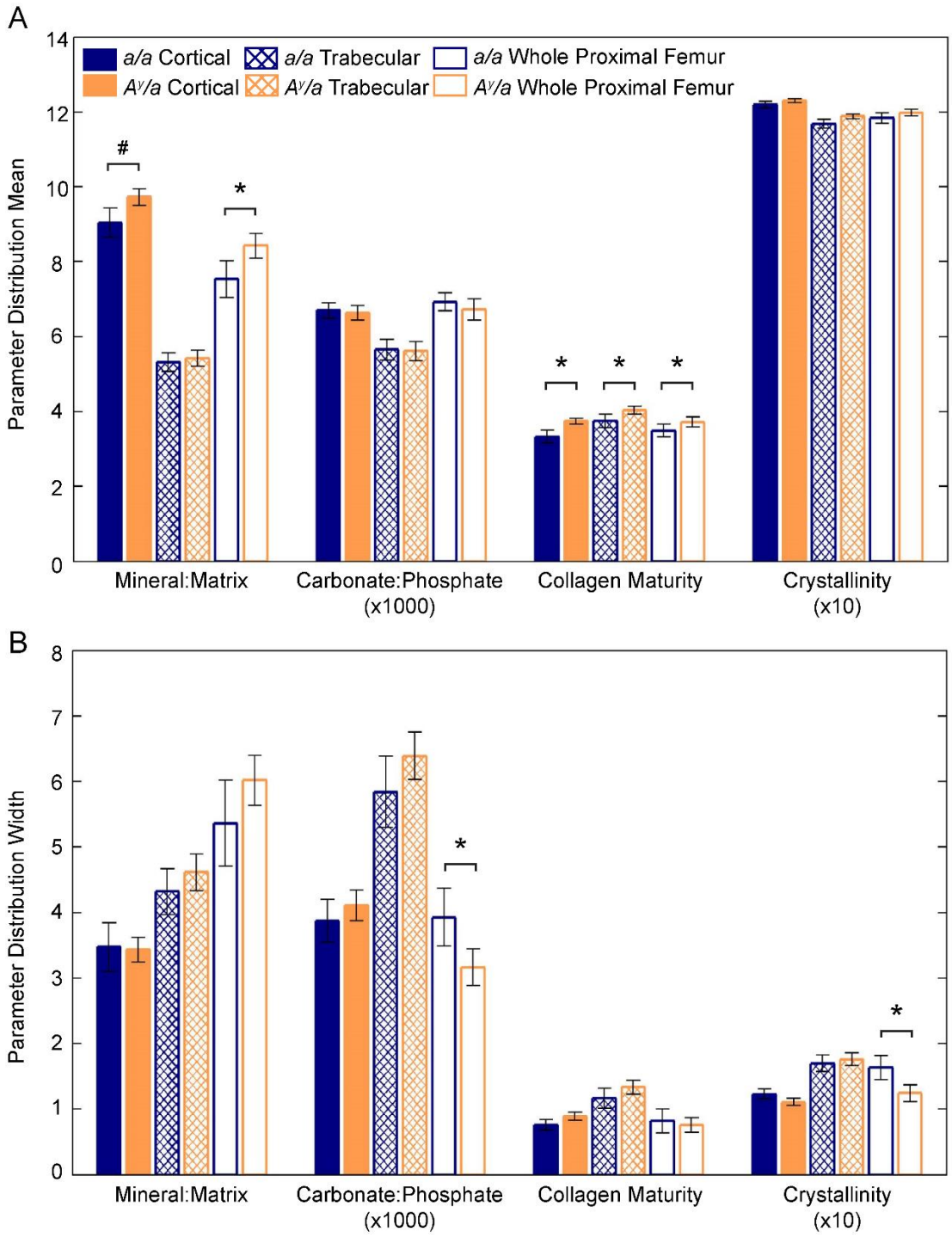

Figure 3.3-1: FTIR parameter distribution means (A) and widths (B) for cortical, trabecular, and whole-proximal-femur regions by group. Bar heights indicate the parameter means, and error bars denote the 95% confidence interval. * indicates $p<0.05$ and # $p<0.10$, after adjustment for repeated measures in the linear mixed models.

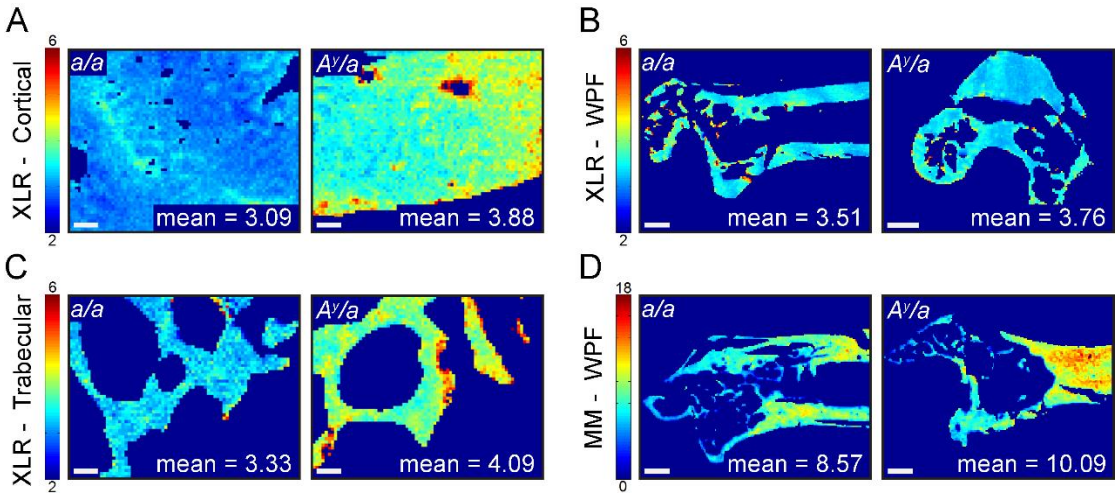

Figure 3.3-2: Representative images of selected FTIR parameters in a/a and Ay/a mouse bone for A) cortical collagen maturity, B) whole proximal femur collagen maturity, C) trabecular collagen maturity, and D) whole proximal femur mineral:matrix ratio. Scale bars indicate 50 μm in cortical and trabecular images and 500 μm in whole-proximal-femur images.

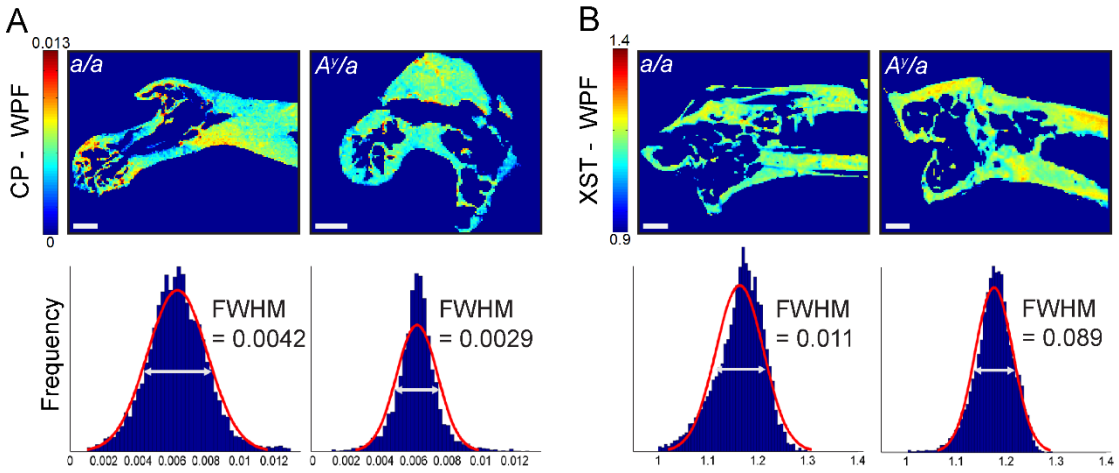

Figure 3.3-3: Representative images of selected FTIR parameters and corresponding pixel histograms in a/a and Ay/a specimens for A) whole proximal femur carbonate:phosphate ratio, and B) whole proximal femur crystallinity. Scale bars on FTIR images indicate 500 μm. The red curve on each pixel histograms indicates the Gaussian distribution fit, and the white horizontal bar with arrows indicates the full width at half maximum (FWHM).

3.3.3 HPLC Collagen Crosslinks

The concentrations of pentosidine, HP, and LP and the parameters HP:LP, HP+LP, and Pentosidine:HP+LP in the whole proximal femur were similar between groups (Table 3.3-1).

Table 3.3-1: Concentrations of collagen crosslinks determined with HPLC and selected collagen crosslink ratios. HP = hydroxylysyl pyridinoline, LP = lysyl pyridinoline. p-value represents Student's t-test between Ay/a and a/a groups.

Outcome	***a/a***	***A^y/a***	***p***
Pentosidine (mmol/mol	2.12 ± 1.04	2.48 ± 1.48	0.6300
HP (mol/mol collagen)	0.59 ± 0.30	0.68 ± 0.28	0.5586
LP (mol/mol collagen)	0.24 ± 0.09	0.24 ± 0.13	0.5380
HP:LP	2.50 ± 0.79	2.95 ± 0.83	0.8788
HP+LP	0.82 ± 0.36	2.42 ± 1.48	0.7055
Pentosidine:HP+LP	2.68 ± 1.00	2.75 ± 1.04	0.5597

Association of Blood Glucose with Collagen Crosslinks and Tissue Material Properties

When relationships between lifetime-average blood glucose and FTIR imaging parameters were examined, these parameters were correlated in trabecular and whole-proximal-femur ROIs, but not in cortical ROIs. In the trabecular ROIs, lifetime-average blood glucose correlated with 1) carbonate:phosphate ratio FWHM and 2) collagen maturity FWHM, and 3) trended towards a correlation with mean collagen maturity (Table 3.3-2). In the whole-proximal-femur ROIs, lifetime-average blood glucose correlated with 1) mean collagen maturity, 2) carbonate:phosphate ratio FWHM, and 3) crystallinity FWHM, and 4) trended towards a correlation with

mineral:matrix ratio FWHM (Table 3.3-2).

Lifetime-average blood glucose did not correlate with the concentrations of pentosidine, HP, and LP assessed by HPLC, or with HP:LP, HP+LP, or Pentosidine:HP+LP (Table 3.3-2). The concentration of pentosidine did not correlate with any whole-proximal-femur FTIR imaging parameters; however, pentosidine correlated with 1) HP, 2) LP, and 3) HP+LP (Table 3.3-2).

Table 3.3-2: Correlations between lifetime-average blood glucose and pentosidine with FTIR imaging parameters and HPLC-determined collagen crosslinks. FWHM = full-width at half-maximum, HP = hydroxylysyl pyridinoline, LP = lysyl pyridinoline. Bold values indicate $p < 0.05$.

	Lifetime-Average Blood Glucose (mg/dL)			**Pentosidine (mmol/mol collagen)**		
Outcome	**Correlation Coefficient (r)**	**R^2**	***p***	**Correlation Coefficient (r)**	**R^2**	***p***
FTIR Imaging						
Trabecular						
Mean Collagen	0.503	0.253	0.0669	N/A	N/A	N/A
Carbonate:Phosphate	0.626	0.392	**0.0166**	N/A	N/A	N/A
Collagen Maturity	0.552	0.305	**0.0407**	N/A	N/A	N/A
Whole Proximal						
Mean Collagen	0.600	0.361	**0.0300**	0.238	0.057	0.3116
Mineral:Matrix Ratio	0.568	0.322	0.0685	0.040	0.002	0.8755
Carbonate:Phosphate	-0.656	0.430	**0.0150**	0.048	0.002	0.8406
Crystallinity FWHM	-0.763	0.582	**0.0024**	0.032	0.001	0.8928
HPLC						
Pentosidine	0.233	0.054	0.4441	N/A	N/A	N/A
HP	0.242	0.059	0.3906	0.597	0.357	**0.0042**
LP	0.339	0.115	0.2573	0.877	0.769	**0.0006**
HP:LP	0.003	0.000	0.9931	0.241	0.058	0.2920
HP+LP	0.293	0.086	0.3312	0.715	0.511	**0.0003**
Pentosidine:HP+LP	0.166	0.027	0.5888	N/A	N/A	N/A

3.4 *Discussion*

In this study, we assessed the effects of hyperglycemia on bone tissue AGEs and material properties in the KK-Ay murine model of T2DM. The blood glucose levels and body masses of the KK-Ay mice in this study are comparable to previously reported values,[21,23] and confirm the KK-Ay mice to be hyperglycemic and obese. The control mice were euglycemic and overweight.

Our data reveal that bone tissue from Ay/a mice has 1) increased collagen maturity, 2) increased mineral content, and 3) less heterogeneous mineral properties compared to control a/a mice. Specifically, the greater mean collagen maturity, assessed with FTIR imaging observed in Ay/a vs. a/a bone tissue, demonstrates a higher ratio of mature enzymatic crosslinks to immature crosslinks, which is consistent with older, more mature tissue.[41] The greater mean mineral:matrix ratio observed in Ay/a vs. a/a bone tissue similarly points to an increased tissue age (i.e., time since tissue formation), as older tissue will have a greater mineral content.[45] The narrower distribution widths of the carbonate:phosphate ratio and crystallinity of Ay/a vs. a/a whole proximal femoral bone tissue suggest the Ay/a mice had less bone turnover.[46]

Several key mechanisms can modulate tissue properties in murine bone, even at cortical sites that lack a robust intra cortical remodeling process. The observed alterations in mean mineral content may arise from 1) differing rates of periosteal expansion and endosteal resorption[47] or 2) direct osteocytic regulation.[48] In healthy tissue, changes in collagen maturity typically reflect turnover; however, the alterations

in this parameter observed in the KK-Ay mice could alternatively arise from an accelerated rate of conversion from divalent to trivalent enzymatic crosslinks. In the absence of double-labels for new bone formation, the current study design precludes discernment of the precise mechanism(s) responsible for the observed changes in tissue properties. Furthermore, prior findings regarding the balance of formation and resorption markers in KK-Ay mice are in conflict: some studies report decreased bone turnover markers,[24] while others report upregulation of bone turnover-related gene expression.[25] Together, these findings indicate complex, compartment-dependent effects of hyperglycemia in the KK-Ay mouse model.

Previous studies of the KK-Ay mouse[25,26] and other rodent models of T2DM[27,32] point to a larger effect of T2DM on BMD in trabecular bone compared to cortical bone and the whole bone. In this study, a greater mean collagen maturity was observed in the bone tissue of A^y/a mice vs. the *a/a* mice in all compartments examined (trabecular, cortical, and whole proximal femur), but no differences in mineral properties were observed in the trabecular compartment. It is likely that two key factors affected our ability to detect subtle differences in mineral properties in trabecular bone: 1) the small analysis area of trabecular compartments (i.e., the number of bone pixels vs. non-bone pixels per ROI) and 2) the inherent variability of the distribution width, particularly in the carbonate:phosphate ratio.

The regressions of FTIR imaging parameters with mean blood glucose support the interpretation that the A^y/a tissue is older with less turnover and that the reduced turnover is in part due to hyperglycemia. Mean collagen maturity in trabecular bone

and the whole proximal femur increased with worsening hyperglycemia ($R^2 = 0.253$, $p = 0.0669$; $R^2 = 0.600$, $p = 0.0300$, respectively), and the carbonate:phosphate ratio and crystallinity distribution widths in the whole proximal femur narrowed with increasing hyperglycemia ($R^2 = 0.430$, $p = 0.0150$; $R^2 = 0.600$, $p = 0.0300$, respectively) (Table 3.3-2). Together, these results indicate that the *A^y/a* bone tissue is older, consistent with the observations of disrupted and/or reduced remodeling processes in T2DM.[15–18]

One potential explanation for the greater mineral content observed in the *A^y/a* vs. *a/a* mice is body mass. Because the *A^y/a* mice were heavier than the *a/a* controls, the greater tissue mineral content observed in the *A^y/a* mice may reflect an adaptive response. When body mass was added as a factor in the linear mixed models for the mean mineral:matrix ratio and collagen maturity parameters, body mass had a significant positive effect on mean mineral:matrix ratio in the cortical compartment ($p < 0.001$). Thus, it is likely that body mass is a contributing factor for the increased mineral content in the *A^y/a* vs. *a/a* mice; however, the lack of an effect of body mass with respect to the collagen maturity indicates body mass alone does not describe the observed changes to the collagen in the *A^y/a* mice.

AGE accumulation in the whole proximal femur assessed by pentosidine concentration did not increase with hyperglycemia in *A^y/a* mice, as demonstrated by the lack of correlation between lifetime-average blood glucose and pentosidine concentration in the whole proximal femur (Table 3.3-2). Although bone tissue ribosylated and glycated at supra-physiological concentrations *in vitro* is characterized

by increased total AGEs and pentosidine,[8,9,49,50] evidence of AGE accumulation due to T2DM *in vivo* is currently inconclusive. Specifically, bone tissue pentosidine concentration increased in T2DM rats compared to non-DM controls;[11] however, no difference in pentosidine concentration was found in a study of human bone from T2DM and non-DM patients.[28]

There are several factors that may explain the similar levels of pentosidine between A^y/a and *a/a* mice. First, pentosidine is just one of hundreds of AGE species, and while HPLC measurement of pentosidine concentration is accepted as a sensitive assay of this crosslink, it has not yet known if tissue pentosidine concentration is a representative measurement of all tissue AGE species.[51] Second, cortical and trabecular bone differentially accumulate AGEs, but the differences show inconsistent trends. Human trabecular bone accumulated more fluorescent AGEs than cortical bone during *in vitro* glycation and ribosylation,[49,50] but cortical bone accumulated more pentosidine than trabecular bone in *in vivo* studies of type 1 diabetic[52] and non-diabetic women and men.[53] In the current study of the proximal femur, the masses of the murine trabecular and cortical diaphyseal tissue alone were too small to generate detectable signals for HPLC. Consequently, the whole proximal femora were homogenized for HPLC analyses, thereby preventing analysis of compartment-specific pentosidine accumulation. Because of this limitation, a difference in pentosidine concentration between genotypes in trabecular or cortical bone, which may have been detected in a compartment-specific assay, could have been masked in the homogenized assay by equal (or opposite) concentrations across genotypes in the other compartment. Third, the formation of AGEs like pentosidine can take weeks to form

in vivo.[54] It is possible that the 20-week lifespan of these mice was not long enough to accumulate more pentosidine in the A^y/a mice compared to *a/a* mice, even in hyperglycemic conditions. To our knowledge, no study monitoring the progression of AGE accumulation with aging in mice has been performed; however, pentosidine concentrations in T2DM rats did not differ from non-DM rats until 12 months of age.[11]

The concentrations of the enzymatic crosslinks HP and LP were similar between groups which indicates that the concentration of mature pyridinoline crosslinks in the whole proximal femur remained constant with hyperglycemia. These results are consistent with data from a T2DM rodent model[11] and T2DM human tissue.[28,29] Although concentrations of immature crosslinks were not assessed directly, the effects of hyperglycemia on their concentrations can be inferred. Because collagen maturity (as measured with FTIR) increased, and HP and LP (as measured with HPLC) did not change in the A^y/a vs. *a/a* mice, the observed increase in collagen maturity may be due to a decrease in enzymatic crosslinking. This effect is consistent with a decrease in immature enzymatic crosslinking observed in T2DM rats.[11]

There are several limitations and strengths to note for interpreting our findings. First, non-fasting blood glucose measurements were only available for approximately two-thirds of the mice use in this study (A^y/a: n = 10/14, *a/a*: n = 4/8). Due to the yellow coat color of the mice with the A^y allele, we can be confident in the mouse genotype; however, directly evaluating the glycemic control to the extent of tissue material changes was not possible for every mouse. Second, the lack of double-labels

for bone formation prevented identification of the mechanism responsible for the changes in the observed tissue properties. In particular, because onset of T2DM in the *A^{y}/a* mice occurred prior to attainment of skeletal maturity, the contribution of any differences in periosteal expansion and endosteal resorption between groups to the observed compositional differences could not be assessed. Third, the small masses of metaphyseal trabecular tissue and diaphyseal cortical tissue in these specimens precluded separate HPLC analyses of trabecular and cortical bone, and the whole proximal femora were homogenized. Thus, the crosslinks measured by HPLC are a mixture of both cortical and trabecular crosslinks. Because the proximal femora were mostly cortical bone by mass (exemplified in Figure 3.3-1B, Figure 3.3-1D, Figure 3.3-2A, Figure 3.3-2B), it is likely that the measured pentosidine concentration was dominated by pentosidine from cortical tissue. On the other hand, a negligible contribution of pentosidine from trabecular tissue cannot be guaranteed. The inability to differentiate pentosidine concentrations in the trabecular and cortical compartments is a major limitation of this assay because AGEs differentially accumulate in a compartment-dependent manner.[49,50,52,53] However, the HPLC analysis of the homogenized tissue provides insight into collagen crosslinking at the level of the whole proximal femur, and the results of these analyses can be directly compared to the whole-proximal-femur region FTIR parameters. Lastly, we note that the concentrations of HP and LP found in our study are slightly higher than previously reported values;[55] however, our ratio of HP to LP is well within established ranges.[55] Although the femora were carefully cleaned of soft tissue prior to hydrolysis for HPLC analysis, it is possible that small contributions of soft tissue were included in

the HPLC collagen crosslink assessments which could increase HP and LP concentrations.[55] Nevertheless, the data presented here contribute to the understanding of bone material property changes in T2DM due to hyperglycemia.

This work is the first to characterize the compositional characteristics of bone in the KK-Ay mouse. Our study showed spatially-resolved changes in tissue-level material properties due to hyperglycemia in the KK-Ay mouse, and the findings of increased mean collagen maturity and mineral content in the KK-Ay mice compared to controls is consistent with previous documentation of reduced bone turnover with T2DM. Overt T2DM manifests in KK-Ay mice around eight weeks of age as a result of insulin resistance, thus the KK-Ay mouse exhibits an essential feature of T2DM in humans. In summary, the observed changes in the tissue material properties of KK-Ay mice contribute to an evolving understanding of alterations in bone quality with T2DM.

3.5 *Acknowledgements*

The FTIR and HPLC work was supported by NIH K01AR064314, NSF DGE-1144153, and Cornell Engineering Learning Initiatives. The animal study was supported by the Orthopaedic Research and Education Foundation Goldberg Arthritis Research Grant. We thank Michele Chin, Tarryn Tertulien, Daniel Weinreb, Ida Adjivon, and Rena Mazur for assistance with FTIR data collection; Ashley Lloyd for support with the mixed effects modeling; William Schroeder and Ryan Clark for animal care; and Eleftherios Paschalis for assistance with data interpretation.

3.6 *References*

1. De Liefde, I. I., Van Der Klift, M., De Laet, C. E. D. H., *et al.* Bone mineral density and fracture risk in type-2 diabetes mellitus: The Rotterdam Study. *Osteoporos. Int.* **16,** 1713–1720 (2005).
2. Schwartz, A. V., Vittinghoff, E., Bauer, D. C., *et al.* Association of BMD and FRAX Score With Risk of Fracture in Older Adults With Type 2 Diabetes. *JAMA* **305,** 2184 (2011).
3. Janghorbani, M., Van Dam, R. M., Willett, W. C. & Hu, F. B. Systematic review of type 1 and type 2 diabetes mellitus and risk of fracture. *Am. J. Epidemiol.* **166,** 495–505 (2007).
4. Eyre, D. R., Weis, M. A. & Wu, J. J. Advances in collagen cross-link analysis. *Methods* **45,** 65–74 (2008).
5. Avery, N. C. & Bailey, A. J. Enzymic and non-enzymic cross-linking mechanisms in relation to turnover of collagen: Relevance to aging and exercise. *Scand. J. Med. Sci. Sport.* **15,** 231–240 (2005).
6. Oxlund, H., Barckman, M., Ortoft, G., *et al.* Reduced concentrations of collagen cross-links are associated with reduced strength of bone. *Bone* **17,** 365–371 (1995).
7. Nyman, J. S. Effect of diabetes on the fracture resistance of bone. *Clin. Rev. Bone Miner. Metab.* **11,** 38–48 (2013).
8. Tang, S. Y. & Vashishth, D. The relative contributions of non-enzymatic glycation and cortical porosity on the fracture toughness of aging bone. *J. Biomech.* **44,** 330–336 (2011).

9. Vashishth, D., Gibson, G. J., Khoury, J. I., *et al.* Influence of nonenzymatic glycation on biomechanical properties of cortical bone. *Bone* **28,** 195–201 (2001).

10. Nyman, J. S., Even, J. L., Jo, C. H., *et al.* Increasing duration of type 1 diabetes perturbs the strength-structure relationship and increases brittleness of bone. *Bone* **48,** 733–740 (2011).

11. Saito, M., Fujii, K., Mori, Y. & Marumo, K. Role of collagen enzymatic and glycation induced cross-links as a determinant of bone quality in spontaneously diabetic WBN/Kob rats. *Osteoporos. Int.* **17,** 1514–1523 (2006).

12. McCarthy, A. D., Etcheverry, S. B., Bruzzone, L., *et al.* Non-enzymatic glycosylation of a type I collagen matrix: effects on osteoblastic development and oxidative stress. *BMC Cell Biol.* **2,** 16 (2001).

13. Katayama, Y., Akatsu, T., Yamamoto, M., Kugai, N. & Nagata, N. Role of nonenzymatic glycosylation of type I collagen in diabetic osteopenia. *J. Bone Miner. Res.* **11,** 931–937 (2009).

14. Mercer, N., Ahmed, H., Etcheverry, S. B., Vasta, G. R. & Cortizo, A. M. Regulation of advanced glycation end product (AGE) receptors and apoptosis by AGEs in osteoblast-like cells. *Mol. Cell. Biochem.* **306,** 87–94 (2007).

15. Krakauer, J. C., McKenna, M. J., Buderer, N. F., *et al.* Bone loss and bone turnover in diabetes. *Diabetes* **44,** 775–782 (1995).

16. Pedrazzoni, M., Ciotti, G., Pioli, G., *et al.* Osteocalcin levels in diabetic subjects. *Calcif. Tissue Int.* **45,** 331–336 (1989).

17. Shu, A., Yin, M. T., Stein, E., *et al.* Bone structure and turnover in type 2

diabetes mellitus. *Osteoporos. Int.* **23,** 635–641 (2012).

18. Gerdhem, P., Isaksson, A., Åkesson, K. & Obrant, K. J. Increased bone density and decreased bone turnover, but no evident alteration of fracture susceptibility in elderly women with diabetes mellitus. *Osteoporos. Int.* **16,** 1506–1512 (2005).

19. Fajardo, R. J., Karim, L., Calley, V. I. & Bouxsein, M. L. A review of rodent models of type 2 diabetic skeletal fragility. *J. Bone Miner. Res.* **29,** 1025–1040 (2014).

20. Nakamura, M. A Diabetic Strain of the Mouse. *Proc. Japan. Acad.* **38,** 348–352 (1962).

21. Ikeda, H. KK mouse. *Diabetes Res. Clin. Pract.* **24,** S313-6 (1994).

22. Iwatsuka, H., Shino, A. & Suzuoki, Z. General Survey of Diabetic Features of Yellow KK Mice. *Endocrinol. Jpn.* **17,** 23–35 (1970).

23. Taketomi, S., Tsuda, M., Matsuo, T., *et al.* Alterations of hepatic enzyme activities in KK and yellow KK mice with various diabetic states. *Horm. Metab. Res.* **5,** 333–339 (1973).

24. Xu, F., Dong, Y., Huang, X., *et al.* Decreased osteoclastogenesis, osteoblastogenesis and low bone mass in a mouse model of type 2 diabetes. *Mol. Med. Rep.* **10,** 1935–1941 (2014).

25. Fu, C., Zhang, X., Ye, F. & Yang, J. High insulin levels in KK-Ay diabetic mice cause increased cortical bone mass and impaired trabecular micro-structure. *Int. J. Mol. Sci.* **16,** 8213–26 (2015).

26. Takagi, S., Miura, T., Yamashita, T., *et al.* Characteristics of Diabetic

Osteopenia in KK-Ay Diabetic Mice. *Biol. Pharm. Bull* **4383,** 438–443 (2012).

27. Creecy, A., Uppuganti, S., Merkel, A. R., *et al.* Changes in the Fracture Resistance of Bone with the Progression of Type 2 Diabetes in the ZDSD Rat. *Calcif. Tissue Int.* **99,** 289–301 (2016).

28. Pritchard, J., Papaioannou, Schwarcz, H., *et al.* A Comparison of Collagen Crosslink Content in Bone Specimens from Elective Total Hip Arthroplasty Patients with and without Type 2 Diabetes. *J. Bone Reports Recomm.* **2,** (2016).

29. Oren, T. W., Botolin, S., Williams, A., Bucknell, A. & King, K. B. Arthroplasty in veterans: analysis of cartilage, bone, serum, and synovial fluid reveals differences and similarities in osteoarthritis with and without comorbid diabetes. *J. Rehabil. Res. Dev.* **48,** 1195–210 (2011).

30. Prisby, R. D., Swift, J. M., Bloomfield, S. A., Hogan, H. A. & Delp, M. D. Altered bone mass, geometry and mechanical properties during the development and progression of type 2 diabetes in the Zucker diabetic fatty rat. *J. Endocrinol.* **199,** 379–388 (2008).

31. Zhang, L., Liu, Y., Wang, D., *et al.* Bone biomechanical and histomorphometrical investment in type 2 diabetic Goto-Kakizaki rats. *Acta Diabetol.* **46,** 119–126 (2009).

32. Hammond, M. A., Gallant, M. A., Burr, D. B. & Wallace, J. M. Nanoscale changes in collagen are reflected in physical and mechanical properties of bone at the microscale in diabetic rats. *Bone* **60,** 26–32 (2014).

33. McNulty, M. M., Schroeder, W. G., Bucknell, A. J., Rosenthal, A. K. & King, K. B. Hyperglycemia increases incidence of osteophyte formation in a mouse

model of osteoarthritis. *Osteoarthr. Cartil.* **23,** A286 (2015).

34. Glasson, S. S., Blanchet, T. J. & Morris, E. A. The surgical destabilization of the medial meniscus (DMM) model of osteoarthritis in the 129/SvEv mouse. *Osteoarthr. Cartil.* **15,** 1061–1069 (2007).

35. Ayala, J. E., Samuel, V. T., Morton, G. J., *et al.* Standard operating procedures for describing and performing metabolic tests of glucose homeostasis in mice. *Dis Model Mech* **3,** 525–534 (2010).

36. Gourion-Arsiquaud, S., West, P. A. & Boskey, A. L. Fourier Transform-Infrared Microspectroscopy and Microscopic Imaging. in *Osteoporosis: Methods and Protocols* (ed. Westendorf, J. J.) 293–303 (Humana Press, 2008). doi:10.1007/978-1-59745-104-8_20

37. Boskey, A. & Mendelsohn, R. Infrared analysis of bone in health and disease. *J. Biomed. Opt.* **10,** 31102 (2005).

38. Faibish, D., Gomes, A., Boivin, G., Binderman, I. & Boskey, A. Infrared imaging of calcified tissue in bone biopsies from adults with osteomalacia. *Bone* **36,** 6–12 (2005).

39. Taylor, E. A., Lloyd, A. A., Salazar-Lara, C. & Donnelly, E. L. Raman and FT-IR mineral to matrix ratios correlate with physical chemical properties of model compounds and native bone tissue. *Appl. Spectrosc.* **0,** 000370281770928 (2017).

40. Paschalis, E. P., Mayo, W. E., Boskey, A. L. & Mendelsohn, R. Infrared Microscopic Imaging of Bone : Spatial. *J Bone Min. Res* **16,** 893–900 (2001).

41. Paschalis, E. P., Verdelis, K., Doty, S. B., *et al.* Spectroscopic characterization

of collagen cross-links in bone. *J. Bone Miner. Res.* **16,** 1821–1828 (2001).

42. Pleshko, N., Boskey, A. & Mendelsohn, R. Novel infrared spectroscopic method for the determination of crystallinity of hydroxyapatite minerals. *Biophys. J.* **60,** 786–793 (1991).

43. Bank, R. A., Beekman, B., Verzijl, N., *et al.* Sensitive fluorimetric quantitation of pyridinium and pentosidine crosslinks in biological samples in a single high-performance liquid chromatographic run. *J. Chromatogr. B Biomed. Appl.* **703,** 37–44 (1997).

44. Bank, R. A., Jansen, E. J., Beekman, B. & te Koppele, J. M. Amino acid analysis by reverse-phase high-performance liquid chromatography: improved derivatization and detection conditions with 9-fluorenylmethyl chloroformate. *Anal. Biochem.* **240,** 167–76 (1996).

45. Donnelly, E., Boskey, A. L., Baker, S. P. & van der Meulen, M. C. H. Effects of tissue age on bone tissue material composition and nanomechanical properties in the rat cortex. doi:10.1002/jbm.a.32442

46. Donnelly, E., Meredith, D. S., Nguyen, J. T., *et al.* Reduced cortical bone compositional heterogeneity with bisphosphonate treatment in postmenopausal women with intertrochanteric and subtrochanteric fractures. *J. Bone Miner. Res.* **27,** 672–678 (2012).

47. Allen, M. R., Hock, J. M. & Burr, D. B. Periosteum: Biology, regulation, and response to osteoporosis therapies. *Bone* **35,** 1003–1012 (2004).

48. Cheung, M. B. S. W., Majeska, R., Kennedy, O., *et al.* Osteocytes : Master Orchestrators of Bone. *Calcif. Tissue Int.* **94,** 5–24 (2014).

49. Sroga, G. E. G. E. G. E., Siddula, A., Vashishth, D., Gundberg, C. & Vashishth, D. Glycation of human cortical and cancellous bone captures differences in the formation of maillard reaction products between glucose and ribose. *PLoS One* **10,** 1–19 (2015).

50. Karim, L., Tang, S. Y., Sroga, G. E. & Vashishth, D. Differences in non-enzymatic glycation and collagen cross-links between human cortical and cancellous bone. *Osteoporos. Int.* **24,** 2441–2447 (2013).

51. Sell, D. R., Nagaraj, R. H., Grandhee, S. K., *et al.* Pentosidine: A molecular marker for the cumulative damage to proteins in diabetes, aging, and uremia. *Diabetes. Metab. Rev.* **7,** 239–251 (1991).

52. Farlay, D., Armas, L. A. G., Gineyts, E., *et al.* Nonenzymatic Glycation and Degree of Mineralization Are Higher in Bone from Fractured Patients with Type 1 Diabetes Mellitus. *J. Bone Miner. Res.* **31,** 190–195 (2016).

53. Odetti, P., Rossi, S., Monacelli, F., *et al.* Advanced glycation end products and bone loss during aging. *Ann. N. Y. Acad. Sci.* **1043,** 710–717 (2005).

54. Singh, R., Barden, A., Mori, T. & Beilin, L. Advanced glycation end-products: A review. *Diabetologia* **44,** 129–146 (2001).

55. Eyre, D. R., Koob, T. J. & Van Ness, K. P. Quantitation of hydroxypyridinium crosslinks in collagen by high-performance liquid chromatography. *Anal. Biochem.* **137,** 380–388 (1984).

3.7 *Supplemental*

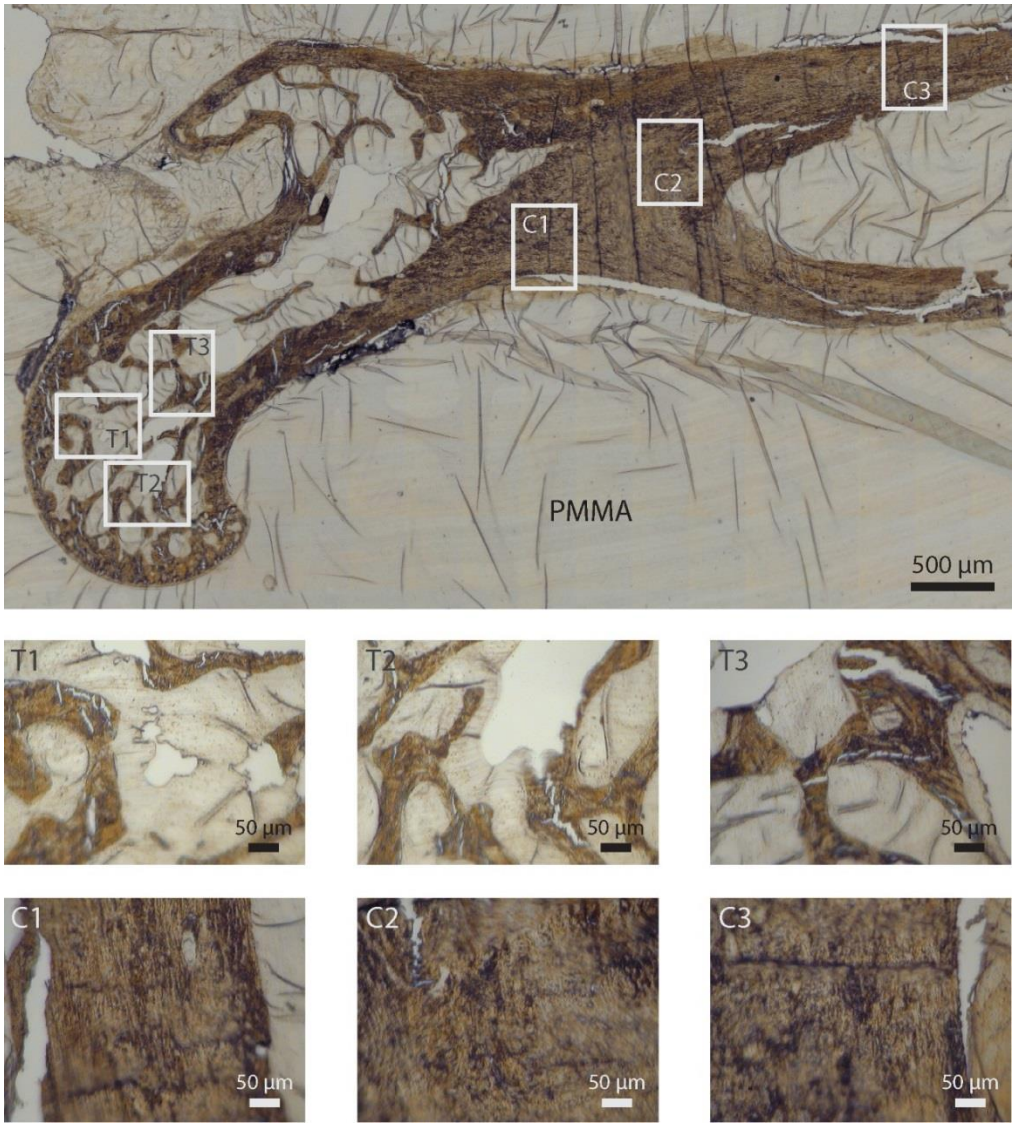

Figure 3.6-S3.6-1: Representative optical image of proximal femur with cortical and trabecular regions of interest noted.

CHAPTER 4

BONE TISSUE COMPOSITION IN POST-MENOPAUSAL WOMEN VARIES WITH GLYCEMIC CONTROL

4.1 *Introduction*

Hip fracture is a devastating event, especially for older adults, and can lead to a lower quality of life, higher medical costs, and an increased risk of mortality.[1–4] The risk of experiencing a fragility fracture increases substantially for people with type 2 diabetes mellitus (T2DM),[5–8] despite people with T2DM having normal or high bone mineral density (BMD), which conventionally signifies skeletal integrity.[9–11] The increase in fracture risk while maintaining bone mass indicates that the T2DM disease state adversely affects bone quality, thereby leading to decreased skeletal performance.[12–14]

Interestingly, people with impaired glucose tolerance (IGT) do not share the significantly greater fracture risk as those with overt T2DM. In the Health Aging and Body Composition study, men and women with T2DM and normal BMD had a 64% increased risk of fracture (relative risk [RR] and 95% confidence interval [CI], 1.64, 1.07-2.51) while those with IGT did not have a significant increased risk.[15] Similar findings were observed in the Rotterdam study: people with overt T2DM and IGT had higher BMD than non-diabetic controls; however, only the T2DM group had a greater fracture risk.[10] Taken together, these findings suggest that the transition from IGT to T2DM, while maintaining BMD, has deleterious effects on bone quality that contribute to the observed greater fracture risk in people with T2DM.

The mechanism by which the transition from normal glucose tolerance (NGT) to IGT to overt T2DM changes bone quality is currently unknown. Current hypotheses, however, include impaired bone remodeling and accumulation of advanced glycation endproducts (AGEs), both of which can alter tissue composition. In cross-sectional studies of people with and without T2DM, people with T2DM had lower bone formation markers[16–21] and bone resorption markers than those without T2DM,[19–21] and these findings were corroborated by histomorphometric analyses.[22] The effects of altered bone remodeling on tissue composition has been extensively demonstrated, particularly through studies of osteoporosis and bisphosphonate treatments.[23,24] In addition, high sugar conditions *in vitro* and *ex vivo* lead to the formation and accumulation of non-enzymatic crosslinks (a.k.a. AGEs) in bone,[25–28] which inherently changes the crosslink profile of the tissue and can have downstream effects on the tissue mechanics. For example, an animal model of T2DM found that the onset of T2DM coincided with the accumulation of AGEs, decreased concentrations of enzymatically formed crosslinks, and decreased energy absorption capabilities.[29] Furthermore, there is evidence that AGE-modified tissue can decrease osteoblast and osteoclast function,[30–33] thus potentially creating a positive feedback cycle of greater AGE accumulation and decreased tissue remodeling.

To understand how progressive glycemic derangement affects bone tissue composition, we used Fourier transform infrared (FTIR) imaging to spatially analyze cortical and cancellous bone from women with normal glucose tolerance, impaired glucose tolerance, and overt type 2 diabetes mellitus. The goal of this research is to elucidate how progressive glycemic derangement changes bone tissue composition.

4.2 ***Methods***

4.2.1 Study Cohort

Post-menopausal women between the ages of 50 and 80 years were sequentially recruited and allocated to three groups: 1) normal glucose tolerance (NGT, n = 32), defined as a 2-hour 75 g oral glucose tolerance test (OGTT) less than 140 mg/dL; 2) impaired glucose tolerance (IGT, n = 25), defined has OGTT greater than 140 but less than 199 mg/dL; and 3) T2DM (n = 23), defined as participants with an existing T2DM diagnosis and on insulin therapy. Women with a T2DM diagnosis but *not* on insulin therapy were excluded from the T2DM group in order to capture the effects of T2DM among the population with the greatest fracture risk.[11] In addition, women with nephropathy were excluded from this study to remove potential confounding effects. The participant characteristics are shown in Table 4.3-1.

All participants gave informed consent, and all procedures were approved by the Johns Hopkins Medicine Internal Review Board. The participants came for a total of five visits: 1) Initial screening to assess medical history and administer OGTT to determine glycemic control; 2) Secondary screening to administer blood and urine analyses; 3) Baseline visit to instruct participants how to administer demeclocycline double-labeling and how to prepare for bone biopsy; 4) Iliac crest bone biopsy visit; and 5) Final visit to remove sutures and address follow-up questions. Participants were compensated for each visit.

4.2.2 Fourier Transform Infrared Imaging

The compositional properties of cortical and trabecular iliac crest bone tissue were evaluated using Fourier transform infrared (FTIR) imaging. The transiliac crest biopsies were dehydrated using organic solvents, embedded in poly(methyl methacrylate) (PMMA), longitudinally microtomed into 1-μm-thick sections (SM2500, Leica Biosystems, Nussloch, Germany), and placed on BaF_2 windows (Spectral Systems, Hopewell Junction, NY). Three sections were taken per biopsy at a minimum of 10 μm of longitudinal distance apart.

For each section, three cortical and three trabecular regions of interest (ROIs) of 400 μm x 500 μm were collected at a spatial resolution of 6.25 μm. FTIR images for each ROI were generated over the spectral range 800-2000 cm^{-1} at a spectral resolution of 4 cm^{-1} using an infrared imaging system (Spotlight 400, Perkin-Elmer Instruments, Waltham, MA). Chemical imaging software (ISys, Malvern Instruments, Worcestershire, UK) was used to baseline the spectra, remove the PMMA contribution from the bone spectra (as described in [34]), and exclude any non-bone pixels.

For each FTIR image of the cortical and trabecular ROIs, the spectrum at each bone tissue pixel was analyzed to determine the following parameters: 1) collagen maturity (XLR), which is the intensity ratio of 1660 cm^{-1} to 1690 cm^{-1} and is related to the ratio of pyridinoline to divalent crosslinks; [35,36] 2) mineral:matrix ratio (M:M), which is the area ratio of the phosphate ν_1-ν_3 peak (916-1180 cm^{-1}) to amide I peak (1596-1712 cm^{-1}) and characterizes tissue mineral content;[37,38] 3) crystallinity (XST), which is the intensity ratio of 1030 cm^{-1} to 1020 cm^{-1} and is related to hydroxyapatite

crystal size and stoichiometric perfection;[39] 4) carbonate:phosphate ratio (C:P), which is the area ratio of the carbonate ν_2 peak (852-890 cm^{-1}) to phosphate ν_1-ν_3 peak (916-1180 cm^{-1}) and characterizes carbonate substitution into hydroxyapatite;[40,41] and 5) and acid phosphate content (AP), which is the intensity ratio of 1127 cm^{-1} to 1096 cm^{-1} and characterizes acid phosphate substitution into stoichiometric hydroxyapatite.[41,42] Next, a histogram of the pixels values for each FTIR parameter of an ROI was generated and a normal distribution was fit to the data. The full-width at half-maximum (FWHM), an indication of parameter heterogeneity, was then calculated from the normal distribution (see reference 11 for an example).

For the FTIR compositional parameters evaluated on each ROI (XLR, M:M, XST, C:P, AP), the following outcome variables were calculated: 1) the mean value of the parameter distribution; 2) the parameter FWHM; 3) the parameter "head" value, which is the 5th percentile of the parameter data; and 4) the parameter "tail" value, which is the 95th percentile of the parameter data.

4.2.3 Statistical Analyses

Differences across groups for participant characteristics were determined by a Kruskal-Wallis H test for continuous variables and by a Chi-square test for nominal variables. Bivariate linear regressions were performed with each of the cortical and trabecular FTIR parameter averages of each sample with 1) T2DM duration (for the T2DM group only), 2) HbA1c, and 3) bone turnover markers. For HbA1c and bone turnover markers, all three groups were included in the regression first, then the NGT group was removed and the regression analyzed again to determine relationships among just deranged

glycemic control. Regressions were considered to be significant if $p < 0.05$ was achieved as well as $R^2 > 0.10$.

Cortical and trabecular outcome variables were analyzed separately. Linear mixed effects models were used to assess the relationship between group (NGT, IGT, T2DM) and each FTIR imaging outcome variable while controlling for the repeated measurements made per biopsy (3 sections/biopsy) and per section (3 cortical and 3 trabecular ROIs/section). Pairwise differences between groups were assessed with Tukey post-hoc tests. Percent differences of the FTIR imaging outcome variables between groups were calculated from the raw data, while the corresponding reported p-values were determined by the linear mixed effects models. A significance level of 0.05 was used for all analyses.

4.3 ***Results***

4.3.1 Study Cohort

Thirty-five women were included in the NGT group, 26 in the IGT group, and 25 in the T2DM group. The ages were similar among groups. As expected, the HbA1c confirmed T2DM status in the T2DM group (> 6.5%), and the HbA1c of the T2DM group was significantly higher than the NGT and IGT groups (Table 4.3-1). BMI in the IGT and T2DM groups was 16% and 23% greater than that of the NGT group, respectively (both $p < 0.05$), and did not differ between the IGT and T2DM groups (Table 4.3-1). There were more white women in the NGT group than the T2DM group and more black women in the T2DM group than the NGT group (Table 4.3-1). The characteristics of

the participating women were otherwise not different among groups.

Serum and urinary analyses revealed a 39% greater parathyroid hormone (PTH) concentration in the IGT versus NGT group, and a 20% and 21% greater alkaline phosphatase (ALP) concentration in the T2DM group versus the NGT an IGT groups, respectively (all $p < 0.05$) (Table 4.3-1). 25-hyrdoxyvitamin D, creatinine, calcium, phosphorous, eGFR, sclerostin, and pentosidine were not different between groups (Table 4.3-1). In terms of bone turnover markers, there was a 25% and 24% lower P1NP concentration in the T2DM group versus the NGT and IGT groups, respectively; a 31% decrease in CTx concentration in the T2DM versus the NGT group; and a 25% decrease in ucOC concentration in the T2DM versus the NGT group (all $p < 0.05$) (Table 4.3-1).

Table 4.3-1: Participant characteristics by group. Values shown are mean ± std unless otherwise noted. Statistical significance determined by Kruskal-Wallis H test or Chi-square test at a significance level of 0.05. † indicates difference between NGT and IGT groups; ‡ indicates difference between NGT and T2DM groups; ≠ indicates difference between IGT and T2DM groups. Abbreviations: NGT = normal glucose tolerance group; IGT = impaired glucose tolerance group; T2DM = type 2 diabetes mellitus group; OGTT = oral glucose tolerance test; eGFR = estimated glomerular filtration rate; CTx = carboxy-terminal telopeptide of type 1 collagen; P1NP = amino-terminal propeptide of type 1 collagen; ucOC = undercarboxylated osteocalcin; n/a = not applicable.

Characteristics	**NGT**	**IGT**	**T2DM**	**Sig. Key**
n	35	26	25	
Anthropometric				
Age (years)	64.8 ± 6.8	64.4 ± 5.4	63.8 ± 6.2	
Weight (kg)	76.4 ± 14.6	94.0 ± 22.9	94.3 ± 16.4	† ‡
Height (cm)	160.8 ± 6.7	165.6 ± 6.5	160.9 ± 5.9	† ≠
BMI (kg/m^2)	29.6 ± 5.6	34.3 ± 8.4	36.5 ± 6.9	† ‡
Race/ethnicity				
White, n (%)	27 (77)	13 (50)	6 (24)	‡
Black, n (%)	8 (23)	11 (42)	17 (68)	‡
Asian, n (%)	0 (0)	1 (4)	0 (0)	
Hispanic, n (%)	0 (0)	0 (0)	0 (0)	
Other, n (%)	0 (0)	1 (4)	2 (8)	
T2DM Status				
T2DM dx duration (years)	n/a	n/a	14.5 ± 8.4	n/a
OGTT (mg/dL)	95.5 ± 18.2	163.5 ± 29.8	n/a	†
HbA1c (%)	5.76 ± 0.26	6.03 ± 0.42	9.13 ± 2.16	‡ ≠

T2DM-related Drugs				
Insulin, n (%)	0 (0)	0 (0)	25 (100)	‡ ≠
Metformin, n (%)	0 (0)	0 (0)	14 (56)	‡ ≠
Sulfonylurea, n (%)	0 (0)	0 (0)	2 (8)	
Serum and Urinary Parameters				
25-hydroxyvitamin D (ng/mL)	33.46 ± 9.41	33.23 ± 10.11	30.64 ± 7.31	
Creatinine (mg/dL)	0.81 ± 0.16	0.87 ± 0.20	0.84 ± 0.16	
Calcium (mg/dL)	9.44 ± 0.30	9.51 ± 0.42	9.44 ± 0.39	
Phosphorous (mg/dL)	3.65 ± 0.49	3.48 ± 0.51	3.57 ± 0.66	
Alkaline phosphatase (U/L)	73.57 ± 17.95	72.96 ± 19.84	88.08 ± 24.09	‡ ≠
Parathyroid Hormone (pg/mL)	28.77 ± 13.00	39.93 ± 17.59	33.48 ± 16.66	†
eGFR (mL/min/1.73 m^2)	80.49 ± 16.29	80.81 ± 13.46	80.08 ± 15.99	
P1NP (ng/mL)	58.78 ± 23.65	57.83 ± 18.62	44.20 ± 14.07	‡ ≠
CTx (ng/mL)	0.32 ± 0.18	0.31 ± 0.22	0.22 ± 0.11	‡
Sclerostin (pmol/L)	238.34 ± 98.96	224.50 ± 68.44	229.95 ± 101.36	
Pentosidine (nmol/L)	56.25 ± 15.94	51.49 ± 13.54	53.89 ± 13.80	
ucOC (ng/mL)	3.53 ± 2.00	3.15 ± 2.13	2.66 ± 2.37	‡
Other Supplements				
Calcium, n (%)	8 (23)	6 (23)	3 (12)	
Vitamin D, n (%)	13 (37)	11 (42)	11 (44)	
Multi-vitamin, n (%)	15 (43)	10 (38)	4 (16)	
Statin, n (%)	8 (23)	9 (35)	12 (48)	
Acetylsalicylic acid (aspirin), n (%)	15 (43)	7 (27)	12 (48)	

4.3.2 Composition of cortical tissue evaluated with FTIR imaging

In the cortical tissue, the mineral:matrix mean was 7% greater in the T2DM group compared to the NGT group, which indicates greater tissue mineral content in the T2DM specimens ($p < 0.05$) (**Figure 4.3-1**A, Figure 4.3-2A). Also in the cortical tissue, the mineral:matrix distribution was 10% narrower in the T2DM versus NGT group ($p < 0.05$) (Figure 4.3-2A) and trended towards a narrower distribution in the T2DM versus IGT group (-9%, $p = 0.06$). The cortical mineral:matrix head value was 10% greater in the T2DM versus NGT group ($p < 0.5$) (**Figure 4.3-1**E, Figure 4.3-2A), and the cortical mineral:matrix tail value trended towards a greater value in the T2DM versus NGT group (+6%, $p = 0.07$) (**Figure 4.3-1**G, Figure 4.3-2A). Representative FTIR images and distributions for cortical mineral:matrix ROIs in the NGT and T2DM groups are shown in Figure 4.3-2A.

The cortical crystallinity mean and head value did not differ between groups (**Figure 4.3-1**A, **Figure 4.3-1**E, Figure 4.3-2A); however, in the T2DM versus NGT group, the cortical crystallinity distribution width was 16% wider ($p < 0.05$) (**Figure 4.3-1**C, Figure 4.3-2B) and the cortical crystallinity tail value was 2% greater ($p < 0.05$) (**Figure 4.3-1**G, Figure 4.3-2B). Representative FTIR images and distributions for cortical crystallinity ROIs in the NGT and T2DM groups are shown in Figure 4.3-2B.

The cortical acid phosphate content distribution width was 14% narrower in the T2DM versus NGT group and 14% narrower in the T2DM versus IGT group (both

$p < 0.05$) (**Figure 4.3-1**C, Figure 4.3-2C). All other cortical acid phosphate content outcome variables did not differ between groups (**Figure 4.3-1**A, **Figure 4.3-1**E, **Figure 4.3-1**G). Representative FTIR images and distributions for cortical acid phosphate content ROIs in the NGT and T2DM groups are shown in Figure 4.3-2C.

None of the cortical collagen maturity and carbonate:phosphate parameters differed among groups (**Figure 4.3-1**A, **Figure 4.3-1**C, **Figure 4.3-1**E, **Figure 4.3-1**G).

4.3.3 Composition of trabecular tissue evaluated with FTIR imaging

There were subtle differences in trabecular collagen maturity outcomes that were not observed in the cortical collagen maturity outcomes. In the T2DM versus NGT group, the trabecular collagen maturity mean trended towards a lower value (-5%, $p = 0.05$) (**Figure 4.3-1**B, Figure 4.3-2D), the trabecular collagen maturity head value trended towards a lower value (-3%; $p = 0.07$) (**Figure 4.3-1**F, Figure 4.3-2D), and the trabecular collagen maturity tail value was lower (-9%, $p < 0.05$) (**Figure 4.3-1**H, Figure 4.3-2D). Additionally, the trabecular collagen maturity distribution width trended towards a narrower width in the T2DM versus IGT group (-18%; $p = 0.09$) (**Figure 4.3-1**D, Figure 4.3-2D). Representative FTIR images and distributions for trabecular collagen maturity ROIs in the NGT and T2DM groups are shown in Figure 4.3-2D.

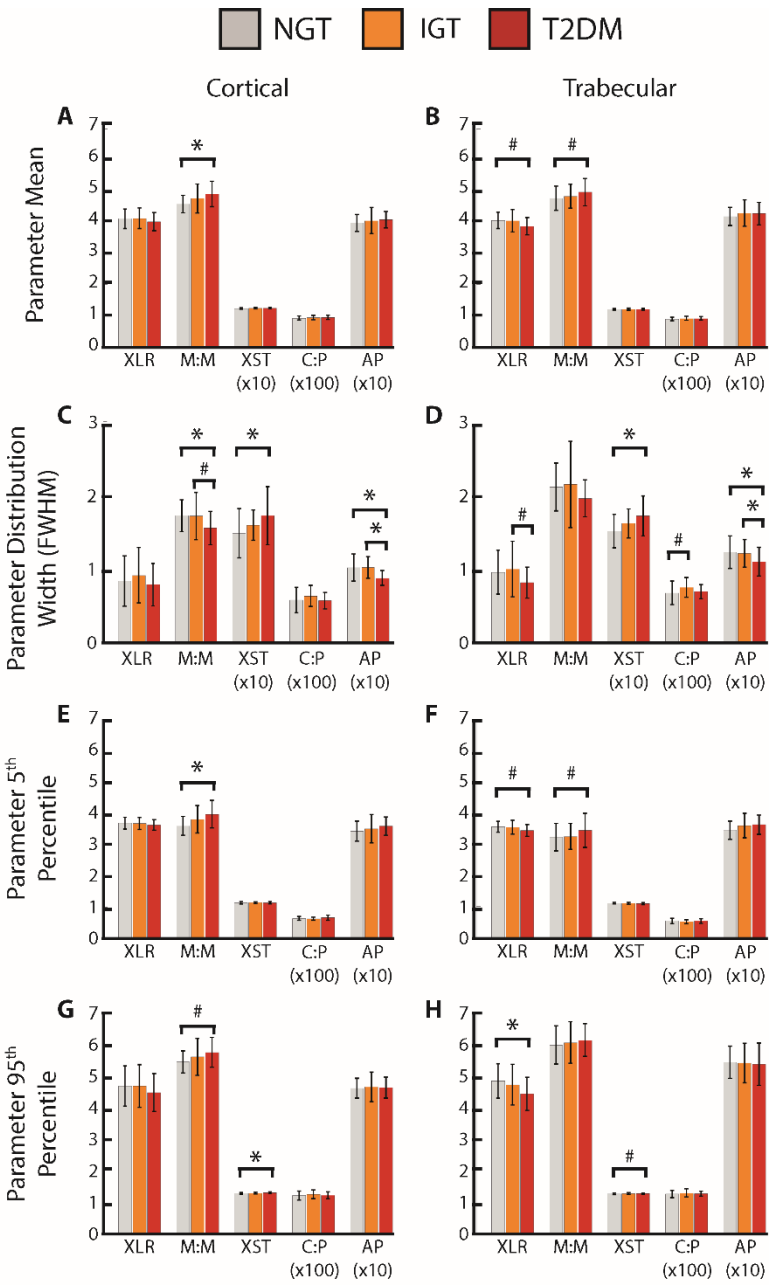

Figure 4.3-1: FTIR results for (A) cortical parameter means, (B) trabecular parameter means, (C) cortical distribution widths, (D) trabecular distribution widths, (E) cortical parameter 5th percentile values, (F) trabecular parameter 5th percentile values, (G) cortical parameter 95th percentile values, and (H) trabecular parameter 95th percentile values. Bars denote the raw mean values of each parameter ± standard deviation, while the significance levels were determined from linear mixed models. Abbreviations: NGT = normal glucose tolerance; IGT = impaired glucose tolerance; T2DM = type 2 diabetes mellitus; FWHM = full-width at half-maximum. * $p < 0.05$, # $p < 0.10$.

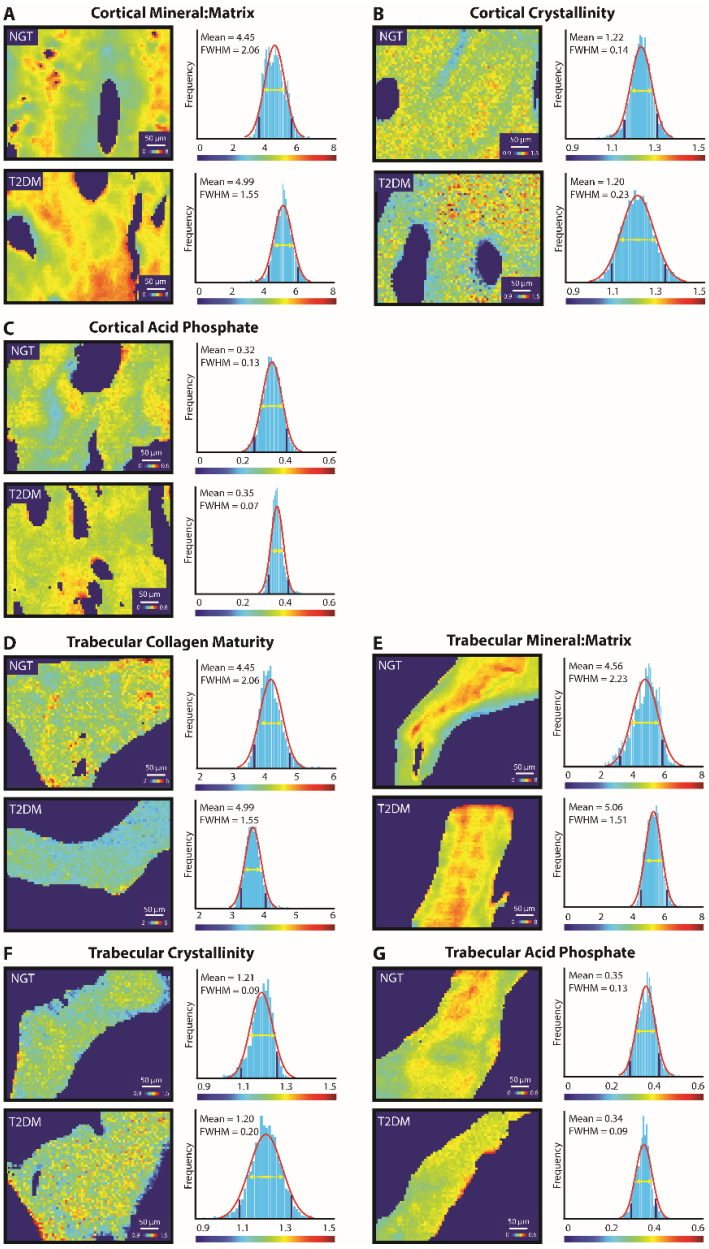

Figure 4.3-2: Representative FTIR images and parameter distributions of NGT and T2DM ROIs for (A) cortical mineral:matrix, (B) cortical crystallinity, (C) cortical acid phosphate content, (D) trabecular collagen maturity, (E) trabecular mineral:matrix, (F) trabecular crystallinity, and (G) trabecular acid phosphate content. On the parameter histograms, the Gaussian fit to the data is shown in red, the FWHM is shown with a yellow horizontal double arrow, and the 5th percentile and 95th percentile values are shown with dark blue vertical lines. Scale bar in each FTIR image is 50 µm, Abbreviations: NGT = normal glucose tolerance; T2DM = type 2 diabetes mellitus; full-width at half-maximum = FWHM; ROI = region of interest.

Similar findings were observed with mineral:matrix, crystallinity, and acid phosphate content in the trabecular tissue as in the cortical tissue. Specifically, the trabecular mineral:matrix mean and head value trended towards greater values in the T2DM group than the NGT group (mean: +4%, $p = 0.09$, head: +7%, $p = 0.09$) (**Figure 4.3-1**, Figure 4.3-2E, **Figure 4.3-1**F, Figure 4.3-2E), while the mineral:matrix distribution width and the mineral:matrix tail value did not differ between groups (**Figure 4.3-1**D, Figure 4.3-2H). Representative FTIR images and distributions for trabecular mineral:matrix ROIs in the NGT and T2DM groups are shown in Figure 4.3-2E.

The trabecular crystallinity distribution width was 14% greater ($p < 0.05$) **Figure 4.3-1**D, Figure 4.3-2F) and the trabecular crystallinity tail value trended towards a greater value in the T2DM group compared to the NGT group +1%, $p = 0.09$) (**Figure 4.3-1**H, Figure 4.3-2F). The trabecular crystallinity mean and head value did not differ between groups (**Figure 4.3-1**B, **Figure 4.3-1**F). Representative FTIR images and distributions for trabecular crystallinity ROIs in the NGT and T2DM groups are shown in Figure 4.3-2F.

Again similar to the cortical tissue findings, the trabecular acid phosphate content distribution width was 11% narrower in the T2DM versus NGT group and 10% narrower in the T2DM versus IGT group (both $p < 0.05$) (**Figure 4.3-1**D, Figure 4.3-2G), and all other cortical acid phosphate content outcome variables did not differ between groups (**Figure 4.3-1**B, **Figure 4.3-1**F, **Figure 4.3-1**H). Representative FTIR images and distributions for trabecular acid phosphate content ROIs in the NGT and T2DM groups are shown in Figure 4.3-2.

The trabecular carbonate:phosphate trended towards a wider distribution width in the IGT group versus the NGT group (+11%, $p = 0.08$) (**Figure 4.3-1**D). All other trabecular carbonate:phosphate variable outcomes did not differ between groups (**Figure 4.3-1**B, **Figure 4.3-1**F, **Figure 4.3-1**H).

4.3.4 Association of tissue composition with T2DM duration and HbA1c

T2DM duration (T2DM group only) and OGTT level (NGT and IGT groups only) were not associated with mean or distribution width FTIR outcomes. HbA1c and cortical acid phosphate content distribution width were correlated only when the IGT and T2DM groups were pooled and the NGT group was excluded ($R^2 = 0.172$, $p < 0.05$). T2DM duration and HbA1c were not correlated; however, OGTT level and HbA1c were correlated ($R^2 = 0.146$, $p < 0.05$).

4.3.5 Association of tissue composition with bone turnover markers

When all three groups were included in the regression, mean and distribution with FTIR outcomes for cortical and trabecular bone were not associated with P1NP, PTH, ucOC, or CTx with the exception of cortical carbonate:phosphate distribution width and CTx ($R^2 = 0.142$, $p < 0.05$). Similarly, serum pentosidine was not correlated with any FTIR parameter outcomes when all three groups were included. Several parameters were significantly associated ($p < 0.05$), but the correlation coefficient was weak ($R^2 < 0.10$).

When just the IGT and T2DM groups were included in the regression analysis, there were several significant associations. Cortical and trabecular mean collagen

maturity were correlated with CTx (c-XLR: $R^2 = 0.224$, t-XLR: $R^2 = 0.136$, both $p < 0.05$) (Figure 4.3-3A), as was cortical mean acid phosphate content (c-AP: $R^2 = 0.219$, $p < 0.05$) (Figure 4.3-3E). The distribution widths of cortical and trabecular collagen maturity were correlated with CTx (c-XLR: $R^2 = 0.262$, t-XLR: $R^2 = 0.171$, both $p < 0.05$) (Figure 4.3-3B), in addition to the distribution widths of cortical and trabecular carbonate:phosphate ratio (c-C:P: $R^2 = 0.262$, t-C:P: $R^2 = 0.115$, both $p < 0.05$) (Figure 4.3-3D). P1NP was only correlated with the distribution width of trabecular collagen maturity (t-XLR: $R^2 = 0.181$, $p < 0.05$) (Figure 4.3-3C). PTH, ucOC, and pentosidine were not correlated with any FTIR parameter when only the IGT and T2DM groups were included in the regression.

Figure 4.3-3: Regression models of the IGT and T2DM groups for (A) cortical and trabecular mean collagen maturity vs. CTx; (B) cortical mean acid phosphate content vs. CTx; (C) cortical and trabecular collagen maturity distribution width vs. CTx; (D) cortical and trabecular carbonate:phosphate ratio distribution width vs. CTX; and (E) trabecular collagen maturity distribution width vs. P1NP. Orange indicates the IGT group, red indicates the T2DM group, circles indicate cortical tissue, triangles indicate trabecular tissue, solid black lines indicate the regression fit for the cortical samples, and dotted black line indicate the regression fit for the trabecular samples. Each circle or triangle is the arithmetic mean of all FTIR ROIs for that parameter.

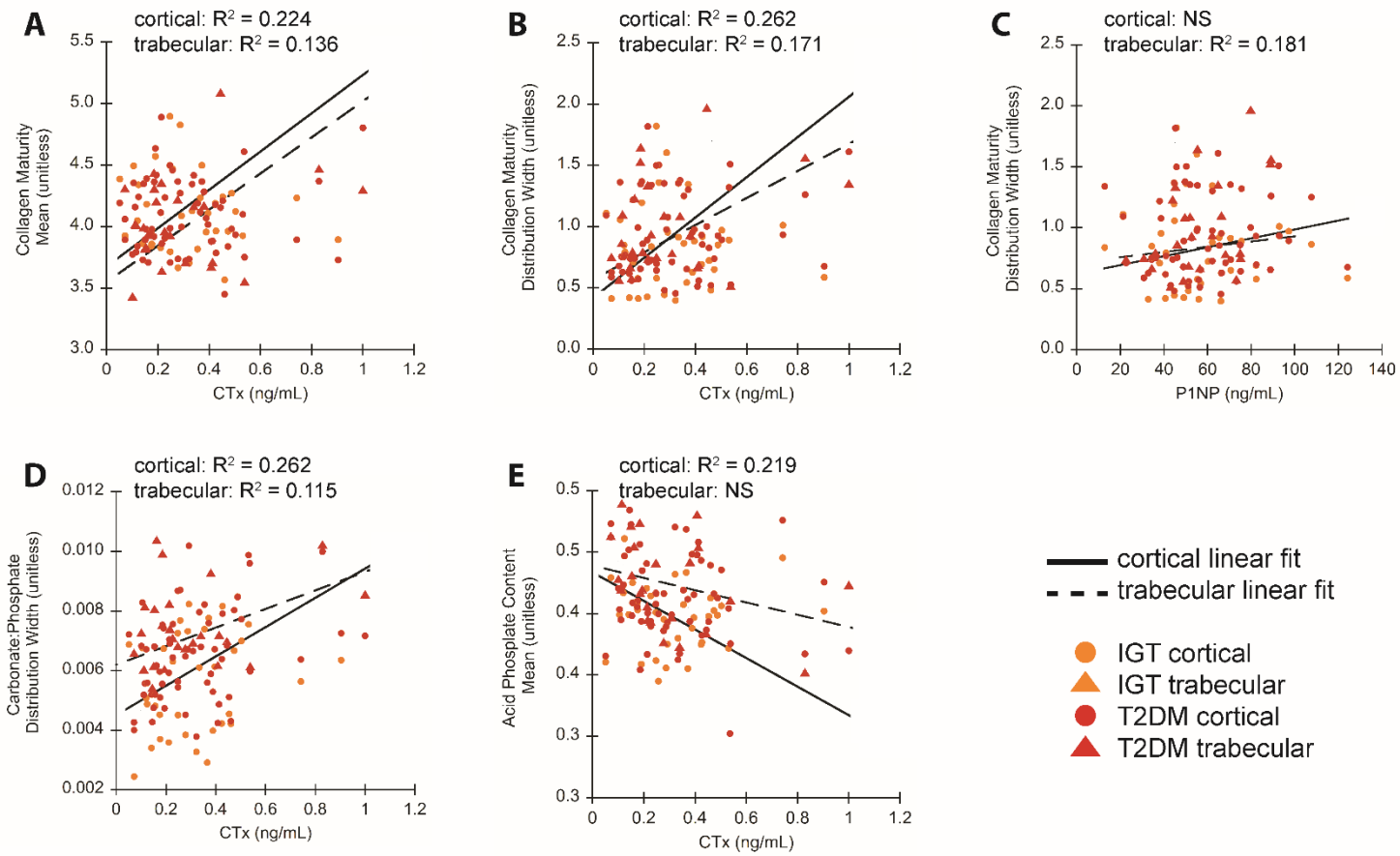
A
cortical: R² = 0.224
trabecular: R² = 0.136
Collagen Maturity Mean (unitless)
CTx (ng/mL)
B
cortical: R² = 0.262
trabecular: R² = 0.171
Collagen Maturity Distribution Width (unitless)
CTx (ng/mL)
C
cortical: NS
trabecular: R² = 0.181
Collagen Maturity Distribution Width (unitless)
P1NP (ng/mL)
D
cortical: R² = 0.262
trabecular: R² = 0.115
Carbonate:Phosphate Distribution Width (unitless)
CTx (ng/mL)
E
cortical: R² = 0.219
trabecular: NS
Acid Phosplate Content Mean (unitless)
CTx (ng/mL)
cortical linear fit
trabecular linear fit
IGT cortical
IGT trabecular
T2DM cortical
T2DM trabecular

4.4 *Discussion*

In this study, we assessed the compositional changes due to progressive glucose intolerance (normal glucose tolerance to impaired glucose tolerance to overt type 2 diabetes mellitus) on cortical and trabecular bone tissue using FTIR imaging.

Our data show compositional alterations in cortical and trabecular tissue from normal glucose tolerance to overt T2DM. In the cortical and trabecular tissue, we observed the following group-wise differences in the T2DM group compared to the NGT group: 1) greater tissue mineral content; 2) less heterogeneous mineral content; 3) less heterogenous acid phosphate substitution; 4) more heterogeneous crystallinity; and in the trabecular compartment only, 5) trends towards less mature and less heterogeneous collagen maturity. Moreover, our bone turnover marker data show lower bone resorption and formation that decreases with worsening glycemic derangement.

The P1NP concentration in the T2DM group was lower than both the NGT and IGT groups (T2DM vs. NGT: -25%; T2DM vs. IGT: -24%), which indicates that bone formation is decreased in the progression from IGT to T2DM, but not in progression from NGT to IGT. The CTx and ucOC concentrations were also lower in the T2DM versus the NGT group (CTx: -31%; ucOC: -25%), which indicates lower bone resorption in the progression from NGT to T2DM, but not in the progression from NGT to IGT or from IGT to T2DM. Nevertheless, these findings support prior studies that demonstrated decreased bone turnover with T2DM compared to non-diabetic controls.[16–21]

Our first main group-wise finding is that the cortical and trabecular tissue of the T2DM group had greater mineral content (assessed by mineral:matrix) compared to the NGT group. This is indicative of older tissue (i.e., time since tissue formation) because older tissue has a higher mineral content than younger tissue.[43] The greater average mineral content is distinctly illustrated in the representative FTIR images in Figure 4.3-2A and Figure 4.3-2E, as the T2DM tissue has more numerous high values of mineral:matrix (shown in red) and less numerous low values of mineral:matrix (shown in blue) compared to the NGT tissue. Additionally, the greater mineral:matrix head and tail values in the cortical tissue indicate a shift of the whole mineral:matrix distribution to the right (e.g., a shift to higher mineral:matrix values) (Figure 4.3-2A) and corroborates the greater mineral:matrix mean result in the cortical tissue in the T2DM versus NGT group (**Figure 4.3-1**A). In the trabecular tissue, the head value only was borderline greater in the T2DM versus NGT group, which suggests that the higher average mineral content in the T2DM group is likely due to less numerous low mineral:matrix values. Our results are in agreement with prior reports that found subjects with T2DM had greater mineral content than subjects without T2DM in femoral neck trabecular tissue.[44,45]

While our study did not directly evaluate the energy absorption capabilities of tissue from patients with and without T2DM, the observed greater mineral content may help explain the increased fracture rates among patients with T2DM. In general, a more mineralized tissue is stiffer and stronger than a less mineralized tissue;[46] but this increase in strength is accompanied by a reduction of the tissue's ability to absorb energy before failure (i.e., reduced toughness).[46,47] For example, a rodent model of

aging found increased mineral content to be associated with reduced ductility, as the greater degree of mineralization purportedly impaired collagen fiber mobility (i.e., reduced ductility and toughness).[48] In our study, it is likely that the greater mineral content in cortical and trabecular tissue in the T2DM versus NGT group deleteriously affects the deformability of the collagen matrix, leading to impaired fracture resistance at the whole-bone level.

Our second main group-wise finding is that the distribution widths of mineral:matrix values in cortical and trabecular tissue were narrower in the T2DM group than the NGT group (Figure 4.3-2A, Figure 4.3-2E), which indicates a less heterogenous distribution of mineral content in T2DM tissue compared to NGT or IGT tissue (**Figure 4.3-1**C, Figure 4.3-2A). The heterogeneity of bone tissue at multiple length scales has direct implications for the mechanical performance of the tissue.[49,50] Specifically, more narrow distributions of mineral content in diseased versus control bone has been linked to decreased bone turnover and has been documented in patients with osteoporosis[51] and patients receiving bisphosphonate treatment for osteoporosis.[24] Therefore, in our study, the narrower distributions of mineral content in the T2DM group compared to the NGT group may similarly point to decreased bone turnover with T2DM.

Our third main group-wise finding is that the distribution widths of acid phosphate content in cortical and trabecular bone were narrower in the T2DM group compared to both the NGT and IGT groups (**Figure 4.3-1**C, **Figure 4.3-1**D), which indicates that the T2DM group has less heterogenous acid phosphate content than the

NGT and IGT groups. Newly mineralized, young tissue has a high acid phosphate content, while more mature, older tissue has a lower acid phosphate content.[42] As such, the narrower distribution of acid phosphate content indicates the T2DM group has a narrower range of tissue ages than the NGT and IGT groups, which, like the mineral:matrix results, is consistent with a lower-turnover tissue.

Our fourth main group-wise finding is that the distribution widths of mineral crystallinity in cortical and trabecular tissue were wider in the T2DM group compared to the NGT group (**Figure 4.3-1**C, **Figure 4.3-1**D), which indicates a more heterogenous mineral crystallinity in the T2DM specimens. In addition, the tail crystallinity values were greater in the T2DM group than the NGT group for both cortical and trabecular tissue, but the head crystallinity values were similar among groups, which suggests that the wider crystallinity distributions were due to more numerous high crystallinity values, not more numerous low crystallinity values (Figure 4.3-2C, Figure 4.3-2D, Figure 4.3-2E, Figure 4.3-2F, Figure 4.3-2G, Figure 4.3-2H). Because the crystallinity parameter determined from FTIR spectra measures a combination of both mineral crystal size and stoichiometry perfection,[39] a more heterogenous crystallinity can arise from greater variations in size, perfection, or both. However, the lower heterogeneity of acid phosphate content points to more stoichiometric mineral in the T2DM group compared to the NGT group (**Figure 4.3-1**C, **Figure 4.3-1**D); therefore, we can infer that the greater overall crystallinity heterogeneity is due to, or mostly due to, a greater crystal size heterogeneity. In general, longer, more mature crystals increase tissue stiffness and strength, but decrease energy absorption capabilities.[52] In this light, the evidence of more

numerous high crystallinity values in the T2DM tissue versus the NGT tissue may signify that the T2DM tissue would be less resistant to fracture.

Our final main group-wise finding is that the trabecular collagen maturity mean, distribution width, head value, and tail value were borderline lower in the T2DM versus the NGT group (**Figure 4.3-1**B, **Figure 4.3-1**D, **Figure 4.3-1**F, **Figure 4.3-1**H), which suggests the collagen in the T2DM group is less mature and less heterogenous. The more narrow trabecular collagen maturity distribution width in the T2DM versus NGT group is due to a decrease in head value (-3%) and a larger decrease in tail value (-5%), resulting in the distribution narrowing and shifting left to lower collagen maturity values (Figure 4.3-2D). Collagen maturity calculated from FTIR spectra is a ratio of mature trivalent pyridinoline crosslinks to immature divalent crosslinks, hence the observed decrease in collagen maturity in the T2DM versus NGT group may arise from a decrease in mature crosslinks, an increase in immature crosslinks, or both.

Even though the precise concentrations of enzymatic crosslinks cannot be measured with FTIR spectroscopy, a change in collagen maturity can result in vastly altered mechanical behavior. For example, inhibiting lysyl oxidase in rats resulted in a decrease in the concentration of mature collagen crosslinks by ~45% and a decrease in femoral bending strength by 26% compared to controls.[53] In addition, lysyl hydroxylases regulate the organization of enzymatic crosslinks in type 1 collagen, and there is growing evidence that disrupted lysyl hydroxylase action can have downstream effects on subsequent mineralization processes.[54]

Taken together, these data point to complex effects in the mineral and collagen matrix properties of tissue from patients with T2DM compared to those with normal or impaired glucose control. The greater mean mineral content and less heterogenous mineral content, acid phosphate content, and collagen maturity in the T2DM group compared to the NGT group are consistent with an older tissue that has experienced lower bone turnover.[55] In contrast, the lower mean collagen maturity and more heterogeneous mineral crystallinity are consistent with a younger tissue.

The correlations between bone turnover markers and compositional properties also signify complicated effects with glycemic derangement, and the regression analyses of CTx and P1NP with FTIR compositional parameters in the IGT and T2DM groups allowed for a more focused analysis in women with some level of glucose derangement. In the IGT and T2DM pooled data, the mean and distribution width of collagen maturity increased with an increase in resorption marker CTx concentration in cortical and trabecular regions (Figure 4.3-3A, Figure 4.3-3B), and the distribution width of collagen maturity increased with an increase in the formation marker P1NP concentration in trabecular bone (Figure 4.3-3C). Conventionally, increases in bone resorption and formation lead to a younger tissue on average that is more heterogeneous overall;[24] therefore, the wider collagen maturity distribution widths with higher turnover is in line with convention, but the increased collagen maturity with higher turnover is not. The relationship between mean acid phosphate content in cortical tissue and CTx concentration is also inconsistent with conventional thought. That is, higher values of CTx, which signifies more bone resorption, should correspond to mineral with lower acid phosphate content (because acid phosphate

content is high in young tissue), but the opposite was observed (Figure 4.3-3E).

There are several possible explanations the apparent tissue-age and bone turnover inconsistencies within the FTIR compositional properties in patients with T2DM. First, the maturation of collagen from divalent to trivalent crosslinks can be inhibited by secondary mineralization processes, which would result in a less mature collagen but a more mature mineral.[54] On the other hand, upregulation of one isoform of lysyl hydroxylase, LH2, can lead to disrupted mineralization processes such as the location of hydroxyapatite nucleation, which would result in altered mineral properties without altered collagen properties.[54] In either of these two scenarios, the maturation of the collagen matrix and the maturation of the mineral crystals could be decoupled from each other.

The accumulation of AGEs has also been proposed as a mechanism by which bone tissue can be altered because of T2DM. AGEs are known to accumulate with normal aging, and they have been implicated in osteoporosis and T2DM as a mechanism by which the collagen crosslink profile can be altered.[54] Firstly, it is possible that AGEs can form on the collagen residues that are normally designated for enzymatic crosslinks. This would result in a tissue with decreased collagen maturity and increased AGE content. Secondly, AGE accumulation can change the charge profile of collagen fibrils,[56,57] thereby disrupting the otherwise highly controlled mineralization process.[58–60] Thirdly, high concentrations of AGEs can reduce the solubility of the collagen matrix,[54] which in turn could lead to lower resorption of AGE-heavy tissue. Finally, *in vitro* studies on AGE-modified collagen point to

decreased osteoblast[30–32,61] and osteoclast[62] function, thus AGEs can disrupt the remodeling processes.

The main strength of this study is the inclusion of the IGT group which allowed for analysis of the intermediate stage of impaired glycemic control. The FTIR compositional parameters of the IGT group frequently fell between the values of the NGT and T2DM groups, though the differences between the NGT versus IGT and IGT versus T2DM groups were not always significant. Additionally, the availability of detailed participant information, including T2DM duration and bone turnover markers, and a large enough biopsy to spatially assess compositional parameters allowed for a deeper assessment of tissue composition changes with glucose derangement than in comparable studies that relied on opportunist collection of specimens during total hip arthroplasty.[44,63] A limitation of this study is that the iliac crest is not a clinically relevant fracture site, and it is currently unknown how tissue composition varies across site for people with and without T2DM. Another limitation of this study is that only serum pentosidine was available to measure AGE content. Tissue AGEs and serum pentosidine are only moderately, if at all, correlated,[63] thus serum pentosidine may not be a representative measure of tissue AGE content. Moreover, it is not known to what extent pentosidine, a single AGE, contributes to the total influence of AGEs because there are potentially hundreds of different types of AGEs in bone tissue.[64] Nevertheless, this study contributes to the broader understanding of how worsening glycemic derangement leads to alterations in bone tissue composition.

4.5 *Conclusion*

In this work, we spatially assessed the composition of bone from post-menopausal women with varying degrees of glycemic derangement. Traditional clinical measurements of bone mass (i.e., BMD) underpredict bone fragility in people with T2DM; therefore, a broader approach that includes measures of bone quality is increasingly necessary to evaluate bone tissue to better prevent fragility fractures in people with T2DM. We found evidence of altered mineral and collagen properties between normal glucose tolerance, impaired glucose tolerance, and overt T2DM groups. In general, we observed that glycemic derangement was associated with increased mineral content, decreased collagen maturity, and non-conventional mineral maturation. While the precise underlying causes for these changes in tissue composition have yet to be elucidated, a more mineralized tissue and a less mature organic matrix can both deleteriously affect bone mechanics at the tissue level, and these compositional alterations at the micro-scale likely play a role in whole-bone mechanical integrity. In conclusion, these data are the first to offer evidence of progressive altering of bone tissue composition with worsening glycemic control in humans, and these findings can ultimately offer insight into when these changes occur.

4.6 *Acknowledgements*

We thank Patricia Maldonado and Dr. Stephen Doty for assistance with specimen preparation; Jared Pearl and Jing Han Zhang for assistance with data collection.

4.7 *References*

1. Leibson, C. L., Tosteson, A. N. A., Gabriel, S. E., Ransom, J. E. & Melton, L. J. Mortality, disability, and nursing home use for persons with and without hip fracture: A population-based study. *J. Am. Geriatr. Soc.* **50,** 1644–1650 (2002).
2. Melton, L. J., Gabriel, S. E., Crowson, C. S., *et al.* Cost-equivalence of different osteoporotic fractures. *Osteoporos. Int.* **14,** 383–388 (2003).
3. Arinzon, Z., Fidelman, Z., Zuta, A., Peisakh, A. & Berner, Y. N. Functional recovery after hip fracture in old-old elderly patients. *Arch. Gerontol. Geriatr.* **40,** 327–336 (2005).
4. Tosteson, A. N., Gabriel, S. E., Grove, M. R., *et al.* Impact of hip and vertebral fractures on quality-adjusted life years. *Osteoporos. Int.* **12,** 1042–9 (2001).
5. Napoli, N., Strotmeyer, E. S., Ensrud, K. E., *et al.* Fracture risk in diabetic elderly men: The MrOS study. *Diabetologia* **57,** (2014).
6. Bonds, D. E., Larson, J. C., Schwartz, A. V., *et al.* Risk of Fracture in Women with Type 2 Diabetes: the Women's Health Initiative Observational Study. *J Clin Endocrinol Metab* **91,** 3404–3410 (2006).
7. Wallander, M., Axelsson, K. F., Nilsson, A. G., Lundh, D. & Lorentzon, M. Type 2 Diabetes and Risk of Hip Fractures and Non-Skeletal Fall Injuries in the Elderly: A Study From the Fractures and Fall Injuries in the Elderly Cohort (FRAILCO). *J. Bone Miner. Res.* **32,** 449–460 (2017).
8. Majumdar, S. R., Leslie, W. D., Lix, L. M., *et al.* Longer duration of diabetes strongly impacts fracture risk assessment: The Manitoba BMD cohort. *J. Clin. Endocrinol. Metab.* **101,** (2016).

9. Vestergaard, P. Discrepancies in bone mineral density and fracture risk in patients with type 1 and type 2 diabetes - A meta-analysis. *Osteoporos. Int.* **18,** 427–444 (2007).

10. De Liefde, I. I., Van Der Klift, M., De Laet, C. E. D. H., *et al.* Bone mineral density and fracture risk in type-2 diabetes mellitus: The Rotterdam Study. *Osteoporos. Int.* **16,** 1713–1720 (2005).

11. Schwartz, A. V., Vittinghoff, E., Bauer, D. C., *et al.* Association of BMD and FRAX Score With Risk of Fracture in Older Adults With Type 2 Diabetes. *JAMA* **305,** 2184 (2011).

12. Moseley, K. F. Type 2 diabetes and bone fractures. *Curr. Opin. Endocrinol. Diabetes. Obes.* **19,** 128–35 (2012).

13. Hernandez, C. J. & Keaveny, T. M. A biomechanical perspective on bone quality. *Bone* **39,** 1173–1181 (2006).

14. Bouxsein, M. L. Bone quality: where do we go from here? *Osteoporos. Int.* **14,** 118–127 (2003).

15. Strotmeyer, E. S., Cauley, J. A., Schwartz, A. V., *et al.* Nontraumatic Fracture Risk with Diabetes Mellitus and Impaired Fasting Glucose in Older White and Black Adults. *Arch. Intern. Med.* **165,** 1612–1617 (2005).

16. Pedrazzoni, M., Ciotti, G., Pioli, G., *et al.* Osteocalcin levels in diabetic subjects. *Calcif. Tissue Int.* **45,** 331–336 (1989).

17. Dobnig, H., Piswanger-Sölkner, J. C., Roth, M., *et al.* Type 2 Diabetes Mellitus in Nursing Home Patients: Effects on Bone Turnover, Bone Mass, and Fracture Risk. *J. Clin. Endocrinol. Metab.* **91,** 3355–3363 (2006).

18. Shu, A., Yin, M. T., Stein, E., *et al.* Bone structure and turnover in type 2 diabetes mellitus. *Osteoporos. Int.* **23,** 635–641 (2012).

19. Akin, O., Göl, K., Aktürk, M. & Erkaya, S. Evaluation of bone turnover in postmenopausal patients with type 2 diabetes mellitus using biochemical markers and bone mineral density measurements. *Gynecol. Endocrinol.* **17,** 19–29 (2003).

20. Gerdhem, P., Isaksson, A., Åkesson, K. & Obrant, K. J. Increased bone density and decreased bone turnover, but no evident alteration of fracture susceptibility in elderly women with diabetes mellitus. *Osteoporos. Int.* **16,** 1506–1512 (2005).

21. Farr, J. N., Drake, M. T., Amin, S., *et al.* In vivo assessment of bone quality in postmenopausal women with type 2 diabetes. *J. Bone Miner. Res.* **29,** 787–795 (2014).

22. Krakauer, J. C., McKenna, M. J., Buderer, N. F., *et al.* Bone loss and bone turnover in diabetes. *Diabetes* **44,** 775–782 (1995).

23. Lloyd, A. A., Gludovatz, B., Riedel, C., *et al.* Atypical fracture with long-term bisphosphonate therapy is associated with altered cortical composition and reduced fracture resistance. *Proc. Natl. Acad. Sci.* **114,** 201704460 (2017).

24. Donnelly, E., Meredith, D. S., Nguyen, J. T., *et al.* Reduced cortical bone compositional heterogeneity with bisphosphonate treatment in postmenopausal women with intertrochanteric and subtrochanteric fractures. *J. Bone Miner. Res.* **27,** 672–678 (2012).

25. Vashishth, D., Gibson, G. J., Khoury, J. I., *et al.* Influence of nonenzymatic

glycation on biomechanical properties of cortical bone. *Bone* **28,** 195–201 (2001).

26. Tang, S. Y., Zeenath, U. & Vashishth, D. Effects of non-enzymatic glycation on cancellous bone fragility. *Bone* **40,** 1144–1151 (2007).

27. Sroga, G. E. G. E. G. E., Siddula, A., Vashishth, D., Gundberg, C. & Vashishth, D. Glycation of human cortical and cancellous bone captures differences in the formation of maillard reaction products between glucose and ribose. *PLoS One* **10,** 1–19 (2015).

28. Karim, L., Tang, S. Y., Sroga, G. E. & Vashishth, D. Differences in non-enzymatic glycation and collagen cross-links between human cortical and cancellous bone. *Osteoporos. Int.* **24,** 2441–2447 (2013).

29. Saito, M., Fujii, K., Mori, Y. & Marumo, K. Role of collagen enzymatic and glycation induced cross-links as a determinant of bone quality in spontaneously diabetic WBN/Kob rats. *Osteoporos. Int.* **17,** 1514–1523 (2006).

30. McCarthy, A. D., Etcheverry, S. B., Bruzzone, L., *et al.* Non-enzymatic glycosylation of a type I collagen matrix: effects on osteoblastic development and oxidative stress. *BMC Cell Biol.* **2,** 16 (2001).

31. Katayama, Y., Akatsu, T., Yamamoto, M., Kugai, N. & Nagata, N. Role of nonenzymatic glycosylation of type I collagen in diabetic osteopenia. *J. Bone Miner. Res.* **11,** 931–937 (2009).

32. Terada, M., Inaba, M., Yano, Y., *et al.* Growth-inhibitory effect of a high glucose concentration on osteoblast-like cells. *Bone* **22,** 17–23 (1998).

33. Valcourt, U., Merle, B., Gineyts, E., *et al.* Non-enzymatic glycation of bone collagen modifies osteoclastic activity and differentiation. *J. Biol. Chem.* **282,** 5691–5703 (2007).

34. Gourion-Arsiquaud, S., West, P. A. & Boskey, A. L. Fourier Transform-Infrared Microspectroscopy and Microscopic Imaging. in *Osteoporosis: Methods and Protocols* (ed. Westendorf, J. J.) 293–303 (Humana Press, 2008). doi:10.1007/978-1-59745-104-8_20

35. Paschalis, E. P., Verdelis, K., Doty, S. B., *et al.* Spectroscopic characterization of collagen cross-links in bone. *J. Bone Miner. Res.* **16,** 1821–1828 (2001).

36. Paschalis, E. P., Gamsjaeger, S., Tatakis, D. N., *et al.* Fourier transform infrared spectroscopic characterization of mineralizing type i collagen enzymatic trivalent cross-links. *Calcif. Tissue Int.* **96,** 18–29 (2014).

37. Boskey, A. L., Pleshko, N., Doty, S. & Mendelsohn, R. Applications of fourier transform infared microscopy to the study of mineralization in bone and cartilage. *Cells Mater.* **2,** (1992).

38. Taylor, E. A., Lloyd, A. A., Salazar-Lara, C. & Donnelly, E. L. Raman and FT-IR mineral to matrix ratios correlate with physical chemical properties of model compounds and native bone tissue. *Appl. Spectrosc.* **0,** 000370281770928 (2017).

39. Pleshko, N., Boskey, A. & Mendelsohn, R. Novel infrared spectroscopic method for the determination of crystallinity of hydroxyapatite minerals. *Biophys. J.* **60,** 786–793 (1991).

40. Ou-Yang, H., Paschalis, E. P., Mayo, W. E., Boskey, a L. & Mendelsohn, R.

Infrared microscopic imaging of bone: spatial distribution of CO3(2-). *J. Bone Miner. Res.* **16,** 893–900 (2001).

41. Rey, C., Renugopalakrishman, V., Collins, B. & Glimcher, M. J. Fourier transform infrared spectroscopic study of the carbonate ions in bone mineral during aging. *Calcif. Tissue Int.* **49,** 251–258 (1991).

42. Spevak, L., Flach, C. R., Hunter, T., Mendelsohn, R. & Boskey, A. Fourier transform infrared spectroscopic imaging parameters describing acid phosphate substitution in biologic hydroxyapatite. *Calcif. Tissue Int.* **92,** 418–428 (2013).

43. Donnelly, E., Boskey, A. L., Baker, S. P. & van der Meulen, M. C. H. Effects of tissue age on bone tissue material composition and nanomechanical properties in the rat cortex. doi:10.1002/jbm.a.32442

44. Hunt, H. B. Altered tissue composition, microarchitecture, and mechanical performance in cancellous bone from men with type 2 diabetes mellitus. *J. Bone Miner. Res.* (2018).

45. Pritchard, J. M., Papaioannou, A., Tomowich, C., *et al.* Bone mineralization is elevated and less heterogeneous in adults with type 2 diabetes and osteoarthritis compared to controls with osteoarthritis alone. *Bone* **54,** 76–82 (2013).

46. Currey, J. D. The Mechanical Consequences of Variations in the Mineral Content of Bone. *J. Biomech.* **2,** 1–11 (1969).

47. Ritchie, R. O. The conflicts between strength and toughness. *Nat. Mater.* **10,** 817–822 (2011).

48. Akkus, O., Adar, F. & Schaffler, M. B. Age-related changes in

physicochemical properties of mineral crystals are related to impaired mechanical function of cortical bone. *Bone* **34,** 443–453 (2004).

49. Lloyd, A. A., Wang, Z. X. & Donnelly, E. Multiscale Contribution of Bone Tissue Material Property Heterogeneity to Trabecular Bone Mechanical Behavior. *J. Biomech. Eng.* **137,** 010801 (2015).

50. Tai, K., Dao, M., Suresh, S., Palazoglu, A. & Ortiz, C. Nanoscale heterogeneity promotes energy dissipation in bone. *Nat. Mater.* **6,** 454–62 (2007).

51. Boskey, A. & Mendelsohn, R. Infrared analysis of bone in health and disease. *J. Biomed. Opt.* **10,** 31102 (2005).

52. Yerramshetty, J. S. & Akkus, O. The associations between mineral crystallinity and the mechanical properties of human cortical bone. *Bone* **42,** 476–482 (2008).

53. Oxlund, H., Barckman, M., Ortoft, G., *et al.* Reduced concentrations of collagen cross-links are associated with reduced strength of bone. *Bone* **17,** 365–371 (1995).

54. Saito, M. & Marumo, K. Collagen cross-links as a determinant of bone quality: A possible explanation for bone fragility in aging, osteoporosis, and diabetes mellitus. *Osteoporos. Int.* **21,** 195–214 (2010).

55. Gourion-Arsiquaud, S., Burket, J. C., Havill, L. M., *et al.* Spatial variation in osteonal bone properties relative to tissue and animal age. *J. Bone Miner. Res.* **24,** 1271–81 (2009).

56. Avery, N. C. & Bailey, A. J. Enzymic and non-enzymic cross-linking

mechanisms in relation to turnover of collagen: Relevance to aging and exercise. *Scand. J. Med. Sci. Sport.* **15,** 231–240 (2005).

57. Almora-Barrios, N., Austen, K. F. & de Leeuw, N. H. Density Functional Theory Study of the Binding of Glycine, Proline, and Hydroxyproline to the Hydroxyapatite (0001) and ($01\bar{1}0$) Surfaces. *Langmuir* **25,** 5018–5025 (2009).

58. Addadi, L. & Weiner, S. Control and Design Principles in Biological Mineralization. *Angew. Chemie Int. Ed. English* **31,** 153–169 (1992).

59. Stock, S. R. The Mineral–Collagen Interface in Bone. *Calcif. Tissue Int.* **97,** 262–280 (2015).

60. Saito, M., Fujii, K. & Marumo, K. Degree of mineralization-related collagen crosslinking in the femoral neck cancellous bone in cases of hip fracture and controls. *Calcif. Tissue Int.* **79,** 160–168 (2006).

61. Alikhani, M., Alikhani, Z., Boyd, C., *et al.* Advanced glycation end products stimulate osteoblast apoptosis via the MAP kinase and cytosolic apoptotic pathways. *Bone* **40,** 345–353 (2007).

62. Xu, F., Dong, Y., Huang, X., *et al.* Decreased osteoclastogenesis, osteoblastogenesis and low bone mass in a mouse model of type 2 diabetes. *Mol. Med. Rep.* **10,** 1935–1941 (2014).

63. Karim, L., Moulton, J., Van Vliet, M., *et al.* Bone microarchitecture, biomechanical properties, and advanced glycation end-products in the proximal femur of adults with type 2 diabetes. *Bone* **114,** 32–39 (2018).

64. Sroga, G. E. & Vashishth, D. UPLC methodology for identification and quantitation of naturally fluorescent crosslinks in proteins: A study of bone

collagen. *J. Chromatogr. B Anal. Technol. Biomed. Life Sci.* **879,** 379–385 (2011).

CHAPTER 5

ALTERED TISSUE COMPOSITION, MICROARCHITECTURE, AND MECHANICAL PERFORMANCE IN CANCELLOUS BONE FROM MEN WITH TYPE 2 DIABETES MELLITUS

5.1 *Introduction*

People with type 2 diabetes mellitus (T2DM) have normal to high bone mineral density (BMD), but counterintuitively, also have a greater fracture risk than people without diabetes.[1–4] Furthermore, clinical fracture risk assessments (e.g., FRAX) that account for hip BMD, age, body mass index (BMI), fracture history, neuropathy, retinopathy, and falls consistently underpredict fractures in people with T2DM.[1,5,6] Because these factors do not fully account for the increased fracture risk observed in patients with T2DM, additional factors, including bone quality,[7] may also contribute to the pathophysiology of T2DM-realted fractures. Aspects of bone quality that may contribute to decreased fracture resistance in T2DM include bone microarchitecture and tissue material properties, which can arise from changes in bone remodeling. Hyperglycemia and hyperinsulinemia, two conditions that typically characterize T2DM, alter bone remodeling and therefore are hypothesized to alter microarchitecture and tissue material properties.

Hyperglycemia may alter bone tissue material properties through two primary mechanisms: 1) disruption of bone remodeling via osteoblasts and osteoclasts and 2) formation of advanced glycation endproducts. In T2DM, bone remodeling can be

altered by suppression of bone formation as well as bone resorption, as evidenced by *in vitro* studies,[8–10] reports of decreases in the bone formation markers [11–16] and bone resorption markers in patients,[14–16] and histomorphometric analyses.[17] Moreover, serum glucose correlates with a decrease in bone turnover markers,[18] and excess oral glucose intake is associated with decreased bone formation in otherwise healthy individuals.[19] In contrast to hyperglycemia, insulin is an anabolic agent, and hyperinsulinemia may help explain the greater BMD observed in people with T2DM.[20] Insulin signaling helps regulate osteoblastic proliferation and supports osteoclastogenesis.[21] Additionally, insulin levels post-oral glucose tolerance test are positively correlated with BMD at the hip and spine in men and women with and without T2DM.[22] Nevertheless, the extent to which bone remodeling and material properties are affected by the competing effects of hyperglycemia and hyperinsulinemia is not yet known.

In addition to altered remodeling, excess glucose can lead to changes in bone tissue material properties through the accumulation of advanced glycation endproducts (AGEs). AGEs are the reaction products of reducing sugars with free amino groups in proteins and result in a diverse array of structures including crosslinking and non-crosslinking products. Crosslinking AGEs have been implicated in embrittling the collagen matrix in rodent models of T2DM[23] and in *in vitro* ribosylation/glycosylation studies of human and bovine bone tissue.[24,25] Non-crosslinking AGEs, like carboxymethyllysine (CML), can also be deleterious to bone tissue through interaction with the receptor for AGEs (RAGE), which induces oxidative stress and inflammation.[26] In a study of CML-modified collagen compared

to unmodified collagen, apoptosis of bone lining cells was increased *in vivo* and in osteoblast cell cultures.[27] Together, AGE accumulation and the downstream effects of AGE-RAGE interactions may compound the changes in tissue material properties with T2DM and worsen mechanical performance.

Cross-sectional studies also indicate that bone microarchitecture may be altered in patients with T2DM compared to non-diabetic controls, though the precise mechanisms and relationships to hyperglycemia and hyperinsulinemia are unknown. Patients with T2DM had similar or greater trabecular volumetric BMD at the femoral neck[28] and tibia versus non-diabetic controls.[29] Observations of cortical bone microarchitecture are mixed; cortical porosity of T2DM versus non-DM tissue has been reported to decrease at the proximal femoral shaft,[18] to increase at the distal radius,[30] and to not significantly differ in the distal radius and distal tibia.[16,31] The divergent findings between trabecular and cortical microarchitecture highlight the need for compartment-specific analyses in T2DM bone tissue in humans.

Although microarchitectural changes have been documented in patients with T2DM, the functional consequences of these changes are largely unknown. Just two studies have shown differences in T2DM versus non-DM tissue, and both have been in cortical tissue. One study reported decreased resistance to *in vivo* indention in cortical bone at the tibial diaphysis in patients with T2DM versus those without T2DM,[16] and the other found increased indentation distance and indentation distance increase in cyclic reference point indentation in cortical proximal femur tissue.[32] With the exception of these two studies, the majority of evidence that T2DM deleteriously

affects bone mechanical performance is from rodent models. In rodent models, strength[23,33,34] and work-to-failure[23,34,35] were consistently decreased in T2DM compared to non-DM controls[36] and were often accompanied by concomitant changes in bone quality including altered microarchitecture,[33–35,37] BMD,[34,35,37] osteoid surface and thickness,[35] and AGE content.[23]

Similarly, the availability of data on tissue material properties in bone from humans with T2DM is limited. There are reports of greater concentrations of tissue AGEs[38] and greater mean calcium content in bone from people with T2DM compared to non-DM controls;[39] however, rodent models of T2DM provide the bulk of evidence that T2DM alters tissue material properties. Multiple rodent models of T2DM report increased mineral content (assessed by mineral:matrix ratio) in Zucker diabetic Sprague-Dawley (ZDSD) rats[40,41] and KK-Ay mice compared to controls.[42] The same studies report no differences in concentrations of mature enzymatic crosslinks (pyridinoline and deoxypyridinoline) or in the AGE pentosidine;[40–42] however, the collagen maturity (ratio of mature to immature enzymatic crosslinks) of the KK-Ay mice was increased compared to controls.[42] In contrast, a study of WBN/Kob rats that found a decrease in concentration of enzymatic crosslinks with a simultaneous increase in pentosidine concentration,[23] which suggests phenotype-specific changes in tissue material properties with T2DM.

In summary, although bone from people with T2DM may possess altered tissue material and microarchitecture properties , the effects of such changes on bone tissue mechanical properties have not been assessed, and the mechanism by which

T2DM affects bone fracture resistance is unknown. Moreover, most fragility fractures occur at cancellous sites, and the mechanical properties of cancellous bone from patients with T2DM have not yet been characterized.

Therefore, the objectives of this study were to relate material properties and microarchitecture to the mechanical performance of cancellous bone from the femoral neck in men with and without T2DM. We focused on cancellous bone because it preferentially accumulates AGEs relative to cortical bone.[43] We hypothesized that cancellous bone specimens from men with T2DM would have increased AGE concentrations, have greater bone volume fraction, and would be more brittle relative to non-DM controls.

5.2 ***Methods***

5.2.1 Study Cohort

Men undergoing total hip arthroplasty for osteoarthritis were sequentially recruited at a single, metropolitan training hospital (Hospital for Special Surgery, New York, NY) where participating surgeons obtained informed consent. Prior to arthroplasty, HbA1c was measured in all subjects. All procedures were approved by the institutional review boards of the Hospital for Special Surgery and Cornell University.

Initial power analyses to detect 20% differences in mean mechanical properties at 80% power and 5% level of significance indicated 17 specimens/group were needed. A total of 75 subjects were recruited and allocated to two groups based on

T2DM diagnosis at the time of surgery: men with a type 2 diabetes mellitus diagnosis (T2DM, n = 35) and men without a T2DM diagnosis (non-DM, n = 40). Four T2DM subjects and six non-DM subjects were excluded based on the following criteria: diagnosis of type 1 diabetes mellitus; a prior fragility fracture; any disease of bone such as osteogenesis imperfecta, fibrous dysplasia, or malignancy; renal or hepatic disorder involving the bone such as hyperparathyroidism or vitamin D deficiency; a history of avascular necrosis of the hip; treatment with medications that affect bone metabolism such as thiazolidinediones, teriparatide, glucocorticoids, bisphosphonates, or anticonvulsants; or pathological evidence of bone metastasis.

In total, 31 T2DM subjects and 34 non-DM subjects were included in the analyses for this study.

5.2.2 Specimen Retrieval and Preparation

Femoral head and neck tissue retrieved from total hip arthroplasty was wrapped in saline-soaked gauze and stored at -20 ˚C prior to specimen preparation. For a subset of the specimens (T2DM: n = 20, non-DM: n = 25), 8-mm-diameter cores of cancellous bone from the femoral neck were excised for microarchitecture analysis and compression testing. The cortical tissue of the femoral head and neck specimens were retained for separate future analyses.

The cancellous specimens were aligned along the principal trabecular axis which was determined from a radiograph. The specimens were then cut to 10 mm in length using a high-speed precision saw and a custom jig that ensured parallel ends.

The tissue removed from the ends of the original core (~3 mm total length removed per end) was retained for compositional analyses. Figure 5.2-1 shows the allocation of tissue for all analyses. For 20 specimens (T2DM: n = 11, non-DM: n = 9), a 10-mm uniform core could not be obtained because the size of the retrieved proximal femur specimen was too small or was otherwise damaged during retrieval or pathological analysis. For the 20 specimens that did not undergo mechanical testing, cancellous tissue along the principal trabecular axis was excised for compositional analyses.

In all specimens, the tissue allocated for compositional testing was prepared as follows: Bone marrow from the excess tissue was removed with a dental water pick, defatted using three 15-minute soaks in isopropyl ether, and rinsed for 15 minutes in DI water. The tissue was then homogenized and allocated into two groups for compositional analysis: 1) FTIR and 2) HPLC and fluorescence spectroscopy.

Figure 5.2-1: Anatomical location, size of cancellous specimen excised, and allocation of tissue for each characterization technique.

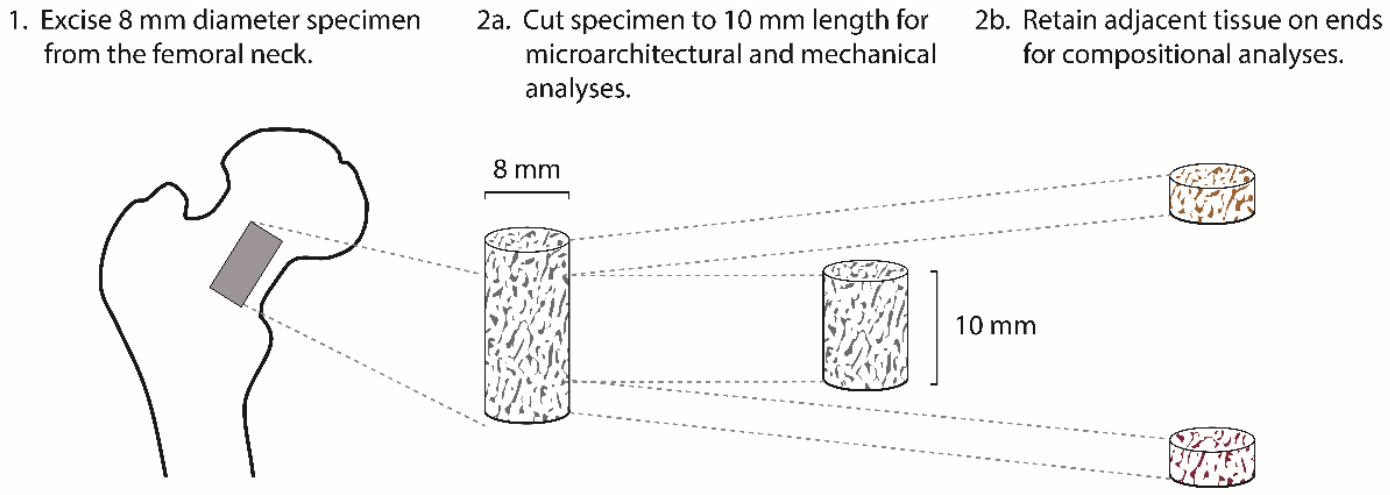
1. Excise 8 mm diameter specimen from the femoral neck.
2a. Cut specimen to 10 mm length for microarchitectural and mechanical analyses.
2b. Retain adjacent tissue on ends for compositional analyses.
8 mm
10 mm
3. Combine tissue on ends.
4. Divide tissue for compositional analyses.
5. Hydrolyze tissue for HPLC and fAGEs analyses.
HPLC and fAGEs
FTIR (native tissue)
FTIR (demineralized tissue)

5.2.3 Micro-computed Tomography

Micro-computed tomography was used to assess the microarchitecture of the cancellous bone from the mechanical testing cohort. Specimens were scanned in saline at 55 kVp and a resolution of 10 μm (μCT 35, Scanco Medical, Brüttisellen, Switzerland). Trabecular microarchitecture, including bone volume fraction (BV/TV), bone surface to volume ratio (BS/BV), connective density (Conn.D), trabecular number (Tb.N), trabecular thickness (Tb.Th), trabecular separation (Tb.Sp), and degree of anisotropy (DA) was evaluated (μCT 40, Scanco Medical, Brüttisellen, Switzerland).

5.2.4 Mechanical Testing

Monotonic compression testing was performed to determine the apparent-level mechanical properties of the specimens. Specimens were thawed, press-fit into custom, shallow-welled, brass endcaps, and secured with cyanoacrylate glue. The glue was allowed to cure for at least 10 minutes while maintaining specimen hydration. The load regimen consisted of 10 preconditioning cycles from 0% to 0.1% strain at a rate of 0.5% s^{-1}, followed by a single compressive load to 3% strain at a rate of 0.5% s^{-1} before unloading to zero load (858 Mini Bionix, MTS, Eden Prairie, MN). Load was measured with a load cell (SSM-1000, Transducer Techniques, Temecula, CA), and strain was measured with an external extensometer (634.12 Axial Extensometer, MTS, Eden Prairie, MN) attached to the specimen endcaps.

Stress-strain curves were used to evaluate apparent-level Young's modulus,

yield strain, yield, stress, ultimate strain, ultimate stress, post-yield strain, post-yield toughness, toughness, and residual strain. Yield strain and stress were determined using the 0.2% strain offset method; ultimate strain and stress were determined from the maximum load; and post-yield strain was calculated as difference between ultimate strain and yield strain. Two different measures of toughness were determined: 1) toughness, which was defined as the toughness from zero strain to ultimate strain and 2) post-yield toughness, which was defined as the toughness from yield strain to ultimate strain. In five non-DM specimens, failure was not observed before the end of the test at 3% strain; therefore, ultimate strain, ultimate stress, post-yield toughness, and toughness data were not available for those specimens.

5.2.5 Fourier Transform Infrared Spectroscopy

FTIR spectroscopy was used to evaluate the compositional properties of cancellous bone tissue. The demarrowed and defatted tissue was lyophilized in a vacuum drier then powdered using a cryomill (6770, SPEX SamplePrep, Metuchen, NJ). Two mg of tissue was added to 200 mg of dried KBr, then pressed into a pellet using a 13-mm-diameter die. FTIR spectra were collected at a spectral resolution of 4 cm^{-1} over the spectral range of 800 to 2000 cm^{-1} using an FTIR spectrometer (Spotlight 400, Perkin-Elmer Instruments, Waltham, MA).

Using custom Matlab code (2014a, The MathWorks, Inc., Natick, MA), the spectra were baseline corrected (as detailed in [44]) and the following parameters were calculated: 1) the mineral:matrix ratio (area ratio of the phosphate ν_1-ν_3 peak [916-1180 cm^{-1}] to amide I peak [1596-1712 cm^{-1}]) which characterizes tissue mineral

content;[45,46] 2) the collagen maturity (intensity ratio of 1660 cm^{-1} to 1690 cm^{-1}) which is related to the ratio of pyridinoline to divalent crosslinks;[47,48] 3) the mineral crystallinity (intensity ratio of 1030 cm^{-1} to 1020 cm^{-1}) which is related to crystal size and stoichiometric perfection;[49] the carbonate:phosphate ratio (area ratio of the carbonate ν_2 peak [852-890 cm^{-1}] to phosphate ν_1-ν_3 peak [916-1180 cm^{-1}]) which characterizes carbonate substitution into hydroxyapatite;[50] and the acid phosphate content (intensity ratio of 1127 cm^{-1} to 1096 cm^{-1}) which characterizes acid phosphate substitution into stoichiometric hydroxyapatite.[51]

Additionally, the sugar:matrix ratio, was examined to assess sugars bound to the collagen matrix. The sugar:matrix ratio (area ratio of ν CO and ν CC peaks [900-1100 cm^{-1}][52] to amide I peak [1596-1712 cm^{-1}]) is related to the amount of sugars (including glucose and ribose) attached to the matrix.[53] The sugar:matrix ratio was evaluated following decalcification (see 5.8 S1) because the prominent ν_1 phosphate overlaps the sugar peaks. For a subset of the specimens, there was not enough tissue after demineralization to detect an infrared signal (T2DM: n = 5, non-DM: n = 5).

5.2.6 High-Performance Liquid Chromatography

The concentrations of pentosidine and two enzymatic crosslinks, pyridinoline (Pyd) and deoxypyridinoline (Dpd), were determined using HPLC and expressed normalized to collagen concentration (e.g., mol/mol collagen). The total content of mature enzymatic crosslinks (sum of Pyd and Dpd) was calculated, as well as the ratio of non-enzymatic crosslinks (pentosidine) to mature enzymatic crosslinks, which indicates the

ratio of physiologically disadvantageous crosslinks to advantageous crosslinks (similar to [54]).

Tissue allocated for HPLC and fluorescence spectroscopy analyses was lyophilized then hydrolyzed in 6 N HCl at 110 °C for 18 h. An aliquot of the hydrolysate was reserved for fluorescence spectroscopy, and the remainder was dried in a vacuum centrifuge (Speed Vac SC110A, Savant, Farmingdale, NY). The dried hydrolysate was re-suspended in an internal standard solution containing 10 nM pyridoxine and 2.4 µM homoarginine (30 µl internal standard per 1 mg dried bone) and filtered with a 0.45 µm membrane. The re-suspended samples were diluted 1:5 with 10% acetonitrile (v/v) and 0.5% heptafluorobutyric acid (v/v).

Pentosidine, Pyd, and Dpd were separated on a C-18 column (Gemini-NX C-18, Phenomenex, Torrance, CA) using two isocratic steps[55] and a programmable HPLC system (Model 126, Beckman Coulter, Inc., Fullerton, CA) attached to a fluorescence detector (Model FP1520, Jasco, Easton, MD). The calibration standard containing pentosidine (Case Western Reserve University, Cleveland, OH), Pyd (8004, Quidel, Athens, OH), and Dpd (8004, Quidel, Athens, OH) was created through serial dilution.

The concentrations of pentosidine, Pyd, and Dpd were normalized by collagen concentration determined by hydroxyproline concentration (assuming 300 mol hydroxyproline per mol collagen). To measure hydroxyproline, amino acid analysis was performed on an aliquot of the further diluted sample from the crosslink analysis.[56] Briefly, the crosslink sample used for separation was diluted 1:50 with 6

µM homoarginine (amino acid internal standard) in 0.1 M borate buffer (pH 11.4). For enhanced detection, the sample solution was derivatized using 6 mM 9-fluorenylmethyl chloroformate for 40 minutes, and extracted three times with pentane. After derivatization, 25% (v/v) acetonitrile in 0.25 M boric acid (pH 5.5) was added. A calibration standard of purified hydroxyproline (Sigma-Aldrich, St. Louis, MO) and 6 µM homoarginine in 0.1 M borate buffer (pH 11.4) was created through serial dilution. The separation of amino acids was run using the injection sequence described by Bank et al.[56] Data analysis for crosslink and hydroxyproline determination was performed using 32 Karat Workstation software (v. 5.0, Beckman Coulter, Inc., Brea, CA) and Matlab (2014a, The MathWorks, Inc., Natick, MA).

5.2.7 Fluorescence Spectrometry

Total fluorescent AGEs (fAGEs) were measured using fluorescence spectrometry and normalized to collagen concentration. The endogenous fluorescence of cancellous bone tissue was compared to the fluorescence of a quinine standard (149504, Sigma Aldrich, St. Louis, MO). The aliquot of hydrolysate, reserved from that used for the HPLC separations, was diluted with DI water to a concentration of 3 µg bone/ml solution. The fluorescence of diluted bone hydrolysate and the quinine standards were measured in a 96-well plate using a multi-mode microplate reader (Synergy H1, BioTek, Winooski, VT) at an excitation of 360 nm and an emission of 460 nm.

A colorimetric assay of hydroxyproline was used to determine collagen content and normalize the bulk fluorescence. For the bone tissue samples, the hydrolysate measured for bulk fluorescence was diluted with deionized water to 0.3 µg bone/ml.

To initiate the reaction, chloramine-T was added to the hydroxyproline standards and the diluted sample hydrolysates. The standards and samples were incubated for 20 minutes at room temperature, then 3.15 M perchloric acid was added to stop the reaction. After sitting 5 minutes at room temperature, p-dimethylaminobenzaldehyde was added. The standards and samples were incubated at 60 °C in a water bath for 20 minutes, then cooled in cold water in darkness to room temperature. The absorbance of the specimens and standards was measured at a wavelength of 570 nm in a 96-well plate a multi-mode microplate reader. Total fAGEs are reported in units of ng quinine fluorescence/mg collagen.

5.2.8 Statistical Analyses

Between-group differences in the compositional, microarchitectural, and mechanical outcomes were determined by a Student's t-tests, Welch's t-tests, Mann-Whitney U tests, or Kolmogorov-Smirnov tests were performed, as appropriate, after testing for normality and homogeneity of variances. Univariate linear regressions were performed with all mechanical, compositional, and microarchitectural outcomes as the dependent variable and pre-operative HbA1c as the independent variable to determine if recent glycemic control, a clinically available measure, is related to characteristics of bone tissue that are only measurable with biopsies. A significance level of $p = 0.05$ was used for all analyses.

A principal component analysis (PCA) was used to determine whether variation in the large number of interrelated measured compositional variables could be explained in terms of a smaller number of independent variables (factors). Because

many of the primary compositional variables are interrelated (e.g., pentosidine and fAGEs; crystallinity and carbonate:phosphate ratio), we expected that PCA would yield a smaller number of independent compositional factors for use in regression modeling. Specifically, PCA was performed on mineral:matrix ratio, collagen maturity, crystallinity, carbonate:phosphate ratio, acid phosphate content, Pyd concentration, Dpd concentration, pentosidine concentration, and total fAGEs to detect underlying relationships in the compositional variables. A more detailed summary of the rationale for creating factors can be seen in 5.8 Section S4.

Regression modeling was used to determine which compositional and microarchitectural factors were the most important explanatory variables of mechanical performance and how a single explanatory variable can influence a mechanical outcome when holding all other, highly influential factors (like BV/TV) constant. Four mechanical properties were modeled: 1) Young's modulus, 2) ultimate stress, 3) post-yield strain, and 4) post-yield toughness. These properties respectively describe the bulk tissue stiffness, strength, ductility, and toughness, and together offer a comprehensive evaluation of the monotonic compressive properties of bulk cancellous tissue. First, stepwise selection regressions using the Akaike information criterion with the small sample size correction (AICc)[57,58] were used to determine which compositional (AGEs, enzymatic crosslinks, mineral properties) and microarchitectural parameters were the most important determinants of mechanical performance. Linear[59,60] and power law[61,62] relationships were assessed to determine the influence of BV/TV on mechanical properties (see 5.8 Section S2 and Supplemental Table S1), and a linear BV/TV term was elected for use in these models.

For highly collinear variables (e.g., Tb.Th, Tb.N, Tb.Sp), only one was included in the stepwise model. Patient age was included as a fixed effect, and the factor that emerged from the principal components analysis of the compositional outcomes was included as a potential model effects in place of the variables that constituted the factor. The interaction of Group with all potential compositional and microarchitecture predictors was also included. To ascertain whether or not the influence of T2DM-realted complications (e.g., CVD, CKD, Table 4.3-1) influenced the measured mechanical properties, dichotomous variables for these complications were also included as potential effects. To maintain power for the regression analyses (T2DM: n = 20, non-DM: n = 25), the sugar:matrix ratio was not included as a potential effect.

A visual representation that shows the direction and magnitude of each predictor in the post-yield toughness model was generated. The grand mean of all predictor variables was calculated for the non-DM and T2DM groups, and these values were entered into the model for post-yield toughness to ascertain the predicted average post-yield toughness. Next, the predicted post-yield toughness was calculated for a one standard deviation increase to the grand mean of each predictor variable while holding all other predictors at their respective grand means. Group was set to T2DM, and age was set to 63 years. This same method of adding one standard deviation to the grand mean was performed for all predictor variables, and the predicted post-yield toughnesses were plotted together on the same axis. The resulting figure shows the direction and magnitude of a one standard deviation unit increase from the grand mean for each predictor, thereby allowing for visual comparison of different compositional or microarchitectural effects. Low, medium, and high risk

scenarios were generated and plotted in the same manner.

5.3 ***Results***

5.3.1 Group Characteristics

In the full cohort, the T2DM group had a higher pre-operative HbA1c than the non-DM group (+28%, $p < 0.05$), and hyperglycemia in the T2DM group and euglycemia in the non-DM group was confirmed (Table 5.3-1). Age, past surgical history, height, weight, and BMI did not differ across groups, and the T2DM group possessed a higher prevalence of coronary artery disease ($p < 0.05$) with a trend toward a higher prevalence of hypertension ($p = 0.099$) compared to the non-DM group (Table 5.3-1). Twenty-three percent of the T2DM group used insulin (n = 7/31), 74% used metformin (n = 25/31), and 45% used other antidiabetic medications (n = 13/31) (Table 5.3-1).

The mechanical testing cohort differed slightly from the full cohort. First, although the mean ages of the T2DM and non-DM groups were not statistically different in the full cohort, the T2DM group was borderline older than the non-DM group in the mechanical testing cohort (+7%, $p = 0.073$) (Table 5.3-1). Accordingly, mechanical testing data were adjusted for age (see Statistical Analyses). Second, in the mechanical testing cohort, the T2DM group had a higher prevalence vitamin D supplementation than the non-DM group ($p < 0.05$) (Table 5.3-1).

5.3.2 Advanced Glycation Endproducts

The concentration of the AGE pentosidine was 36% greater, and the sugar:matrix ratio was 42% greater in the T2DM group compared to the non-DM group (both $p < 0.05$) (Figure 5.3-1A). Concentration of total fAGEs did not differ across groups (Figure 5.3-1A). Pentosidine, the sugar:matrix ratio, and total fAGEs were not correlated among each other.

5.3.3 Enzymatic Crosslinks

The concentration of the enzymatic crosslink Pyd trended towards being lower in the T2DM group than the non-DM group (-10%, $p = 0.071$) (Figure 5.3-1B), while the concentration of Dpd did not differ across groups (Figure 5.3-1B). The total content of mature/trivalent enzymatic crosslinks (sum of Pyd and Dpd) measured with HPLC and collagen maturity (XLR, Figure 5.3-1B) measured with FTIR did not differ across groups.

Table 5.3-1: Group characteristics of the full cohort and the mechanical testing cohort. Values are shown as means ± standard deviation, unless otherwise noted. Coexisting conditions were determined from medical records at the time of total hip arthroplasty. *p* values assessed by Student's t-test, Welch's t-test, Mann-Whitney U test, Kolmogorov-Smirnov test, or Pearson chi-square test, as appropriate. Abbreviations: non-DM: non-diabetic group, T2DM: type 2 diabetic group; THA: total hip arthroplasty; TKA: total knee arthroplasty. [1]Antidiabetic medications include sulfonylureas (SUs): glyburide, glipizide, glimepiride; glinides: nateglinide; glucagon-like peptide 1 (GLP-1) agonists: dulaglutide, liraglutide, exenatide; and depeptidyl peptidase 4 (DPP-4) inhibitor: sitagliptin.

Characteristic	Full Cohort			Mechanical Testing Cohort		
	non-DM (n = 34)	**T2DM** (n = 31)	***p***	**non-DM** (n = 25)	**T2DM** (n = 20)	***p***
Demographic						
Age (years)	61.6 ± 8.6	64.8 ± 8.1	0.131	60.6 ± 8.0	64.8 ± 7.1	0.073
Past surgical THA or TKA, n (%)	10 (29.4)	6 (19.4)	0.347	9 (36.0)	4 (20.0)	0.239
Biochemical						
Pre-operative HbA1c (%)	5.53 ± 0.39	7.07 ± 0.89	**< 0.05**	5.52 ± 0.40	7.21 ± 1.01	**< 0.05**
Anthropometry						
Height (cm)	178.9 ± 6.9	177.2 ± 8.0	0.369	180.0 ± 6.9	176.4 ± 8.1	0.126
Weight (kg)	93.7 ± 21.1	99.6 ± 17.7	0.222	97.7 ± 21.9	97.2 ± 18.6	0.945
Body mass index (kg/m2)	29.8 ± 6.3	32.3 ± 5.3	0.084	30.9 ± 6.7	32.2 ± 6.0	0.508
Coexisting conditions						
Hypertension, n (%)	15 (44.1)	20 (64.5)	0.099	11 (44.0)	14 (70.0)	0.081
Hyperlipidemia, n (%)	15 (44.1)	18 (58.1)	0.261	11 (44.0)	14 (70.0)	0.081
Chronic kidney disease, n (%)	1 (2.9)	2 (6.5)	0.501	1 (4.0)	2 (10.0)	0.427
Coronary artery disease, n (%)	1 (2.9)	6 (19.4)	**< 0.05**	1 (4.0)	2 (10.0)	0.427
Current medications/supplements						
Insulin, n (%)	0 (0.0)	7 (22.6)	**< 0.05**	0 (0.0)	4 (20.0)	**< 0.05**
Biguanides (Metformin), n (%)	0 (0.0)	23 (74.2)	**< 0.05**	0 (0.0)	13 (65.0)	**< 0.05**
Other antidiabetic medications1, n (%)	0 (0.0)	14 (45.2)	**< 0.05**	0 (0.0)	7 (35.0)	**< 0.05**
Vitamin D, n (%)	3 (8.8)	8 (25.8)	0.068	2 (8.0)	8 (40.0)	**< 0.05**

5.3.4 Ratio of Non-enzymatic to Enzymatic Crosslinks

The ratio of non-enzymatic crosslinks to mature crosslinks (or disadvantageous crosslinks to advantageous crosslinks[54]), calculated as pentosidine/(Pyd+Dpd), was 61% greater in the T2DM group compared to the non-DM group (T2DM: 9.94 ± 6.42, non-DM: 6.17 ± 2.42, $p < 0.05$).

5.3.5 Mineral Properties

The mineral:matrix ratio was 7% greater in the T2DM group versus the non-DM group ($p < 0.05$) (Figure 5.3-1C). The crystallinity, carbonate:phosphate ratio, and acid phosphate content did not differ across groups (Figure 5.3-1C).

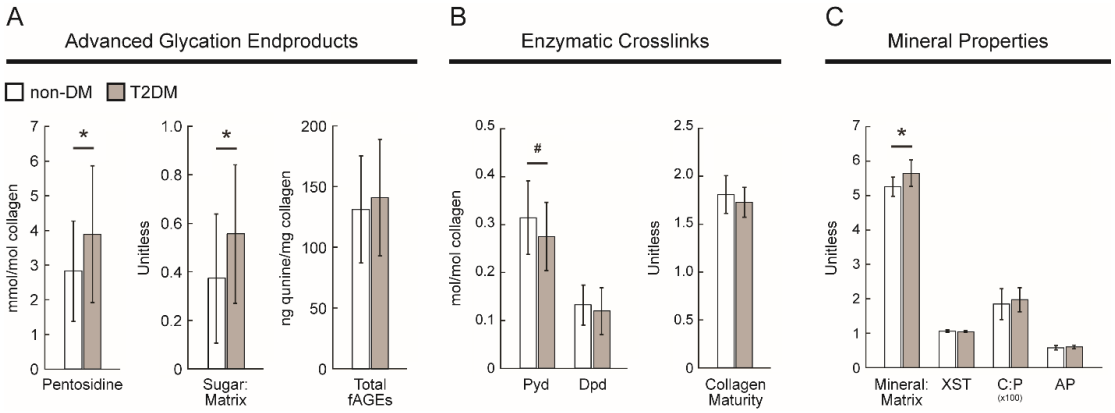

Figure 5.3-1: Compositional properties of the full cohort organized by (A) measures of advanced glycation endproducts, (B) measures of enzymatic crosslinks, and (C) measures of mineral properties. * $p < 0.05$ and # $p < 0.10$ assessed by Student's t-test, Welch's t-test, Mann-Whitney U test, or Kolmogorov-Smirnov test. Abbreviations: non-DM: non-diabetic group; T2DM: type 2 diabetic group; Total fAGEs: total fluorescent advanced glycation endproducts; Pyd: pyridinoline; Dpd: deoxypyridinoline; XST = crystallinity; C:P = carbonate:phosphate ratio; AP = acid phosphate content.

5.3.6 Microarchitecture

In T2DM compared to non-DM specimens, Tb.Sp was lower (-13%, $p < 0.05$), Tb.N trended toward a greater value (+20%, $p = 0.059$), and Conn.D trended toward greater value (+96%, $p = 0.061$) (Table 5.3-2). All other microarchitectural parameters (BV/TV, BS/BV, Tb.Th, and DA) did not differ across groups (Table 5.3-2). Neither patient weight nor BMI were correlated with BV/TV suggesting that body mass did not increase bone volume.

Table 5.3-2: Microarchitecture assessed with microCT of the mechanical cohort specimens. Values are shown as means ± standard deviation. *p* values assessed by Student's t-test, Welch's t-test, Mann-Whitney U test, or Kolmogorov-Smirnov test. Abbreviations: non-DM: non-diabetic group, T2DM: type 2 diabetic group; BV/TV: bone volume fraction; BS/BV: specific bone surface; Conn.D: connectivity density; Tb.N: trabecular number; Tb.Th: trabecular thickness; Tb.Sp: trabecular separation; DA: degree of anisotropy.

Microarchitecture Parameter	**non-DM** (n = 25)	**T2DM** (n = 20)	**T2DM vs. non-DM** (% difference)	***p***
BV/TV (%)	15.81 ± 7.30	19.63 ± 8.69	24	0.125
BS/BV (mm^2/mm^3)	19.01 ± 3.79	18.22 ± 4.24	-4	0.520
Conn.D ($1/mm^3$)	10.52 ± 9.19	20.65 ± 21.52	96	0.061
Tb.N (1/mm)	1.27 ± 0.29	1.52 ± 0.49	20	0.059
Tb.Th (mm)	0.15 ± 0.03	0.16 ± 0.07	7	0.534
Tb.Sp (mm)	0.80 ± 0.15	0.71 ± 0.12	-13	**< 0.05**
DA	1.77 ± 0.24	1.84 ± 0.23	4	0.394

5.3.7 Mechanical Properties

Compression testing revealed that Young's modulus was 86% greater ($p < 0.05$) (Figure S1A), yield stress was 91% greater ($p < 0.05$) (Figure S1C), and ultimate

stress was 90% greater ($p < 0.05$) (Figure S1F) in the T2DM versus non-DM group. Yield strain, ultimate strain, post-yield strain, post-yield toughness, toughness, and residual strain did not differ across groups (Figure S1B, S1E, S1G, S1H, S1I, S1K).

The mechanical property outcomes of Young's modulus, yield stress, ultimate stress, and both measures of toughness were linearly normalized by each specimen's respective BV/TV (mechanical property/BV/TV, see 5.8 S2 and Table S1). Normalized Young's modulus (Figure 5.3-2A), normalized yield stress, and normalized ultimate stress (Figure 5.3-2B) remained 51%, 55%, 45% greater in the T2DM versus non-DM group, respectively (all $p < 0.05$). Normalized post-yield toughness (Figure 5.3-2C) and normalized toughness did not differ across groups.

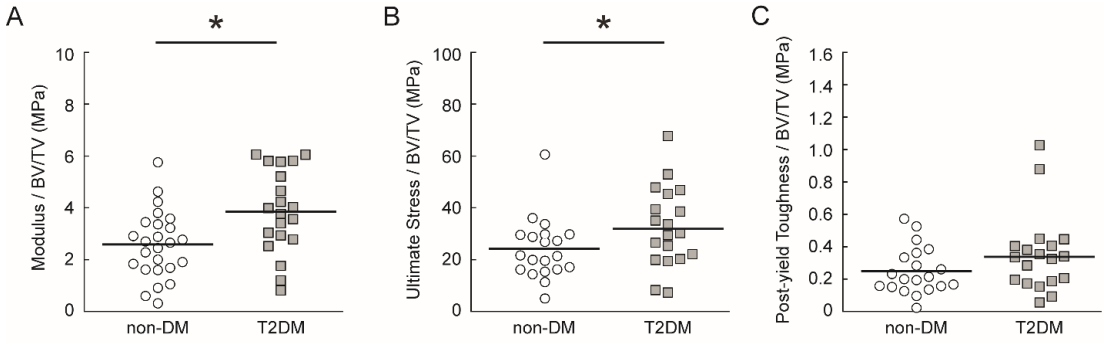

Figure 5.3-2: (A) Young's modulus normalized by BV/TV, (B) Ultimate stress normalized by BV/TV, and (C) Post-yield toughness normalized by BV/TV. Horizontal lines indicate group means. * $p < 0.05$ by Student's t-test. Abbreviations: non-DM: non-diabetic group, T2DM: type 2 diabetic group; BV/TV: bone volume fraction. A version of this figure that also shows the relationship of mineral content with the mechanical properties normalized by BV/TV can be seen in 5.8 Supplemental Figure S3.

5.3.8 Mineral Maturity Factor

PCA was used to determine whether variation in the interrelated compositional variables could be explained in terms of a smaller number of independent variables (factors). Using PCA, we identified a factor (factor loadings > |0.8|, eigenvalue = 2.68) that we termed the mineral maturity factor (MMF) because it consisted of FTIR crystallinity, carbonate:phosphate ratio, and acid phosphate content, all variables that characterize the composition and size of bone mineral crystals. The original variables were standardized and coded such that higher MMF values indicate a more mature mineral crystal, with larger/more perfect crystals and lower carbonate and acid phosphate substitution. The MMF captured 89% of the variance of the three included parameters and was included in the subsequent regression analyses.

The MMF was not statistically different across groups (T2DM: MMF = -0.172, non-DM: MMF = 0.129, p = 0.237); however, the lower T2DM group MMF value indicates that the T2DM specimens had a less mature mineral compared to the specimens in the non-DM group on average.

5.3.9 Regression Analyses with Pre-operative HbA1c

Correlations between pre-operative HbA1c and compositional parameters revealed that pre-operative HbA1c was weakly and positively correlated the mineral:matrix ratio ($R^2 = 0.182$, $p < 0.05$). All other compositional parameters were not correlated with pre-operative HbA1c.

Correlations between pre-operative HbA1c and microarchitectural parameters

revealed that pre-operative HbA1c weakly and positively correlated with Tb.N (R^2 = 0.077, $p < 0.05$) and weakly and negatively correlated with Tb.Sp ($R^2 = 0.091$, $p < 0.05$). No other microarchitectural parameters were correlated with pre-operative HbA1c.

Correlations between pre-operative HbA1c and mechanical properties revealed that Young's modulus was weakly and positively correlated with HbA1c ($R^2 = 0.088$, $p < 0.05$). Pre-operative HbA1c was not correlated with any other mechanical outcomes.

5.3.10 Predicted Regression Analyses for Mechanical Properties

A combination of microarchitectural and compositional parameters explained between 12% and 83% of the observed variation in Young's modulus, ultimate stress, post-yield strain, and post-yield toughness (Table 5.3-3). Age was included as a fixed effect for each model to control for variations in patient age (Table 5.3-1); however, age was not a significant explanatory variable in any of the models of mechanical properties.

Eighty-three percent of the variation in Young's modulus was explained by BV/TV, Tb.Th, mineral:matrix ratio, Group, and the interaction of Group with Tb.Th; 70% of the variance in ultimate stress was explained by BV/TV and mineral:matrix ratio; 12% of the variance in post-yield strain was explained by the mineral maturity factor and pentosidine; and 74% of the variance in post-yield toughness was explained by BV/TV, the mineral maturity factor, pentosidine, total fAGEs, Group, and the interaction of Group with total fAGEs (Table 5.3-3).

Table 5.3-3: Final regression models of selected mechanical properties organized by parameter type (fixed effect, microarchitecture, or composition). Values are shown as parameter coefficients with standard error in parentheses. Regression coefficients were determined from forward stepwise regressions using the Akaike information criterion (AICc). Abbreviations: BV/TV: bone volume fraction; Tb.Th: trabecular thickness; Total fAGEs: total fluorescent AGEs.

Parameter	**Young's Modulus (MPa)**	**Ultimate Stress (MPa)**	**Post-yield Strain (%)**	**Post-yield Toughness (kPa)**
Intercept	-1444.4 (676.1)	-12.44 (7.45)	1.446 (0.485)	-3.86 (38.60)
Group	-58.2 (36.4)	---	---	-8.79 (4.68)
Fixed Effect				
Age (years)	3.4 (4.1)	0.05 (0.06)	-0.005 (0.008)	-0.08 (0.58)
Microarchitecture				
BV/TV (%)	43.8 (66.6)	0.51 (0.06)	---	5.57 (0.73)
TbTh (mm)	2731.6 (1634.5)	---	---	---
TbTh*Group	-3039.4 (980.9)	---	---	---
Composition				
Mineral:Matrix (unitless)	120.5 (100.6)	1.15 (1.20)	---	---
Mineral Maturity Factor (unitless)	---	---	-0.208 (0.070)	-10.56 (5.62)
Pentosidine (mmol/mol collagen)	---	---	-0.038 (0.032)	-6.10 (2.72)
Total fAGEs (nq quinine/mg collagen)	---	---	---	-0.10 (0.09)
Total fAGEs*Group	---	---	---	0.17 (0.09)
Adjusted R^2	0.826	0.694	0.116	0.739

5.3.11 Magnitude and Direction of Model Predictors and Hypothetical Risk Scenarios

The predicted post-yield toughness was calculated from the regression model (Table 5.3-3) using the grand mean values for the non-DM and T2DM specimens combined and group set to T2DM (Figure 5.3-3, top gray box and corresponding vertical gray dashed line). Next, one parameter at a time was varied from the grand mean to the grand mean plus one standard deviation (Figure 5.3-3, gray boxes), or in the case of group, set to non-DM. As seen in Figure 5.3-3A, a one standard deviation increase in BV/TV from the grand mean increases predicted post-yield toughness by 68% (third gray box from the top), while a one standard deviation increase in MMF, pentosidine, or total fAGEs decreases predicted post-yield toughness by 14%, 16%, or 19%, respectively (bottom three gray boxes of Figure 5.3-3A). The direction of these changes match the signs of the predictor coefficients in Table 5.3-3.

Three different risk scenarios were hypothesized for post-yield toughness based on the regression model coefficients and Figure 5.3-3A. The low risk scenario for the T2DM group includes a high (grand mean + one standard deviation) BV/TV, but average (grand mean) MMF, pentosidine, and total fAGEs values (Figure 5.3-3B). The sum of all the effects was positive and equal to that of the effect of BV/TV, as shown on the bottom row of Figure 5.3-3B with the solid black box. The medium risk scenario for the T2DM group includes an average BV/TV, but high (grand mean + one standard deviation) values for MMF, pentosidine, and total fAGEs. The sum of all the effects was negative, as shown with the solid black box along the bottom row of Figure 5.3-3C. The high risk scenario for the T2DM group includes moderately-low

BV/TV (mean – one half of one standard deviation) and high (grand mean + one standard deviation) values for MMF, pentosidine, and total fAGEs. The sum of all the effects was more negative than the medium risk, as shown with the solid black box along the bottom row of Figure 5.3-3D.

Figure 5.3-3: The regression model for post-yield toughness (Table 5.3-3) was used to calculate predicted post-yield toughness under different circumstances. (A) The predicted post-yield toughness of a specimen with grand mean values of BV/TV, MMF, pentosidine, and total fAGEs is shown with the top gray box and the vertical black dashed line. The predicted post-yield toughness of each predictor parameter was varied one at a time from the grand mean to the grand mean plus one standard deviation to show the magnitude and direction of change and is indicated with a gray box. For (B-D), MMF, pentosidine, and total fAGEs were evaluated at the mean plus one standard deviation and BV/TV was evaluated at (B) the grand mean of BV/TV plus one standard deviation, which illustrates a low risk scenario; (C) the grand mean of BV/TV, which illustrates a medium risk scenario; and (D) the grand mean of BV/TV minus one half of one standard deviation, which illustrates a high risk scenario. The bottom black box in Panels B-D indicates the predicted post-yield toughness for that scenario, and it is also the cumulative effects of all predictor parameters compared to the predicted post-yield toughness evaluated with every parameter at the grand mean. The horizontal gray lines indicate the 95% CI.

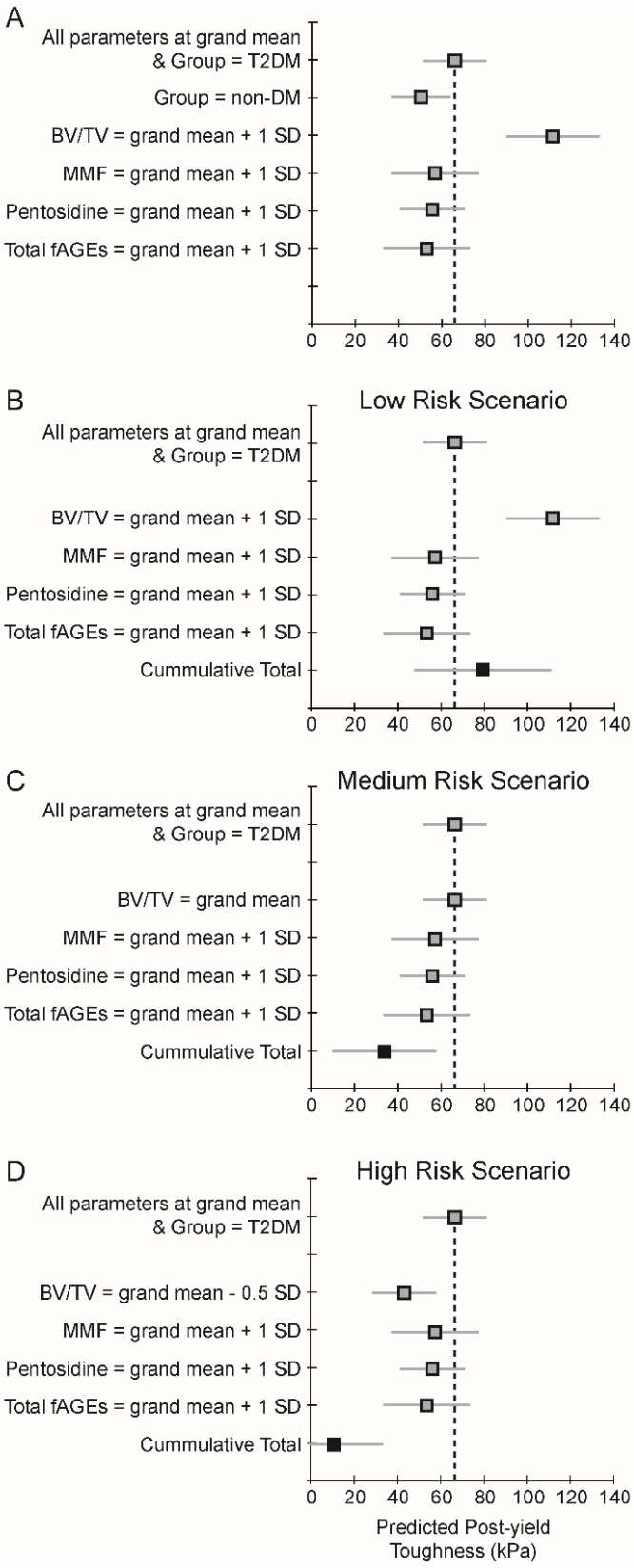
A
All parameters at grand mean & Group = T2DM
Group = non-DM
BV/TV = grand mean + 1 SD
MMF = grand mean + 1 SD
Pentosidine = grand mean + 1 SD
Total fAGEs = grand mean + 1 SD
0 20 40 60 80 100 120 140
B
Low Risk Scenario
All parameters at grand mean & Group = T2DM
BV/TV = grand mean + 1 SD
MMF = grand mean + 1 SD
Pentosidine = grand mean + 1 SD
Total fAGEs = grand mean + 1 SD
Cummulative Total
0 20 40 60 80 100 120 140
C
Medium Risk Scenario
All parameters at grand mean & Group = T2DM
BV/TV = grand mean
MMF = grand mean + 1 SD
Pentosidine = grand mean + 1 SD
Total fAGEs = grand mean + 1 SD
Cummulative Total
0 20 40 60 80 100 120 140
D
High Risk Scenario
All parameters at grand mean & Group = T2DM
BV/TV = grand mean - 0.5 SD
MMF = grand mean + 1 SD
Pentosidine = grand mean + 1 SD
Total fAGEs = grand mean + 1 SD
Cummulative Total
0 20 40 60 80 100 120 140
Predicted Post-yield Toughness (kPa)

5.4 *Discussion*

In this work, we describe the compositional, microarchitectural, and mechanical properties of cancellous bone at the femoral neck in men with and without T2DM. As hypothesized, the concentration of AGEs was greater in cancellous tissue in the T2DM group. Contrary to our hypothesis, post-yield properties were similar across groups at the femoral neck; however, after accounting for the large influence of BV/TV, we observed that the altered tissue composition in the T2DM group decreases post-yield stain and post-yield toughness.

Compositional characterization revealed a greater concentration of pentosidine and a greater sugar:matrix ratio in the T2DM specimens compared to the non-DM specimens. These results confirm increased accumulation of the AGE pentosidine and sugars bound to the collagen matrix in cancellous tissue with T2DM and are consistent with other reporting of bone tissue pentosidine in patients with and without T2DM.[38] In contrast, total fAGEs were not different between groups; nevertheless, this result is consistent in scope and magnitude with other reporting of fAGEs in proximal femoral cancellous bone in people with and without T2DM[32] and in non-DM femoral neck cadaveric tissue.[25] Although in vitro glycosylation/ribosylation studies of human and bovine tissue and collagen gels offer the ability to isolate the effects of AGE accumulation, the extent of glycosylation/ribosylation is two to ten times greater than the physiologic levels measured in the current study.[24,25,53]

The apparent discrepancy between a highly specific measure of AGEs (i.e.,

pentosidine), a global measure of sugars attached to the collagen matrix (i.e., sugar:matrix ratio), and a non-specific measure of AGEs that fluoresce at a specific wavelength (i.e., total fAGEs) underscores the current limitations of measuring AGE accumulation. For example, pentosidine is just one of hundreds of AGEs, so despite its ability to precisely characterize pentosidine concentration, its overall contribution to total AGE accumulation is unknown. Conversely, measurement of total fAGEs may capture a wider range of AGEs, but only fluorescent AGEs are measured, and all non-fluorescent AGEs like CML are undetected. Finally, the ratio of non-enzymatic crosslinks to mature enzymatic crosslinks was 61% greater in the T2DM specimens compared to the non-DM specimens. Together, these findings provide clear evidence of detrimental crosslink accumulation in T2DM tissue and have translational relevance because crosslink accumulation stiffens the collagen matrix, which could in turn make bone in people with T2DM more brittle and less resistant to fracture.

In addition to a greater accumulation of AGEs in the T2DM specimens compared to the non-DM specimens, we observed additional evidence of altered collagen and mineral properties. The concentration of the trivalent enzymatic crosslink Pyd measured with HPLC trended towards being lower in the T2DM specimens compared to the non-DM specimens. This finding, though not statistically significant, may indicate a less mature collagen matrix and is consistent with a study of WBN/Kob rats that found reductions in enzymatic crosslinks with T2DM.[23] Reductions in mature crosslinks in tissue from patients with T2DM may similarly lead to decreased strength as evidenced by the association of mature pyridinoline crosslinks and tissue strength.[63,64]

The mineral:matrix ratio, which characterizes tissue mineral content, was 7% greater in the T2DM specimens than the non-DM specimens. Our finding of increased mineral content with T2DM is consistent with findings of greater mean calcium content in the proximal femur of men and women with T2DM compared to non-diabetic controls.[39] A more mineralized tissue is consistent with decreased ductility,[65] thus the greater mineral content observed in the tissue from the T2DM group likely contributes to the increased fracture risk in people with T2DM. The observed greater mineral content may indicate an increased tissue age (i.e., time since formation),[66] of the T2DM versus non-DM tissue. Alternatively, an increase in tissue mineral content may be due to an increase in mineralization nucleation sites.[67] FTIR-assessed mineral properties and the mineral maturity factor (MMF), which combined mineral crystallinity with carbonate substitution and acid phosphate content, were not different across groups. This suggests that the overall maturity of the mineral in the T2DM group is similar to that of the non-DM group.

The simultaneous increase in mineral content without an increase in mineral maturity conveys complex effects of T2DM on mineralization, and it is likely that multiple processes responsible for the observed properties are occurring concurrently. One potential process is that hyperglycemia and AGE accumulation, which have been implicated in decreased osteoblastic function and proliferation in vitro, [8–10,27] may disrupt remodeling and could account for the increased bulk tissue mineral content. A second possible process is that AGE accumulation decreases mineralization rates and alters normal mineralization processes,[54] as evidenced by decreases in mineral apposition rates, bone formation rates, and the number of bone formation sites in

AGE-modified rat tissue.[68] A third possibility is that the formation of AGEs inherently alters the charge profile of the collagen fibers,[69,70] thereby disrupting cell-matrix interactions that could cause downstream effects for collagen and mineral maturation.[67,71] The current study was not designed *a priori* to study these biochemical pathways; however, it is feasible that a simultaneous reduction in remodeling rates and disruption of mineralization and collagen maturation with T2DM via these proposed processes would culminate in the tissue properties observed here.

In the microarchitectural analyses, the T2DM specimens had smaller separation distances between trabecula than the non-DM specimens. Additionally, the T2DM specimens had a borderline greater number of trabecula (+20%, $p = 0.059$) and borderline greater connective density (+96%, $p = 0.061$) than the non-DM specimens. The BV/TV of the T2DM specimens was not different than the non-DM specimens (+23%, $p = 0.125$). Even though not all of the differences in microarchitecture outcomes met the 0.05 threshold for statistical significance, overall, the T2DM specimens had more numerous, more connected, and closer trabeculae, which are known to contribute to a greater BV/TV. Therefore, the 23% greater BV/TV observed in the T2DM group versus non-DM group, though not significant, is consistent with these other measured microarchitectural parameters. Furthermore, the 23% difference in BV/TV is similar to significant differences reported in larger studies of trabecular microarchitecture in patients with T2DM[72] and is consistent with prior observations of greater trabecular hip vBMD in patients with T2DM compared to those without.[28] Interestingly, cancellous microarchitecture may vary between the hip and the spine. Using DXA images to calculate trabecular bone score (TBS), the TBS of the lumbar

spine was lower in people with T2DM compared to those without T2DM,[73,74] indicating a poor-quality microarchitecture.[75]

The Young's modulus and ultimate stress of specimens from the T2DM group were greater than those from the non-DM group, indicating that the T2DM specimens were stiffer and stronger. The post-yield properties, including post-yield strain and post-yield toughness, however, did not differ across groups. Because the apparent stiffness, strength, and toughness of bulk cancellous tissue are all strongly influenced by the quantity of bone in the tested specimen (i.e., BV/TV),[62,76,77] we normalized these apparent properties by each specimen's BV/TV. Contrary to our hypothesis, the stiffness and strength remained greater in the T2DM specimens after normalization, though to a lesser magnitude (Figure 5.3-2). The post-yield properties remained similar across groups after normalization by BV/TV. Thus, the decreased resistance to fracture at the whole-bone level observed clinically in T2DM patients was not mirrored in the monotonic compressive behavior of cancellous explants.

The increased mineral content of the T2DM specimens compared to the non-DM specimens is largely responsible for the greater stiffness and strength of the specimens in the T2DM group observed after normalization by BV/TV. The specimens with higher mineral content (as measured by the FTIR mineral:matrix ratio) had consistently greater moduli, ultimate stresses, and post-yield toughnesses before and after accounting for BV/TV (see 5.8 Supplemental Figure S3).

The importance of bone volume fraction and the mineral content on the bulk cancellous bone behavior is further exemplified by the regression models (Table 3),

which show the strong contribution of these two parameters on Young's modulus and ultimate stress. These results demonstrate that tissue mineral content is consistently important for elastic behavior (which has been previously documented).[65]

In the regression model of post-yield strain, which modeled the tissue's ductility or ability to deform plastically prior to failure, measures of bone quality (i.e., the Mineral Maturity Factor [MMF] and pentosidine) were significant explanatory variables (Table 3). Similarly, the predictive factors for post-yield toughness, a quantity that characterizes the tissue's ability to absorb energy prior to failure and depends on the product of strength and ductility, were the combination of the predictive factors observed in strength (BV/TV) and in post-yield strain (MMF, pentosidine). The MMF and AGE outcomes had distinctly opposite effects as BV/TV and the mineral:matrix ratio. For example, greater values of BV/TV increased post-yield toughness, while greater values of AGEs, like pentosidine, decreased post-yield toughness (Table 3). Our regression models of post-yield properties clearly demonstrate the important role of tissue composition after controlling for the greater bone volume fraction of cancellous bone in patients with T2DM. One limitation of our regression models, however, is the large confidence interval for each parameter as a result of our limited sample size (n = 40-45) and the inherent variability in human data.

The regression modeling is essential to elucidating the relative contributions of microarchitecture and tissue material properties to contributions of tissue-level material properties with T2DM that occur concurrent with changes in BV/TV. Here,

the between-group differences in the quantity of bone (measured as BV/TV) were so large that they dominated the monotonic mechanical properties and essentially masked any other, lower-magnitude differences in material properties with T2DM. By performing regression modeling, we were able to elucidate compositional and microarchitectural changes in T2DM tissue that can be observed after controlling for BV/TV. For example, post-yield toughness was not different by group, but was strongly influenced by BV/TV (as shown in Table 5.3-3). Using stepwise regression models to isolate the effect of BV/TV, we were able to see that the mineral maturity factor, pentosidine, and total fAGEs, had an effect on post-yield toughness, albeit a smaller effect than that of BV/TV (Figure 5.3-3). Of the mineral maturity factor, pentosidine, and total fAGEs, only pentosidine was significantly different by group (Figure 5.3-1); however, the presence of the mineral maturity factor and total fAGEs in the predicted models indicates that these two predictors capture aspects of post-yield toughness that are not necessarily as heavily influence by group.

The different scenarios hypothesized in Figure 5.3-3B-D for low, medium, and high risks further exemplify the large influence of BV/TV; however the influence of tissue AGEs and mineral maturity can also be appreciated. For example, a one standard deviation increase from the mean in mineral maturity, pentosidine, or total fAGEs decreases the predicted post-yield toughness compared to the predicted post-yield toughness for an average specimen (Figure 5.3-3A). The scenarios proposed in Figure 5.3-3B, Figure 5.3-3C, and Figure 5.3-3D demonstrate how deleterious effects in tissue composition can affect bone toughness, especially in the absence of the compensatory effect of BV/TV. Specifically, in the low risk scenario, the high BV/TV

improves post-yield toughness to a greater extent than the deleterious effects due to compositional changes (Figure 5.3-3B). In the medium risk scenario, BV/TV still compensates for the negative influences of the compositional changes, but to a lesser extent, and there is a cumulative decrease in post-yield toughness (Figure 5.3-3C). Finally, in the high risk scenario where BV/TV is moderately lower than the grand mean, BV/TV no longer compensates for the compositional changes, and there is a drastic reduction in predicted post-yield toughness (Figure 5.3-3D). While the regression model presented here is only representative of this study cohort, our models demonstrate how there can be various stages of skeletal fragility risk associated with changes in microarchitecture or tissue composition.

The variable Group modulated trabecular thickness in the model of modulus and on total fAGEs in the model of post-yield toughness (Table 5.3-3). Neither trabecular thickness nor total fAGEs alone were statistically different between groups (Figure 5.3-1); nevertheless, the significant effect of group in these two models indicates that there are important characteristics relating to trabecular thickness and total fAGEs that were not captured by the models.

Tying together the differences in material properties in T2DM versus non-DM specimens and the regression model results, it is evident that T2DM has both beneficial and adverse effects on the mechanical performance of bone. First, T2DM patients had a greater bone volume fraction at the femoral neck, though not statistically significant, which is consistent with clinical assessments of BMD at the femoral neck[1,2] and hip.[3] Furthermore, the greater quantity of bone had a large and

favorable influence on the monotonic apparent stiffness, strength, and toughness. Second, the greater mineral content in the T2DM specimens compared to the non-DM specimens resulted in greater apparent-level strength; however, greater strength typically comes at the expense of ductility and results in more brittle tissue. While we did not detect a group-wise difference in post-yield strain or post-yield toughness, the tradeoff between strength and toughness is well documented.[65,78] It is possible that the large effect of BV/TV overshadowed any smaller effects of T2DM on post-yield properties and inhibited our ability to detect such differences in group comparisons.

One key benefit of our regression models is that they allowed us to estimate the potential effect of material properties separate from the compensatory effects of increased BV/TV with T2DM. For example, our data show greater concentrations of AGEs (e.g., pentosidine) in cancellous tissue from patients with T2DM than those without T2DM, and after accounting for differences in BV/TV, our models revealed the adverse effect of pentosidine accumulation on the post-yield properties. This indicates that if a patient with T2DM has very large accumulation of tissue AGEs, like pentosidine, but does not have a concurrent increase in BV/TV, the adverse effects of T2DM can outweigh any potential compensating effects of increased BV/TV with T2DM. Because post-yield toughness is indicative of the amount of energy that can be absorbed before failure, our model demonstrates how poor bone quality without an advantageous increase in bone mass can lead to decreased fracture resistance in patients with T2DM.

Although the mechanical testing (which showed that bulk cancellous tissue

from the T2DM group was stronger than that from non-DM controls) appear in conflict with clinical observations of reduced whole-bone fracture resistance, they highlight the complexity of identifying the key factors that contribute to fracture behavior across multiple levels of structural hierarchy. Our study focused on the cancellous tissue properties at the millimeter-scale, and our results suggest that patients with T2DM have a greater quantity of bone that is more highly mineralized. While these changes will ultimately increase cancellous bone strength at the millimeter-scale, a more highly mineralized bone will be inherently more brittle and less capable of plastic deformation and thus potentially less fracture resistant.[65,79] In addition, our models of post-yield strain and post-yield toughness demonstrate an adverse effect of AGE accumulation on energy absorption once the large influence of BV/TV is controlled for. Finally, it is important to note that both cancellous and cortical bone contribute to structural performance at the whole-bone level, and cortical bone is more critical for load bearing in the hip.[80] Because growing evidence indicates that T2DM compromises cortical tissue integrity,[16,29,31] it is possible that adverse changes due to T2DM in the cortical compartment may outweigh any beneficial changes in the cancellous compartment, and this may help to explain whole-bone fragility observed clinically at the hip. Future work includes analysis of the accompanying cortical tissue in these specimens.

Our study design has several important limitations and advantages. The main shortcoming of this study was the limited availability of patient information related to T2DM. Even though the pre-operative HbA1c and diagnosis of T2DM were recorded at the time of total hip arthroplasty, the patients' long-term HbA1c history or duration

of T2DM were not available. Therefore, our information on the patients' glycemic control was only on the order of months, which is much shorter than the years required for skeletal changes due to T2DM to fully manifest. Furthermore, the severity and duration of T2DM are known to greatly affect fracture risk,[31,81] and therefore may also affect the degree of compositional changes due to T2DM. Thus, the single time point for HbA1c level limits our ability to relate clinical measures of glycemic control to the tissue properties that may govern fracture behavior and likely influenced our ability to detect stronger correlations between HbA1c and tissue material properties. Similarly, we were not able to directly account for any T2DM-related complications that may affect bone, such as cardiovascular disease, renal osteodystrophy, retinopathy, or systemic inflammation. Similarly, although we accounted for the presence of CVD and CKD in our model, our ability to directly account for other T2DM-related complications that may affect bone, such as renal osteodystrophy, retinopathy, or systemic inflammation[82] was limited by the lack of detailed information on these comorbidities collected prior to surgery. We also could not assess whether bone remodeling was altered in the T2DM group via serum biomarkers or dynamic bone labeling. Lastly, although we collected and characterized femoral neck tissue at the farthest distance possible from the joint surface, all subjects in our study had osteoarthritis. A recently published study with a similar cohort of patients undergoing total hip arthroplasty for osteoarthritis did not report differential effects of osteoarthritis in patients with and without T2DM on the trabecular tissue; however, it is possible that osteoarthritis may have altered the joint tissue properties in our specimens.[83] The medical management of patients with T2DM, as well as OA, may

affect the results and may also help explain some of the apparent discrepancies between our findings and the findings of T2DM animal models. Our study did not include women because female age-matched specimens accrued much more slowly; however, future analyses should include women participants. While the surgical setting of our specimen collection imposed several limitations, one major benefit of our study is that the explants characterized here are from the femoral neck, a highly clinically relevant fracture site with a large volume of cancellous bone. Moreover, tissue from the femoral neck allows for tissue characterization at the bulk level and for compartment-specific analysis of cancellous and cortical bone. Finally, our study is among the first to characterize changes in bone quality and mechanical properties in cancellous bone from a clinical population of men with T2DM.

5.5 *Conclusion*

In this study, we quantified the accumulation of AGEs, characterized the mineral and matrix composition, assessed the microarchitecture, and mechanically assessed cancellous bone from men with and without T2DM. Our findings showed clear evidence, for the first time, of AGE accumulation and altered tissue material properties in a clinical population with T2DM. Additionally, we used statistical models to predict and compare the mechanical performance of hypothetical low, medium, and high risk scenarios based on the observed changes in tissue composition and microarchitecture with T2DM. Our regression models showed, as expected, that bone volume fraction was by far the greatest determinant of compressive mechanical properties. Furthermore, the T2DM group had a greater tissue mineral content than the

non-DM group which increased strength. After accounting for the greater bone volume fraction in the T2DM group, our analyses revealed the deleterious effects of T2DM such AGE accumulation and altered mineral maturity. Specifically, we illustrated that poor bone quality (e.g., high AGE concentrations) in the absence of increased bone volume fraction can drastically reduce the ability of cancellous bone to absorb energy prior to failure in patients with T2DM. Our findings echo epidemiological evidence that the quantity of bone alone does not explain fracture risk, and our results provide a foundation for future investigations of changes in bone quality with T2DM. Although our methods are not available in a typical diabetes clinic, our findings are clinically relevant because they demonstrate that different populations of T2DM patients may have distinctly different bone fragilities as a result of varying tissue composition and microarchitecture.

5.6 *Acknowledgements*

We thank Lyudmila Lukashova for assistance with microCT data collection; Dr. Edward DiCarlo and Dr. Adele Boskey for assistance with specimen processing; Dr. Erika Mudrak for assistance with statistical analysis; and Dr. Richard Bockman and Erik Taylor for helpful discussions. We also thank the following orthopedic surgeons for assistance with specimen collection: Dr. Michael Alexiades, Dr. Friedrich Boettner, Dr. Mathias Bostrom, Dr. Robert Buly, Dr. Charles Cornell, Dr. Michael Cross, Dr. Mark Figgie, Dr. Alejandro Gonzalez Della Valle, Dr. Allan Inglis, Dr. Seth Jerabek, Dr. David Mayman, Dr. Michael Maynard, Dr. Douglas Padgett, Dr. Michael Parks, Dr. Amar Ranawat, Dr. Eduardo Salvati, Dr. Thomas Sculco, Dr.

Edwin Su, and Dr. Geoffrey Westrich.

5.7 *References*

1. Schwartz, A. V., Vittinghoff, E., Bauer, D. C., *et al.* Association of BMD and FRAX Score With Risk of Fracture in Older Adults With Type 2 Diabetes. *JAMA* **305,** 2184 (2011).
2. De Liefde, I. I., Van Der Klift, M., De Laet, C. E. D. H., *et al.* Bone mineral density and fracture risk in type-2 diabetes mellitus: The Rotterdam Study. *Osteoporos. Int.* **16,** 1713–1720 (2005).
3. Vestergaard, P. Discrepancies in bone mineral density and fracture risk in patients with type 1 and type 2 diabetes - A meta-analysis. *Osteoporos. Int.* **18,** 427–444 (2007).
4. Janghorbani, M., Van Dam, R. M., Willett, W. C. & Hu, F. B. Systematic review of type 1 and type 2 diabetes mellitus and risk of fracture. *Am. J. Epidemiol.* **166,** 495–505 (2007).
5. Bonds, D. E., Larson, J. C., Schwartz, A. V., *et al.* Risk of Fracture in Women with Type 2 Diabetes: the Women's Health Initiative Observational Study. *J Clin Endocrinol Metab* **91,** 3404–3410 (2006).
6. Schwartz, A. V, Sellmeyer, D. E., Ensrud, K. E., *et al.* Older women with diabetes have an increased risk of fracture: a prospective study. *J. Clin. Endocrinol. Metab.* **86,** 32–38 (2001).
7. Hunt, H. B. & Donnelly, E. Bone Quality Assessment Techniques: Geometric, Compositional, and Mechanical Characterization from Macroscale to Nanoscale. *Clin. Rev. Bone Miner. Metab.* **14,** 133–149 (2016).
8. McCarthy, A. D., Etcheverry, S. B., Bruzzone, L., *et al.* Non-enzymatic

glycosylation of a type I collagen matrix: effects on osteoblastic development and oxidative stress. *BMC Cell Biol.* **2,** 16 (2001).

9. Katayama, Y., Akatsu, T., Yamamoto, M., Kugai, N. & Nagata, N. Role of nonenzymatic glycosylation of type I collagen in diabetic osteopenia. *J. Bone Miner. Res.* **11,** 931–937 (2009).

10. Terada, M., Inaba, M., Yano, Y., *et al.* Growth-inhibitory effect of a high glucose concentration on osteoblast-like cells. *Bone* **22,** 17–23 (1998).

11. Pedrazzoni, M., Ciotti, G., Pioli, G., *et al.* Osteocalcin levels in diabetic subjects. *Calcif. Tissue Int.* **45,** 331–336 (1989).

12. Dobnig, H., Piswanger-Sölkner, J. C., Roth, M., *et al.* Type 2 Diabetes Mellitus in Nursing Home Patients: Effects on Bone Turnover, Bone Mass, and Fracture Risk. *J. Clin. Endocrinol. Metab.* **91,** 3355–3363 (2006).

13. Shu, A., Yin, M. T., Stein, E., *et al.* Bone structure and turnover in type 2 diabetes mellitus. *Osteoporos. Int.* **23,** 635–641 (2012).

14. Akin, O., Göl, K., Aktürk, M. & Erkaya, S. Evaluation of bone turnover in postmenopausal patients with type 2 diabetes mellitus using biochemical markers and bone mineral density measurements. *Gynecol. Endocrinol.* **17,** 19–29 (2003).

15. Gerdhem, P., Isaksson, A., Åkesson, K. & Obrant, K. J. Increased bone density and decreased bone turnover, but no evident alteration of fracture susceptibility in elderly women with diabetes mellitus. *Osteoporos. Int.* **16,** 1506–1512 (2005).

16. Farr, J. N., Drake, M. T., Amin, S., *et al.* In vivo assessment of bone quality in

postmenopausal women with type 2 diabetes. *J. Bone Miner. Res.* **29,** 787–795 (2014).

17. Krakauer, J. C., McKenna, M. J., Buderer, N. F., *et al.* Bone loss and bone turnover in diabetes. *Diabetes* **44,** 775–782 (1995).

18. Osima, M., Kral, R., Borgen, T. T., *et al.* Women with type 2 diabetes mellitus have lower cortical porosity of the proximal femoral shaft using low-resolution CT than nondiabetic women, and increasing glucose is associated with reduced cortical porosity. *Bone* **97,** 252–260 (2017).

19. Clowes, J. A., Allen, H. C., Prentis, D. M., Eastell, R. & Blumsohn, A. Octreotide Abolishes the Acute Decrease in Bone Turnover in Response to Oral Glucose. *J. Clin. Endocrinol. Metab.* **88,** 4867–4873 (2003).

20. Thrailkill, K. M., Lumpkin, C. K., Bunn, R. C., Kemp, S. F. & Fowlkes, J. L. Is insulin an anabolic agent in bone? Dissecting the diabetic bone for clues. *Am. J. Physiol. Endocrinol. Metab.* **289,** E735-45 (2005).

21. Lecka-Czernik, B. Safety of Antidiabetic Therapies on Bone. *Clin. Rev. Bone Miner. Metab.* **11,** 49–58 (2013).

22. Stolk, R. P., Van Daele, P. L. A., Pols, H. A. P., *et al.* Hyperinsulinemia and Bone Mineral Density in an Elderly Population: The Rotterdam Study. *Bone* **18,** 545–549 (1996).

23. Saito, M., Fujii, K., Mori, Y. & Marumo, K. Role of collagen enzymatic and glycation induced cross-links as a determinant of bone quality in spontaneously diabetic WBN/Kob rats. *Osteoporos. Int.* **17,** 1514–1523 (2006).

24. Vashishth, D., Gibson, G. J., Khoury, J. I., *et al.* Influence of nonenzymatic glycation on biomechanical properties of cortical bone. *Bone* **28,** 195–201 (2001).

25. Tang, S. Y., Zeenath, U. & Vashishth, D. Effects of non-enzymatic glycation on cancellous bone fragility. *Bone* **40,** 1144–1151 (2007).

26. Yamagishi, S.-I. Role of advanced glycation end products (AGEs) and receptor for AGEs (RAGE) in vascular damage in diabetes. *EXG* **46,** 217–224 (2011).

27. Alikhani, M., Alikhani, Z., Boyd, C., *et al.* Advanced glycation end products stimulate osteoblast apoptosis via the MAP kinase and cytosolic apoptotic pathways. *Bone* **40,** 345–353 (2007).

28. Melton, L. J., Riggs, B. L., Leibson, C. L., *et al.* A bone structural basis for fracture risk in diabetes. *J. Clin. Endocrinol. Metab.* **93,** 4804–4809 (2008).

29. Burghardt, A. J., Issever, A. S., Schwartz, A. V., *et al.* High-resolution peripheral quantitative computed tomographic imaging of cortical and trabecular bone microarchitecture in patients with type 2 diabetes mellitus. *J. Clin. Endocrinol. Metab.* **95,** 5045–5055 (2010).

30. Yu, E. W., Putman, M. S., Derrico, N., *et al.* Defects in cortical microarchitecture among African-American women with type 2 diabetes. *Osteoporos Int* **26,** 673–679 (2015).

31. Patsch, J. M., Burghardt, A. J., Yap, S. P., *et al.* Increased Cortical Porosity in Type-2 Diabetic Postmenopausal Women with Fragility Fractures. *J. Bone Miner. Res.* **28,** 313–324 (2013).

32. Karim, L., Moulton, J., Van Vliet, M., *et al.* Bone microarchitecture,

biomechanical properties, and advanced glycation end-products in the proximal femur of adults with type 2 diabetes. *Bone* **114,** 32–39 (2018).

33. Kawashima, Y., Fritton, J. C., Yakar, S., *et al.* Type 2 diabetic mice demonstrate slender long bones with increased fragility secondary to increased osteoclastogenesis. *Bone* **44,** 648–55 (2009).

34. Reinwald, S., Peterson, R. G., Allen, M. R. & Burr, D. B. Skeletal changes associated with the onset of type 2 diabetes in the ZDF and ZDSD rodent models. *Am. J. Physiol. Endocrinol. Metab.* **5120,** 765–774 (2009).

35. Zhang, L., Liu, Y., Wang, D., *et al.* Bone biomechanical and histomorphometrical investment in type 2 diabetic Goto-Kakizaki rats. *Acta Diabetol.* **46,** 119–126 (2009).

36. Nyman, J. S. Effect of diabetes on the fracture resistance of bone. *Clin. Rev. Bone Miner. Metab.* **11,** 38–48 (2013).

37. Prisby, R. D., Swift, J. M., Bloomfield, S. A., Hogan, H. A. & Delp, M. D. Altered bone mass, geometry and mechanical properties during the development and progression of type 2 diabetes in the Zucker diabetic fatty rat. *J. Endocrinol.* **199,** 379–388 (2008).

38. Oren, T. W., Botolin, S., Williams, A., Bucknell, A. & King, K. B. Arthroplasty in veterans: analysis of cartilage, bone, serum, and synovial fluid reveals differences and similarities in osteoarthritis with and without comorbid diabetes. *J. Rehabil. Res. Dev.* **48,** 1195–210 (2011).

39. Pritchard, J. M., Papaioannou, A., Tomowich, C., *et al.* Bone mineralization is elevated and less heterogeneous in adults with type 2 diabetes and

osteoarthritis compared to controls with osteoarthritis alone. *Bone* **54,** 76–82 (2013).

40. Hammond, M. A., Gallant, M. A., Burr, D. B. & Wallace, J. M. Nanoscale changes in collagen are reflected in physical and mechanical properties of bone at the microscale in diabetic rats. *Bone* **60,** 26–32 (2014).

41. Creecy, A., Uppuganti, S., Merkel, A. R., *et al.* Changes in the Fracture Resistance of Bone with the Progression of Type 2 Diabetes in the ZDSD Rat. *Calcif. Tissue Int.* **99,** 289–301 (2016).

42. Hunt, H. B., Pearl, J. C., Diaz, D. R., King, K. B. & Donnelly, E. Bone Tissue Collagen Maturity and Mineral Content Increase With Sustained Hyperglycemia in the KK-Ay Murine Model of Type 2 Diabetes. *J. Bone Miner. Res.* **33,** 921–929 (2017).

43. Karim, L., Tang, S. Y., Sroga, G. E. & Vashishth, D. Differences in non-enzymatic glycation and collagen cross-links between human cortical and cancellous bone. *Osteoporos. Int.* **24,** 2441–2447 (2013).

44. Dehring, K. A., Crane, N. J., Smukler, A. R., *et al.* Identifying chemical changes in subchondral bone taken from murine knee joints using raman spectroscopy. *Appl. Spectrosc.* **60,** 1134–1141 (2006).

45. Boskey, A. L., Pleshko, N., Doty, S. & Mendelsohn, R. Applications of fourier transform infared microscopy to the study of mineralization in bone and cartilage. *Cells Mater.* **2,** (1992).

46. Taylor, E. A., Lloyd, A. A., Salazar-Lara, C. & Donnelly, E. L. Raman and FT-IR mineral to matrix ratios correlate with physical chemical properties of

model compounds and native bone tissue. *Appl. Spectrosc.* **0,** 000370281770928 (2017).

47. Paschalis, E. P., Verdelis, K., Doty, S. B., *et al.* Spectroscopic characterization of collagen cross-links in bone. *J. Bone Miner. Res.* **16,** 1821–1828 (2001).

48. Paschalis, E. P., Gamsjaeger, S., Tatakis, D. N., *et al.* Fourier transform infrared spectroscopic characterization of mineralizing type i collagen enzymatic trivalent cross-links. *Calcif. Tissue Int.* **96,** 18–29 (2014).

49. Pleshko, N., Boskey, A. & Mendelsohn, R. Novel infrared spectroscopic method for the determination of crystallinity of hydroxyapatite minerals. *Biophys. J.* **60,** 786–793 (1991).

50. Ou-Yang, H., Paschalis, E. P., Mayo, W. E., Boskey, a L. & Mendelsohn, R. Infrared microscopic imaging of bone: spatial distribution of CO3(2-). *J. Bone Miner. Res.* **16,** 893–900 (2001).

51. Spevak, L., Flach, C. R., Hunter, T., Mendelsohn, R. & Boskey, A. Fourier transform infrared spectroscopic imaging parameters describing acid phosphate substitution in biologic hydroxyapatite. *Calcif. Tissue Int.* **92,** 418–428 (2013).

52. Ibrahim, M., Alaam, M., El-Haes, H., Jalbout, A. F. & Leon, A. de. Analysis of the structure and vibrational spectra of glucose and fructose. *Eclética Química* **31,** 15–21 (2006).

53. Roy, R., Boskey, A. & Bonassar, L. J. Processing of type I collagen gels using nonenzymatic glycation. *J. Biomed. Mater. Res. - Part A* **93,** 843–851 (2010).

54. Saito, M., Fujii, K. & Marumo, K. Degree of mineralization-related collagen crosslinking in the femoral neck cancellous bone in cases of hip fracture and

controls. *Calcif. Tissue Int.* **79,** 160–168 (2006).

55. Bank, R. A., Beekman, B., Verzijl, N., *et al.* Sensitive fluorimetric quantitation of pyridinium and pentosidine crosslinks in biological samples in a single high-performance liquid chromatographic run. *J. Chromatogr. B Biomed. Appl.* **703,** 37–44 (1997).

56. Bank, R. A., Jansen, E. J., Beekman, B. & te Koppele, J. M. Amino acid analysis by reverse-phase high-performance liquid chromatography: improved derivatization and detection conditions with 9-fluorenylmethyl chloroformate. *Anal. Biochem.* **240,** 167–76 (1996).

57. Akaike, H. A new look at the statistical model identification. *IEEE Trans. Automat. Contr.* **19,** 716–723 (1974).

58. Cavanaugh, J. E. Unifying the derivations for the Akaike and corrected Akaike information criteria. *Stat. Probab. Lett.* **33,** 201–208 (1997).

59. Rho, J. Y., Hobatho, M. C. & Ashman, R. B. Relations of mechanical properties to density and CT numbers in human bone. *Med. Eng. Phys* **17,** 347–355 (1995).

60. Hernandez, C. J. & Keaveny, T. M. A biomechanical perspective on bone quality. *Bone* **39,** 1173–1181 (2006).

61. Carter, D. R. & Hayes, W. C. The Compressive Behavior of Bone as a Two-Phase Porous Structure. *J. Bone Jt. Surg.* **59–A,** 954–962 (1977).

62. Hernandez, C. J., Beaupré, G. S., Keller, T. S. & Carter, D. R. The influence of bone volume fraction and ash fraction on bone strength and modulus. *Bone* **29,** 74–78 (2001).

63. McNerny, E. M. B., Gong, B., Morris, M. D. & Kohn, D. H. Bone fracture toughness and strength correlate with collagen cross-link maturity in a dose-controlled lathyrism mouse model. *J. Bone Miner. Res.* **30,** 455–464 (2015).

64. Banse, X., Sims, T. J. & Bailey, A. J. Mechanical properties of adult vertebral cancellous bone: correlation with collagen intermolecular cross-links. *J. bone Miner. Res.* **17,** 1621–8 (2002).

65. Currey, J. D. The Mechanical Consequences of Variations in the Mineral Content of Bone. *J. Biomech.* **2,** 1–11 (1969).

66. Paschalis, E. P., Betts, F., DiCarlo, E., Mendelsohn, R. & Boskey, A. L. FTIR microspectroscopic analysis of normal human cortical and trabecular bone. *Calcif. Tissue Int.* **61,** 480–6 (1997).

67. Addadi, L. & Weiner, S. Control and Design Principles in Biological Mineralization. *Angew. Chemie Int. Ed. English* **31,** 153–169 (1992).

68. Yang, X., Mostafa, A. J., Appleford, M., Sun, L.-W. & Wang, X. Bone Formation is Affected by Matrix Advanced Glycation End Products (AGEs) In Vivo. *Calcif. Tissue Int.* **99,** 373–383 (2016).

69. Avery, N. C. & Bailey, A. J. Enzymic and non-enzymic cross-linking mechanisms in relation to turnover of collagen: Relevance to aging and exercise. *Scand. J. Med. Sci. Sport.* **15,** 231–240 (2005).

70. Almora-Barrios, N., Austen, K. F. & de Leeuw, N. H. Density Functional Theory Study of the Binding of Glycine, Proline, and Hydroxyproline to the Hydroxyapatite (0001) and ($01\bar{1}0$) Surfaces. *Langmuir* **25,** 5018–5025 (2009).

71. Stock, S. R. The Mineral–Collagen Interface in Bone. *Calcif. Tissue Int.* **97,**

262–280 (2015).

72. Nilsson, A. G., Sundh, D., Johansson, L., *et al.* Type 2 Diabetes Mellitus Is Associated With Better Bone Microarchitecture But Lower Bone Material Strength and Poorer Physical Function in Elderly Women: A Population-Based Study. doi:10.1002/jbmr.3057

73. Leslie, W. D., Aubry-Rozier, B., Lamy, O. & Hans, D. TBS (Trabecular Bone Score) and Diabetes-Related Fracture Risk. *J. Clin. Endocrinol. Metab.* **98,** 602–609 (2013).

74. Dhaliwal, R., Cibula, D., Ghosh, C., Weinstock, R. S. & Moses, A. M. Bone quality assessment in type 2 diabetes mellitus. *Osteoporos. Int.* **25,** 1969–1973 (2014).

75. Bousson, V., Bergot, C., Sutter, B., *et al.* Trabecular bone score (TBS): available knowledge, clinical relevance, and future prospects. *Osteoporos. Int.* **23,** 1489–1501 (2012).

76. Karim, L. & Vashishth, D. Role of trabecular microarchitecture in the formation, accumulation, and morphology of microdamage in human cancellous bone. *J. Orthop. Res.* **29,** 1739–1744 (2011).

77. Turner, C. H. On Wolff's law of trabecular architecture. *J. Biomech.* **25,** 1–9 (1992).

78. Ritchie, R. O. The conflicts between strength and toughness. *Nat. Mater.* **10,** 817–822 (2011).

79. Currey, J. D. D. Effects of differences in mineralization on the mechanical properties of bone. *Philos. Trans. R. Soc. Lond. B. Biol. Sci.* **304,** 509–18

(1984).

80. Holzer, G., Von Skrbensky, G., Holzer, L. A. & Pichl, W. Hip fractures and the contribution of cortical versus trabecular bone to femoral neck strength. *J. Bone Miner. Res.* **24,** 468–474 (2009).

81. Wallander, M., Axelsson, K. F., Nilsson, A. G., Lundh, D. & Lorentzon, M. Type 2 Diabetes and Risk of Hip Fractures and Non-Skeletal Fall Injuries in the Elderly: A Study From the Fractures and Fall Injuries in the Elderly Cohort (FRAILCO). *J. Bone Miner. Res.* **32,** 449–460 (2017).

82. Moseley, K. F. Type 2 diabetes and bone fractures. *Curr. Opin. Endocrinol. Diabetes. Obes.* **19,** 128–35 (2012).

83. Li, B. & Aspden, R. M. Composition and mechanical properties of cancellous bone from the femoral head of patients with osteoporosis or osteoarthritis. *J. Bone Miner. Res.* **12,** 641–51 (1997).

84. Boskey, A. L., DiCarlo, E., Paschalis, E., West, P. & Mendelsohn, R. Comparison of mineral quality and quantity in iliac crest biopsies from high- and low-turnover osteoporosis: an FT-IR microspectroscopic investigation. *Osteoporos. Int.* **16,** 2031–8 (2005).

5.8 ***Supplemental***

S1: Decalcification of Cancellous Tissue for FTIR Analyses

The cancellous tissue allocated for analysis of the sugar:matrix ratio was demineralized using a 9.5% ethylene diamine tetra-acetic acid (EDTA) solution in phosphate-buffered saline. The tissue was submerged in the EDTA solution for five days at 4 ˚C, with a solution change every 24 hours. After five days, the demineralized tissue was rinsed twice with acetone for 10 minutes, then rinsed twice with deionized water for 10 minutes. The demineralized tissue was lyophilized, powdered using a cryomill, and pressed into a pellet with a tissue:KBr ratio of 1:100.

S2: Normalization of Mechanical Properties by Bone Volume Fraction

Linear[59,60] and power law[61,62] relationships were assessed to determine, and ultimately account for, the influence of BV/TV on mechanical properties. Linear relationships were determined by performing univariate linear regressions between the mechanical properties (Young's modulus, yield stress, post-yield toughness, toughness) as the dependent variable and BV/TV as the independent variable. Power law relationships were assessed by performing univariate linear regressions on logarithmically transformed mechanical properties and BV/TV. The resulting coefficients of determination (R^2) were compared for the linear and the log transformed regressions. The interaction of group and BV/TV was also evaluated for the linear and power law relationships to ascertain if there was a group-dependent effect of BV/TV on mechanical properties.

The power law relationships between BV/TV and yield stress, ultimate stress, post-yield toughness, and toughness had higher coefficient of determinations compared to the linear relationships; however, using a power law relationship only explained up to 7% more of the observed variation in the aforementioned mechanical properties with BV/TV. Moreover, a power law relationship decreased the explained variance of BV/TV with Young's modulus compared to a linear relationship. We opted to use a linear normalization of mechanical properties with BV/TV because of the marginal difference in explanatory power between linear and power law relationships and for simplicity.

There was a group-dependent effect of BV/TV on Young's modulus, yield stress, and ultimate stress (BV/TV*Group: all $p < 0.05$); however, this group different became insignificant when other compositional variables were included in the models (i.e., mineral:matrix ratio).

Supplemental Table S1: Coefficients for linear and power law regressions of mechanical properties with BV/TV. The coefficient of determination (R^2) is shown.

Regressed on BV/TV	Linear Relationship to BV/TV			Power Law Relationship to BV/TV		
	Slope	Intercept	R^2	Slope	Intercept	R^2
Young's Modulus (MPa)	58.20	-390.74	0.796	1.91	0.77	0.731
Yield Stress (MPa)	0.41	-2.98	0.702	2.01	-4.54	0.727
Ultimate Stress (MPa)	0.61	-4.77	0.748	1.89	-3.87	0.766
Post-yield Toughness (kPa)	6.98	-60.62	0.591	2.01	-1.95	0.664
Toughness to (kPa)	9.29	-77.79	0.634	1.96	-1.46	0.696

S3: Tertiles of Mineral:Matrix Ratio

Mineral:matrix ratio had a large influence on stress, which also affects toughness. To show the effect of mineral content on mechanical properties after the normalization by BV/TV, we created tertiles of the mineral:matrix ratio to designate groups in the lower, middle, and upper thirds of mineral content. There were more specimens in the lower tertile from the non-DM group than the T2DM group (non-DM: 88%; T2DM: 12%), and there were more specimens in the upper tertile from the T2DM group than the non-DM group (T2DM: 75%; non-DM: 25%) as determined by Chi-squared test ($p < 0.05$).

Tertiles of mineral:matrix are shown in Figure S3 to 1) show that specimens with high mineral:matrix values also had greater stiffness, strength, and toughness; and 2) that most of the specimens with high mineral:matrix values were in the T2DM group.

S4: Rationale for PCA and Description of MMF

The rationale for performing PCA on compositional variables was to reduce the collinearity of variables used in the stepwise regression modeling. Thus, we performed PCA out of mathematical necessity rather than to propose a new metric to describe bone quality.

To simplify related variables to explain how mineral maturity influences mechanical properties, we developed the Mineral Maturity Factor (MMF). The MMF consists of three closely related, independently validated constituent variables

(crystallinity,[49] carbonate:phosphate ratio,[50] acid phosphate content[51]). Moreover, all three variables are strongly and linearly correlated with each other, and all three variables indicate the maturity of the mineral crystals in bone in slightly different ways. To avoid a high collinearity of predictor variables and overfitting, we could not include all three variables in the stepwise linear regression models. Therefore, our options were to 1) make a factor with all three variables, or 2) choose a single mineral characteristic to include. We chose to use a factor to describe these three related mineral characteristics.

Importantly, the constituent variables in the MMF have also been reported as evidence of changes in bone quality with T2DM (crystallinity, type 2 diabetic mouse model[42]) and other pathologies that affect bone fragility (carbonate:phosphate ratio and acid phosphate content, low and high turnover bone[84]).

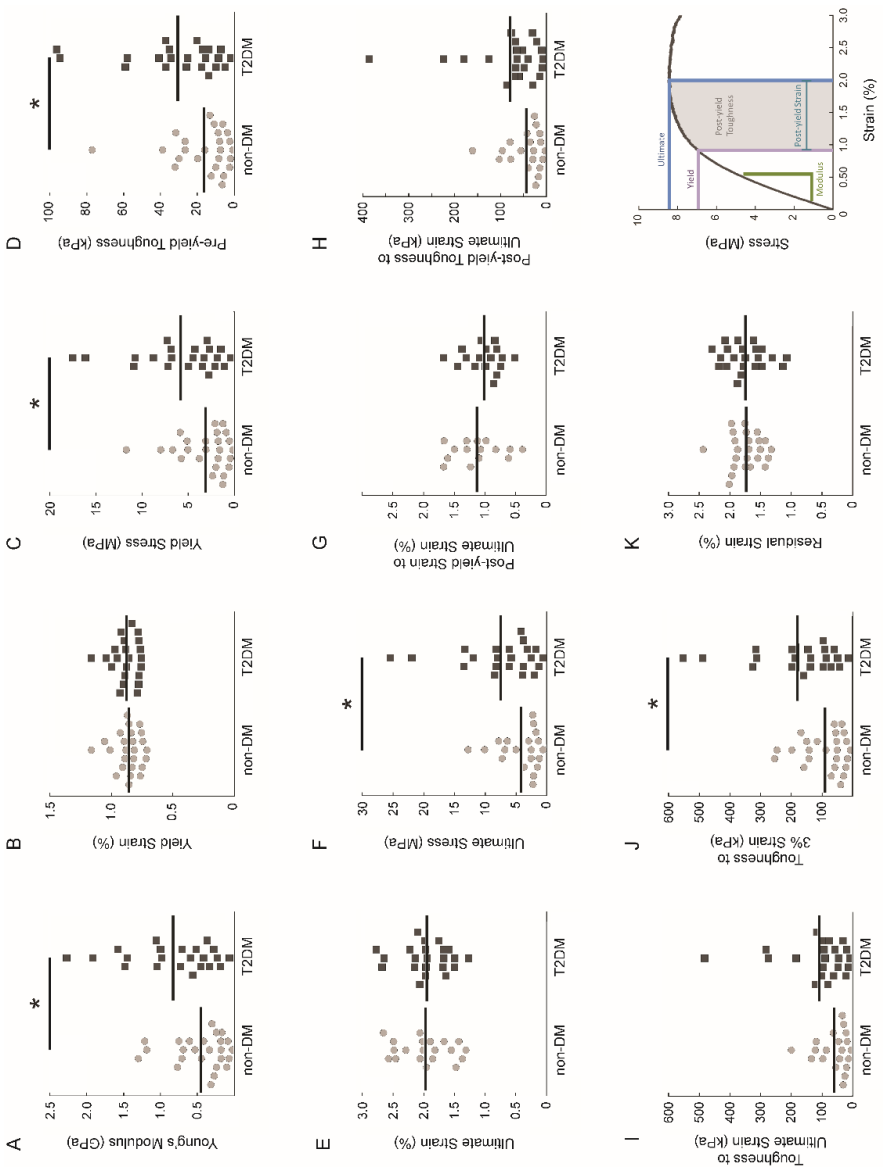

Supplemental Figure S1: Mechanical properties from monotonic compression testing of cancellous specimens by group. The T2DM group include two specimens from men who were on TZDs and were excluded from the analysis in the main manuscript. Abbreviations: non-DM: non-diabetic group; T2DM: type 2 diabetic group.

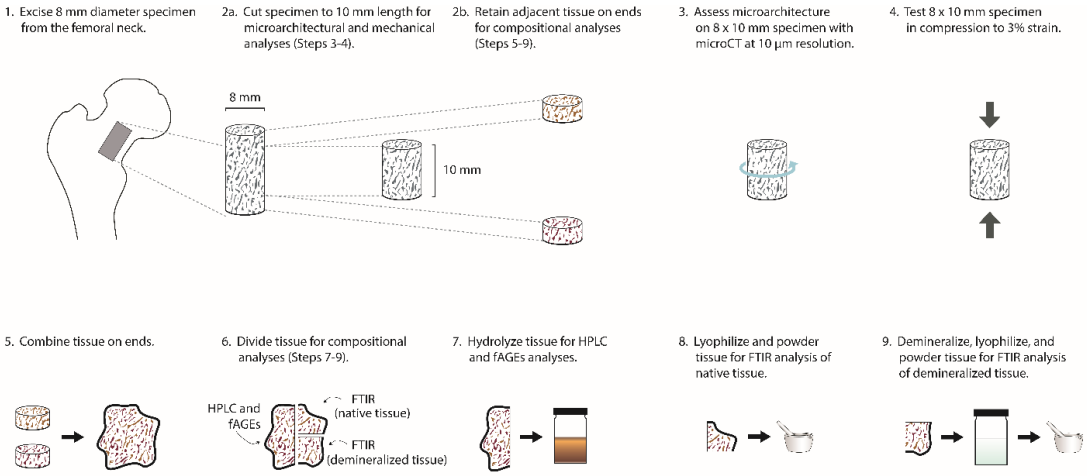

Supplemental Figure S2: Methods overview.

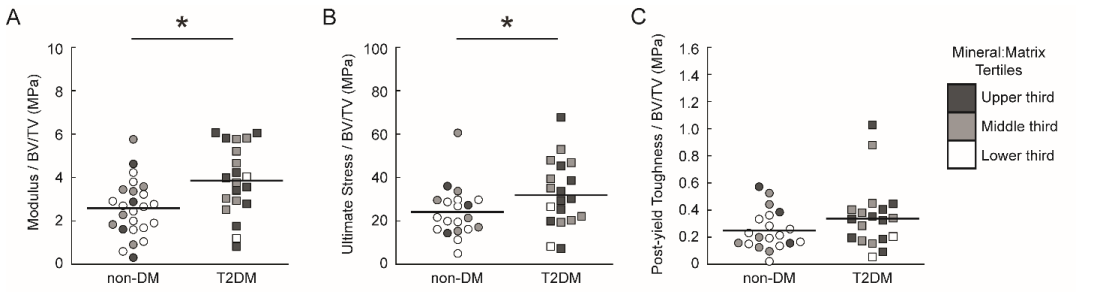

Supplemental Figure S3: (A) Young's modulus normalized by BV/TV, (B) Ultimate stress normalized by BV/TV, and (C) Post-yield toughness normalized by BV/TV. Horizontal lines indicate group means. Mineral:matrix data (Figure 5.3-1C) were used to divide the 65 FTIR samples (both DM and non-DM groups) into tertiles of lower (white squares), middle (light grey squares), and upper (dark grey squares) (see Supplemental S3). Abbreviations: non-DM: non-diabetic group, T2DM: type 2 diabetic group; BV/TV: bone volume fraction.

CHAPTER 6

SUMMARY, CONCLUSIONS, AND RECOMMENDATIONS FOR FURTHER STUDY

6.1 *Summary of Key Results*

The main objectives of this research were 1) to elucidate the material factors that may contribute to whole-bone fragility with T2DM by characterizing the material properties, microarchitecture, and bulk-tissue mechanical properties of bone from subjects with and without T2DM, and 2) to relate material changes to the pathophysiology of T2DM. The properties of bone tissue from a rodent model and two clinical populations of T2DM were evaluated.

In Chapter 2, measurement techniques available to assess the geometric, compositional, and mechanical properties of tissue were discussed, as well as how the technique is currently being used or can be used in the near future. Several of the techniques discussed were used to evaluate bone tissue in Chapters 3-5, including FTIR in Chapters 3, 4, and 5, and apparent-level mechanical testing, micro-CT, and HPLC in Chapter 5.

In Chapter 3, the compositional characteristics of bone in the KK-Ay mouse were characterized. Overt T2DM manifests in KK-Ay mice around eight weeks of age as a result of insulin resistance; therefore, the KK-Ay mouse exhibits an essential feature of T2DM in humans. In the KK-Ay mice with overt T2DM, we observed changes in tissue-level material properties, including increased mean collagen

maturity and mineral content in the KK-Ay mice compared to littermate non-DM controls. Greater mean collagen maturity and greater mean mineral content are both consistent with older tissue and with previous documentation of reduced bone turnover with T2DM.

In Chapter 4, the composition of iliac crest bone from post-menopausal women with varying degrees of glycemic derangement was characterized using FTIR imaging. We found evidence of altered mineral and collagen properties between normal glucose tolerance, impaired glucose tolerance, and overt T2DM groups. In general, glycemic derangement was associated with increased mineral content, decreased collagen maturity, and atypical mineral maturation. A more mineralized tissue and a less mature organic matrix can both deleteriously affect bone mechanics at the tissue level; however, the precise underlying causes for these changes in tissue composition and the resulting macro-scale consequences to bone fragility are unknown. We also observed progressive changes in tissue composition from normal glucose tolerance to impaired glucose tolerance to overt T2DM, though these differences were not always statistically significant. Serum analyses indicated that the T2DM group had lower markers of bone turnover than the normal glucose tolerance group.

In Chapter 5, the structure, composition, and mechanical properties of bulk cancellous tissue from the femoral neck of men were assessed. These results were subsequently used in statistical models to better understand how changes in the structure and composition of bone due to T2DM impact bulk tissue-level mechanical performance. We found clear evidence of AGE accumulation, increased mineral content, and atypical mineral maturation in the specimens from the T2DM group

compared to the non-DM group. Our regression models indicated that bone volume fraction was by far the greatest determinant of compressive mechanical properties, as expected. After accounting for the greater bone volume fraction in the T2DM group, the models demonstrated how AGE accumulation and altered mineral maturity can drastically reduce the ability of cancellous bone to absorb energy prior to failure in patients with T2DM.

6.2 *Conclusions*

The compositional assessment of tissue from the KK-Ay mouse model and from both clinical populations confirmed increased mineral content with T2DM. Greater mineral content is indicative of older tissue (i.e., time since formation)[1] and is associated with a stronger, but more brittle material.[2,3] Furthermore, the lower bone turnover rates that are observed with T2DM[4–9] may help explain our observations of more mineralized tissue across these populations.

Conversely, the rodent model tissue and the clinical tissue showed different effects of T2DM on collagen maturity and mineral maturity. In general, more mature collagen has a higher ratio of divalent to trivalent enzymatic crosslinks, and more mature mineral typically has larger, more perfect crystal, and these maturations processes are contemporaneous. The whole proximal femora of the KK-Ay mice had 7% more mature collagen and a 24% narrower distribution of crystallinity, both of which are consistent with a more mature, or older, tissue. In contrast, tissue from the iliac crest of post-menopausal women with T2DM versus those with normal glucose tolerance had similar collagen maturities, but a 16% wider distribution of crystallinity,

which indicates a less mature mineral, but unchanged collagen maturity, with T2DM. The distributions of compositional properties were not assessed in the tissue from Chapter 5 (cancellous femoral neck tissue from men with and without T2DM) because this tissue was homogenized; however, the T2DM specimens in this cohort had a lower mineral maturity factor (factor that includes crystallinity, carbonate:phosphate ratio, and acid phosphate content) than the non-DM specimens. In summary, the mineral was more mature in the KK-Ay mouse model of T2DM versus controls, but less mature in the clinical human tissue from people with T2DM versus those without T2DM, and collagen maturity was different in the tissue of the KK-Ay mice vs. controls, but similar across groups in the human tissue. These discrepancies point to different effects of T2DM on the mineral and matrix components of bone.

The discrepancy of greater mineral content without an increase in mineral maturity in the human tissue is particularly surprising, and it is likely that multiple pathological factors are responsible. One potential factor is that hyperglycemia leads to greater AGE accumulation.[10] Hyperglycemic conditions and AGE accumulation have been shown to decrease osteoblast and osteoclast function;[11–14] therefore, hyperglycemia and AGE accumulation may work in concert to disrupt bone turnover. Slower turnover may account for the increased tissue mineral content because older tissue that is not remodeled will be more mineralized than younger tissue. In addition to lower turnover caused by AGE-cell interactions, AGE accumulation may also inherently alter the mineralization process and rates[15][16] by changing the charge profile of the collagen fibers,[17,18] thereby disrupting cell-matrix interactions that control mineral maturation.[19,20]

On the other hand, the differences in the effects of T2DM on rodent tissue compared to human tissue may lie in the different mechanisms by which bone grows and is turned over. Mice continue to grow after sexual maturity (~ 6-8 weeks of age) and they reach peak bone mass around 4-6 months of age, which is markedly different than human bone growth which ceases with sexual maturity.[21] In addition, mice do not have osteons; therefore, the osteonal remodeling observed in human cortical bone is not possible. Turnover in cancellous bone occurs similarly in both mice and humans; however, the rate at which murine cancellous bone remodels is roughly 10 times faster than that of humans.[21] In this light, the differences observed in collagen maturity between the KK-Ay murine tissue and human tissue may be due to the variations in turnover. Specifically, it takes weeks to months for AGEs to fully form;[22] therefore, murine bone may not age long enough for high concentrations of AGEs to accumulate. While the time formation of AGEs in different species has not been fully explored, the anecdotal evidence that AGEs accumulate in rat and human tissue, but not in murine tissue, may indicate that tissue lifetime matters.

The precise pathological mechanism by which T2DM disrupts mineral and matrix maturation is presently unknown; however, the consequences of these changes are evidenced in Chapter 5 with the evaluation of mechanical performance of T2DM and non-DM human cancellous bone. The main finding of the Chapter 5 study was that bone volume fraction can compensate for suboptimal tissue material properties to a certain extent; however, in the absence of greater bone mass, the deleterious effects of T2DM on bone tissue can result in increased bone fragility. While the models generated in Chapter 5 with a small sample size are unlikely to be universally

applicable to all people with T2DM, this study was the first to comprehensively evaluate tissue mineral and matrix properties, including tissue AGE accumulation, in clinical specimens from people with T2DM. Moreover, it one of only two studies of clinical T2DM specimens that relates the compositional and microarchitectural changes to measured mechanical properties (the other was performed by Karim et. al. [23]).

The study presented in Chapter 4 regarding iliac crest tissue from post-menopausal women with varying degrees of glycemic control is also a novel contribution to the understanding of how the pathophysiology of T2DM changes the composition of bone. Specifically, the inclusion of three groups with progressive glucose intolerance allows for the determination of which compositional properties are affected between the normal glucose tolerance phase to the impaired glucose tolerance phase and then from the impaired glucose tolerance phase to the overt T2DM phase. Moreover, the measurement of bone turnover markers allows for the direct assessment of the hypothesis that altered bone turnover affects tissue composition.

6.3 *Statement of Impact*

Taken together, Chapters 3-5 contribute to the growing body of evidence that T2DM has deleterious consequences for the skeletal integrity of bone. The study of spontaneously diabetic KK-Ay mice compared to littermate controls (Chapter 3) is the first to characterize tissue composition in this particular mouse model of T2DM, which contributes to the evolving understanding of T2DM rodent model selection and T2DM tissue composition in general. The characterization of tissue composition from

three groups of women with varying degrees of glycemic control (normal glucose tolerance, impaired glucose tolerance, and overt T2DM) (Chapter 4) is the first to explicitly characterize tissue properties in an intermediate and pre-T2DM stage, which allows us to link glycemic control/the duration of T2Dm to changes in tissue properties. Also, this study is the first to characterize tissue composition in a spatially-resolved fashion from a clinical T2DM population. Finally, the collective compositional, microarchitectural, and mechanical assessment of bulk cancellous tissue from men with and without T2DM (Chapter 5) is the first study to directly correlate changes in tissue composition, including AGE accumulation, with mechanical performance in a clinical population with T2DM.

In summary, it is vital to assess tissue from populations with T2DM to 1) better understand how T2DM is detrimental to skeletal integrity, 2) better predict populations that are at a higher risk of experiencing fragility fractures based on their bone tissue characteristics, and 3) use these findings to eventually prevent T2DM-related fragility fractures.

6.4 *Strengths and Limitations*

One major strength of translational research is the ability to relate the results of laboratory experiments to clinical practice; however, research on clinical specimens has several unique limitations.

To begin, there is often a tradeoff in the extent of controllable cohort characteristics (e.g., the ability to age match between groups) and the usefulness of tissue available to study from the study participants. The tradeoffs between knowable

patient information and the traits of the excised tissue specimen is particularly exemplified in Chapters 4 and 5: The women in the clinical study detailed in Chapter 4 were specifically recruited such that a wide range of glycemic control (HbA1c ranged from 4.9 to 13.3%) was captured while maintaining an otherwise homogeneous population; however, the iliac crest biopsies were too small to perform many mechanical characterization assays, and the tissue was not from a clinically-relevant fracture site. On the other hand, little to no diabetic history was known for the men recruited for the study detailed in Chapter 5, who had better glycemic control (HbA1c ranged from 5.0 to 9.3%); however, the excised specimens were from a highly-relevant fracture site and there was a large quantity of tissue for a comprehensive characterization of compositional, structural, and mechanical properties.

Nevertheless, the study designs of Chapters 4 and 5 are complementary and 1) allow for a more comprehensive understanding of how T2DM affects bone tissue at different length scales and different sites, and 2) provide a framework for identifying factors that can mitigated the negative effects of T2DM on skeletal integrity. Moreover, the clinical studies described in Chapter 4 and 5 are two of five published studies that directly characterize tissue from people with T2DM (the other studies are: Pritchard. *J. Bone Miner. Res.* 2014; Farr. *J. Bone Miner. Res.* 2016; and Karim *Bone* 2018).

6.5 ***Recommendations for Further Study***

Because many aspects of the research discussed in this dissertation were the first steps of their kind towards understanding how T2DM affects bone tissue, there are many

potential avenues for future research that can build off these foundational results. In the succeeding section, I have outlined potential future studies that further explore the effects of T2DM on bone tissue, specifically regarding microdamage accumulation and the complex observations of mineral and matrix maturation.

The ability of bone to resist fracture is dependent upon the dissipation of energy throughout the bone matrix, and one key mechanism by which energy is dissipated is the formation and propagation of microdamage. Microdamage accumulates in both the cortical and cancellous compartments with age as a result of normal daily loads;[24] however, extensive damage induced through fatigue or a single overload events can also occur. Microdamage is categorized as either crack-like or diffuse from damage morphology, which is typically evaluated through staining. Crack-like microdamage appears with distinct edges and is associated with more brittle tissue that requires lower energies for damage to propagate, whereas diffuse microdamage has more of a pooled or muddled morphology (sometimes described as cross-hatched[25,26]) and is associated with a more ductile material that requires higher energies for damage to propagate.[27] In cancellous bone for example, crack-like microdamage accumulates along the more mineralized, stiffer, and older cores of trabeculae where the tissue is most brittle, and diffuse microdamage localizes along the less mineralized, less stiff, and younger trabecular edges.[28]

The presence of microdamage catalyzes the remodeling process to remove the old, damaged tissue and replace it with new, more structurally sound tissue.[29,30] The main trigger for microdamage removal is osteocyte apoptosis, and definitive casual links between osteocyte apoptosis and osteoclast recruitment to remove the damaged

tissue have been demonstrated.[31–33] Interestingly, osteocytes immediately surrounding the microdamaged tissue do not undergo apoptosis and instead express anti-apoptotic responses, such as the upregulation of RANKL and Bcl-2, to quickly recruit osteoclast precursors to the damaged area.[34] After the osteoclasts are recruited to the damaged site, the bone remodeling process continues with the subsequent recruitment of osteoblasts which then lay down new organic matrix.[29] From these processes, it is evident how excessive microdamage accumulation and/or disrupted microdamage removal can lead to a tissue with reduced mechanical integrity.

Under T2DM disease state conditions, it is possible that lower bone turnover (see Chapter 4 and references [4–9]) and AGE accumulation[11–14] can lead to more microdamage accumulation because the damaged tissue is not removed in a timely manner. Because the extent of microdamage is associated with reductions in stiffness and strength,[25,26,35,36] it is possible that the greater skeletal fragility observed in people with T2DM compared to those without[37–44] is a macro-scale mechanical consequence of micro-scale damage accumulation. In this framework, there are several avenues for the continuation of the work described in Chapters 4 and 5 to further elucidate the effects of T2DM on skeletal integrity, and they are briefly outlined here.

6.5.1 Proposed Study #1: Microdamage assessment in cancellous tissue from people with and without T2DM

Microdamage accumulation in cancellous bone from people with T2DM compared to those without has not yet been reported. Therefore, the main goals for this proposed

study are to evaluate the extent and type of microdamage in specimens from people with T2DM compared to those without T2DM, and if possible, to relate microdamage accumulation to the severity of T2DM. I hypothesize that there will more microdamage per unit volume of tissue in specimens from people with T2DM compared to those without T2DM, that worsening glycemic control will be associated with more microdamage, and that the microdamage in the T2DM specimens will exhibit more crack-like than diffuse microdamage.

In preparation for future microdamage quantification, the cancellous cores from both the T2DM and non-DM groups were stained with lead uranyl acetate (LUA) immediately after mechanical compression to 3% strain, then underwent secondary micro-CT scanning (see Appendix B for LUA staining methods). LUA is a bulk, double contrast, and heavy metal stain that infiltrates the void spaces in bone tissue and attaches to damaged areas.[36,45] When scanned with x-rays in micro-CT, the LUA complexes appears as bright white regions which distinctly indicates damage tissue along the contours of the native tissue. LUA staining and subsequent micro-CT assessment allows for 3-D quantification of microdamage that is not possible with most other microdamage staining assays.[36,46] Because existing damage prior to mechanical testing is not distinguishable from damaged induced during compression, T2DM and non-DM controls that were not mechanically tested, but were stained with LUA, should be used as a baseline value for pre-existing damage.

Post-processing of the micro-CT image stacks (currently ongoing) allows for assessment of the following outcome variables: damage volume per bone volume (DV/BV), which is the summation of volumetric damaged pixels over volumetric bone

pixels and therefore independent of bone volume fraction; damaged surface area per damaged volume (DS/DV), which is a surface-to-volume ratio of damage where higher DS/DV values indicate more crack-like damage and lower DS/DV values indicate more diffuse damage; and the distribution of DS/DV values across each damaged region, such that a wide distribution indicates a mix of crack-like and diffuse damage and a narrow distribution indicates more crack-like than diffuse character or vice versa.

In summary, the outcomes of this Proposed Study #1 will indicate whether or not tissue from people with T2DM have more microdamage than tissue from people without T2DM and the overall morphology of the microdamage (crack-like or diffuse) under single overload conditions. Preliminary results of the DV/BV for the T2DM and non-DM group specimens are provided in Appendix C.

6.5.2 Proposed Study #2: Trabecular morphology, microdamage, and mechanical performance

In addition to the quantification of BV/DV, BS/BV, and the distribution of BS/BV, another key question is whether or not microdamage is more likely to form on specific morphologies of trabeculae. In general for compressive loading, the plate-like trabeculae support the bulk of mechanical loads and are axially aligned with the principal stress, especially in the femur, whereas the rod-like trabeculae are oriented transverse to the principal stress and contribute less to stiffness and strength.[47,48] Thus, trabecular morphology, which plays a key role in mechanical performance and differs in cancellous bone from T2DM subjects vs. non-DM subjects,[49–52] may also

influence the location and extent of microdamage with T2DM. Therefore, the goals of this proposed study are to ascertain if microdamage outcomes (DV/BV, DS/DV) are related to trabecular morphology (plate vs. rod, orientation) and to deduce whether or not the location and type of microdamage are associated with mechanical outcomes in specimens from people with and without T2DM. I hypothesize that the rod-like trabeculae will accumulate more damage than plate-like trabeculae, especially in transversely- and obliquely-oriented rods, and that the thicker plates and rods (observed in tissue from people with T2DM vs. without T2DM, Chapter 5)[52] will have greater DV/BV in the T2DM vs. non-DM specimens.

The conventional measure to assess the rod-like or plate-like character of cancellous bone is the structure model index (SMI)[53] which ranges from a value of 0 to 3 indicating completely plate-like or rod-like, respectively, in an idealized structure.[54] SMI provides a simple, single value for how plate-like or rod-like a structure is; however, the algorithm for SMI assumes all trabecular surfaces are convex, which is almost certainly untrue for most cancellous bone specimens.[55] While many studies have reported associations between SMI and mechanical properties, it is likely that SMI is more of a surrogate for BV/TV than an indicator of rod-like or plate-like character.[55] Thus, a more detailed characterization of trabecular morphology is desired.

To this end, analysis using the Individual Trabecular Segmentation (ITS) software developed at Columbia University[56] has been begun on the specimens from Chapter 5. The ITS software is specifically designed for the isolation and classification of trabeculae into rod-like or plate-like and longitudinally-, horizontally-, or obliquely-

oriented and can be run on the same micro-CT image stacks of LUA-stained specimens. The ITS outcomes for each trabecula (i.e., plate or rod; longitudinal, transverse, or oblique; and all possible combinations thereof [e.g. longitudinal plates, oblique rods]) can then be correlated pixel by pixel to the microdamage determined through LUA staining. Figure 6.5-1 shows damaged tissue vs. undamaged tissue, plate-like vs. rod-like trabeculae, and longitudinal vs. transverse vs. oblique trabecular orientations on the same specimen.

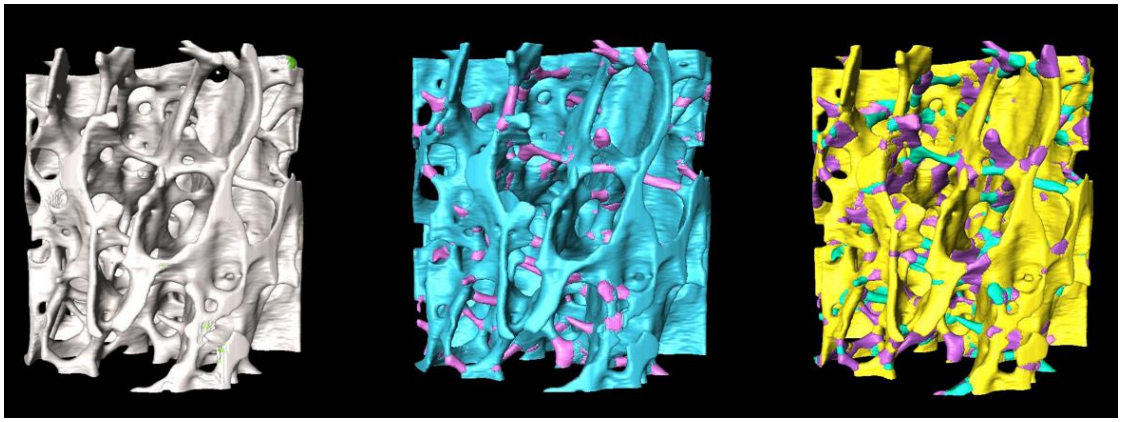

Figure 6.5-1: Left: Damaged pixels are denoted by bright green coloring. Center: Blue pixels denote plate-like trabeculae and magenta pixels denote rod-like trabeculae. Right: Yellow pixels denote longitudinal trabeculae, teal pixels denote transverse trabeculae, and purple pixels denote oblique trabeculae.

Essentially, the 3-D structure that depicts microdamage with LUA stain can be superimposed on the 3-D structure derived from ITS-assessed trabecular morphology to ultimately determine if there are differences in microdamage location between specimens from people with and without T2DM. Additionally, and arguably more importantly, this analysis will help determine if the confluence of microdamage

location and trabecular morphology better explains the compressive, monotonic mechanical properties than traditional microarchitecture outcomes alone in a population with T2DM.

Appendix C details the methods for ITS analysis on previously mechanically tested and LUA stained cancellous cores. A checklist detailing the ITS preparation steps that have already been performed on the Chapter 5 samples is in Appendix D. Preliminary ITS and microdamage results for a subset of specimens from the non-DM and T2DM groups are reported in Appendix E.

6.5.3 Proposed Study #3: Colocalization of AGEs, composition, mechanical properties, and tissue age with varying degrees of glycemic control

While the cancellous specimens described in Chapter 5 offer the ability to further study bulk cancellous tissue properties, the iliac crest specimens described in Chapter 4 will allow for further assessment of direct spatial comparison of AGE content, tissue composition, and mechanical properties at the micro-scale. Moreover, the study design of Chapter 4 included comprehensive characterization of the participant population, including T2DM severity and biomarkers of bone turnover, and double-labeling for bone formation. The main goals of this proposed study are to determine 1) if local regions of altered tissue composition are associated with diminished mechanical properties, and 2) if the former outcome is associated with T2DM severity. I hypothesize that regions of high AGE content will be associated with older tissue (determined bone formation double-labels), with regions of greater mineral content and greater collagen maturity (determined by FTIR imaging), and with greater

stiffness and hardness, but lower energy absorption (determined by mechanical testing). Furthermore, I hypothesize that the aforementioned associations between AGEs, tissue composition, and mechanical properties will be more pronounced with worsening glycemic control.

The FTIR image collection and analysis of specimens from women with NGT (n = 32, age = 65±7, HbA1c = 5.8±0.3), IGT (n = 25, age = 64±5, HbA1c = 6.0±0.4), and overt T2DM on insulin (n = 25, age = 64±6, HbA1c = 9.13±0.6) is complete (Chapter 4) and the biopsies have already been double-labeled for bone formation; therefore, the key remaining tasks are AGE assessment and mechanical testing. The locations of AGE accumulation on the same sections used for FTIR imaging can be determined by auto-fluorescence using a confocal microscope using 405/488 nm excitation/emission and an exposure time of 150 ms;[57] however, the sections may need to be demineralized beforehand to generate a strong enough fAGE signal.

The remainder of the biopsies that were not section for FTIR image analysis are currently embedded in PMMA, which makes nano-indentation the logical choice for mechanical assessment. The outcomes for nano-indentation are hardness; which is the average pressure under load and is calculated as the maximum load divided by the indentation contact area; reduced modulus, which includes contributions from both the specimen and the indenter and is calculated from the slope of the unloading portion of the force-displacement curve; and elastic modulus, which can be calculated from the reduced modulus, the Poisson's ratio of the specimen, and the material properties of the indenter.[58] Moreover, the capability for dynamic load- and displacement-control during nanoindentation allow acquisition of full force-displacement curves at the

micron scale. By performing multiple nano-indents in a gridded pattern along the same region of interest as the FTIR imaging, a 2-D map of mechanical properties across the specimen can be generated[59,60] and subsequently compared to the composition outcomes.

Finally, the FTIR imaging maps, the fAGE maps, and the nanoindentation maps can be compiled to assess the extent to which fAGEs and tissue compositional properties influence the mechanical properties in regions of new bone formation vs. older bone tissue as well as across NGT, IGT, and T2DM groups.

6.6 *Final Remarks*

In conclusion, this dissertation provides a foundation for studying the effects of T2DM on bone tissue in terms of compositional, microarchitectural, and mechanical properties and offers several opportunities for further investigation using available valuable clinical specimens.

6.7 *References*

1. Boskey, A. L., Pleshko, N., Doty, S. & Mendelsohn, R. Applications of fourier transform infared microscopy to the study of mineralization in bone and cartilage. *Cells Mater.* **2,** (1992).
2. Currey, J. D. The Mechanical Consequences of Variations in the Mineral Content of Bone. *J. Biomech.* **2,** 1–11 (1969).
3. Ritchie, R. O. The conflicts between strength and toughness. *Nat. Mater.* **10,** 817–822 (2011).
4. Pedrazzoni, M., Ciotti, G., Pioli, G., *et al.* Osteocalcin levels in diabetic subjects. *Calcif. Tissue Int.* **45,** 331–336 (1989).
5. Dobnig, H., Piswanger-Sölkner, J. C., Roth, M., *et al.* Type 2 Diabetes Mellitus in Nursing Home Patients: Effects on Bone Turnover, Bone Mass, and Fracture Risk. *J. Clin. Endocrinol. Metab.* **91,** 3355–3363 (2006).
6. Shu, A., Yin, M. T., Stein, E., *et al.* Bone structure and turnover in type 2 diabetes mellitus. *Osteoporos. Int.* **23,** 635–641 (2012).
7. Akin, O., Göl, K., Aktürk, M. & Erkaya, S. Evaluation of bone turnover in postmenopausal patients with type 2 diabetes mellitus using biochemical markers and bone mineral density measurements. *Gynecol. Endocrinol.* **17,** 19–29 (2003).
8. Gerdhem, P., Isaksson, A., Åkesson, K. & Obrant, K. J. Increased bone density and decreased bone turnover, but no evident alteration of fracture susceptibility in elderly women with diabetes mellitus. *Osteoporos. Int.* **16,** 1506–1512

(2005).

9. Farr, J. N., Drake, M. T., Amin, S., *et al.* In vivo assessment of bone quality in postmenopausal women with type 2 diabetes. *J. Bone Miner. Res.* **29,** 787–795 (2014).

10. Vashishth, D., Gibson, G. J., Khoury, J. I., *et al.* Influence of nonenzymatic glycation on biomechanical properties of cortical bone. *Bone* **28,** 195–201 (2001).

11. McCarthy, A. D., Etcheverry, S. B., Bruzzone, L., *et al.* Non-enzymatic glycosylation of a type I collagen matrix: effects on osteoblastic development and oxidative stress. *BMC Cell Biol.* **2,** 16 (2001).

12. Katayama, Y., Akatsu, T., Yamamoto, M., Kugai, N. & Nagata, N. Role of nonenzymatic glycosylation of type I collagen in diabetic osteopenia. *J. Bone Miner. Res.* **11,** 931–937 (2009).

13. Terada, M., Inaba, M., Yano, Y., *et al.* Growth-inhibitory effect of a high glucose concentration on osteoblast-like cells. *Bone* **22,** 17–23 (1998).

14. Valcourt, U., Merle, B., Gineyts, E., *et al.* Non-enzymatic glycation of bone collagen modifies osteoclastic activity and differentiation. *J. Biol. Chem.* **282,** 5691–5703 (2007).

15. Saito, M., Fujii, K. & Marumo, K. Degree of mineralization-related collagen crosslinking in the femoral neck cancellous bone in cases of hip fracture and controls. *Calcif. Tissue Int.* **79,** 160–168 (2006).

16. Yang, X., Mostafa, A. J., Appleford, M., Sun, L.-W. & Wang, X. Bone Formation is Affected by Matrix Advanced Glycation End Products (AGEs) In

Vivo. *Calcif. Tissue Int.* **99,** 373–383 (2016).

17. Avery, N. C. & Bailey, A. J. Enzymic and non-enzymic cross-linking mechanisms in relation to turnover of collagen: Relevance to aging and exercise. *Scand. J. Med. Sci. Sport.* **15,** 231–240 (2005).

18. Almora-Barrios, N., Austen, K. F. & de Leeuw, N. H. Density Functional Theory Study of the Binding of Glycine, Proline, and Hydroxyproline to the Hydroxyapatite (0001) and ($01\bar{1}0$) Surfaces. *Langmuir* **25,** 5018–5025 (2009).

19. Addadi, L. & Weiner, S. Control and Design Principles in Biological Mineralization. *Angew. Chemie Int. Ed. English* **31,** 153–169 (1992).

20. Stock, S. R. The Mineral–Collagen Interface in Bone. *Calcif. Tissue Int.* **97,** 262–280 (2015).

21. Jilka, R. L. The relevance of mouse models for investigating age-related bone loss in humans. *J. Gerontol. A. Biol. Sci. Med. Sci.* **68,** 1209–17 (2013).

22. Oliveira, M. I. A., Souza, E. M. de, Pedrosa, F. de O., *et al.* RAGE receptor and its soluble isoforms in diabetes mellitus complications. *J. Bras. Patol. e Med. Lab.* **49,** 97–108 (2013).

23. Karim, L., Moulton, J., Van Vliet, M., *et al.* Bone microarchitecture, biomechanical properties, and advanced glycation end-products in the proximal femur of adults with type 2 diabetes. *Bone* **114,** 32–39 (2018).

24. Burr, D. B. Bone material properties and mineral matrix contributions to fracture risk or age in women and men. *J. Musculoskelet. Neuronal Interact.* **2,** 201–204 (2002).

25. Fyhrie, D. P. & Schaffler, M. B. Failure mechanisms in human vertebral

cancellous bone. *Bone* **15,** 105–109 (1994).

26. Burr, D. B., Turner, C. H., Naick, P., *et al.* Does microdamage accumulation affect the mechanical properties of bone? *J. Biomech.* **31,** 337–345 (1998).

27. Schaffler, M. B., Pitchford, W. C., Choi, K. & Riddle, J. M. Examination of compact bone microdamage using back-scattered electron microscopy. *Bone* **15,** 483–488 (1994).

28. Wenzel, T. E., Schaffler, M. B. & Fyhrie, D. P. In vivo trabecular microcracks in human vertebral bone. *Bone* **19,** 89–95 (1996).

29. Seeman, E. Bone quality: The material and structural basis of bone strength. *J. Bone Miner. Metab.* **26,** 1–8 (2008).

30. Parfitt, A. M. Age-related structural changes in trabecular and cortical bone: Cellular mechanisms and biomechanical consequences. *Calcif. Tissue Int.* **36,** (1984).

31. Verborgt, O., Gibson, G. J. & Schaffler, M. B. Loss of osteocyte integrity in association with microdamage and bone remodeling after fatigue in vivo. *J. Bone Miner. Res.* **15,** 60–67 (2000).

32. Cardoso, L., Herman, B. C., Verborgt, O., *et al.* Osteocyte Apoptosis Controls Activation of Intracortical Resorption in Response to Bone Fatigue. *J. Bone Miner. Res.* **24,** 597–605 (2009).

33. Cheung, M. B. S. W., Majeska, R., Kennedy, O., *et al.* Osteocytes : Master Orchestrators of Bone. *Calcif. Tissue Int.* **94,** 5–24 (2014).

34. Kennedy, O. D., Herman, B. C., Laudier, D. M., *et al.* Activation of resorption in fatigue-loaded bone involves both apoptosis and active pro-osteoclastogenic

signaling by distinct osteocyte populations. *Bone* **50,** 1115–1122 (2012).

35. Hernandez, C. J. & Microstructure, A. Cancellous Bone. 15–22 (2016). doi:10.1007/978-1-4939-3305-1

36. Tang, S. Y. & Vashishth, D. A non-invasive in vitro technique for the three-dimensional quantification of microdamage in trabecular bone. *Bone* **40,** 1259–1264 (2007).

37. Napoli, N., Strotmeyer, E. S., Ensrud, K. E., *et al.* Fracture risk in diabetic elderly men: The MrOS study. *Diabetologia* **57,** (2014).

38. Bonds, D. E., Larson, J. C., Schwartz, A. V., *et al.* Risk of Fracture in Women with Type 2 Diabetes: the Women's Health Initiative Observational Study. *J Clin Endocrinol Metab* **91,** 3404–3410 (2006).

39. Wallander, M., Axelsson, K. F., Nilsson, A. G., Lundh, D. & Lorentzon, M. Type 2 Diabetes and Risk of Hip Fractures and Non-Skeletal Fall Injuries in the Elderly: A Study From the Fractures and Fall Injuries in the Elderly Cohort (FRAILCO). *J. Bone Miner. Res.* **32,** 449–460 (2017).

40. Majumdar, S. R., Leslie, W. D., Lix, L. M., *et al.* Longer duration of diabetes strongly impacts fracture risk assessment: The Manitoba BMD cohort. *J. Clin. Endocrinol. Metab.* **101,** (2016).

41. Vestergaard, P. Discrepancies in bone mineral density and fracture risk in patients with type 1 and type 2 diabetes - A meta-analysis. *Osteoporos. Int.* **18,** 427–444 (2007).

42. De Liefde, I. I., Van Der Klift, M., De Laet, C. E. D. H., *et al.* Bone mineral density and fracture risk in type-2 diabetes mellitus: The Rotterdam Study.

Osteoporos. Int. **16,** 1713–1720 (2005).

43. Schwartz, A. V., Vittinghoff, E., Bauer, D. C., *et al.* Association of BMD and FRAX Score With Risk of Fracture in Older Adults With Type 2 Diabetes. *JAMA* **305,** 2184 (2011).

44. Schwartz, A. V, Sellmeyer, D. E., Ensrud, K. E., *et al.* Older women with diabetes have an increased risk of fracture: a prospective study. *J. Clin. Endocrinol. Metab.* **86,** 32–38 (2001).

45. Brock, G. R., Kim, G., Ingraffea, A. R., *et al.* Nanoscale Examination of Microdamage in Sheep Cortical Bone Using Synchrotron Radiation Transmission X-Ray Microscopy. *PLoS One* **8,** e57942 (2013).

46. Wang, X. *Cortical Bone Mechanics and Composition: Effects of Age and Gender*. *Skeletal Aging and Osteoporosis* **5,** (2013).

47. Zhou, B., Sherry Liu, X., Wang, J., *et al.* Dependence of mechanical properties of trabecular bone on plate-rod microstructure determined by individual trabecula segmentation (ITS). *J. Biomech.* **47,** 702–708 (2014).

48. Liu, X. S., Sajda, P., Saha, P. K., Wehrli, F. W. & Guo, X. E. Quantification of the roles of trabecular microarchitecture and trabecular type in determining the elastic modulus of human trabecular bone. *J. Bone Miner. Res.* **21,** 1608–1617 (2006).

49. Melton, L. J., Riggs, B. L., Leibson, C. L., *et al.* A bone structural basis for fracture risk in diabetes. *J. Clin. Endocrinol. Metab.* **93,** 4804–4809 (2008).

50. Burghardt, A. J., Issever, A. S., Schwartz, A. V., *et al.* High-resolution peripheral quantitative computed tomographic imaging of cortical and

trabecular bone microarchitecture in patients with type 2 diabetes mellitus. *J. Clin. Endocrinol. Metab.* **95,** 5045–5055 (2010).

51. Starr, J. F., Bandeira, L. C., Agarwal, S., *et al.* Robust Trabecular Microstructure in Type 2 Diabetes Revealed by Individual Trabecula Segmentation Analysis of HR-pQCT Images. *J. Bone Miner. Res.* (2018). doi:10.1002/jbmr.3465

52. Hunt, H. B. Altered tissue composition, microarchitecture, and mechanical performance in cancellous bone from men with type 2 diabetes mellitus. *J. Bone Miner. Res.* (2018).

53. Bouxsein, M. L., Boyd, S. K., Christiansen, B. A., *et al.* Guidelines for assessment of bone microstructure in rodents using micro-computed tomography. *J. Bone Miner. Res.* **25,** 1468–1486 (2010).

54. Hildebrand, T. & Ruegsegger, P. Quantification of Bone Microarchitecture with the Structure Model Index. *Comput. Methods Biomech. Biomed. Engin.* **1,** 15–23 (1997).

55. Salmon, P. L., Ohlsson, C., Shefelbine, S. J. & Doube, M. Structure Model Index Does Not Measure Rods and Plates in Trabecular Bone. *Front. Endocrinol. (Lausanne).* **6,** 162 (2015).

56. Liu, X. S., Sajda, P., Saha, P. K., *et al.* Complete Volumetric Decomposition of Individual Trabecular Plates and Rods and Its Morphological Correlations With Anisotropic Elastic Moduli in Human Trabecular Bone. *J. Bone Miner. Res.* **23,** 223–235 (2007).

57. Torres, A. M., Matheny, J. B., Keaveny, T. M., *et al.* Material heterogeneity in

cancellous bone promotes deformation recovery after mechanical failure. *Proc. Natl. Acad. Sci.* **113,** (2016).

58. Oliver, C. & Pharr, M. An improved technique for determining hardness and elastic modulus using load and displacement sensing indentation experiments. *J. Mater. Res.* **7,** 1564–1583 (1992).

59. Constantinides, G., Ravi Chandran, K. S., Ulm, F. J. & Van Vliet, K. J. Grid indentation analysis of composite microstructure and mechanics: Principles and validation. *Mater. Sci. Eng. A* **430,** 189–202 (2006).

60. Uskokovic, P. S., Tang, C. Y., Tsui, C. P., Ignjatovic, N. & Uskokovic, D. P. Micromechanical properties of a hydroxyapatite/poly-l-lactide biocomposite using nanoindentation and modulus mapping. *J. Eur. Ceram. Soc.* **27,** 1559–1564 (2007).

APPENDIX A

PROTOCOL FOR MICRODAMAGE STAINING USING LEAD URANYL ACETATE

Summary: This protocol describes how to stain for microdamage in human cancellous bone using lead uranyl acetate. For cancellous bone cores, this staining should be performed after the pre-mechanical testing microCT scan and after mechanical testing.

Chemical List:

Chemical	Supplier	Catalog Number
Uranyl acetate dihydrate	Electron Microscopy Sciences	22400 (25 g)
Lead(II) acetate trihydrate	Sigma-Aldrich	467863-250G
Ammonium sulfide 20% aq solution	Sigma-Aldrich	A1952-500ML
Acetone, 99.5%	Acros (Fisher)	67-64-1

I. Before you begin…

1) Everything must be performed in the hood, even weighing chemicals.
2) Read attached Appendix I to familiarize yourself with the specific hazards of this process.
3) A description of how each solution is made is given in Appendix II.
4) Typically, 10-15 mL of lead uranyl acetate stain is needed to cover an 8 mm diameter x 10 mm length cancellous bone core.

II. Sample Preparation

1) Remove marrow from cancellous bone cores using DI water and water pick.
2) Place sample in 70% acetone to fix. See Appendix II for notes on how to make 70% acetone.
3) Put on shake table at a low speed for at least one day.

III. Preparing Lead Uranyl Acetate Solutions

Uranyl Acetate

1) Prepare solution of 8% uranyl acetate in 70% acetone in an amber glass bottle. See Appendix II for notes on how to make the uranyl acetate solution.
2) Wrap bottle in aluminum foil to prevent light exposure.

3) Place small magnetic stir bar in solution and let stir on stir plate in fume hood for at least one day.

Lead Acetate

4) Prepare solution of 20% lead (II) acetate in 70% acetone in a glass bottle. See Appendix II for notes on how to make the lead acetate solution.
5) Place small magnetic stir bar in solution and let stir on stir plate in fume hood for at least two hours, but preferably longer.

Lead Uranyl Acetate

6) Combine uranyl acetate and lead acetate (of equal volumes) into an amber glass bottle. You can use the same bottle from the uranyl acetate step and just add the lead acetate to your uranyl acetate solution. The final solution will have a yellowish-orange milky color (it looks like a mango smoothie).
7) Wrap with foil.
8) Continue to stir on stir plate in fume hood for at least one hour.

IV. Staining Samples

LUA Staining

1) Add solution to bone samples. Typically if using the wide-mouth glass vials, 10-15 mL of lead uranyl acetate is enough to submerge an 8 mm diameter x 10 mm length cancellous bone core. See Figure 6.7-1below.

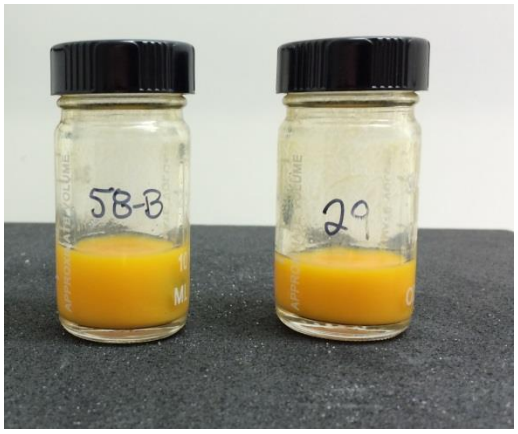

Figure 6.7-1: Samples in LUA Stain

2) Wrap each vial with foil.
3) Place on shake table in fume hood at a speed of 120 rpm. This is an adequate speed to prevent the stain from settling, but not so fast as to damage the samples.
4) If staining many samples at a time, you can combine the foil-wrapped-vials in a secondary container, like an old micropipette tip box. Make sure vials are secure on the shake table and make sure there is no light penetration of staining solution.

5) Let samples shake in stain for 14 days.

Fixing LUA Stain with Ammonium Sulfide

6) Note: This step is very smelly!! Warn people in the lab.
7) Remove bone sample from LUA stain and rinse with 70% acetone.
8) Create 1% ammonium sulfide in 70% acetone solution. See Appendix II for this recipe.
9) Place bone sample in ammonium sulfide solution for one week, changing the solution after three days. Sample will turn black immediately, this is normal.
10) Keep sample vials wrapped in foil and on shake table.
11) After one week of soaking in ammonium sulfide, rinse samples with 70% acetone.
12) Place samples back in 70% acetone for up to 1 week. This will help remove smell.

Sonicate

13) Rinse samples again with 70% acetone.
14) Sonicate for 10 minutes in 70% acetone to remove solution from the pores.

V. Waste Removal and Cleanup

1) Note: Lead uranyl acetate is both toxic *and* radioactive, so it needs a special radioactive waste removal. Appendix III is the email conversation between Heather and an EHS employee specifying the waste removal procedure. Keep this email as a record (just in case)!
2) All liquid waste solutions should be placed in a glass waste container. You can usually use the amber glass bottle from the uranyl acetate solution step. Label properly!
3) All solid waste, including sample vials, beakers, weigh boats, etc., needs to be placed in a ziplock bag clearly labeled "Radioactive Waste".
4) You will need to call and order a radioactive waste pickup from EHS, which is separate from the usual waste pickup.

APPENDIX B

WORK IN PROGRESS: SUMMARY OF DV/BV RESULTS

The following tables and figure are preliminary results of the microdamage assessment of the femoral neck cancellous specimens from Chapter 5 that were compressed to 3% strain.

Notes: These damage volume calculations are *not* ready for publication. Many of the samples need to be further cleaned before doing a damage analysis (see final column on Table 2). The cleaning process involves removing globs of stain by subtracting the initial, unstained microCT image stacks from the stained microCT image stacks. Also, many of these specimens were later cleaned through the ITS analysis procedures, so the DV/BV from those calculations (when done) should most likely be used instead of these values.

Table 1 and Figure 1 summarize the preliminary results. There was no difference between DV/BV between groups. DV/BV also did not correlate with patient age or HbA1c

Table 1: N, mean, and standard deviation by group. Student's t-test used to assess group-wise difference.

	Age	**HbA1c**	**DV/BV**
Non-DM count	36	36	22
T2DM count	33	33	22
Non-DM average	61.4	5.55	0.056
Non-DM stdev	9.0	0.41	0.044
T2DM average	64.9	7.11	0.047
T2DM stdev	8.8	0.91	0.044
% difference	5.7	28.01	-15.012
Student's t-test	0.109	0.000	0.532

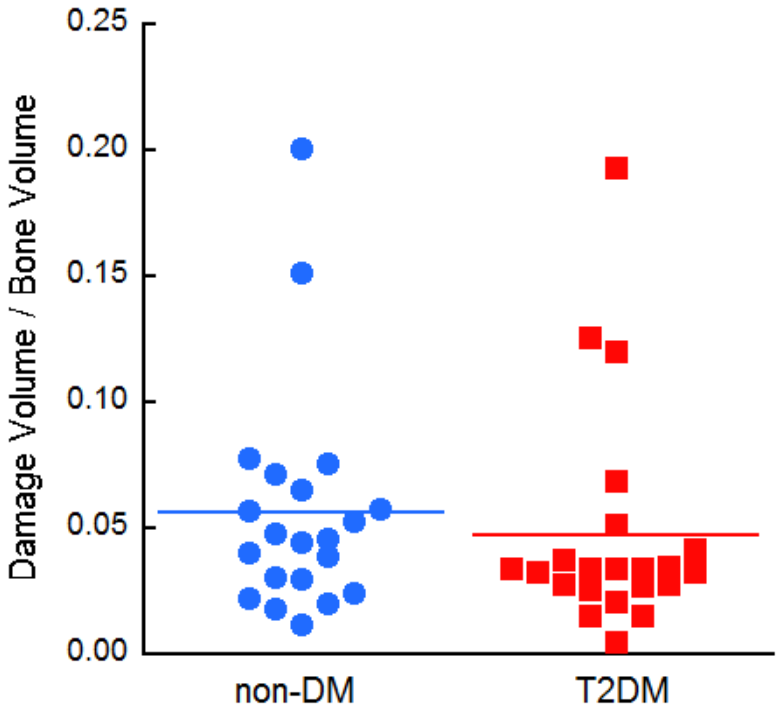

Figure 1: Preliminary microdamage results for cancellous specimens mechanically compressed to 3% strain (see Chapter 5).

Table 2: Notes on DV/BV calculations.

Group	Core Number	Age	HbA1c	DV/BV	Further cleaning required?
Non-DM	52	44	6.44	0.039	maybe
Non-DM	33	47	5.20	0.057	maybe
Non-DM	165	47	5.00	0.201	no
Non-DM	80B	50	5.16	0.075	no
Non-DM	40	51	5.78		not stained
Non-DM	128	51	5.56	0.053	no
Non-DM	22B	52	5.67	0.045	no
Non-DM	72	55	6.04		
Non-DM	152	55	5.10	0.152	no
Non-DM	116	56	5.57		yes
Non-DM	122B	56	5.92	0.058	maybe
Non-DM	48	57	5.88		not stained
Non-DM	37	58	6.17		not stained
Non-DM	62B	58	5.59	0.018	maybe
Non-DM	159	58	5.10	0.020	no
Non-DM	6	60	5.21		not stained
Non-DM	154	60	5.40	0.030	no
Non-DM	12	62	5.37	0.066	no
Non-DM	39B	62	5.67	0.048	no
Non-DM	157	62	5.30		not stained
Non-DM	17	63	5.51	0.039	maybe
Non-DM	121	63	5.37	0.025	no
Non-DM	161	63	7.00		yes
Non-DM	84	65	5.42		not stained
Non-DM	23	66	5.49	0.012	maybe
Non-DM	123B	66	5.65	0.041	no
Non-DM	13	67	4.97		not stained
Non-DM	151	67	5.80	0.078	no
Non-DM	9B	68	5.45	0.046	no
Non-DM	75	70	5.64		yes
Non-DM	5	72	5.21		
Non-DM	149	73	5.20	0.071	no
Non-DM	38B	74	5.37	0.023	no
Non-DM	44	75	5.62	0.030	maybe
Non-DM	36	78	5.50		not stained
Non-DM	16	81	5.58		not stained

Group	Core Number	Age	HbA1c	DV/BV	Further cleaning required?
T2DM	29	52	8.64	0.005	maybe
T2DM	24	53	6.34		
T2DM	27	54	6.98		not stained
T2DM	170	54	9.30	0.033	no
T2DM	32	56	6.62		not stained
T2DM	145	56	7.00		not stained
T2DM	156	56	5.70	0.052	no
T2DM	160	56	6.80	0.069	maybe
T2DM	146	58	6.50		not stained
T2DM	155	58	6.30	0.126	maybe
T2DM	166B	58	8.70	0.028	no
T2DM	169	58	7.50	0.034	maybe
T2DM	51B	61	6.12	0.016	maybe
T2DM	162	61	6.00	0.028	no
T2DM	31	63	6.60		
T2DM	164	63	6.80	0.193	no
T2DM	163	64	8.80		not stained
T2DM	167	64	6.50	0.034	redone already
T2DM	168	65	7.30	0.035	redone already
T2DM	76B	66	7.28		yes
T2DM	88	68	7.08	0.033	no
T2DM	35B	69	6.98	0.042	no
T2DM	96	70	7.54	0.021	maybe
T2DM	19	73	5.93		
T2DM	64	73	6.60	0.034	maybe
T2DM	112	74	7.08	0.034	maybe
T2DM	41B	75	8.83	0.027	no
T2DM	46	75	7.65		not stained
T2DM	153	75	7.50	0.120	maybe
T2DM	70B	76	6.51	0.038	no
T2DM	43B	77	7.34		
T2DM	59	77	7.60	0.015	no
T2DM	34B	85	6.16	0.025	no

APPENDIX C

PROTOCOL FOR ITS ANALYSIS ON CANCELLOUS CORES

Notes: This protocol describes the steps I used to perform ITS analysis on the cancellous cores from Chapter 5. The ITS software stopped working around June 2018, and I was not able to finish running all of my specimens. In theory, once the ITS software bugs have been fixed, the following steps will work perfectly. All of the specimens I prepped for ITS analysis have a .raw and .aim file on the "Heather Cancellous" hard drive (so you can skip to step 6 for these). All of the referenced Matlab codes are in the Donnelly Lab archive folder under /Heather Hunt/ITS.

1) Output LUA scan into stack of tiffs using Scanco and Filezilla.
2) Clean LUA images with Matlab
    a. Crop to 8-9 mm (outer core)
    b. Clean (threshold, Gaussian blur, etc.)
    c. Make binary
    d. Convert binary and clean to 21 um resolution
    e. Save all of these steps in the sample folder
3) Save 21 um clean binary tiffs as .raw file
    a. Use Biomech 10
    b. Import -> Binary -> Despecle -> Purify -> Save as .raw
4) Transfer to Biomechanics Lab Scanco
    a. Filezilla into folder [MICROCT.DATA.00000773]
5) Convert .raw to .aim
    a. @rawaim3.com;12
6) Transfer .aim file back to hard drive using Filezilla
7) Run ITS software on Biomech 10
    a. Processing -> Batch Processing -> select all .aim files you want to run
8) Run ITS_BoneMatrix_Aim4_HH.m
    a. Makes .seg files for orientation and type
9) Import .seg files into ImageJ and save as stack of tiffs into relevant folder (folder 7)
    a. 16 bit signed integer
    b. 0 header
    c. 0 spaces between slices
    d. x, y, z from image stack
10) Make inner core mask using ImageJ (to exclude the damaged edges)
    a. Save as sample#_inner core_mask.tif

11) Run ITS_DamageTypeOri_Analysis_July172018.m
    a. Makes all flavors of trabecula images (e.g. longitudinal plate, oblique rod) and saves them in the appropriate folder
    b. Multiplies all relevant things by the inner core mask
    c. Overlaps stain from folder 4.5 with each flavor of trabecula and saves in step 8 folder
    d. Runs analysis on inner 286 slices of inner core masked images (so final analysis is on 6 mm diameter by 6 mm in length core)
    e. Output excel file sample#_IC Short – ITS Analysis Pixel Counts.

APPENDIX D

ITS PROGRESS CHECKLIST

Notes: This checklist describes the step I was at with the ITS analysis as of August 1, 2018. The designation of _Kelsie or _Jesse indicates that either Kelsie or Jesse performed pre-ITS analysis "cleaning" to remove stain chunks. The designation of B or C indicates the second or third core, respectively, obtained from a specimen.

Sample Name	Notes	Convert to .raw	Convert to .aim	Run ITS software
9B Stained	good, ends just ok	yes	yes	yes
96 Stained	scraggly, needs extra attention	yes		
96 Kelsie Stained				
9 Stained	fine, ends not great	yes	yes	yes
88 Stained	slightly slanted, but probably ok	yes	yes	yes
80B Stained	almost good, minor chunks	yes	yes	yes
80B Kelsie Stained				
80 Stained	almost good, minor chunks	yes	yes	yes
76C Stained	fine	yes	yes	yes
76B Stained	slightly slanted, stain on edges but may be ok	yes	yes	yes
75 Stained	very messy - needs special attention			
75 Kelsie Stained				
72B Stained	??			
70B Stained	mostly good, but some chunks	yes	yes	yes
70B Kelsie Stained				
64 Stained	fine ac K	yes	yes	yes
64 Jesse Stained	good	yes	yes	yes
62B Stained	almost good, minor chunks	yes	yes	yes
62B Kelsie Stained				
59A Stained	slightly slanted, ends not great	yes	yes	yes
58B Stained	fine ac K	yes	yes	yes
58B Jesse Stained	redo	yes	yes	yes
53B Stained	use redo by Kelsie	yes	yes	yes
53B Jesse	use redo by Kelsie	yes	yes	yes

Stained				
52 Stained	check with K	yes	yes	yes
52 Jesse Stained	use redo by Kelsie	yes	yes	yes
51B Stained	slightly slanted, may be ok	yes	yes	yes
51B Kelsie Stained				
51 Stained	stain on edges, may be ok	yes	yes	yes
46 Stained	??			
44 Stained	slanted, maybe messy stain, could be ok	yes	yes	yes
41B Stained	use redo by Kelsie	yes	yes	yes
41B Kelsie Stained				
41B Jesse Stained	maybe ok, maybe use K's	yes	yes	yes
39B Stained	redo	yes	yes	yes
39B Kelsie Stained				
38B Stained	good	yes	yes	yes
38 Stained	??			
38 Kelsie Stained				
35B Stained	use redo by Kelsie			
35B Kelsie Stained				
35B Jesse Stained	use redo by Kelsie	yes	yes	yes
34B Stained	fine, some chunks	yes	yes	yes
33 Stained	use redo by Kelsie	yes	yes	yes
33 Kelsie Stained				
33 Jesse Stained	use redo by Kelsie	yes	yes	yes
29 Stained	scraggly edges, slanted, needs extra attention	yes		
23 Stained	scraggly edges, needs extra attention	yes		
22B Stained	good	yes	yes	yes
170 Stained	slightly slanted, but probably ok	yes	yes	yes
17 Stained	messy, needs extra attention	yes		
169 Stained	too thick, needs extra attention	yes		
169 Kelsie Stained				
168 Stained	stain on edges	yes	yes	yes
167 Stained	slanted, ends chunked, lots of stain chunks	yes		
167 Kelsie				

Stained				
166B Stained	good, edges just meh	yes	yes	yes
165 Stained	slanted and ends chunked	yes	yes	yes
164 Stained	good, but slanted	yes	yes	yes
162 Stained	a little messy, but may be ok?	yes	yes	yes
161 Stained	good, but slanted	yes	yes	yes
160A Stained	stain on edges, maybe have K redo	yes	yes	yes
159 Stained	stain on edges, but probably ok	yes	yes	yes
158 Stained	good, but slightly slanted, may be ok	yes	yes	yes
156 Stained	good	yes	yes	yes
155 Stained	random splotches, should be easy to fix	yes		
154 Stained	stain chunks, maybe only on edges	yes		
154 Kelsie Stained				
153 Stained	too thick, needs extra attention	yes		
153 Kelsie Stained				
152 Stained	square, but ok, ends not great	yes	yes	yes
151 Stained	good, ends are just meh	yes	yes	yes
149 Stained	slanted, missing pieces?	yes		
134 Stained	big chunks of bone missing and weird stain	yes		
128 Stained	good, but slanted	yes	yes	yes
123B Stained	good, but slightly slanted	yes	yes	yes
122B Stained	slanted, scraggly, but not terrible	yes	yes	yes
122A Stained	too thick, needs extra attention	yes		
122A Kelsie Stained				
121 Stained	slightly slanted, thick??	yes		
12 Stained	fine	yes	yes	yes
118 Stained	good	yes	yes	yes
116 Stained	stain chunks in middle, needs extra attention	yes		
116 Kelsie Stained				
113 Stained	good	yes	yes	yes
112 Stained	too thick, needs extra attention	yes		
112 Kelsie Stained				

APPENDIX E

PRELIMINARY ITS AND MICRODAMAGE RESULTS

Notes: The protocol outlined in Appendix C was followed to obtain the following results. Briefly, the femoral neck cancellous cores from Chapter 5 were compressed to 3% strain, stained with LUA for microdamage, and analyzed using ITS software. The results detailed here are on the inner 6 mm diameter and 6 mm length core which minimizes damage due to specimen prep (coring and cutting) and mounting for mechanical testing (gluing ends).

The following specimens were successfully analyzed for microdamage and trabecular morphology with the ITS software, but they are not age-matched or otherwise paired:

Group	Core Number	Age	A1C
Non-DM	9	68	5.45
Non-DM	12	62	5.37
Non-DM	123B	66	5.65
Non-DM	128	51	5.56
Non-DM	151	67	5.80
Non-DM	152	55	5.10
Non-DM	159	58	5.10
T2DM	34B	85	6.16
T2DM	88	68	7.08
T2DM	156	56	5.70
T2DM	162	61	6.00
T2DM	164	63	6.80
T2DM	166B	58	8.70
T2DM	170	54	9.30

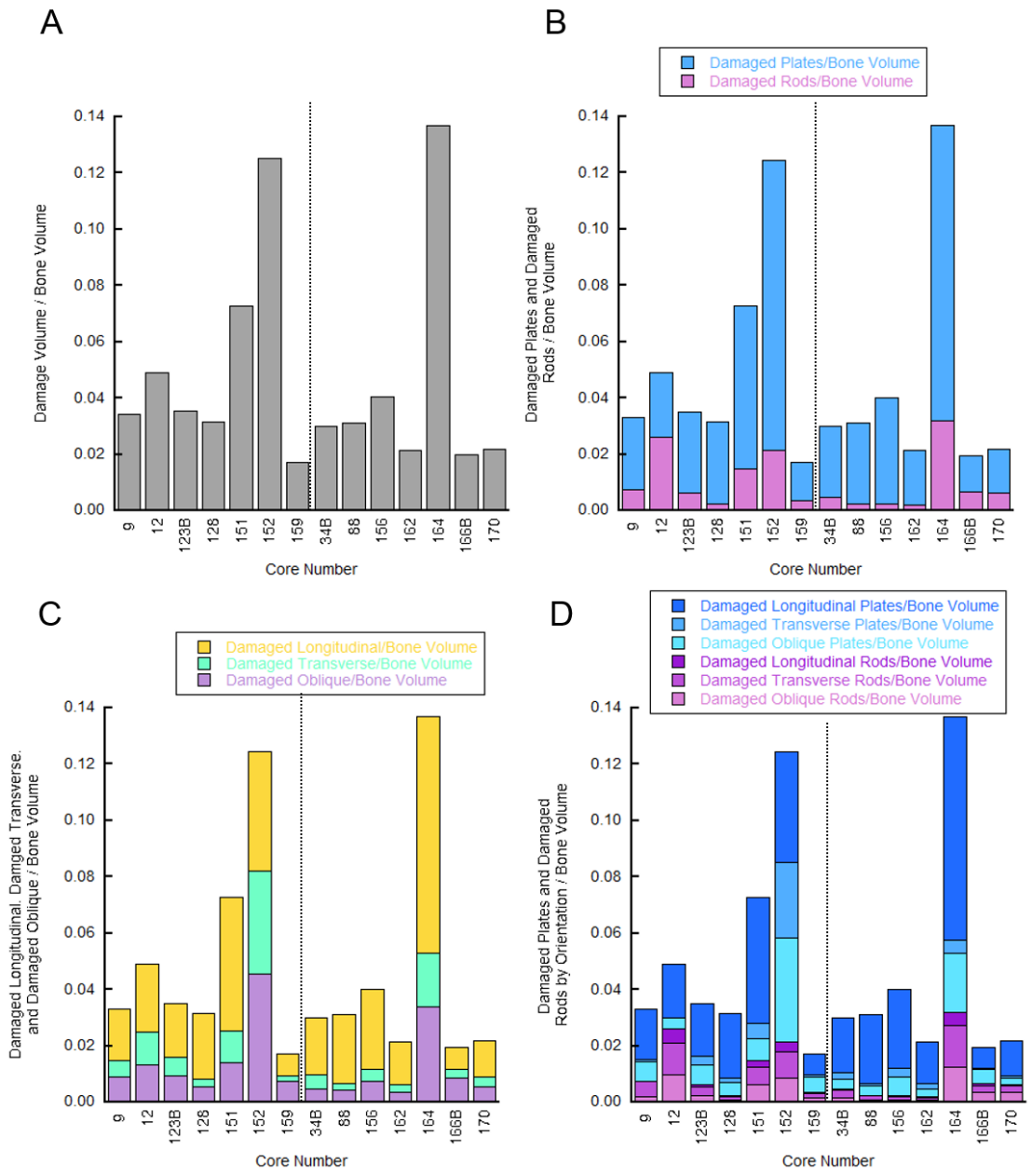

Figure 1: Damaged volume per bone volume categorized by ITS by (B) plate vs. rod, (C) longitudinal vs. transverse vs. oblique, and (D) plate/rod and orientation for each specimen. Non-DM group specimens are to the left of the vertical dashed line and T2DM group specimens are to the right. There were no significant differences between groups for the above classifications of damage.

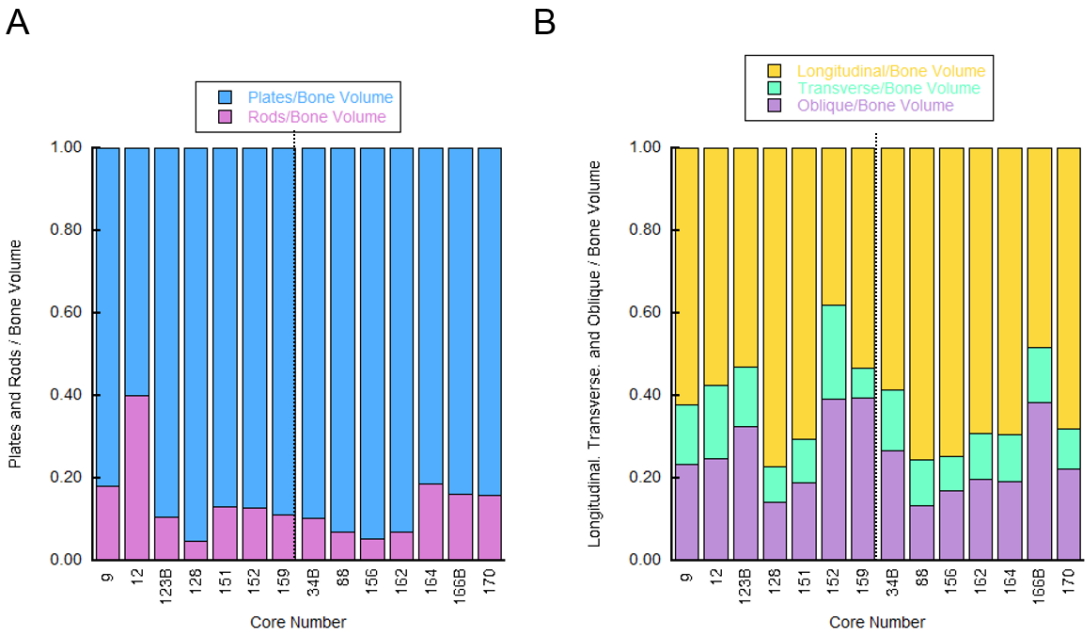

Figure 2: (A) Plate and rod volume per bone volume. (B) Longitudinal, transverse, or oblique orientation per bone volume. Non-DM group specimens are to the left of the vertical dashed line and T2DM group specimens are to the right. There were no significant differences between groups for the above classifications of trabeculae.